N° d'ordre : 4464

THÈSE DE DOCTORAT

PRESENTEE A

L'UNIVERSITÉ BORDEAUX I

ECOLE DOCTORALE DES SCIENCES CHIMIQUES

Par **Rumi TAMOTO**

POUR OBTENIR LE GRADE DE

DOCTEUR

SPÉCIALITÉ : CHIMIE-PHYSIQUE

****

Nano/Micro Auto-Assemblages Chiraux de Tensioactifs Cationiques:
du comportement dynamique des architectures supramoléculaires jusqu'aux
nanomatériaux hybrides

****

Chiral Nano/Micro Self-Assemblies of Cationic Surfactants:
from dynamic behavior of supramolecular architectures towards hybrid nanomaterials

****

Soutenue le : **19 décembre 2011**

Après avis de :

M.	N. AVARVARI	Directeur de Recherche, CNRS, Université Angers	**Rapporteur**
M.	C. TRIBET	Directeur de Recherche, CNRS, École Normale Supérieure	**Rapporteur**

Devant la commission d'examen formée de :

Mme	M.-H. DELVILLE	Directeur de Recherche, CNRS, Université Bordeaux I	**Examinateur**
M.	K. KINBARA	Professeur, Université Tohoku	**Examinateur**
Mme	S. LECOMTE	Chargé de Recherche, CNRS, Université Bordeaux I	**Examinateur**
Mme	R. ODA	Directeur de Recherche, CNRS, Université Bordeaux I	**Directrice de thèse**

– 2011 –

N° d'ordre : 4464

THÈSE DE DOCTORAT

PRESENTEE A

L'UNIVERSITÉ BORDEAUX I

ECOLE DOCTORALE DES SCIENCES CHIMIQUES

Par **Rumi TAMOTO**

POUR OBTENIR LE GRADE DE

DOCTEUR

SPÉCIALITÉ : CHIMIE-PHYSIQUE

****

Nano/Micro Auto-Assemblages Chiraux de Tensioactifs Cationiques:
du comportement dynamique des architectures supramoléculaires jusqu'aux
nanomatériaux hybrides

****

Chiral Nano/Micro Self-Assemblies of Cationic Surfactants:
from dynamic behavior of supramolecular architectures towards hybrid nanomaterials

****

Soutenue le : **19 décembre 2011**

Après avis de :

M.	N. AVARVARI	Directeur de Recherche, CNRS, Université Angers	**Rapporteur**
M.	C. TRIBET	Directeur de Recherche, CNRS, École Normale Supérieure	**Rapporteur**

Devant la commission d'examen formée de :

Mme	M.-H. DELVILLE	Directeur de Recherche, CNRS, Université Bordeaux I	**Examinateur**
M.	K. KINBARA	Professeur, Université Tohoku	**Examinateur**
Mme	S. LECOMTE	Chargé de Recherche, CNRS, Université Bordeaux I	**Examinateur**
Mme	R. ODA	Directeur de Recherche, CNRS, Université Bordeaux I	**Directrice de thèse**

– 2011 –

A Timothée

- Acknowledgement -

- Outline -

Chapter II : Micrometric helical structures from nucleolipids

Chapter IV : Mineralization through bio-inspired materials: Bibliographic study

Chapter V : Gold nanoparticles deposition on silica nanohelices: A novel 3D substrate for optical sensing

- *General introduction* -

Molecular self-assembly is ubiquitous in nature, which can provide attractive architectures. Self-assembly describes the spontaneous association of numerous individual entities into a coherent organization and well-defined structure to maximize the benefit of the individual without external instruction. This is an extremely powerful tool to engineer functional materials through the construction of complex structures starting from smaller, simpler subunits, avoiding tricky synthetic manipulations. These self-assembled structures mainly results from non-covalent and weak interactions, which can build up the hierarchically controlled structures over a wide size dimension ranging from 0.1 nm ~ macroscopic scales. Due to the non-covalent bonding, the formation of these self-assembled structures is reversible in nature. This is an advantage, since the process can be in principle designed to be controlled by external stimuli. However, this also presents a disadvantage, since the self-assembled architectures can be fragile in nature, and their lack of robustness can limit their practical applications. To counter this problem, these structures can be mineralized to impart stability and strength, still retaining the complexity of the original assembly. This approach combines the advantages of the 'bottom-up' self-assembly approach with the durability of inorganic nanostructures.

In this thesis, we first give a comprehensive introduction on the general aspects of the self-assembly of amphiphilic molecules. We investigate how the amphiphiles can define to organize the morphology in chapter I of bibliographical study. Particularly, we focus on the control of various chiral fibrous morphologies obtained by chiral amphiphile. In addition, we have interests about "out-of-equilibrium" process in chiral supramolecular aggregates, especially *in situ* morphology transition caused by external factors.

Oda's group has been working on the self-assembly of non-chiral cationic surfactants, with chiral counterions, wherein, the chirality of the anion introduces chirality in the self-assembled amphiphile membrane. In continuation of this work, in Chapters II and III,

utilizing the fact that the counterions regulate the organization of this self-assembly system, we demonstrate that these chiral morphologies can be controlled by the exchange of the counterions. In particular, *in situ* achiral (vesicle, micelle) to chiral (helix), or handedness transition are performed at constant temperature.

In chapter IV, we study mineralization; especially we focus on the chiral silica, which was obtained by self-assembled chiral amphiphiles as organic template via sol-gel polycondensation. We show that the organic structures (generated from amine based gemini amphiphiles) can be successfully transcribed, generating twisted ribbons, helices and nanotubes of silica

In the last chapter, we discuss the functionalization of these silica nanostructures, and the subsequent organization of gold NPs on these nanofibers, and demonstrate the viability of these materials as SERS substrates.

Chapter I

Supramolecular structures by self-assembled amphiphiles: Bibliographic study

I.1 Introduction

Self-assembly is the driving force for the formation of numerous nanometric to micrometric scale structures from a broad diversity of building blocks. Understanding self-assembly is important both from scientific and technological point of view, in particular comprehending a number of systems in nature.[1,2] For example, the cell contains an amazing range of complex structures such as lipid membrane, folded proteins, protein aggregates, molecular machines, and various structures of biological molecules are designed by self-assembly.[3] Molecular self-organization has been emerged as a discrete field of synthetic strategy.

Since several decades, various structures derived from molecular self-assembly have been reported. These include monolayers,[4] lipid bilayers,[5] molecular crystals,[6] but also phase separated polymers,[7] folding the polypeptide chains into proteins,[8] as well as the association of a ligand with a receptor.[9]

The study of self-assembled supramolecular systems is an attractive approach for the construction of complex in chemistry, material science and biology.[10] Supramolecular architectures have largely capitalized on non-covalent and weak interactions, such as coordinate bonding, ionic interactions, $\pi-\pi$ stacking, van der Waals binding, hydrophobic effect, and particularly hydrogen bonding.[11,12] An example of stepwise process of supramolecular structures based on molecular process are shown in Figure I.1; the monomeric building block is stacked and self-assemble to a supramolecular structure.
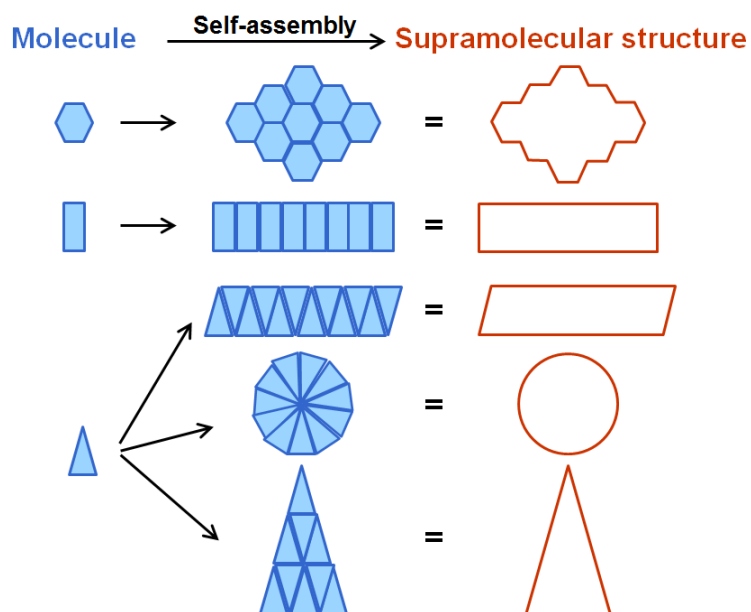
Figure I.1 Schematic illustrations of building block process *via* molecular self-assembly.

Among the self-assembled supramolecular systems, amphiphilic molecules represent particularly common behavior. Molecular amphiphilicity (amphi : from the Greek amphi- : on both sides : of both kinds, phile : from Greek–philos–philous: lover: one having an affinity for or strong attraction (Merriam-Webster's Collegiate® Dictionary, Tenth Edition)) can be defined as chemical character of molecules to have two or more parts with each part having different affinities for solvents that do not mix with each other, among which, the most common example will be those having both hydrophilic headgroup (polar) and hydrophobic tail (non-polar) (Figure I.2).[13] This character is the origin of aggregation processes.
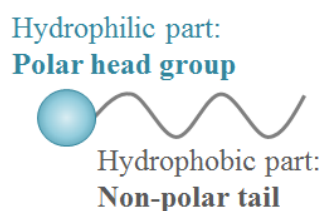
Figure I.2 Schematic illustration of structure of amphiphilic molecule.

The head groups of amphiphilic molecules can be charged (cationic or anionic) or neutral (non-ionic or zwitterionic). Non-ionic head group is generally composed by sugar, or oxyethylene, *etc*. The most general hydrophobic chains are formed by hydrocarbons with 5-22

carbon atoms. In the aqueous medium, these molecules are self-assembled with each other such that their hydrophobic parts are laterally-directed, and their hydrophilic parts show inward direction.

Amphiphilic molecules are generally categorized five groups (Figure I.3): monomeric amphiphiles which have one hydrophilic head group and one hydrophobic chain (A), the bulky amphiphiles which are typified by lipid have one hydrophilic head group and two hydrophobic chain (B), gemini or molecules which have spacers between two or more head groups and each having a hydrophobic tails (C), the cationic or anionic amphiphiles (D) and bola amphiphile (E).
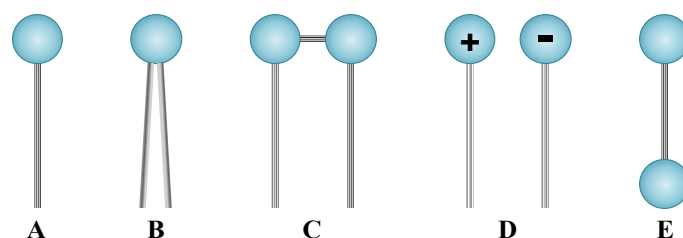
Figure I.3 Schematic illustration of 5 classified amphiphilic molecules.

In this chapter, we will present the bibliography of self-assembled supramolecular structures, which can form particularly chiral nano to micrometric fibers. At first, we will describe the various supramolecular morphologies depending on the amphiphilic molecules, and then present some examples of chiral fibers. In the next step, we will present the effect of counter-anion on the construction of such fibers. One section of this chapter will also be devoted to the out-of-equilibrium system in natural self-assembled structures.

I.2 Aggregation behaviour of amphiphiles in solution

I.2.1 Phase behaviors of the assemblies of amphiphilic molecules

The properties of amphiphiles are widely used for the detergents, wetting agents, dispersing agents or bubble with numerous applications. In biological systems, the amphiphiles

are also crucial factors because an important part of cell membranes is composed by phospholipids aggregation of which leads to the formation of lipid bilayer.

When amphiphilic molecules are dissolved in water, their hydrophobic groups are directed away from the water and the free energy of the solution is minimized.[14] This effect is called "hydrophobic effect". Figure I.4 summarizes several mechanisms of self-assembled amphiphiles in order to limit the increasing of free energy.
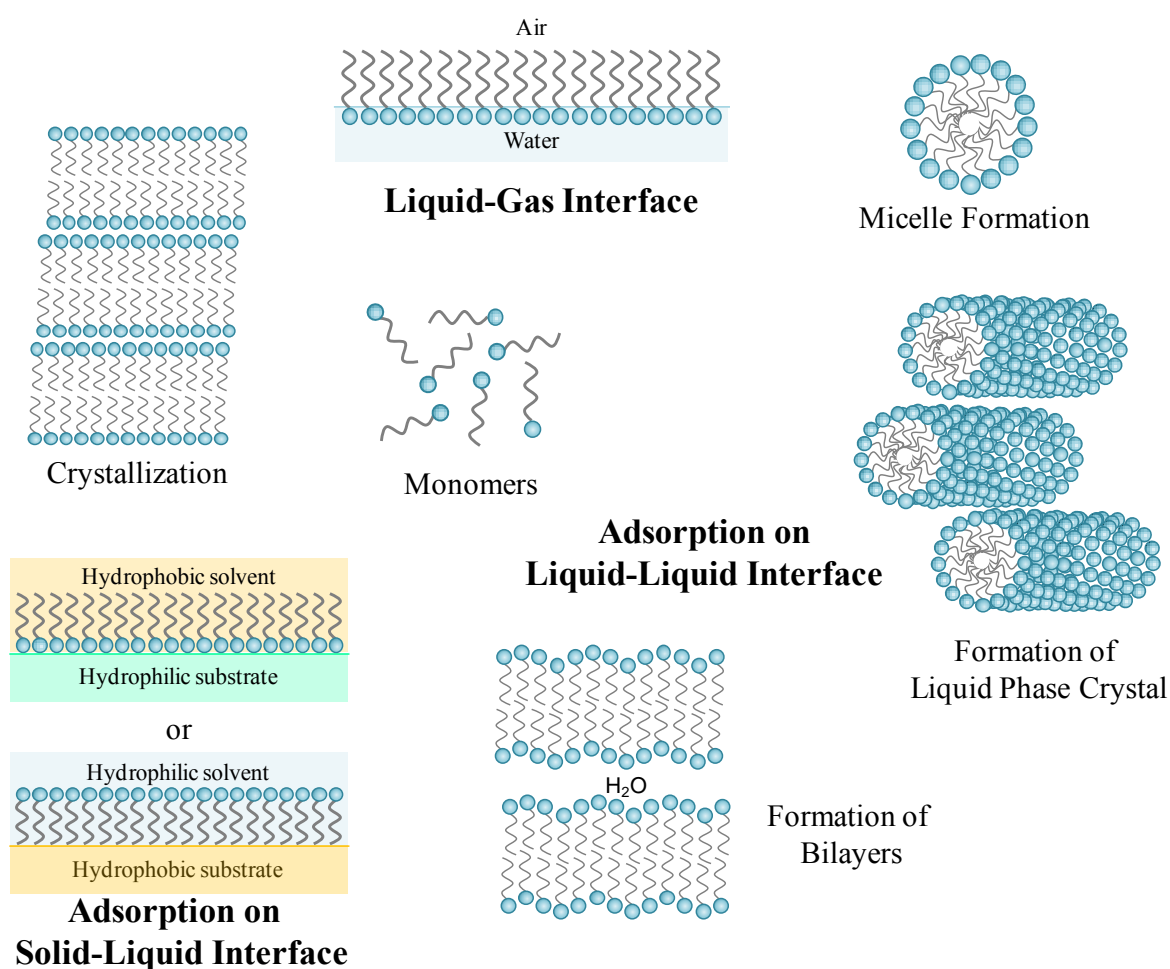
Figure I.4 Schematic illustrations of typical aggregations and adsorption by self-assembled amphiphiles at the surface and interface.

In aqueous solutions, the amphiphiles are oriented with a hydrophobic tail inside (away from water), and hydrophilic head outside; the smallest structure of this kind is called "micelle". To form micelles, the concentration and temperature are particularly important

parameters. These two physicochemical parameters are typically used for describing the micelle formation (Figure I.5).

Critical micelle concentration (cmc) is the minimum concentration from which the surfactant changes from soluble monomeric state to soluble aggregation (micelles or lamellar phases) states in water. Furthermore, micelles are only formed above specific temperature, Kraft point. The micellisation is a spontaneous phenomenon in the aspect of thermodynamics, which leads to a significant increase in the solubility of the surfactant.

Krafft temperature (T_k) is the minimum temperature at which surfactants form micelles. There is no value for the CMC below the Krafft temperature whereas the solubility of surfactant increases constantly after leaching Krafft point because the dominant species in solution is no longer the surfactant monomer, but the micelle. When the temperature is lower than T_k, the amphiphiles form precipitate/gel instead of solubilizing in water.
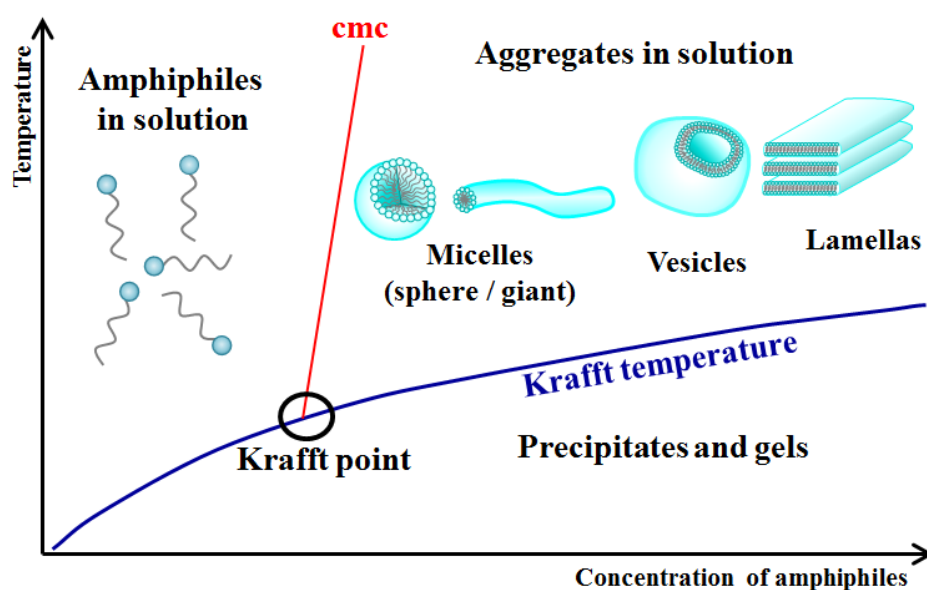
Figure I.5 Diagram of aggregation of amphiphiles in solution. The functions are depending on the concentration and temperature.

Just above cmc, micelle is formed by around 50 to a hundred amphiphiles. When the concentration of surfactants in water is increased, the aggregation number of micelles increases

gradually and they transform to rod-like micelle, vesicles, then, liquid crystal structures such as cubic phase, hexagonal phase or lamellar phase.

I.2.2 Various self-assembled morphologies

Israelachvili proposed the packing parameter p of amphiphilic molecules, which describes the relationship between the molecular architecture of the amphiphilic molecules based on the molecular structure and the shape of aggregate structures formed in solution.[15] This parameter is defined as follows: $p = v/a_0l$ (a_0 is the area per head group, l is the effect length of hydrophobic chain(s), and v is the volume of the hydrophobic chain(s)). With a very simple approximation, one can approximate v/l as the area per hydrophobic chain. Therefore, p is the ratio of area per chain over area per head group of amphiphilic molecules at interface. As shown schematically in Figure I.6, the value of p is closely related to the morphologies of the amphiphile aggregates.

Packing parameter: $p = V/a_0l$
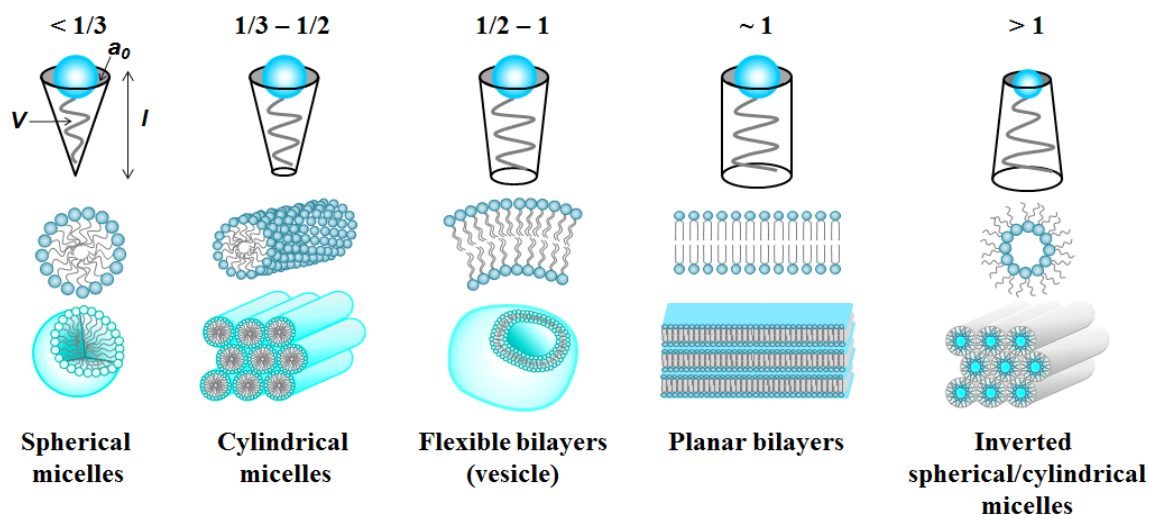
Figure I.6 Packing parameter of amphiphilic molecules as defined by Israelachvili,[15] showing different morphologies of amphiphilic aggregates.

These aggregation are held together principally by non-directional hydrophobic effects, and the molecular structures of amphiphilic molecules (lipids, surfactants, amphipatic

peptides or copolymers) as well as various physical-chemical parameters such as temperature, pH, ionic force, molecular concentration and salinity, have strong effect on p value and the resulting aggregation morphology., Indeed, small variations in such parameters can easily induce significant morphology changes. Other than the most commonly observed structures such as spherical micelles ($p < 1/3$), cylindrical micelles ($1/3 < p < 1/2$) vesicles ($1/2 < p < 1$) and lamellar phases ($p = 1$), structures such as ribbons, tubules, hexagonal, cubic phase, *etc*. are observed. Due to their amphiphilicity, sometimes they can form reversed phases such as inverted micelles or lamellar phases in organic solvents containing trace of water ($p > 1$).

While this parameter is conceptually useful for describing why a given family of molecules assemblies to certain morphology of aggregation, it is still very difficult to predict the morphology that will be formed by a particular molecule in solution.

I.2.3 Counter-ion effect for micellization

Among the various parameters sited above, counterions of charged surfactants play crucial roles determining the morphologies of the aggregation behaviors of the amphiphilic molecules. The solubility of amphiphilic molecules depends on the hydrophilic, hydrophobic and charged counter-ions. The study of counter-ion is particularly important issue in many fields. Since the work by Hofmeister,[16] the ionic specificity has been widely studied in the biological context.[17,18]

At the end of 19th century, Hofmeister proposed the influence of ions on the precipitation of proteins in salt solutions which led establishment of a classification, commonly called "Hofmeister series". This classification is also observed in many physico-chemical mechanisms including the phenomena of micellization of charged surfactants.[19]

Gregory Warr has reported a series of this study to the evaluation of the affinity of some anions (Br^-, Cl^-, I^-, NO_3^-) for gemini cationic structure.[20] The order of affinity for gemini surfactant descends $I^- > NO_3^- > Br^- > Cl^-$, which follows to the Hofmeister series. In fact, the stronger or weaker ability of an ion to associate with cationic surfactant is responsible for affecting the values of cmc and T_k.

More recently, our group has suggested the counter-anion effect complexed with gemini surfactants, dicationic bis-quaternary ammonium *n-2-n* on micellization (Figure I.7).
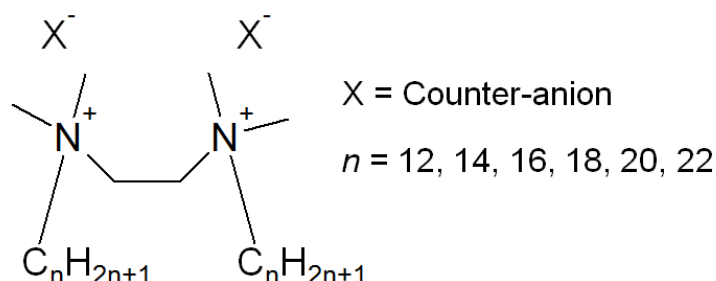
Figure I.7 Molecular structure of gemini surfactant developed in our group.

As a part of her PhD,[21] Sabine Manet studied systematically the influence of counterions to aggregation properties of gemini surfactant. She has shown the ionic specificity of counterions on the behavior of micellization, as well as the morphologies of the molecular assemblies.

She has synthesized 14-2-14 gemini surfactants complexed with more than 30 different counter-ions which are divided into 4 categories (Figure I.8): (1) small counterions, which are principally ions taken from the Hofmeister series, (2) aliphatic carboxylate counterions, in which the hydrophobicity of the anion can be tailored by modifying the alkyl group, while keeping the same ionic nature, (3) aromatic carboxylate counterions with which the effect of substitutions can be examined, and (4) those which do not belong to the first three family but which allow comparisons based on particular properties ("orphan" counterions).[22]

The results obtained show the complex aggregation behavior on charged molecules. The hydrophilicity of ions is the primary effect determining micellization. The high hydrophilicity of counterions leads to high cmc. This order evolves following to Hofmeister series; $I < NO_3 \sim Br < Cl < F \sim C_2 < PH$.
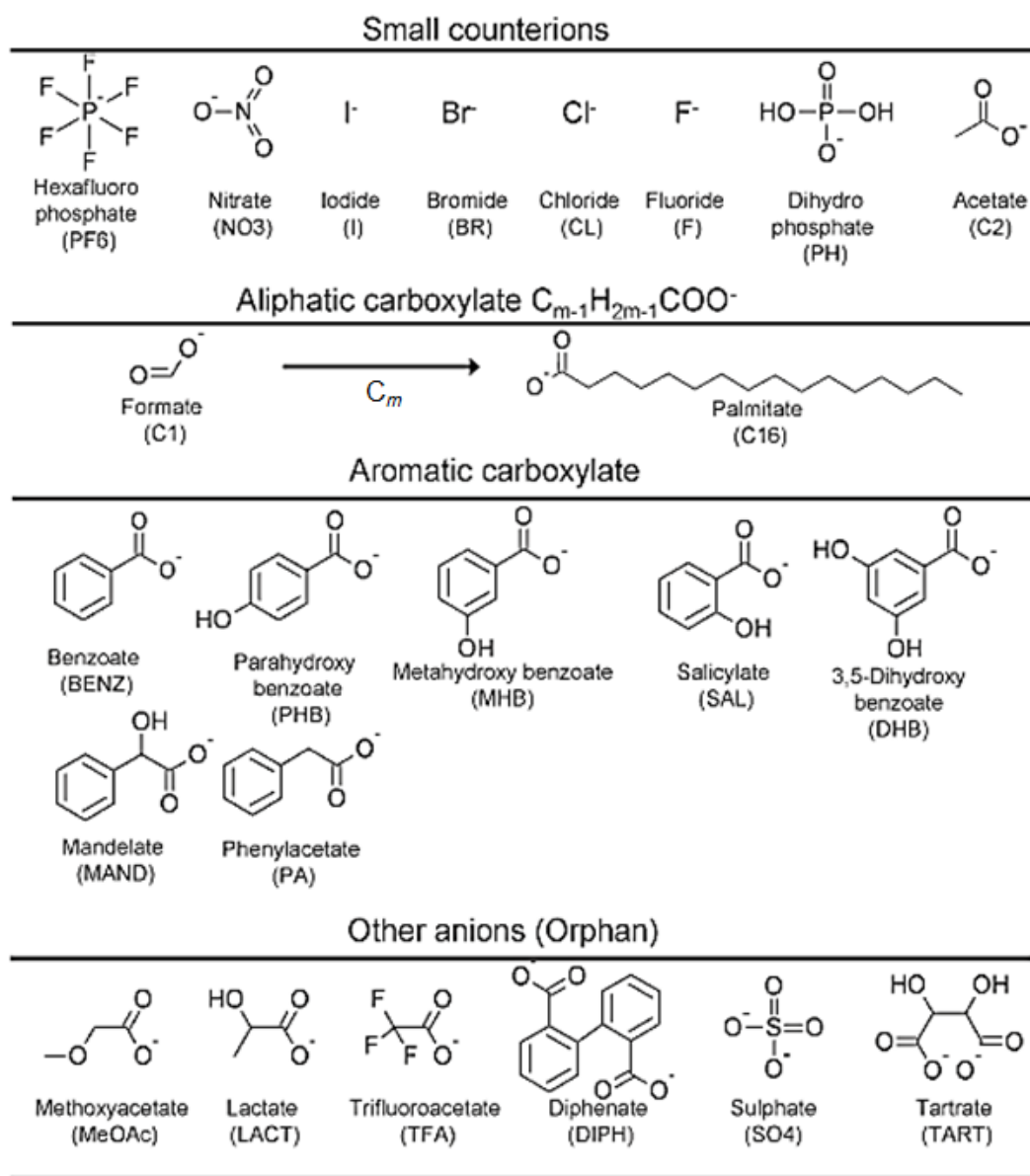
Figure I.8 Structures of 31 there are 10 counterions with alkylcarboxylate counter-anions complexed with gemini surfactant.[22]

Various physicochemical parameters (polarizability, ion radius, intra/intermolecular hydrogen bonds, and steric hindrance) have also influence for micellization and the propensity of the counterions to form ion pairs with the amphiphiles headgroups. In terms of T_k, the determining factor is stability of solid state, mainly determined by the polarizability of counterion. Thus, the higher the polarizability leads the stronger interaction with the gemini surfactant, and the higher T_k (Figure I.9).
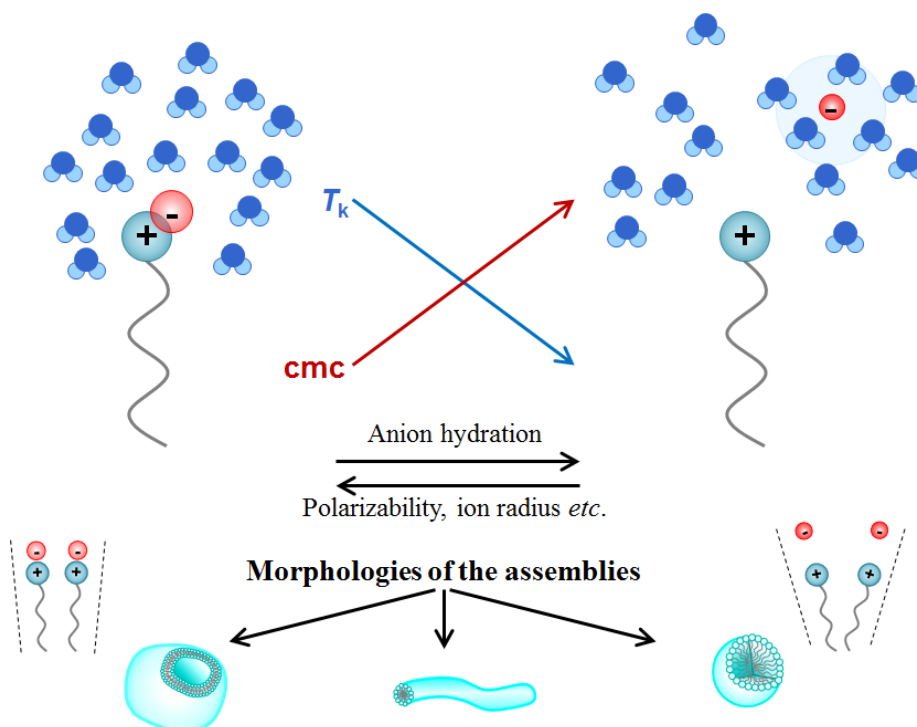
Figure I.9 Schematic illustrations of properties of self-assembly in the presence of counterion complex.

An ion confined to the highly hydrophobic surface of the aggregate is responsible for the decrease in surface charge density, which reduces the curvature of interface. This promotes the bilayers formation compared to the micelle formation.

This study shows the specific complexation effects of ions resulting from the cooperativity of various parameters and the importance of nature of counter-anion on the aggregation behavior of cationic gemini surfactant. Thus, an appropriate selection of counterion allows designing of specific supramolecular architecture and control the morphologies of self-assembly of ionic amphiphilic molecules.

I.2.4 Various amphiphilic molecules which form bilayer structures

A variety of single-chain and double-chain amphiphiles assembled spontaneously to form stable monolayers and bilayers. In 1977, Toyoki Kunitake has reported the first example of totally synthetic membrane obtained by self-assembly of monocationic amphiphilic

molecules consisting of a polar head and hydrophobic double alkyl chains (didodecyl dimethyl ammonium bromide) in water (Figure I.10).[23]
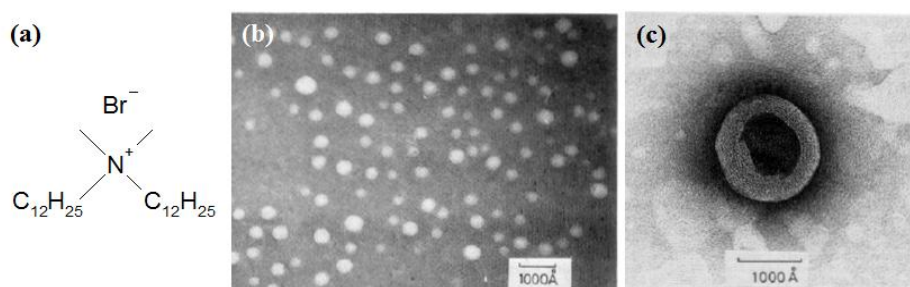
Figure I.10 (a) Structure of amphiphilic molecule and this vesicles observed by electron micrograph with (b) lower and (c) higher magnifications.[23]

Following this work, Kunitake has presented numerous studies suggesting that the diversities of morphologies are accessed from amphiphilic molecules with different structures.[24] The aggregates obtained by double-chain amphiphiles usually are self-assembled to form vesicles and lamellae of the bilayer.[25] They have also reported that bilayer strictures are obtained with single-chain tail amphiphiles which have rigid segment in the tail.[26] Furthermore, the single-chain tail with double-head ammonium amphiphiles can provide rod-like and tubular aggregates, as well as vesicles and lamellae (Figure I.11).[27,28]
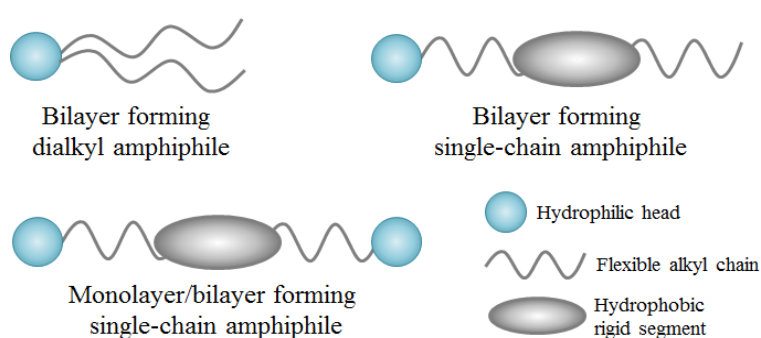
Figure I.11 Schematic illustrations of various amphiphilic molecules which can form bilayer structures. The amphiphiles are composed by single-head with double alkyl chain, single-chain containing rigid segment, and double-head single chain containing rigid segment structures.

The variation of each molecular structure and their aggregated morphologies are shown in Figure I.12. For example, the amphiphile **1** does not form vesicles in water. However, the amphiphile **2**, the homologue to amphiphile 1 with longer hydrophobic alkyl chain (from 4

to 12 carbons), forms multi-walled vesicles (Figure I.12 a). In addition, the nature of rigid segments is particularly an important factor to determine the self-assembled morphology in this type of molecular structures. If the presence of rigid segments such as oligophenyl is required, the nature of the spacer connecting these two or three cycles is also decisive. Indeed the amphiphile **3**, consisting of a triple cycle of phenyl group, self-assembles to form the stacked disk-like aggregates, **4** and **5** produce tubular and rodlike fibers, respectively (Figure I.12 b-d). The surfactant **6** consisted by hydrophilic two-headed with single chain containing rigid segment in center can be self-assembled to form lamellar sheets in water (Figure I.12 e). Such surfactants with two headgroups at the extremities of a hydrophobic chain are called as bola-amphiphiles. Interestingly, when this amphiphile **6** is mixed with cholesterol (3 : 1 molar mixture), morphology transition occurs to vesicle with about 1000-3000 Å in diameter and 60-70 Å in membrane thickness (Figure I.12 f).
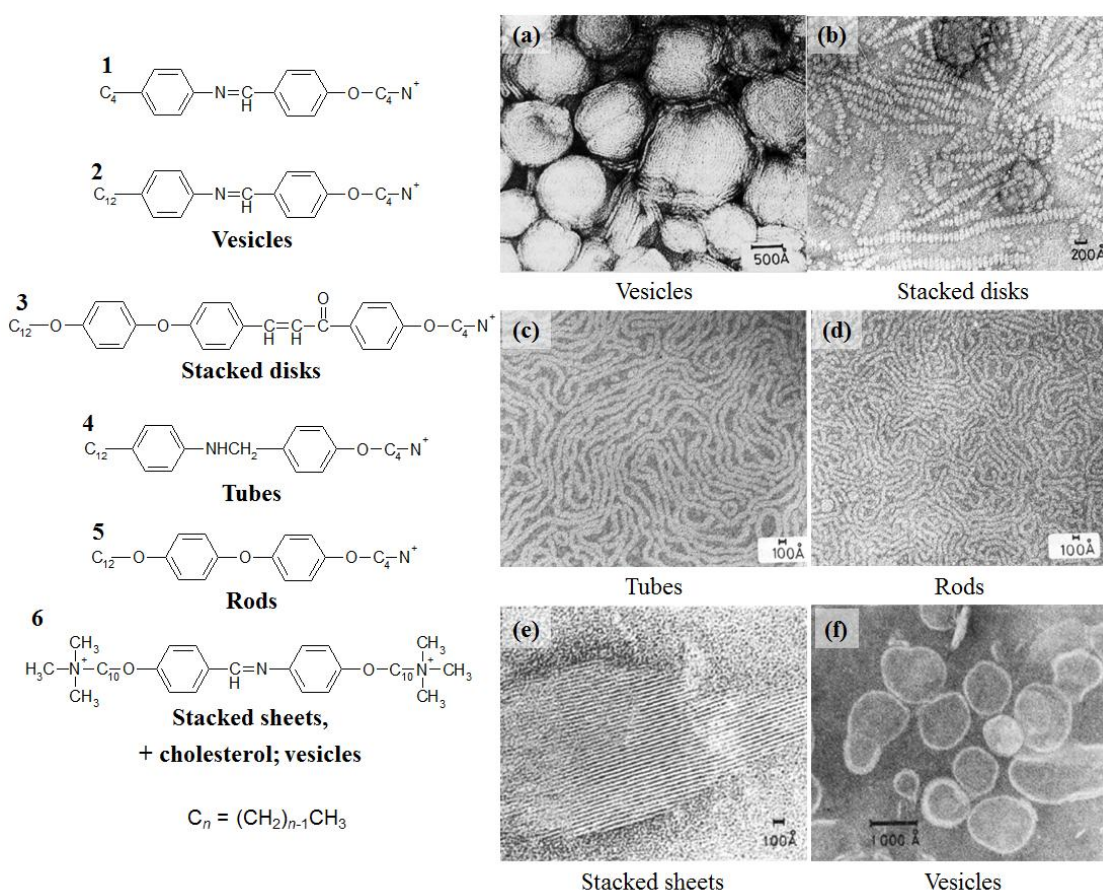
Figure I.12 Examples of amphiphilic molecules developed by Kunitake and the electron microscope images presented by self-assembled amphiphiles (a) 2, (b) 3, (c) 4, (d) 5, (e) 6, and (f) 6 : cholesterol (3 : 1).[27,28]

Other than these double chained surfactants or single chain surfactants with rigid segments and bola-form surfactants, cationic surfactants, gemini surfactants are also known to form bilayer structures.

Among the various assemblies formed by amphiphilic molecules,[29,30,31,32] chiral supramolecular structures such as helical structures, which result from the self-organized surfactants with an asymmetric chiral center in the molecules, have attracted the interest of many research groups.

I.3 Self-assembled surfactant with chiral supramolecular morphologies[33,34]

The chirality is ubiquitous in biological systems. A double-helical structure of DNA or tertiary structure of proteins are particularly good examples of the chiral structures in nature. Many artificial self-assembled nanofibers have also been reported. Most of their root compounds were serendipitously discovered to form self-assembled nanofibers.[23] Various chiral morphologies are classified as helices, tubes, ribbon-like and rod-like (including achiral formation) structures (Figure I.13), these morphologies have been visually identified by optical, electron, and probe microscopic observations. The potential applications of such original molecular assemblies include mechanical, physical, and chemical field such as nano to micrometric springs,[35] low molecular mass gelators,[36] enantioselective catalysts,[37] and organic templates with controllable shape[38] *etc.*, but also at more fundamental level, the understanding the mechanism of these self-assemblies can shed light on the comprehension of biological functional systems.
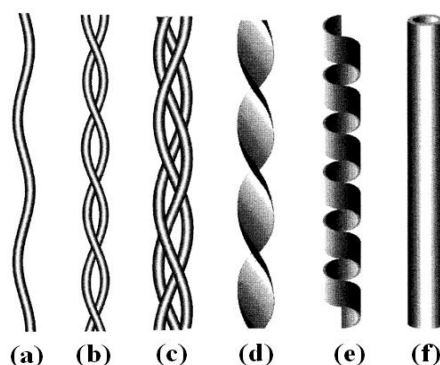
Figure I.13 Classification of nanometric fibrous structures by (a) rope-like fiber, (b,c) multistrand fiber, (d) twisted ribbon, (e) helical ribbon, and (f) tubular fiber. [33]

I.3.1 Chirality transfer

The molecular chirality (~ Å) can sometimes transfer to a much larger scale (supramolecular scale; nm ~ μm) in the morphology of self-assembled fibers. This chirality transfer results in the formation of nano to micrometric helical morphology (Figure I.14)
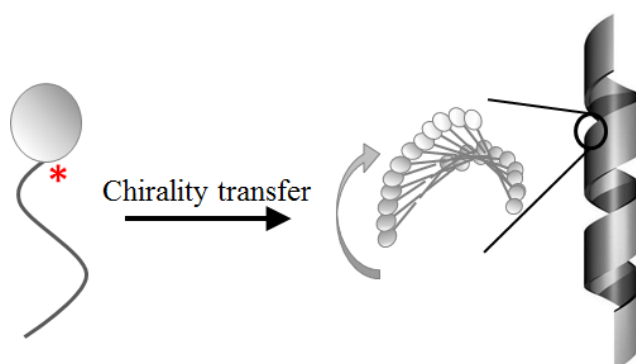
Figure I.14 Schematic illustration of chirality transfer from molecular level to supramolecular level.

Numerous studies have reported the chirality transfer from molecular level to supramolecular level since the first observations using natural lipids such as sodium deoxycholate[39] and deoxycholic acid[40].

For example, group of Kunitake [41 , 42] or Fuhrhop[29, 43 , 44 , 45 , 46] demonstrated the self-assembled chiral superstructures by amphiphilic molecules. (Figure I.15).
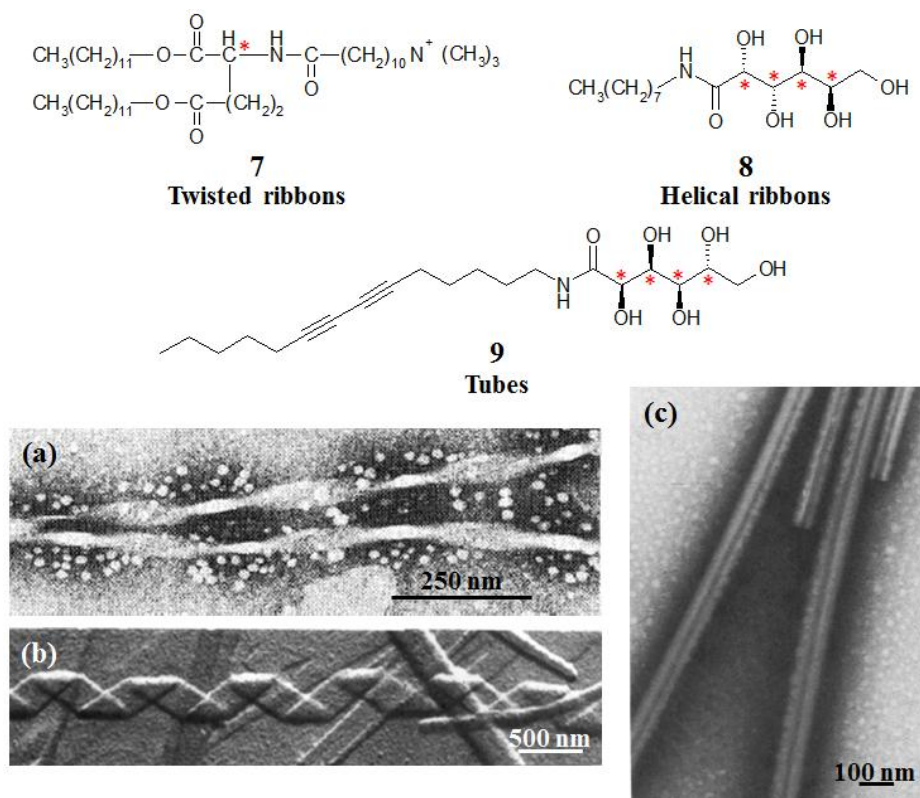
Figure I.15 Molecular structures of chiral amphiphiles and electron microscope observation of self-assembled chiral superstructures consisting with bilayer membranes. (a) Twisted ribbons obtained by amphiphile 7 [41], (b) helical ribbon obtained by amphiphile 8 [43], and (c) tubes obtained by amphiphile 9 [45].

I.3.2 Chiral fibers formed in aqueous system

The self-assembled nano to micrometric fibers can be obtained by simple preparation methods that the compounds are dispersed into media with heat above the T_k or sonication, and then allowing them to rest at a given temperature for a few minutes to several days. Some amphiphiles can form gel network of chiral fibers in solution. Either aqueous or organic solvent can be used as a media, and the amphiphiles are classified "hydrogelators" or "organogelators" respectively. In this section, we will first present the group of hydrogelators.

The natural lipids such as phospholipids can form bilayer membrane structures spontaneously in water.[47] As it has been mentioned above, bilayer membrane structures can be

formed not only by double alkyl chains, but also single chain which has rigid segments. In case of hydrogelator, the hydrophobic effect of tail(s) and the hydrogen bond of head group are important roles to self-assemble the supramolecular structures.

Since 1980's, a large number of hydrogelators have been synthesized as listed in Figure I.16, and these chiral superstructures are also shown in Figure I.17.

The chiral structures consisted bilayer membrane are observed by using synthetic lipids such as amino acids based[48] (10,[49] 11, and 12[50]), and nucleo-based (13)[51] lipids which have one hydrophilic head group and hydrophobic two tails.

Chiral superstructures can also be form by induce the chirality from counter-ion. Most of these works have been developed in Oda's group. For example, non-chiral cationic bis-quaternary diammonium gemini surfactant in the presence of tartrate (14)[52,53] and peptide (15)[54,55,56] counter-anion can form nano or submicrometric twist, helical and tubular structures. Peptide counter-anion complexed with dimethyl-dialkylammonium (16)[54,55,56] or trimethyl-alkylammonium (17)[57] surfactant can also form chiral structures.

This list also includes some other chiral amphiphiles such as asymmetric sugar-based bolaamphiphiles (18[58] and 19[59]) and single chain amphiphiles such as glydolipid including phenyl moiety (20)[60] or amide moiety (21),[61] and peptide based amphiphile (22).[62]

Some of amphiphiles can form micrometric chiral structures, however, the majority of them report nanometer scale fibers.
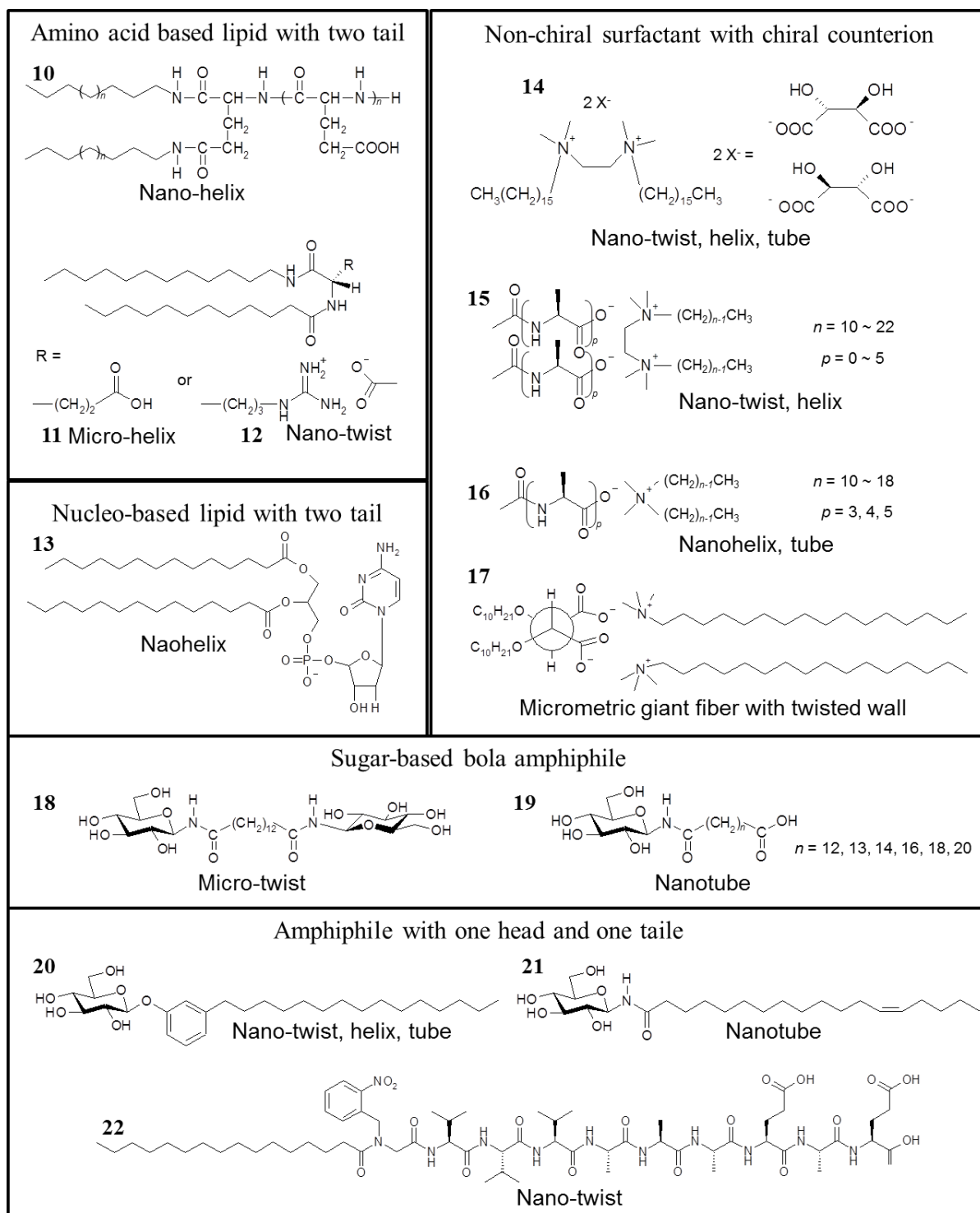
Figure I.15 Molecular structures of chiral amphiphiles which can form chiral fibrous structures consisted bilayer membrane in aqueous solution.
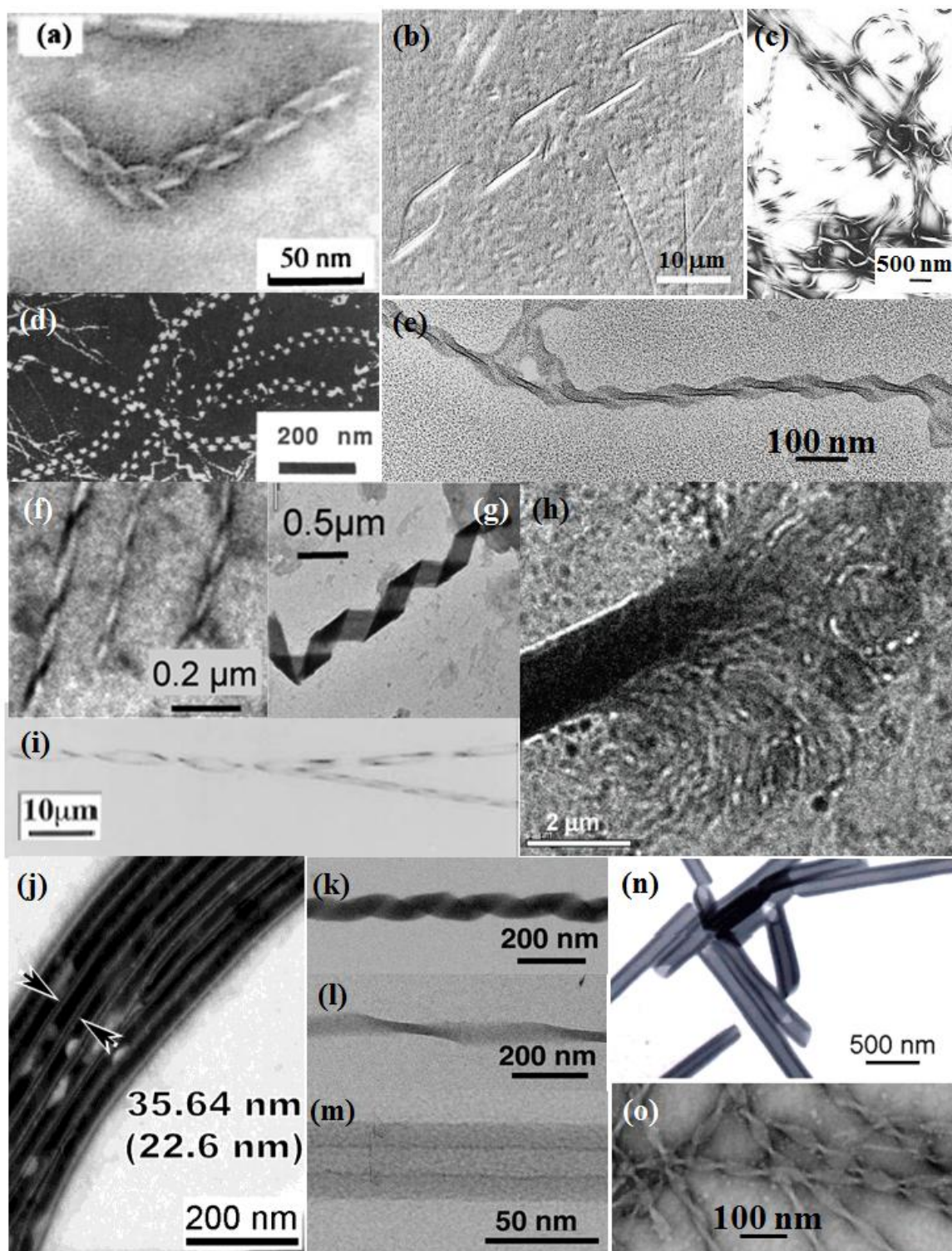
Figure I.16 Various chiral fibular aggregates from lipid bilayers membrane system in aqueous solution. The chiral fibers are corresponding to amphiphile (a) 10, (b) 11, (c) 12, (d) 13, (e) 14, (f, g) 16, (h) 17, (i) 18, (j) 19, (k, l, m) 20, (n) 21, and (o) 22.

I.3.3 Chiral fibers formed in non-polar organic media

Other amphiphiles (these are the majorities) can form gel network with chiral supramolecular structure in non-polar organic media. These can be referred to as organogelators.

From the late 1980's to the early 1990's, many researchers discovered oganogelators based on low molecular weight compounds. The classical organogelators are listed in Figure I.17.[63,64,65,66] These molecules can form nano-sized architectures to develop molecular devices for sensitive sensors, high-density memory storage, and so on.
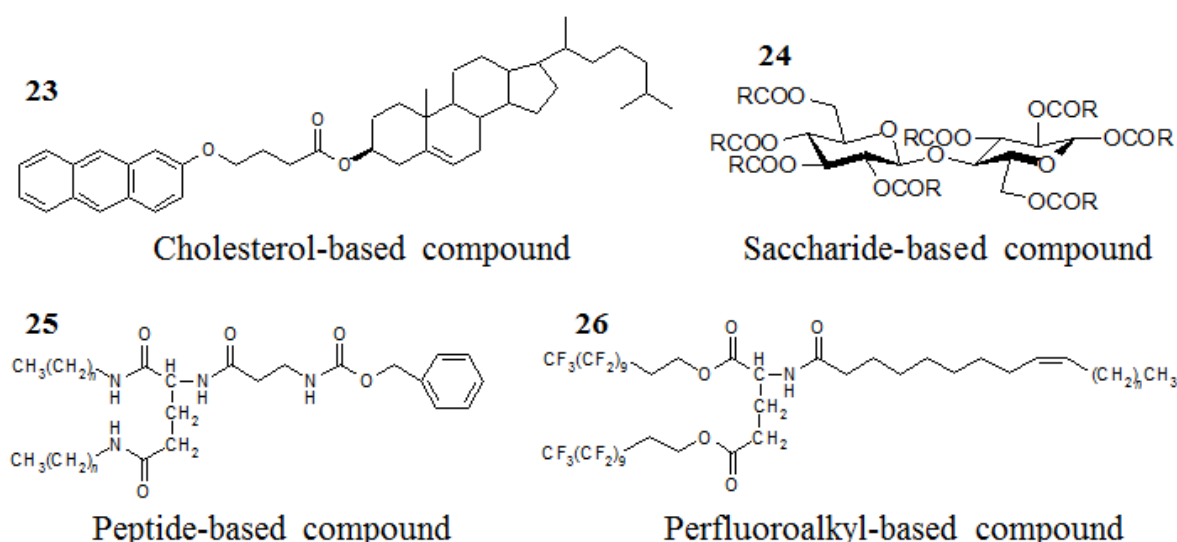
Figure I.17 Molecular structures of chiral amphiphiles of classical organogelators developed in the late 1980's to early 1990's (Ref; 23 [63], 24 [64], 25 [65], and 26 [66]).

Figure I.18 shows more recent examples of chiral organogelators, and these chiral superstructures are shown in Figure I.19.

The hydrophobic effect is the most essential driving force for molecular aggregates in aqueous solution systems. In organic media, on the other hand, intermolecular interactions such as hydrogen bond, ionic interaction, and $\pi-\pi$ stacking play important roles in molecular aggregation.[67] For example, gemini-shaped hexa-*peri*-hexabenzocoronene (HBC) amphiphiles containing stereogenic center into hydrophilic side chain (**27**) form helical-rolled bilayer tapes

in 2-methyltetrahydrofuran solution derived from bilaterally coupled columns of π stacked HBC units.[68,69]

Cholesterol-based amphiphiles can also produce the chiral fiber network in organic media. Cholesterol derivative linked to diphenylbutadine organogelator (**28**) can form nanometric twist ribbons as a result of their slipped-stack arrangement of π–π stacking interaction of diphenyl butadiene core.[70] Crown-appended cholesterol-based organogelators (**29**) can also self-assemble to form micrometric helical ribbons to tubules.[71]

Oligothiophenes are well known for their excellent π–π stacking tendency and the ability of providing a conductive pathway for charge transport.[72] When oligothiophene is complexed with amphiphilic molecules such as peptide-based compounds (**30**), π–π interaction and hydrogen bonding affect the balance of intermolecular forces that lead to self-assembled nanometric twisted structures.[73]

Figure I.18 Molecular structures of organogelators promoted by chiral amphiphiles.
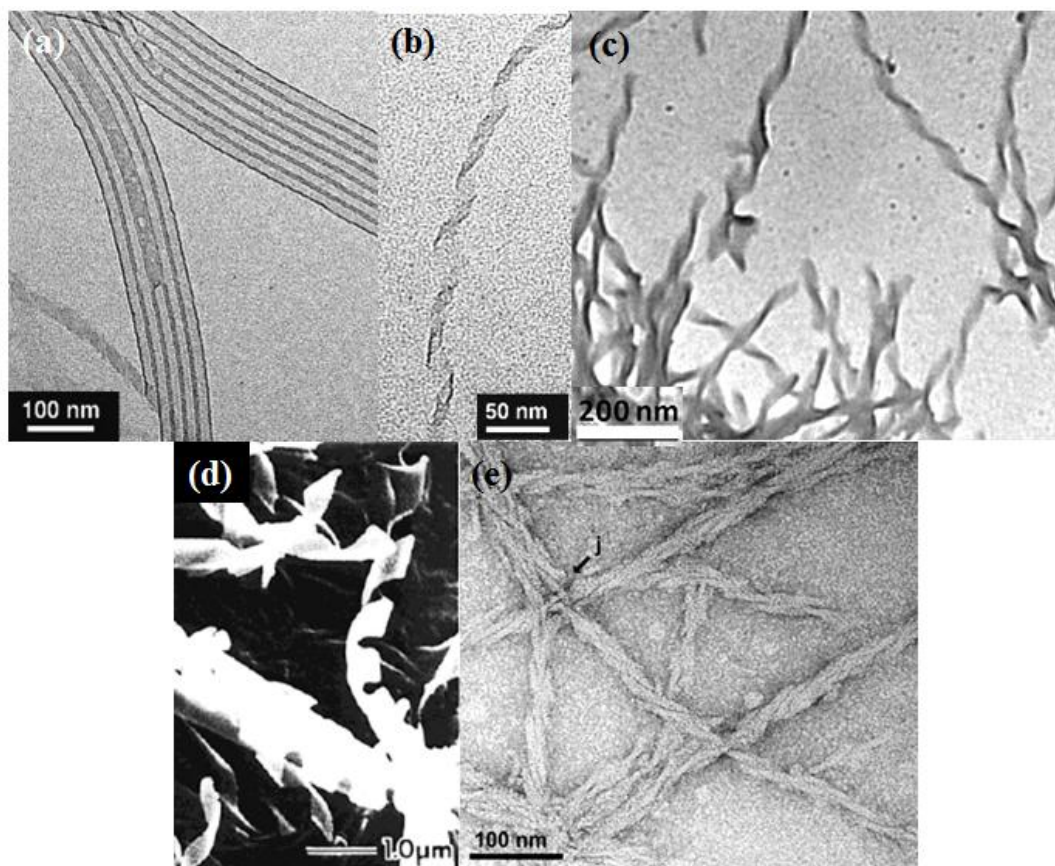
Figure I.19 Various chiral fibular aggregates from lipid bilayers membrane system in organic media. The chiral fibers are corresponding to amphiphile (a, b) 27, (c) 28, (d) 29, and (e) 30.

I.3.4 Twisted, helical ribbons and tubes

Among the variety of chiral fibrous structures, helical and twisted shapes are most commonly described in many literatures, and these morphologies are generally promoted by single or multiple bilayers. These morphologies are characterized by inherent curvature (Figure I.20). Twisted membrane is associated by "saddle-like curvature", in contrast, helical membrane is associated by "cylindrical curvature".[53,74,75]
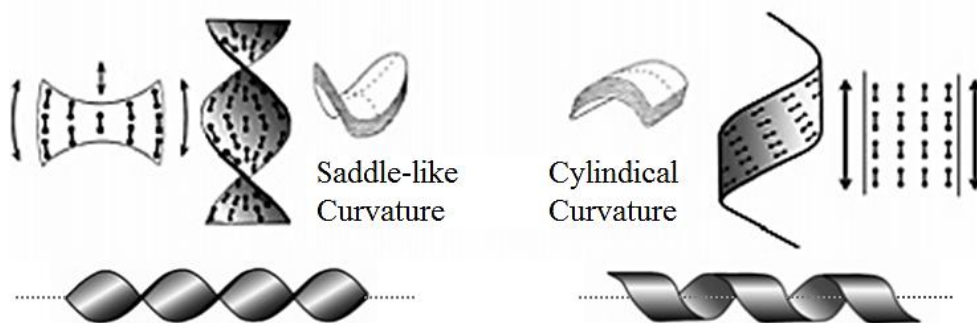
Figure I.20 Schematic illustrations of the formation of twisted ribbon with saddle-like curvature and helical ribbon with cylindrical curvature.

Furthermore, tubular structures are often observed from self-assemblies derived from chiral molecules.[76] The precursor structures to forming tubes are generally helical ribbons, and there are two routes for nanotube formation. The first route proceeds with the shortening of helical pitch and maintaining a constant tape width of ribbon (Figure I.21 a), whereas the second involves widening of tape width and maintaining a constant helical pitch (Figure I.21 b).[77] Actually, when the tube is just formed, the closed edges of helical ribbon are still visible and indicated the chirality of the tubular structure (Figure I.21 c).[78]
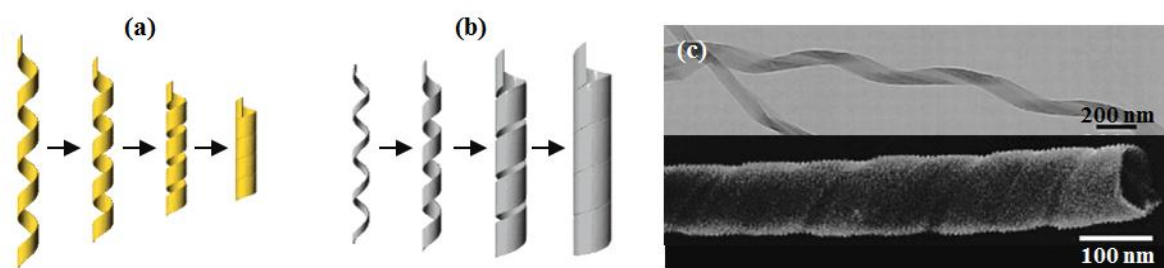
Figure I.12 (a, b) Schematic illustrations of the tubular formation mechanism from helical ribbon precursor. Tube are formed through (a) shortening helical pitch or (b) widening tape width. (c) TEM images of helical formation (upside) and tubular formation keeping with the helical edges (bottom).[78]

I.3.5 Morphology control

These chiral morphologies obtained by self-assemblies of amphiphilic molecules can be controlled in different ways, either by varying the environmental parameters, or by changing the molecular structure of amphiphiles. Some of the key parameters of morphological control

are the length of hydrophobic tails, the nature of the solvent, the gelation concentration, temperature, or the aging time of samples. Indeed, the formation of these chiral assemblies is often strongly controlled by kinetics.

For example, mixture of a short-chain (**31**) and a long-chain (**32**) diacetylenic phospholipid self-assemble to form either nanotube or twisted ribbon depending on the gelation temperature (Figure I.22).[79,80] In this case, tubular structures can be obtained with lower (4 °C) and higher (more than 34 °C) temperature (containing vesicles at 34 °C), however at 27 °C, only twisted ribbons are observed.
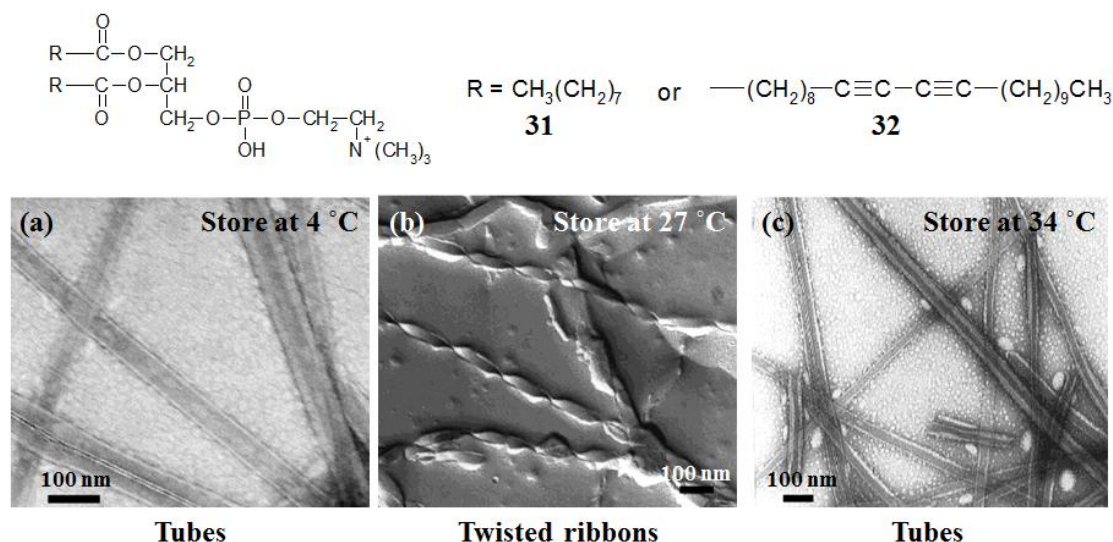
Figure I.22 Example of morphology control by different temperature between tubes to twisted ribbons of self-assembled mixture of 24 and 25. The samples stored at (a) 4 °C to form tubes, (b) 27 °C to form twisted ribbon, and (c) 34 °C to form tubes containing vesicles.[80]

The concentration is also important factor to produce the chiral morphology. Cui et al. have reported that controllable shapes are produced by different concentration of alkylated peptide amphiphiles (**33**) in aqueous solution.[81] Amphiphile **33** can form twisted multiple liner structures at lower concentration of 0.01 wt % (Figure I.23 a). These morphologies are transformed from nanoribbons to nanobelts with broom morphology (Figure I.23 b), then flat and wide nanobelts (Figure I.23 c) upon increase the concentration to 0.1 wt %.
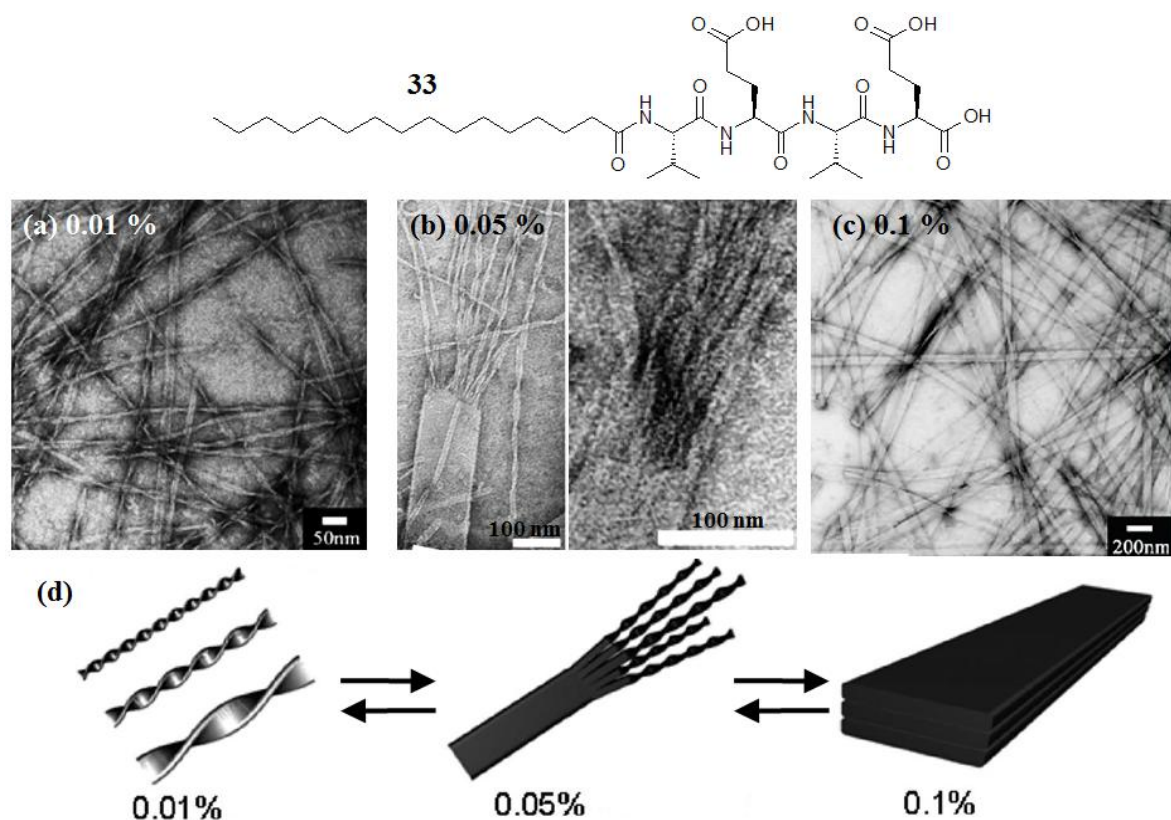
Figure I.23 Example of morphology control by different concentration. Electron microscope images of (a) twisted nanoribbons at 0.01 wt %, (b) intermediate broom morphology of nanobelts transforming into twisted nanoribons at 0.05 wt %, and (c) uniformed nanobelts morphologies at 0.1 wt %. (d) Schematic illustration of morphological transitions with a change in concentration.[81]

More recently, Ziserman et al. have reported the growing steps of chiral morphologies by aging evolution using amino acid amphiphile (**34**) (Figure I.24).[82] The morphology transition until forming the chiral twisted ribbons occurred rapidly, however their transformation to tubular structures are slower.
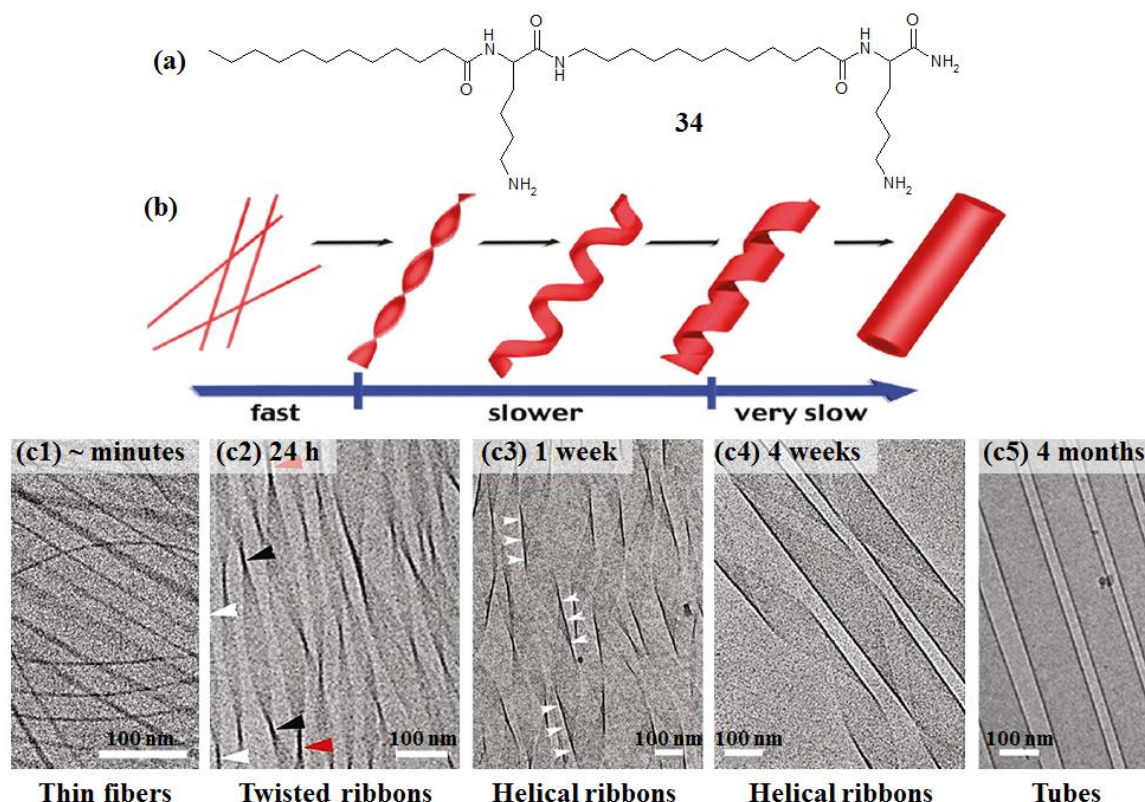
Figure I.24 Example of morphology control by aging variation. (a) The molecular structure of chiral amphiphile, (b) schematic illustration of qualitative description of the time-dependent assembly, and (c) electron microscope images of morphology transitions from thin fibers to tubes.[82]

The specific enantiomers (D and L) of chiral molecules are also important factor to determine the direction of helicity of chiral structures (right-handed or left-handed forms).

Mixing of an equivalent amphiphile of each enantiomer generally leads to form racemic structure which means that no chirality is expressed in the aggregate. For example, the amphiphile **8** (D-glu) can self-assemble to form left-handed helix, on the other hand, right-handed helix can be obtained by opposite chiral amphiphile **35** (L-glu). If these amphiphiles are mixed with the molecular ratio 1 : 1, chirality is balanced and racemic platelets are observed (Figure I.25).[43]
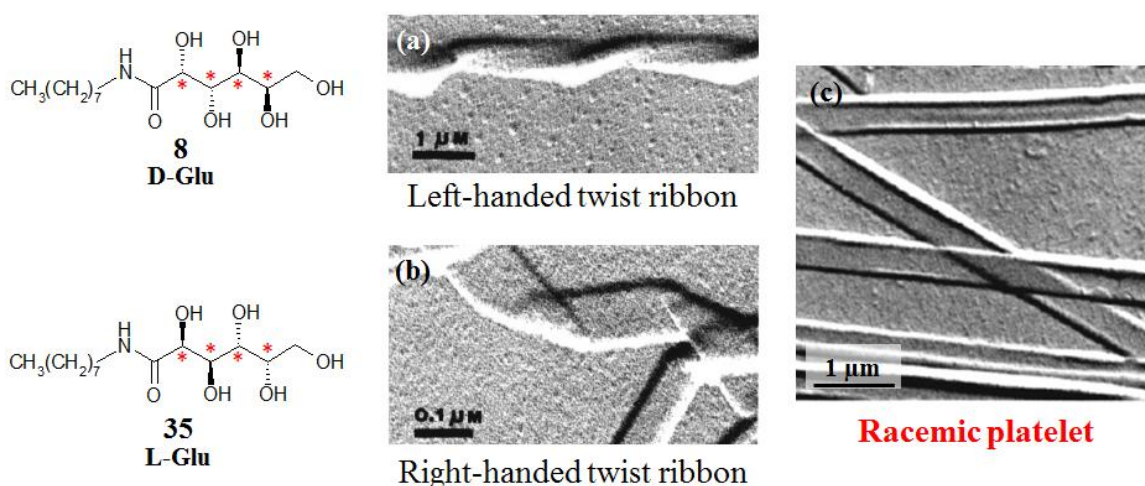
Figure I.25 Molecular structures of opposite enantiomers and electron micrograph of (a) left-handed twist ribbon (8), (b) right-handed twist ribbon (35), and (c) racemic flat fibers from amphiphile 8 + 35 (molecular ratio 1 : 1).

However, some exceptions have been reported in the literature. The coexistence of right and left handed ribbons are sometimes observed with the population of each representing the ratio of the two enantiomers.[83,84,85]

I.4 Study of *in situ* dynamic morphology transition through the out-of- equilibrium process

1.4.1 Dynamic motion in biological systems

In nature, they are many phenomena of *in situ* dynamical behaviors which are caused by external stimuli. Biomembranes are particularly good example to understand the mechanism of morphology transformation caused by the out-of-equilibrium process. In membrane systems, the proteins show various biological functions, for example, transport proteins play the maintenance of ion concentration resulted from the spontaneously conformation change such as unfolding and folding of their structures when they receive and release the ions.[86]

Some proteins are responsible for the diseases due to their denaturation caused by morphological transition. Prion protein is well-known as a factor to course spongiform encephalopathy. Normal prion contains mainly α-helical conformations. If these α-helices transform to β-sheets, diseases develop.[87,88,89] Swietnicki et al. have reported that this transition of α-helix to β-sheet rich oligomers is occurred under the acidic conditions (pH 5 or below) in the presence of guanidine hydrochloride.[90] Furthermore, addition of urea and sodium chloride at acidic pH also trigger a self-association or a conversion to β-sheet structure.[91] Figure I.26 shows clearly *in situ* morphology transition from α-helix to β-sheet proceeded with time by addition of urea and NaCl using circular dichroism spectroscopy. This transition occurs concomitantly with oligomerization of protein.
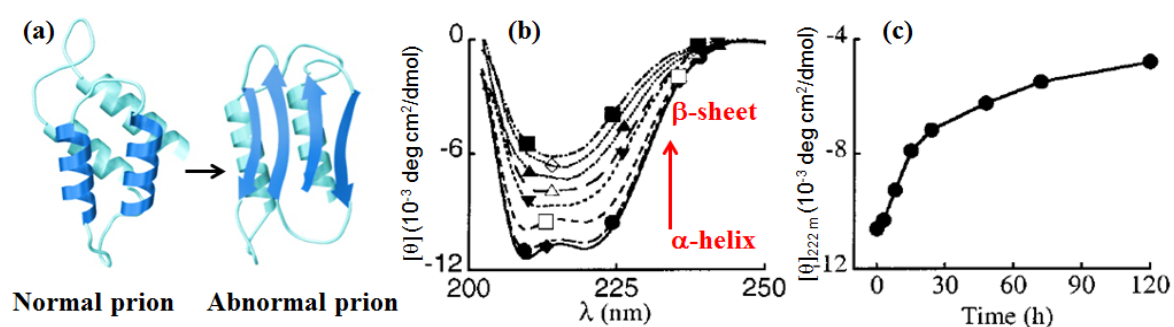
Figure I.26 (a) Model of α-helix-rich (normal) to β-sheet-rich (abnormal) morphology transition of prion. (b) CD spectra of time-dependent transition to β-sheet structure and (c) kinetics of conformational transition in ellipticity at 222 nm.[90]

The designs and investigations of modeling morphology transitions are critically important target for elucidating the structural and dynamic parameters governing functions of biomolecules. The designs of dynamic supramolecular structures from self-assembled amphiphilic molecules are also contributed to the mimic of biological functions.

1.4.2 Artificial morphology transformation by supramolecular self-assembly

Inspired from biological functions, artificial systems are also performed for *in situ* structural changes by external factors.

Many researchers have approached *in situ* morphology transitions such as helix-sheet, random coil-sheet or helix, coil-globule, micelle-fiber, and helix-helix handedness transition *etc*. by using synthetic molecules such as polymer,[92,93,94,95] oligomer,[96,97,98] dendrimer,[99,100] and helicen.[101,102,103]

Especially, supramolecular structures obtained by self-assembled amphiphilic molecules have great advantages since in these systems, we can control morphologies at the mesoscopic level (nm ~ µm scale) due to their intermolecular non-covalent bonding.

The equilibrium of stable structures from self-assembled amphiphiles can be easily shifted by external stimuli such as temperature, pH control, and sometimes additive as well.

Temperature is the most common control parameter to produce the morphology transition. In 1999, Thomas et al. have reported the direct observation of *in situ* morphology transformation from multilamellar vesicles to helical ribbons by 1,2-bis(10,12-tricosadiynoyl) -*sn*-glycero-3-phosphocholine [DC(8,9)PC, amphiphile **32**] under conditions of very slow cooling (Figure I.27).[104] In this system, the transition temperatures from isotropic-to-vesicle (T_{L1}) and vesicle-to-fiber (T_{L2}) are 37 °C and 57 °C, respectively. The samples are heated to ~ 40 °C to form the vesicle structure, and then cooled down with the rate at 0.25 °C/h. While cooling, the helical ribbons grow from nucleating at a nodule (white arrow) at the edge of spherical vesicle.
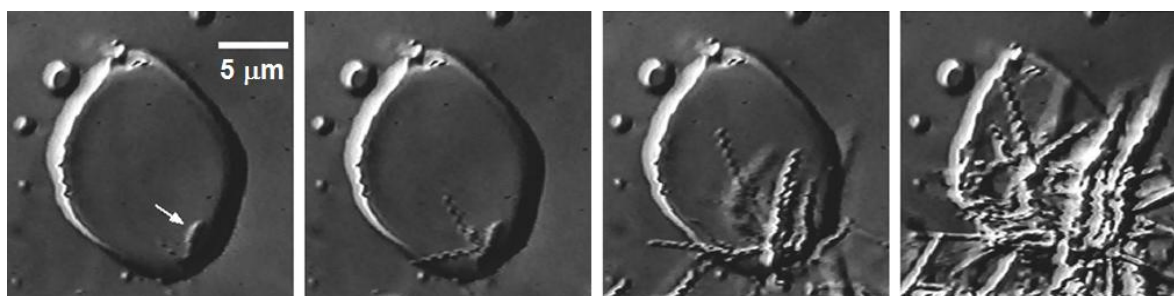
Figure I.27 Direct observation (DIC microscopy) of morphology transition from vesicle to helical ribbons obtained while cooling at 0.25 °C/h.[104]

This system is reversible upon heating to above T_{L2}.

The pH is also important to control the structures. For example, pH sensitive peptide or amino acid based amphiphilic molecules show fiber-micelle/vesicle morphology transition upon adjusting the pH environment.[105]

Recently, Wang et al. have described that self-assembled structure of bolaamphiphiles with L-glutamic acid headgroups and hybrid linkers (36) is controllable upon pH change from 3 (chiral fiber with monolayer membrane) to 12 (giant micellar fibers) (Figure I.28).[106]
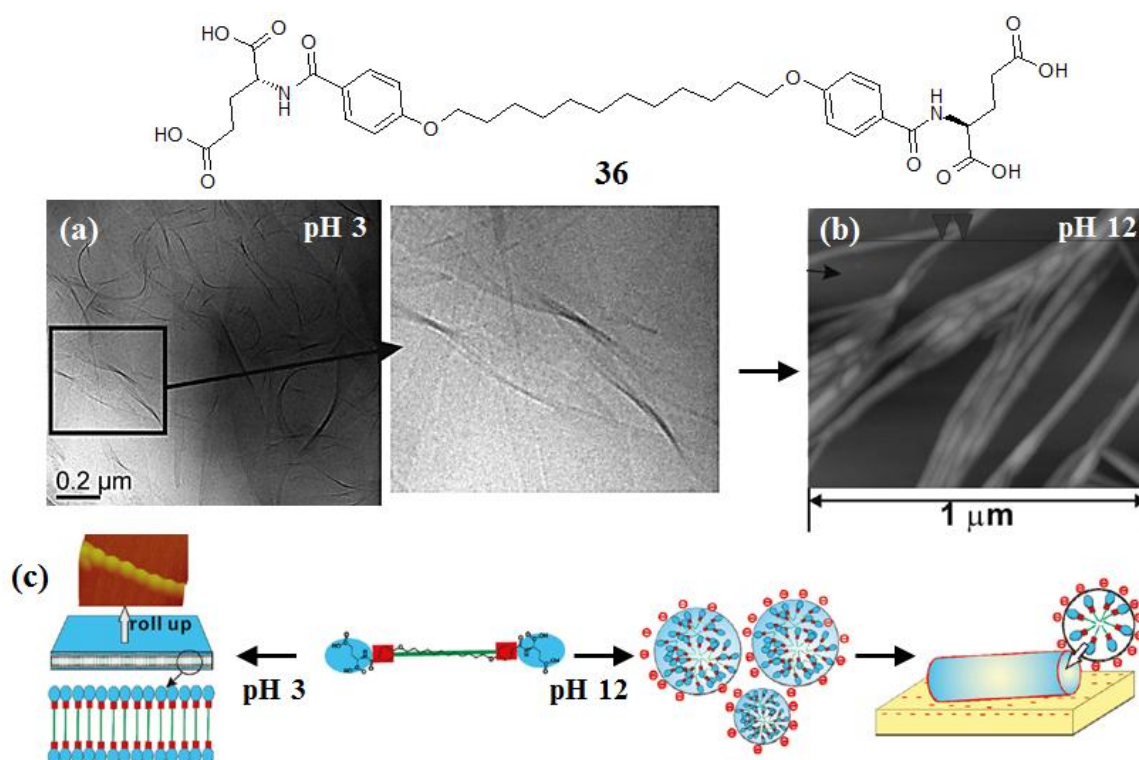
Figure I.28 Example of pH-responsible amphiphile 26. (a)TEM image of chiral fiber with monolayer structure at pH 3, (b) AFM image of giant micellar fibers at pH 12, and (c) schematic illustration of self-assembly in pH 3 and pH 12.[106]

In 2002, Kobayashi et al. have reported the first experiment of vesicle-fiber transition as well as sol-gel transition using chiral bolaamphiphiles consisting of sugar head group and azobenzene segment (amphiphile 37) upon addition of boronic acid-appended poly(L-lysine) as additive agent (Figure I.27).[107]
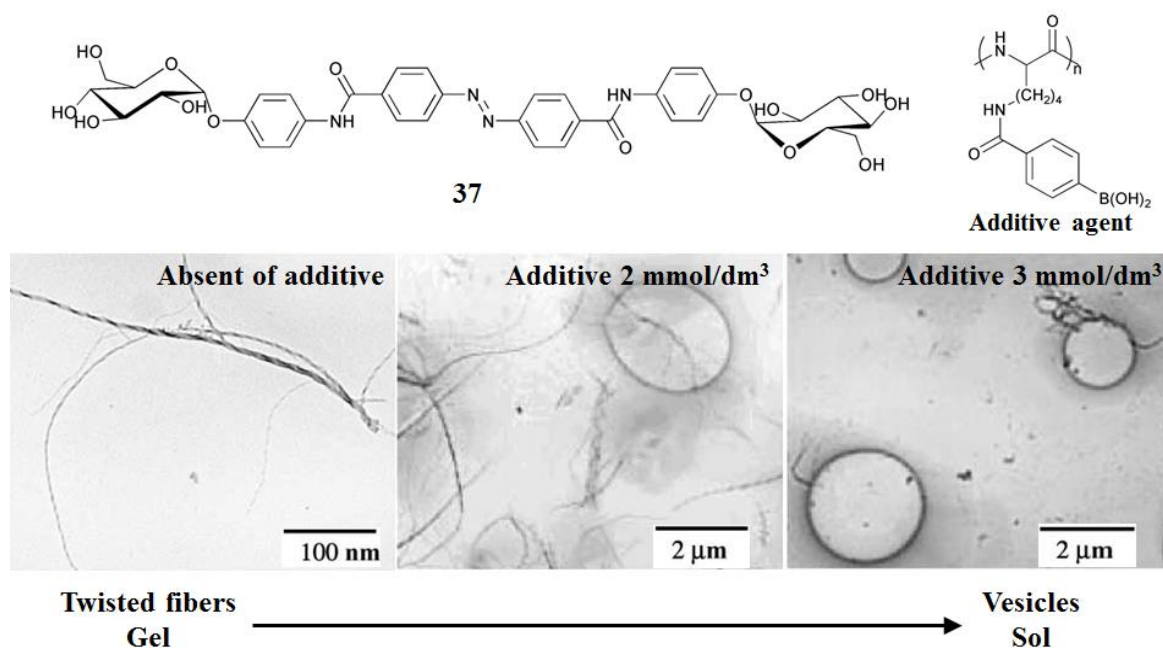
Figure I.27 The molecular structures of bolaamphiphile and boronic acid-appended poly(L-lysine) additive agent, and TEM images of fiber-vesicle transition upon addition of additive agent. The chiral fiber obtained with concentration 1.0×10^{-2} mol/dm^3 in mixture of DMSO/water.[107]

Amphiphile **37** alone self-assemble to form gel by creating extended networks of nanometric twisted fibers in DMSO/water solution. When boronic acid-appended poly(L-lysine) is added, the gel phase was changed into the sol phase in the macroscopic level and the fibrous aggregates are changed into the vesicular aggregates in the microscopic level. This kind of transformation is usually demonstrated by a temperature change, but in this case, it is induced due to the specific boronic acid–sugar interaction at constant temperature. When D-fructose which shows high affinity with the boronic acid group is added to the vesicle solution, the sol phase and the vesicular aggregate are transformed back to the gel phase and the fibrous aggregate, respectively. This means that the phase and morphological changes in the sugar-integrated bolaamphiphiles can be controlled reversibly.

More recently, Lin et al. have designed a functional amphiphile bearing a sugar moiety, azobenzene group and butyl chain (**38**) which can self-assemble to form a double-stranded helical nanofiber in aqueous solution (Figure I.28 b).[108] This double helix is transformed to globule micelles upon addition of acid because the amino atom in **38** is protonated (Figure I.28 a). This process is reversible by addition of base.

34

Furthermore, when ionic surfactant such as sodium dodecylbenzene sulfonate (SDBS) adds to suspension of helical fibers, the shapes can be transformed into fragmentized unfolded nanofibers (Figure I.28 c). These phenomena are rationalized that ionic surfactant penetrate into helical aggregate owing to hydrophobic effect and impart electrostatic repulsion to the adjacent helix, which can result into the unfolding of the double helix. Upon further addition of SDBS, these fibers transform into global vesicles (Figure I.28 d).
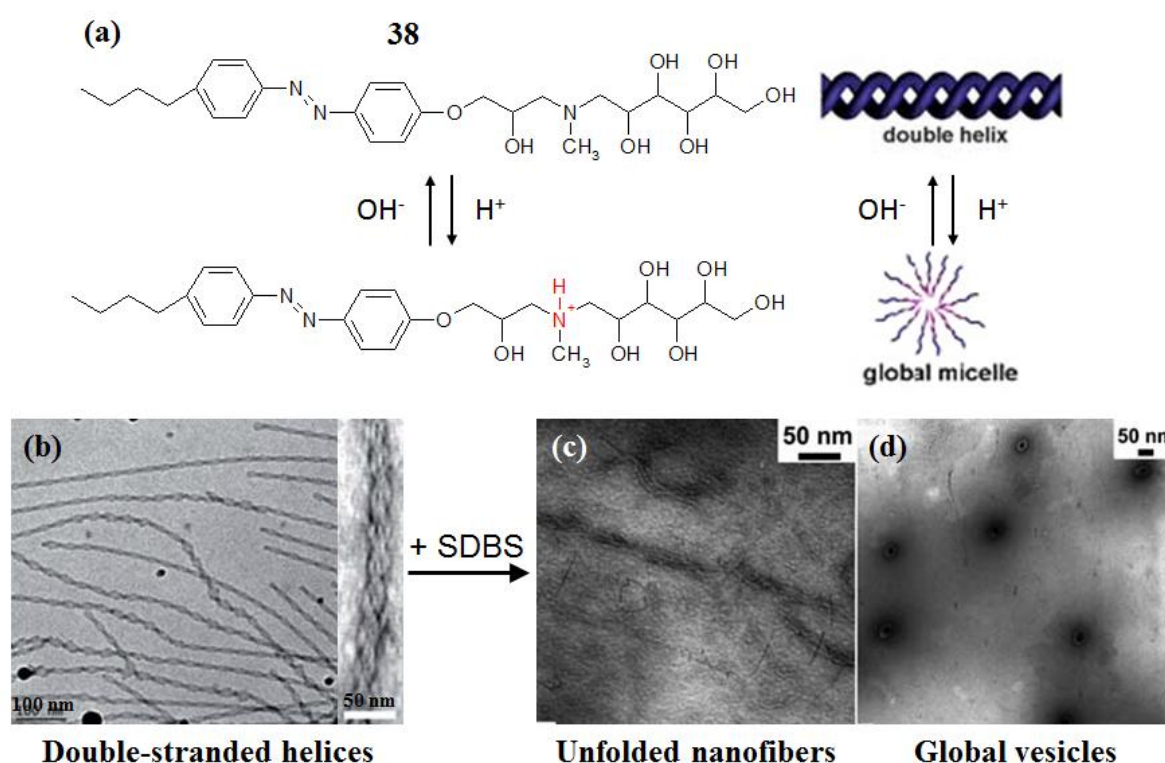
Figure I.28 (a) Structural change of amphiphile (38) with addition of acid or base. TEM images of (b) double-stranded helices. Morphology transition in the presence of ionic surfactant; (c) fragmentized unfolded nanofibers, and (c) global vesicles.[108]

The finding imply that these systems are applicable as new functional soft materials triggered by external stimuli expanding for *e.g.*, switching devises, actuators, nanopipettes, as well as drug delivery systems.

I.5 Conclusion

In this bibliography chapter, we have presented the supramolecular structures obtained by self-assembled amphiphilic molecules. Initially, we focused on structural parameters, how amphiphiles can self-organize to the various structures under the different environment. The driving force responsible for the self-assembly of surfactants in aqueous solution is mainly the hydrophobic effect of nonpolar tails, combined sometimes with hydrogen bonds of polar head groups. The shape and stability of self-assembled supramolecular structures are strongly affected by nature of counterions.

Among the various self-assembled structures, chiral supramolecular structures represent a very interesting group of nano-assemblies. A rich variety of chiral structures such as twisted or helical ribbons as well as tubules have been observed and their size varies from nanometers to microns, that shapes and chirality are tunable by adjusting the environment.

Sometimes these chiral supramolecular structures show *in situ* transformation to different morphologies (*e.g.* vesicle, micelle) by addition of external stimuli. Many literatures have published about morphology transition from chiral to achiral structure, however less examples have reported for achiral to chiral structural transformation, particularly the condition is at constant temperature.

We have therefore asked ourselves, if 1) it is possible to promote *in situ* morphology transformation from achiral to chiral supramolecular structure, or 2) can the opposite chirality be induced a posteriori in chiral aggregate to design the *in situ* reversible helical structures, IF the chirality can be induced by the counterion to stable aggregates of non-chiral surfactant.

Answers to these questions will be proposed later in this manuscript.

References

[1] D. Philip, J. F. Stoddart, *Angew. Chem. Int. Ed. Engl.*, **1996**, *35,* 1155-1196.

[2] J. M. Lehn, P. Ball, in *The New Chemistry*, ed. N. Hall, Cambridge Univ. Press, Cambridge, U. K., **2000**, 300-351.

[3] B. Alberts, D. Bray, J. Lewis, M. Raff, K. Roberts, J. D. Watson, *Molecular Biology of the Cell*, Garland, New York, **1994**.

[4] A. Kumar, N. A. Abbott, E. Kim, H. A. Biebuyck, G. M. Whitesides, *Acc. Chem. Res.*, **1995**, *28*, 219-226.

[5] M. N. Jones, D. Chapman, *Micelles Monolayers and Biomembranes*, Wiley-Liss, Bew York, **1995**.

[6] G. R. Desiraju, *Crystal Engineering: The Design of Organic Solids*, Elsevier, New York, **1989**.

[7] E. L. Thomas, *Science*, **1999**, *286*, 1307-1309.

[8] V. Grantcharova, E. J. Alm, D. Baker, A. L. Horwich, *Curr. Opin. Struct. Biol.*, **2001**, *11*, 70-82.

[9] P. Bongrand, *Rep. Prog. Phys.*, **1999**, *62*, 921-968.

[10] (a) J. M. Lehn, *Angew. Chem. Int. Ed. Engl.*, **1988**, *27,* 89-112. (b) J. M. Lehn, *Angew. Chem. Int. Ed. Engl.*, **1990**, *29,* 1304-1319. (c) J. M. Lehn, *Pure & Appl. Chem.*, **1994**, *66,* 1961-1966.

[11] B. Olenyuk, J. A. Whiteford, A. Fechtenkotter, P. J. Stang, *Nature*, **1999**, *398*, 796-799.

[12] J. M. Lehn, *NATO ASI Ser. Ser. E*, **1996**, *320*, 511-524.

[13] R. Oda, *Molecular Gels*, Kluwer Academic Publishers, Dordrecht, Netherlands, **2005**.

[14] M. J. Rosen, *Surfactant and interfacial phenomena,* Wiley, New York, **2004**.

[15] J. Israelachvili, *Intermolecular & Surface Forces*, 2nd ED., Academic Near, London, **1992**.

[16] *F*. Hofmeister, *Arch. Exp. Pathol. Pharmacol.*, **1888**, *24*, 247-260.

[17] I. A. Shkel, J.D. Ballin, M. T. Jr. Record, *Biochemistry*, **2006**, *45*, 8411-8426.

[18] D. M. Huang, C. Cottin-Bizonne, C. Ybert, L. Bocquet, *Phys. Rev. Lett.*, **2007**, *98*, 177801.

[19] A. Renoncourt, N. Vlachy, P. Bauduin, M. Drechsler, D. Touraud, J. M. Verbavatz, M. Dubois, W. Kunz, B. W. Ninham, *Langmuir*, **2007**, *23*, 2376-2381.

[20] (a) J. D. Morgan, D. H. Napper, G. G. Warr, S. K. Nicol, *Langmuir*, **1994**, *10*, 797-801. (b) M. A. Cassidy, G. G. Warr, *Aust. J. Chem.*, **2003**, *56*, 1065-1070. (c) B. Thalody, G. G. Warr, *Aust. J. Chem.*, **2004**, *57*, 193-196.

[21] S. Manet, Effet de contre ion sur les propriétés d'amphiphiles cationique, *Thesis of Doctrante, Bordeaux 1 Unversity*, **2007.**

[22] S. Manet, Y. Karpichev, D. Bassani, R. Kiagus-Ahmad, R. Oda, *Langmuir*, **2010**, *26*, 10645-10656.

[23] T. Kunitake, Y. Okahata, *J. Am. Chem. Soc.*, **1977**, *99,* 3860-3861.

[24] (a) T. Kunitake, N. Kimizuka, N. Higashi, N. Nakashima, , *J. Am. Chem. Soc.*, **1984**, *106,* 1978-1983. (b) T. Kunitake, *Amgew. Chem. Ed. Int. Engl.*, **1992**, *31,* 709-717.

[25] (a) T. Kunitake, *J. Macromol. Sci. Chem.*, **1979**, *A13,* 587-602. (b) J. H. Fendler, *ACC. Chem. Res.*, **1980**, *13,* 7-13.

[26] (a) T. Kunitake, Y. Okahata, *J. Am. Chem. Soc.*, **1980**, *102,* 549-553. (b) Y. Okahata, T. Kunitake, *Ber.*

Bunsenges. Phys. Chem., **1980**, *84,* 550-556.

27 T. Kunitake, Y. Okahata, M. Shimomura, S. Yasunami, K. Takarabe, *J. Am. Chem. Soc.*, **1981**, *103,* 5401-5413.

28 Y. Okahata, T. Kunitake, *J. Am. Chem. Soc.*, **1979**, *101,* 5231-5234.

29 J. F. MacCrea, S. Angerer, *Biochim. Biophys. Acta*, **1960**, *42*, 357-359.

30 N. Ramanathan, A. L. Currie, J. R. Colvin, *Nature*, **1961**, *190*, 779-871.

31 J. H. Fuhrhop, P. Schnieder, J. Rosenberg, E. Boekema, *J. Am. Chem. Soc.*, **1987**, *109*, 3387-3390.

32 W. Helfrich, J. Prost, *J. Phys. Rev. A,* **1988**, *38*, 3065-3068.

33 H. Ihara, M. Takafuji, T. Sakurai, *Encyclopedia of Nanoscience and Nanotechnology*, American Scientific Publishers, California, **2004**, *9*, 473-495.

34 A. Brizard, R. Oda, I. Huc, *Top Curr. Chem.*, **2005**, *256*, 167-218.

35 (a) B. A. Korgel, *Science*, **2005**, *309*, 1683–1684. (b) A. F. Fonseca, C. P. Malta, D. S. Galvao, *Nanotechnology*, **2007**, *18*, 435606. (c) A. L. Elias, K. D. Harris, C. W. M. Bastiaansen, D. J. Broer, J. Brett,M, *J. Micromech. Microeng.*, **2005**, *15*, 49–54.

36 L. A. Estroff, A. D. Hamilton, *Chemical Reviews*, **2004**, *104*, 1201-1217.

37 F. A. Luzzio, *Tetrahedron*, **2001**, *57*, 915–945.

38 Y. Yan, Y. Lin, Y. Qiao, J. Huang, *Soft Matter.*, **2011**, *7*, 6385-6398.

39 J. F. McCrea, S. Angerer, *Biochim. Biophys. Acta*, **1960**, *42*, 355-357.

40 N. Ramanathan, A. L. Currie, J. R. Colvin, *Nature*, **1961**, *190*, 779-781.

41 N. Nakashima, S. Asakuma, J. M. Kim, T. Kunitake, *Chem. Lett.*, **1984**, 1079-1712.

42 N. Nakashima, S. Asakuma, T. Kunitake, *J. Am. Chem. Soc.*, **1985**, *107*, 509-510.

43 J. H. Fuhrhop, P. Schnieder, E. Boekema, W. Helfrich, *J. Am. Chem. Soc.*, **1988**, *110*, 2861-2867.

44 J. H. Fuhrhop, C. Boettcher, *J. Am. Chem. Soc.*, **1987**, *112*, 1768-1776.

45 J. H. Fuhrhop, P. Blumtritt, C. Lehmann, P. Luger, *J. Am. Chem. Soc.*, **1991**, *113*, 7437-7439.

46 J. H. Fuhrhop, W. Helfrich, *Chem. Rev.*, **1993**, *93*, 1565-1582.

47 A. D. Bungham, M. M. Standish, J. C. Watkins, *J. Mol. Biol.*, **1965**, *13*, 238-252.

48 K. Yamada, H. Ihara, T. Ide, T. Fukumoto, C. Hirayama, *Chem. Lett.*, **1984**, 1713-1716.

49 H. Ihara, T. Fukumoto, C. Hirayama, K. Yamada, *Polym Commum.*, **1986**, *27*, 282-285.

50 C. Cescato, P. Walde, P. L. Luisi, *Langmuir*, **1997**, *13*, 4480-4482.

51 H. Yanagawa, Y. Ogawa, H. Furuta, K. Tasuno, *J. Am. Chem. Soc.*, **1988**, *111*, 4567-4570.

52 R. Oda, I. Huc, M. Schmutz, S. J. Candau, F. C. MacKintosh, *Nature*, **1999**, *399*, 566-569.

53 R. Oda, I. Huc, S. J. Candau, *Angew. Chem. Int. Ed. Engl.*, **1998**, *37,* 2689-2691.

54 A. Brizard, C. Dolain, I. Huc, R. Oda, *Langmuir*, **2006**, *22*, 3591-3600.

55 Roni Ahamad, Oligo-peptide confined on the membrane surface of cationic amphiphiles, *Thesis of Doctrante, Bordeaux 1 Unversity*, **2008.**

56 R. Kiagus-Armad, A. Brizard, C. Tang, R. Blatchly, B. Desbat, R. Oda, *Chem. Eur. J.*, **2011**, *17*, 9999-10009.

[57] B. V. Shankar, A. Patnaik, *J. Phys. Chem. B*, **2007**, *111*, 9294-9300.

[58] (a) T. Shimizu, M. Masuda, *J. Am. Chem. Soc.*, **1997**, *119,* 2812-2818. (b) M. Masuda, T. Shimizu, *J. Carbohydr. Chem.*, **1998**, *17*, 405-416. (c) I. Nakagawa, M. Masuda, Y. Okada, T. Hanada, K. Yase, M. Asai, T. shimizu, *Langmuir*, **1999**, *15*, 4757-4764. (d) I. Nakagawa, S. Suda, M. Asai, T. Shimizu, *Chem. Commun.*, **2000**, 881-882.

[59] M. Masuda, T. Shimizu, *Langmuir*, **2004**, *20,* 5969-5977.

[60] G. John, M. Masuda, Y. Okada, K. Yase, T. Shimizu, *Adv. Mater.*, **2001**, *13*, 715-718.

[61] S. Kamiya, H. Minamikawa, J. H. Jung, B. Yang, M. Matsuda, T. shimizu, *Langmuir*, **2005**, *21*, 743-750.

[62] T. Muraoka, H. Cui, S. I. Stupp, *J. Am. Chem. Soc.*, **2008**, *130,* 2946-2947.

[63] Y. C. Lin, R. G. Weiss, *Macromolecules*, **1987**, *20*, 414-417.

[64] N. Ide, T. Fukuda, T. Miyamoto, *Bull. Chem. Soc. Jpn.*, **1995**, *68*, 3423-3428.

[65] H. Ihara, H. Hachisako, C. Hirayama, K. Yamada, *J. Chem. Soc. Chem. Commun.*, **1992**, 1244-1245.

[66] Y. Ishikawa, H. Kuwahara, T. Kunitake, *J. Am. Chem. Soc.*, **1989**, *111*, 8530-8531.

[67] L. Lu, D. L. Cocker, R. E. Bachman, R. G. Weiss, *Langmuir*, **2000**, *16*, 20-34.

[68] W. Jin, T. Fukushima, M. Niki, A. Kosaka, N. Ishii, T. Aida, *PNAS*, **2005**, *102*, 10801–10806.

[69] W. Jin, T. Fukushima, A. Kosaka, M. Niki, N. Ishii, T. Aida, *J. Am. Chem. Soc.*, **2005**, *127*, 8284–8285.

[70] S. Abraham, K. Vijayaraghavan, S. Das, *Langmuir*, **2009**, *25*, 8507-8513.

[71] J. H. Jung, H. Kobayashi, M. Masuda, T. Shimizu, S. Shinkai, *J. Am. Chem. Soc.*, **2001**, *123*, 8785-8789.

[72] S. Kawano, N. Fujita, S. Shinkai, *Chem. Eur. J.*, **2005**, *11*, 4735–4742.

[73] W. W. Tsai, L. Li, H. Cui H. Jiang, S. I. Stupp, *Tetrahedron*, **2008**, *64*, 8504-8514.

[74] J. V. Selinger, M. S. Spector, J. M. Schnur, *J. Phs. Chem. B*, **2001**, *105*, 7158-7169.

[75] G. John, J. H. Jung, H. Minamikawa, K. Yoshida, T. Shimizu, *Chem. Eur. J.*, **2002**, *8*, 5494-5500.

[76] J. M. Schnur, *Science*, **1993**, *262*, 1669-1676.

[77] T. Shimizu, M. Masuda, H. Minamikawa, *Chem. Rev.* **2005**, *105*, 1401-1443.

[78] J. H. Jung, G. John, K. Yoshida, T. Shimizu, *J. Am. Chem. Soc.* **2002**, *124*, 10674-10675.

[79] S. Svenson, P. B. Messersmith *Langmuir*, **1999**, *15*, 4464-4471.

[80] M. S. Spector, A. Singh, P. B. Messersmith, J. M. Schnur, *Nano Letters*, **2001**, *1*, 375-78.

[81] H. Cui, T. Muraoka, A. G. Cheetham, S. I. Stupp, *Nano Letters*, **2009**, *9*, 945-951.

[82] L. Ziserman, H. Y. Lee, S. R. Raghavan, A. Mor, D. Danino, *J. Am. Chem. Soc.*, **2011**, *133,* 2511-2517.

[83] Y.V. Zastavker, N. Asherie, A. Lomakin, J. Pande, J. M. Donovan, J. M. Schnur, G. B. Benedek, *Proc. Natl. Acad. Sci.*, **1999**, *96,* 7883-7887.

[84] B. N. Thomas, C. M. Lindemann, R. C. Corcoran, C. L. Cotant, J. E. Kirsch, P. J. Persichini, *J. Am. Chem. Soc.*, **2002**, *124*, 1227-1233.

[85] T. Gulik-Krzywicki, C. Fouquey, J. M. Lehn, *Proc. Natl. Acad. Sci.*, **1993**, *90,* 163-167.

[86] V. Vogel, M. Sheetz, *Nature Reviews*, **2006**, *7*, 265-275.

[87] S. B. Prusiner, *Proc. Natl. Acad. Sci. U.S.A.*, **1998**, *95*, 13363-13383.

[88] C. Weismann, *FEBS Lett.*, **1997**, *389*, 3-11.

[89] N. Stahl, M. A. Baldwin, M. A. McKinley, K. A. Bowman, M. B. Braunfeld, R. A. Barry, S. P. Prusiner, *Biochemistry*, **1993**, 1991-2002.

[90] W. Sweitnicki, M. Morillas. S. Chen, P. Gambetti, W. K. Surewicz, *Biochemistry*, **2000**, *39*, 424-431.

[91] M. Morillas, D. L. Vanik, W. K. Surewicz, *Biochemistry*, **2001**, *40*, 6982-6987.

[92] G. Tuchscherer, A. Chandravarkar, M. S. Camus, J. Bérard, K. Murat, A. Schmid, R. Mimna, H. A. Lashuel, M. Mutter, *Peptide Science*, **2007**, *88*, 239-252.

[93] O. A. Gus'kova, P. G. Khalatur, A. R. Khokhlov, *Nanotechnologies In Russia*, **2008**, *3*, 481-493.

[94] Y. Jeong, M. K. Joo, K. H. Bahk, Y. Y. Choi, H. T. Kim, W. K. Kim, H. J. Lee, Y. S. Sohn, B. Jeong, *J. Control. Release*, **2009**, *137*, 25-30.

[95] C. Tsitsilianis, *Soft Matter.*, **2010**, *6*, 2372–2388

[96] C. Tie, J. C. Gallucci, J. R. Parquette, *J. Am. Chem. Soc.*, **2006**, *128*, 1162-1171.

[97] Y. Wang, H. D. Tran, L. Liao, X. Duan, R. B. Kaner, *J. Am. Chem. Soc.*, **2010**, *132*, 10365–10373.

[98] T. B. Schuster, D. de B. Ouboter, C. G. Palivan, W. Meier, *Langmuir*, **2011**, *27*, 4578–4584.

[99] X. Jiang, Y. K. Lim, B. J. Zhang, E. A. Opsitnick, M. H. Baik, D. Lee, *J. Am. Chem. Soc.*, **2008**, *130*, 16812–16822.

[100] P. Duan, L. Qin, X. Zhu, M. Liu, *Chem. Eur. J.*, **2011**, *17*, 6389 – 6395

[101] I. Stary, I. G. Stara, Z. Alexandrova, P. Sehnal, F. Teply, D. Saman, L. Rulisek, *Pure Appl. Chem.*, **2006**, *78*, 495–499.

[102] R. Amemiya, M. Ymaguchi, *The Chemical Record*, **2008**, *8*, 116–127.

[103] R. Amemiya, M. Mizutani, M. Yamaguchi, *Angew. Chem. Int. Ed.*, **2010**, *49*, 1995 –1999.

[104] B. N. Thomas, C0 M. Lindemann, N. A. Clark, *Physical Review E*, **1999**, *59*, 3040-3047.

[105] Y. Jin, X. D. Xu, C. S. Chen, S. Cheng, X. Z. Zhang, R. X. Zhuo, *Macromol. Rapid. Commun.*, **2008**, *29*, 1726-1731.

[106] T. Wang, J. Jiang, Y. Liu, Z. Li, M. Liu, *Langmuir*, **2010**, *26*, 18694-18700.

[107] H. Kobayashi, K. Koumoto, J. H. Jung, S. Shinkai, *J. Chem. Soc.*, *Perkin Trans.*, **2002**, *2*, 1930–1936.

[108] Y. Lin, A. Wang, Y. Qiao, C. Gao, M. Drechsler, J. Ye, Y. Yan, J. Huang, *Soft Matter*, **2010**, *6*, 2031–2036.

Chapter II

Micrometric helical structures from nucleolipids

II.1 Introduction

The supramolecular assemblies are well defined as complexes of molecules which are linked with non-covalent and weak interactions. The supramolecular structures are easily perturbed with out-of-equilibrium process by external factors, which can result in *in situ* morphology transformation at constant temperature. In this chapter, we will discuss *in situ* vesicle to helix transformation produced by interaction between non-chiral cationic vesicles and chiral anion nucleotide.

II.1.1 Study of nucleotide

Using bio-inspired self-assembly systems based on building blocks which mimic biomolecules, one can develop biomimetice systems. The DNA and RNA are good examples in which their double helical structures result from multiple interactions of nucleobases based on specific hydrogen bonds (Watson-Crick configuration) between complementary bases: adenine and thymine/uracil; cytosine and guanosine (Figure II.1) along with unspecific stacking interactions.[1]
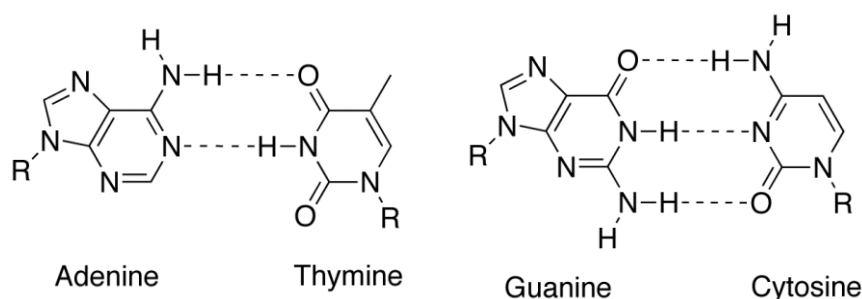
Figure II.1 The formation of hydrogen bonds between complementary nucleobases (A-T and G-C) following the rule of Watson Crick pairing.

The nucleobases are made either of purine base for guanine (G) and adenine (A), and pyrimidine base for cytosine (C), thymine (T), and uracil (U). Each of these bases has multiple sites of acceptors (**A**) and donors (**D**) from hydrogen bonds (Figure II.2). Nucleic acids are composed of a nucleobase (nitrogenous base), a five-carbon sugar (either ribose or

2'-deoxyribose) and a phosphate group connecting in position *3'* or *5'* of sugar (Figure II.3 and Table II.1).
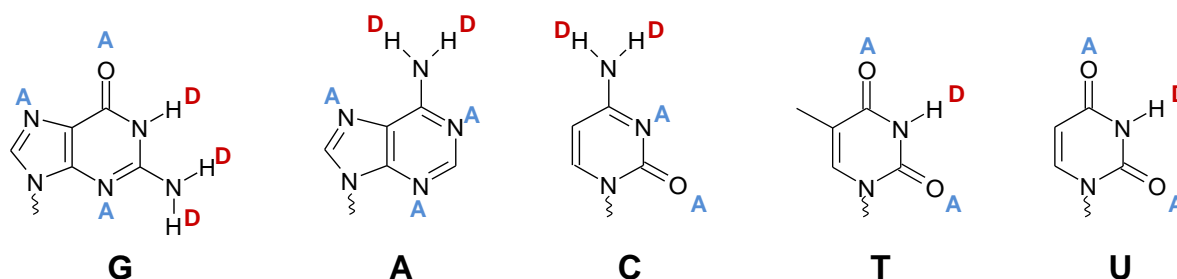
Figure II.2 Molecular structures of nucleobases presenting the site positions of acceptors (A) and donors (D) from hydrogen bonds. G : guanine, A : adenine, C : thymine, and U : uracil.

Adenine   Adenosine   Adenosine 5'-monophosphate
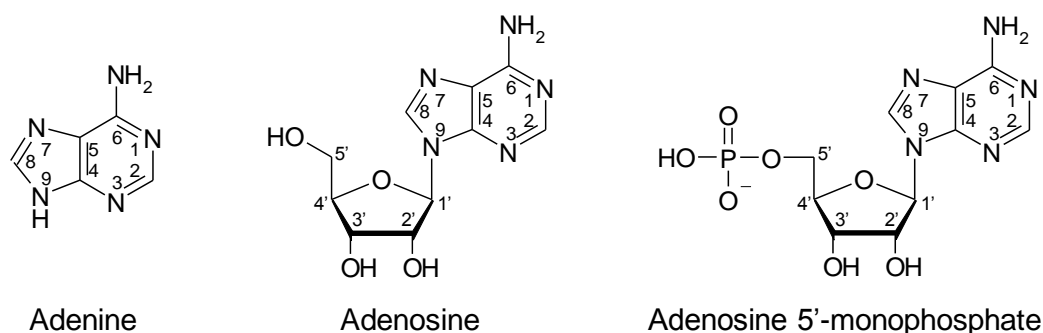
Figure II.3 Molecular structure of a nucleobase (example is adenine), a nucleoside (example is adenosine), and a nucleotide (example is adenosine 5'-monophosphate).

Table II.1 Classification of nucleic acids, nucleosides, and nucleotides.

Base	Nucleoside	Nucleotide
Adenine	Adenosine	Adenosine 5'-monophophate (**AMP**)
Cytosine	Cytidine	Cytidine 5'-monophosphate (**CMP**)
Guanosine	Guanosine	Guanosine 5'-monophophate (**GMP**)
Thymine	Thymidine	Thymidine 5'-monophophate (**TMP**)
Uracile	Uridine	Uridine 5'-monophophate (**UMP**)

The pK_a of each nucleotide is an important factor to determine the molecular conformation based on the protonation. The pK_as of nucleosides and nucleotides vary from 3.5 to 10.5 (about 0.5 units higher for nucleoside than nucleotide (Table II.2)[2] (Figure II.4)[3]). As for these nucleotides, the monoester phosphate group has 3 different pK_a values, 2.5, 7.2 and 12.4 (Figure II.5).

Table II.2 pK_a of nucleosides and nucleotides. These values are from issues of Saenger, 1984.[2]

Composition	Nucleoside	5'-phophate
Adenosine	3.52	3.88
Cytidine	4.17	4.54
Guanosine	9.42	10
Uridine	9.38	10.06
Desoxythimidine	9.93	10.47
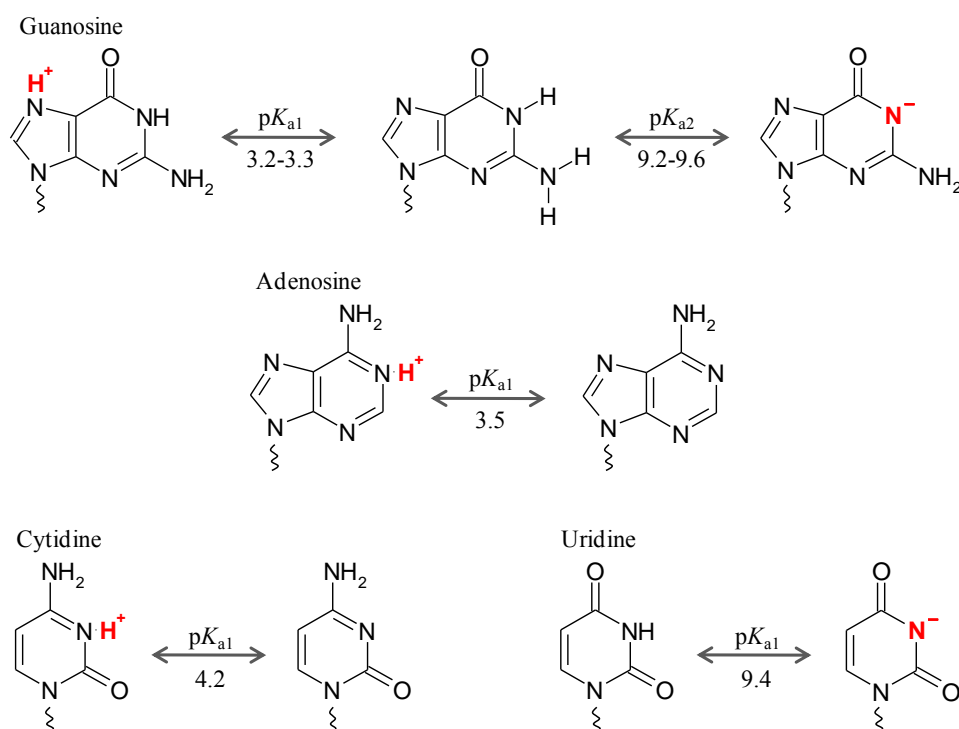
Figure II.4 Intrinsic pK_a values ionisable guanosine, adenosine, cytidine, and uridine in aqueous solution. [3]
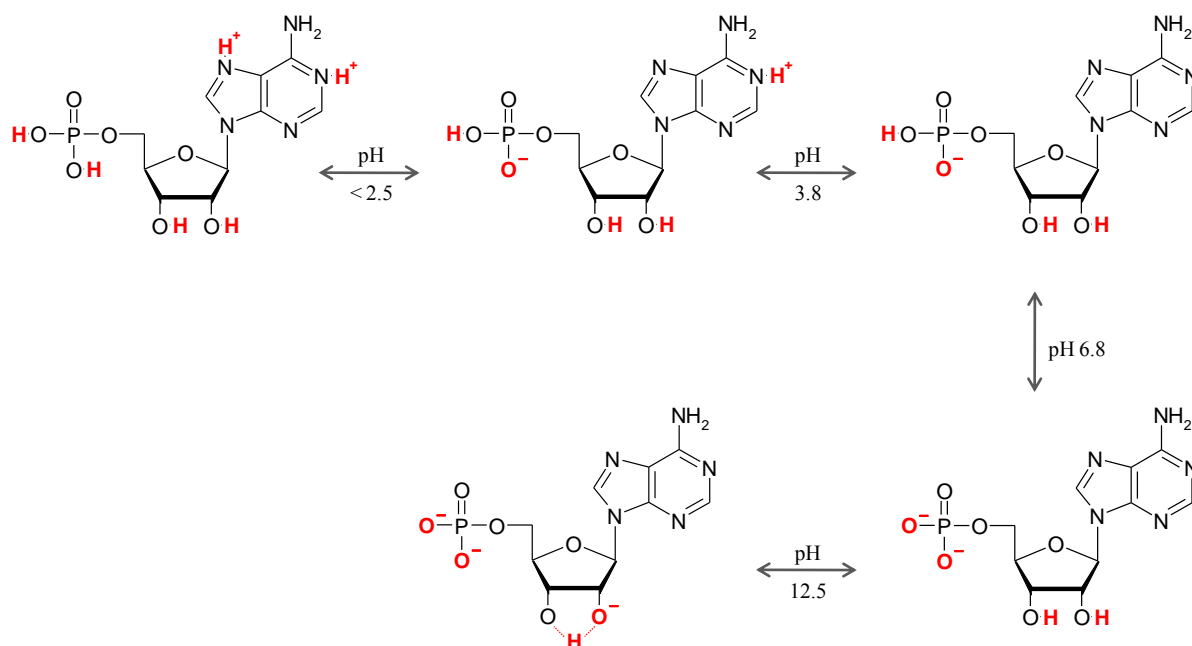
Figure II.5 The protonation sites of AMP. The first ionization of phosphate group is completed around pH 2. Adenine becomes neutral beyond pH 3.8. Secondary protonation of phosphate group occurs at pH 6.8, and then sugar is ionized at pH 12.5.

II.1.2 Complexation of a surfactant by nucleolipids

In the field of self-assemblies, the nucleo-amphiphilic molecules are particularly interesting because of the combination of molecular recognition (*e.g.,* specific hydrogen bond, π-stacking, electrostatics *etc.*) and molecular assembly properties.[4] A variety of synthetic strategies have been used to prepare nucleotide-based amphiphiles.[5]

Figure II.6 shows examples of nucleolipids and their supramolecular morphologies. Barthélémy et al. have reported the structure of nucleolipids with fatty esters (**1**) or fluorocarbon chains (**2**) on the 2' and 3' ribose positions of uridine moiety, which can form multilayer micrometric vesicle.[6,7] Simizu et al. have developed hydrogelators obtained by nucleotide-appended bolaamphiphile, in which two 3'-phosphorylated thymidine moieties are connected to both end of a long alkyl chain spacer (**3**). This nucleolipid can form nanofibers expending to the gel network in water.[8] Cholesterol-modified nucleoside, which is attached to the 2' position of uridine, can self-assemble to form microtubes in the presence of

phospholipid.[9] Chiral nanostructure can be also obtained by nucleo lipid. Adenosine-based phosphatidyl nucleoside (**5**) can form twisted nanoribbons.[10] All systems involve that the hydrophobic chain is connected directly to nucleic acid *via* covalent bonding. Few non-covalent systems of nucleoamphiphiles have been developed in the field of supramolecular self-assembly.
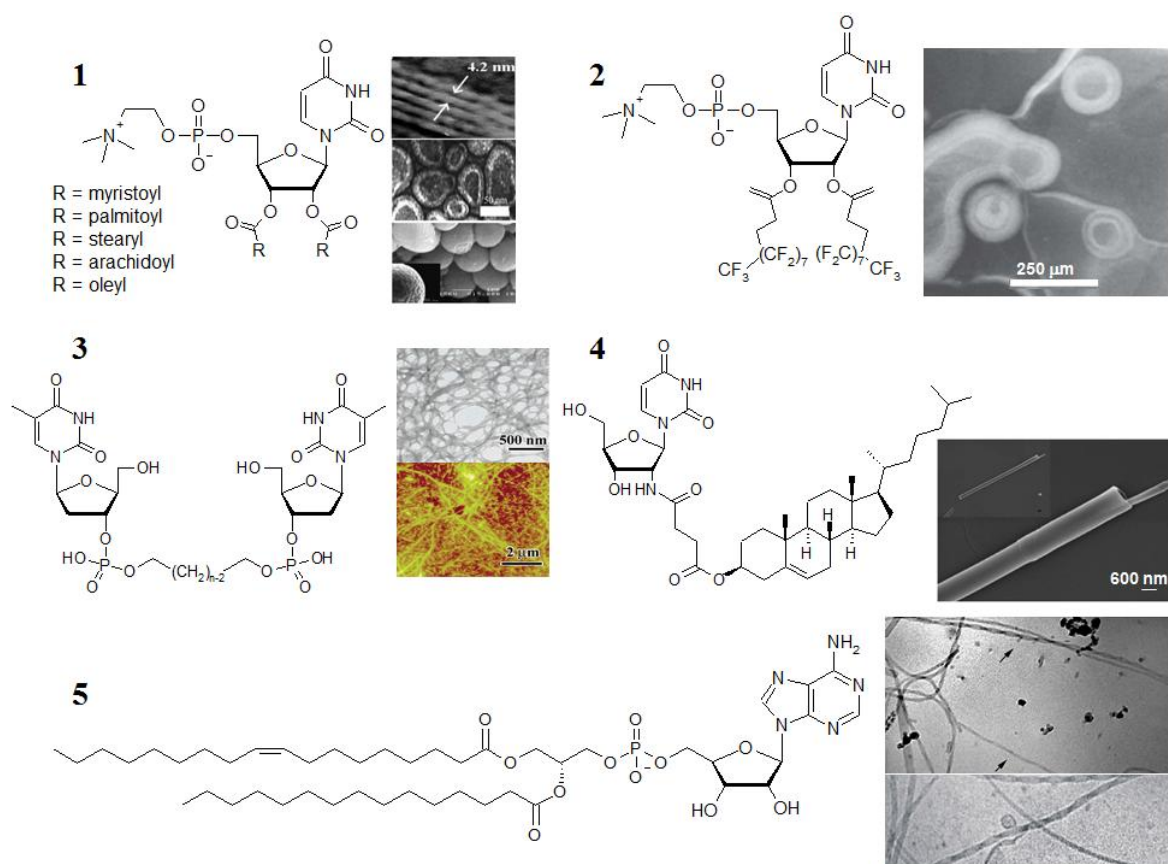
Figure II.6 Examples of various nucleoamphiphiles: molecular structures and their aggregates.

The self-assembly of nucleo-amphiphile provides the containment nucleotides at the surface of aggregates and promote inter-nucleotide interaction (Figure II.7). The mainly driving forces of building blocks are hydrogen bonding and π- π stacking of nucleo-bases.
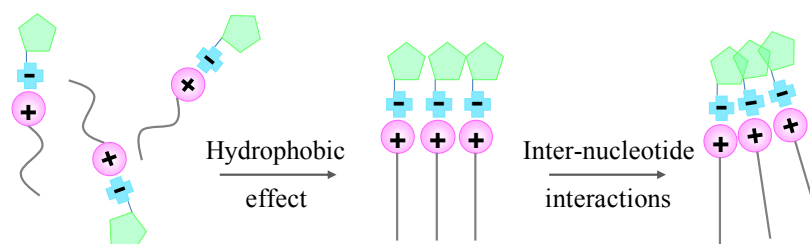
Figure II.7 Schematic illustration of cooperative effect in charge of self-assembly of nucleo-amphiphiles in aqueous solution.

Among various approaches, the group of Oda has proposed the chirality induce by chiral nucleotide as counter-anion complexed with non-chiral cationic surfactant *via* non-covalent bonding.

Carole Aimé has studied complex between lipid-type cationic surfactant with anionic nucleotide by electrostatic interactions in her PhD thesis.[11] The molecules she has developed are made from a monocationic surfactant having two hydrophobic chains of 12 and 14 carbons (C_{12} and C_{14}) complexed with monoanionic nucleotides. It was observed that particularly the complex with adenosine 5'-monophosphate (AMP) and guanosine 5'-monophosphate (GMP) had stronger tendency to form gel in water. This was probably because these nucleic bases are more hydrophobic and form stronger stacking than CMP and UMP.[12] The complex are noted hereafter C_{14}AMP (Figure II.8 a), C_{12}GMP (Figure II.8 b), and C_{14}GMP (Figure II.8 c). She has shown that these nucleoamphiphiles can be self-assembled to form micrometric fibers and left-handed helices in pure water.
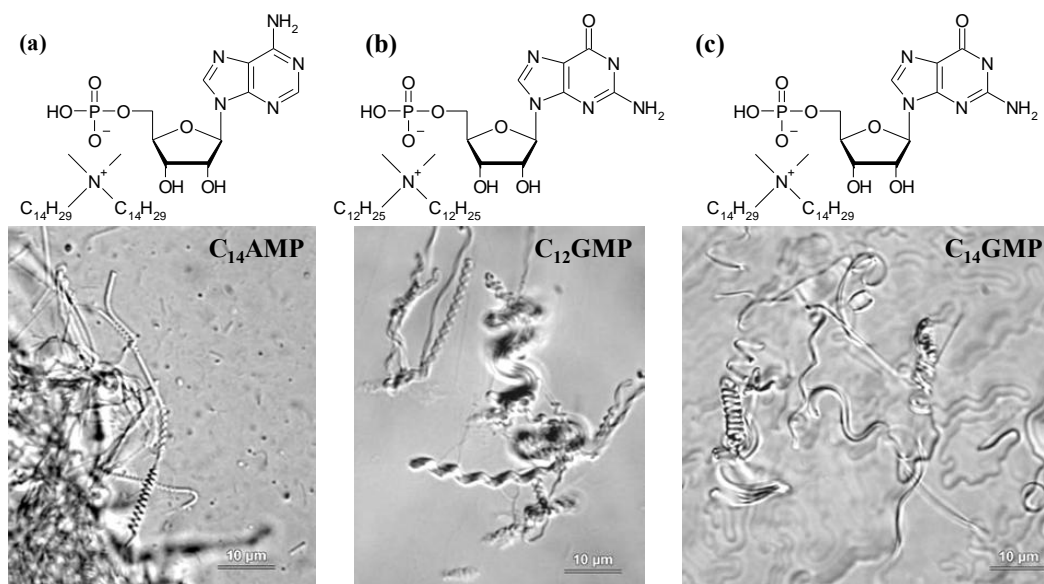
Figure II.8 Formula of the nucleamphiphiles and each optical microscope (OM) images of chiral fibers and helices formation in pure water resulting from self-assembly of (a) C$_{14}$AMP, (b) C$_{12}$GMP, and (c) C$_{14}$GMP.

More recently, the direct observations of morphology transition of self-assembled nucleoamphiphilic systems in aqueous solution are followed with a mesoscopic aspect by optical microscopy.[13] Carole Aimé also reported in her PhD thesis that anionic AMP can interact with cationic vesicles, exchange with the counter-anions of the amphiphiles *in situ,* and organize themselves at the membrane surface.[11] When a solution of AMP in its acid form is added to the suspension of Non-chiral cationic vesicle obtained by C$_{14}$ amphiphile in the presence of non-chiral acetate counter-anion (noted as C$_{14}$Ac), these vesicles are transformed to helices *via* counter-anion exchange (Figure II.9). This system emphasizes the importance of ion exchange kinetics and AMP reorganization in the morphologies of aggregates.
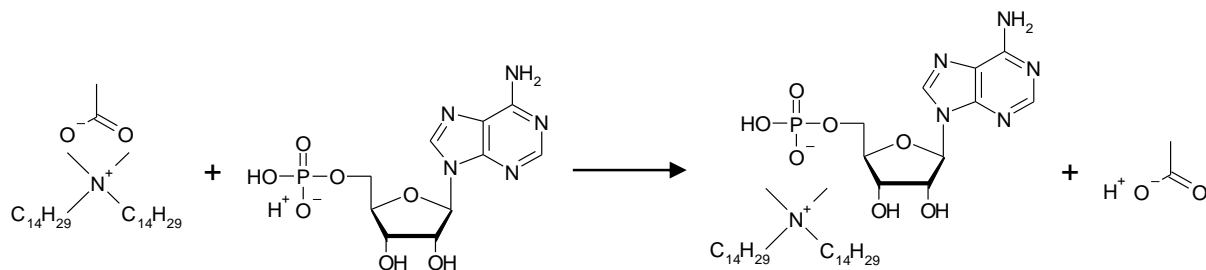
Figure II.9 (a) Scheme of the counter-anion exchange process.

In this chapter, following Aimé's results, we have developed the study on the kinetic aspect of this system. A part of these studies have already initiated Carole Aimé during her PhD thesis, hereafter we have clearly marked when the data are taken from her PhD thesis.

We also reveal another vesicle to helix morphology transition from vesicle to helix formation in C_nAc + GMP systems, and compare both the kinetics at macroscopic, mesoscopic and molecular aspect depending on the different nucleotides. The kinetics of chirality transfer is investigated on the mesoscopic level by optical microscopy observation (OM), on the supramolecular scale by circular dichroisms (CD) studies and on the molecular scale by ^{1}H-NMR and infrared (IR) studies.

II.2 *In situ* kinetics of chirality transfer

As we discussed in the paragraph II.1.2, micrometric helical structures are obtained by the complex of monocationic non-chiral surfactant in the presence of adenosine 5'-monophosphate (AMP) or guanosine 5'-monophosphate (GMP) counter-monoanion.[12] These structures were also observed by morphology transition from vesicles *via* counter-anion exchange from non-chiral acetate ion to chiral AMP at constant temperature. Herein, we demonstrate the *in situ* structural transformation from vesicle solution to helices by addition of GMP.

II.2.1 Experimental description

The vesicles solution was formed by solubilizing dialkyldimethylammonium acetate (C_nAc, n = 12, 14) in water. A 15 mM C_nAc aqueous solution was heated up to about 40 ˚C to solubilize the powder, and then kept at room temperature (Figure II.10). After cooling, vesicles are formed and solution become clear and fluid (Figure II.11 a).
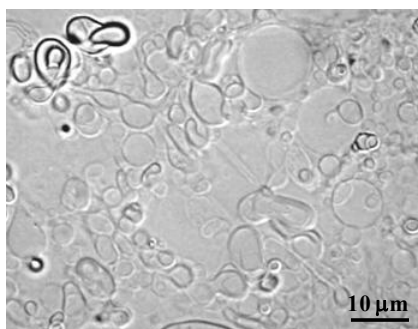
Figure II.10 OM images of vesicles of 15 mM $C_{12}Ac$ self-assembled in water.

A solution of acid form of AMP or GMP was added to this vesicles solution. Different behaviors were observed depending on the nucleotide, hydrophobic chain length of the surfactant, and their concentrations. Hereafter, unless explicitly noted, 1 equivalent of nucleotide was added with respect to C_nAc.

II.2.2 Kinetics study at macroscopic level

First, we considered the different kinetics of morphology transformation depending on the different nucleotides at macroscopic aspect.

When the solution of $C_{14}Ac$ was mixed with AMP solution at a final concentration of 15 mM for each reagent, the white precipitates were observed after few hours (Figure II.11 b).

On the other hand, after the addition of GMP to $C_{14}Ac$ solution at a final concentration of 15 mM, the viscosity of mixture increased immediately and the suspension turned into a gel. The kinetics of gel formation was much faster than the precipitation observed with $C_{14}Ac$ + AMP system at the same concentration.

The same study with the $C_{12}Ac$ system showed that the kinetics of the gel formation for $C_{12}Ac$ + GMP system was slightly slower than that with $C_{14}Ac$, but still much faster than the kinetics of precipitation observed with $C_{14}Ac$ + AMP system. When $C_{12}Ac$ and GMP are mixed at a final concentration of 15 mM, the viscosity of the solution increased immediately. After 1 day, we observed a hard gel, which was continuously shrinking and dewatered for 7 to 10 days (Figure II.11 c).
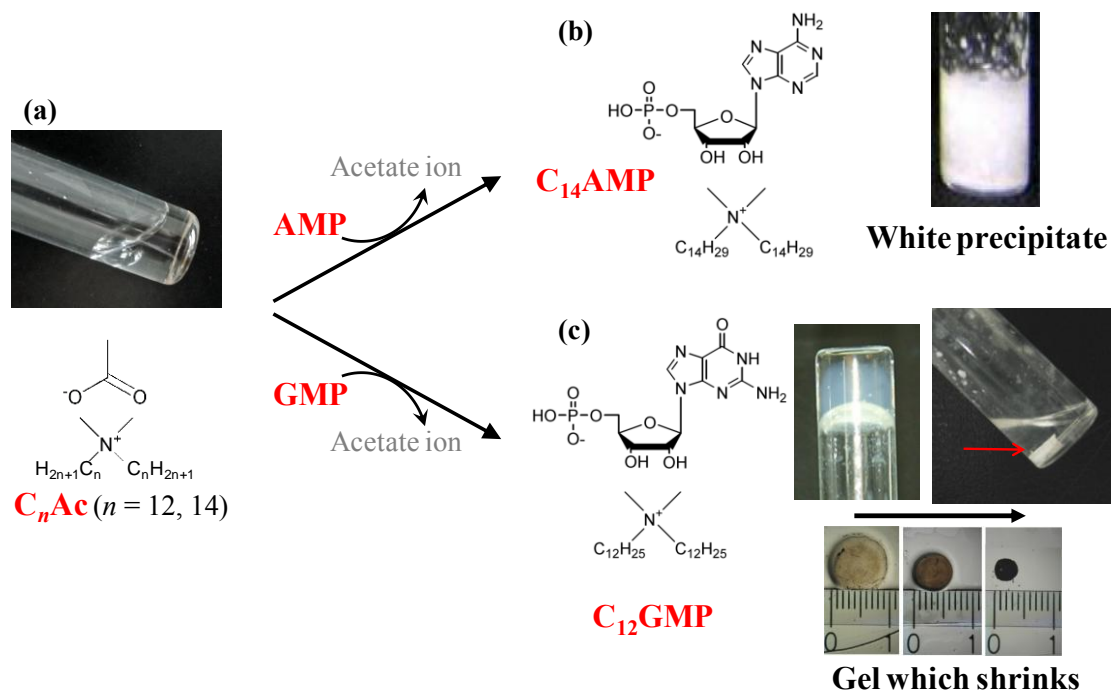
Figure II.11 Scheme of the counter-anion exchange process and sample photographs of (a) solution of C_nAc, (b) precipitate of C_14AMP, and (c) shrinking gels of C_12GMP. From the PhD thesis of Carole Aimé.[11]

II.2.3 *In situ* transition of morphologies

The formation of chiral structure results from the addition of nucleotides to non-chiral vesicles. Upon addition of nucleotide AMP or GMP, ion exchange occurred *in situ*: nucleotide replaced acetate counterions because the pK_a of phosphate group in water is lower than that acetate (2 vs 4.76).

In the following study, we followed the structural transformation of aggregates using optical microscopy (OM).

C_14Ac + AMP

The case of $C_{14}Ac + AMP$ system is shown in Figure II.12. When the AMP was added to the vesicle solution of $C_{14}Ac$, vesicles ruptured immediately to form denser structures

(Figure II.12 a). From denser cores, fibers started growing and chiral helices formed along with needles for 30 min (Figure II.12 b-d). All of denser structures were disappeared after 3 h, and the helix formation continued to grow up with time for a day (Figure II.12 e, f). Finally, the width of helical fibers was $1.5 \sim 2.5$ μm and length was $10 \sim 50$ μm.
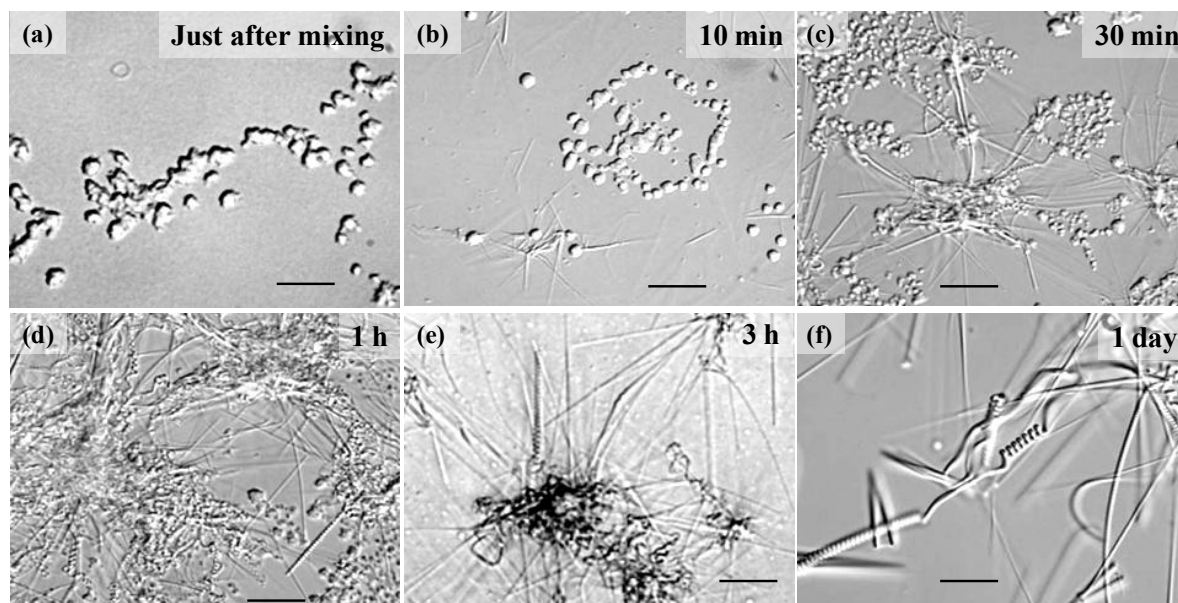
Figure II.12 OM images of helix formation observed with $C_{14}Ac$ + AMP system. The scale bars are 10 μm.

Interestingly, the formation of micrometric helices was limited in the surfactant concentration range of 10-15 mM. At 5 mM, no needles and no fibers were observed, and at 20 mM, mainly needles that did not show apparent chiral structure were observed under OM.

$C_{14}Ac$ + GMP

The case of $C_{14}Ac$ + GMP system is shown in Figure II.13. Right after mixing, the vesicles transformed to continuous thin membranes (Figure II.13 a). These membranes became denser and turned to chiral fibers within 10 min (Figure II.13 b). These chiral fibers continued to grow for about a day (Figure II.13 b-f). As previously, the formation of micrometric helices was limited to $5 - 15$ mM surfactant solutions.
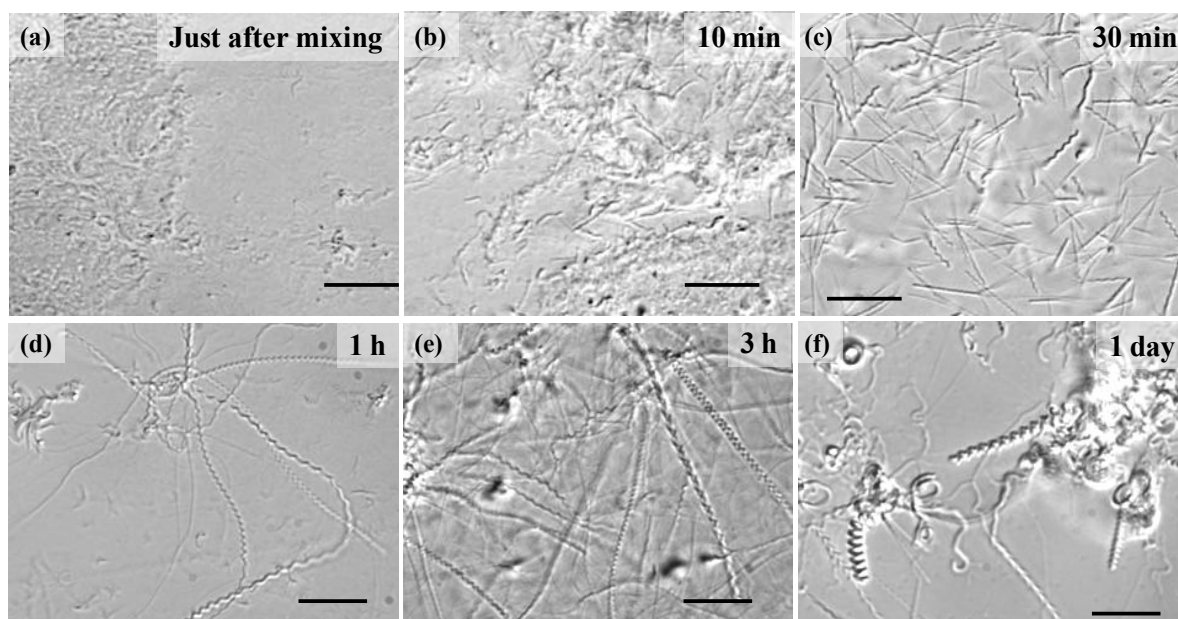
Figure II.13 OM images of helix formation observed with $C_{14}Ac$ + GMP system. The scale bars are 10 μm.

It is noteworthy that the kinetics with $C_{14}Ac$ + GMP was too fast to capture the morphology transition not only at a supramolecular level, but also at molecular level. Therefore, we studied the transition with $C_{12}Ac$ + GMP system as below.

$C_{12}Ac$ + GMP

In the case of $C_{12}Ac$ + GMP system, morphology transition occurred more slowly than that with $C_{14}Ac$. Right after mixing, the vesicles transformed into continuous thin membranes (Figure II.14 a). Some parts of these membranes became fibers and aggregated into denser structures. After about half an hour, these fibers tuned into chiral left-handed helices, and continued to grow (Figure II.14 b-e) for about a week (Figure II.14 f). Finally, the width of helical fibers was 1.5 ~ 3 μm and length was 20 ~ 70 μm. The formation of micrometric helices was limited to 5 – 15 mM surfactant solutions.
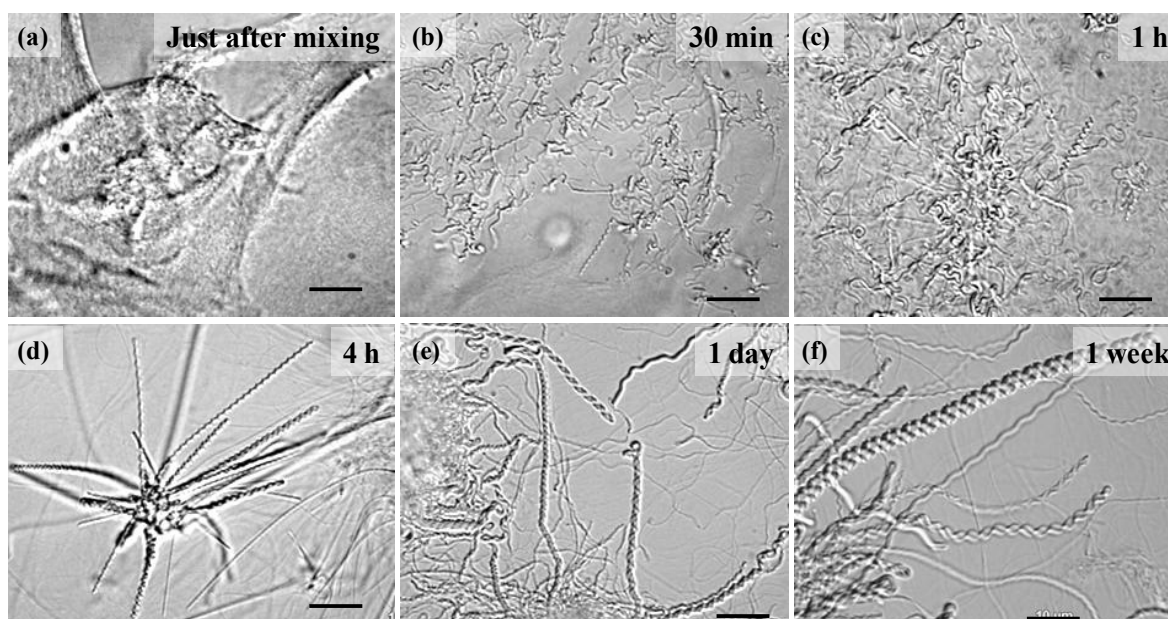
Figure II.14 OM images of helix formation observed with $C_{12}Ac$ + GMP system. The scale bars are 10 μm.

II.2.4 TEM observation at nanometric scale in the difference systems

We then observed the details of these micrometric helices with transmission electron microscope. For both cases, ($C_{14}Ac$ + AMP and $C_{12}Ac$ + GMP) small fibers with the diameter of about 100 nm appeared initially before the formation of micrometric helices (Figure II.15 b, d).

These fibers clearly showed left-handed helical structure with helical pitches of the order of a few 100 nm. For the case of $C_{14}Ac$ + AMP, rigid cigar-like fibers were observed (Figure II.15 b). On the other hand, more flexible helical fibers were observed in the case of $C_{12}Ac$ + GMP (Figure II.15 d)

The differences in the aspect of these elementary nanometric fibers are probably reflected by the differences between precipitate ($C_{14}Ac$ + AMP) and gel formation ($C_{12}Ac$ + GMP).
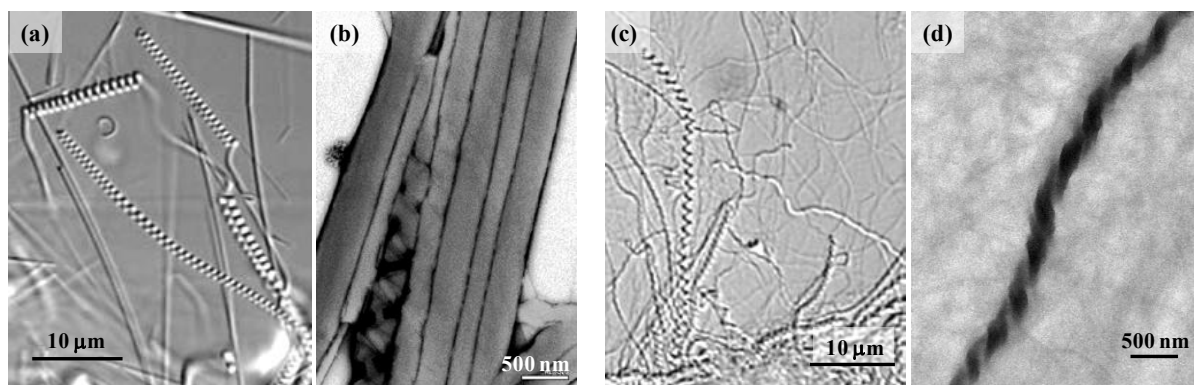
Figure II.15 Kinetics of (a, c) OM and (b, d) TEM presented the formation of chiral fibers over the gel from (a, b) $C_{14}Ac$ + AMP (15 mM) and (c, d) $C_{12}Ac$ + GMP (15 mM). The helical formation observed after 1 day.

II.2.5 Direct observation of morphology transition and helix growth

We then observed in detail how these helices grew.

Figure II.16 shows the monitoring of morphology transformation. In the case of $C_{14}Ac$ + AMP, the vesicles first ruptured to form dense structures, and the fibers grew from dense cores for 5 min, and after 30 min (Figure II.16 a), chirality was expressed and helices continuously grew up. On the other hand, in the case of $C_{12}Ac$ + GMP, continuous films were first formed before helices growth (Figure II.16 b).
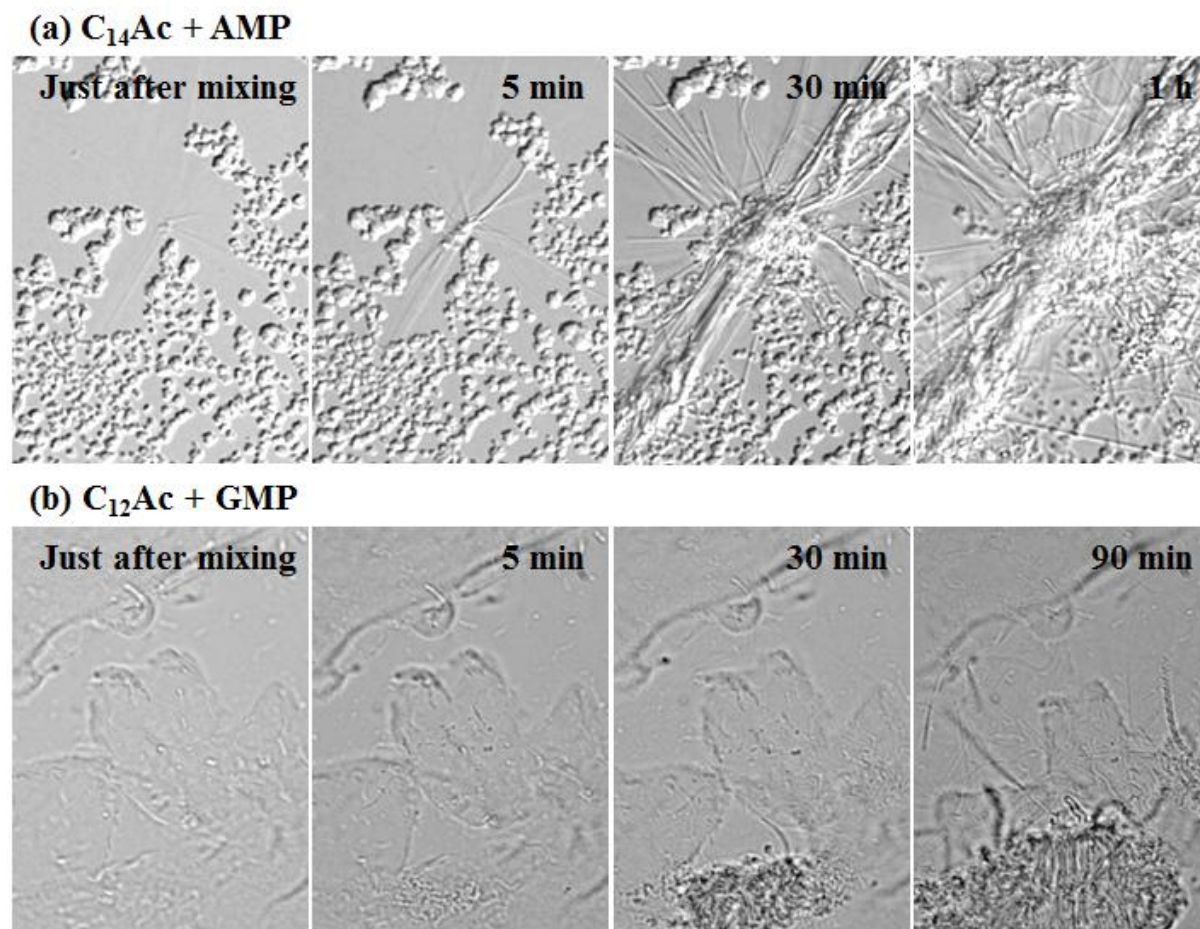
Figure II.16 Kinetics monitoring of morphology transformation observed with (a) C$_{14}$Ac + AMP and (b) C$_{12}$Ac + GMP systems.

The step by step of helix growth was followed by OM in both cases (Figure II.17). The helix growth seems to occur at their extremities with a coiling motion (Figure II.17 a, d). As the helices grew, the denser structures/cores deflated and finally disappeared (Figure II.17 b).
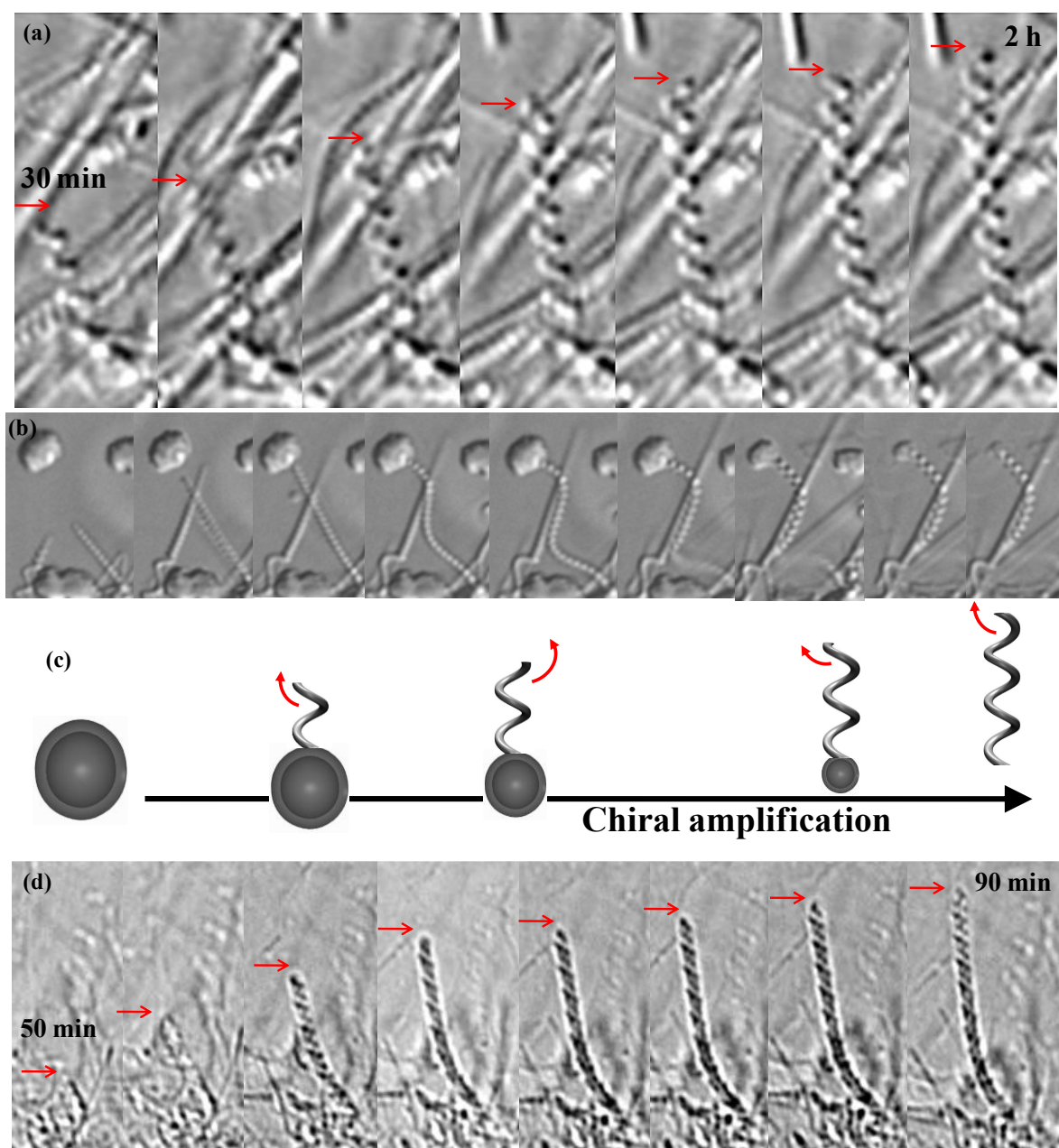
Figure II.17 Step by step helix formation of (a, b) C$_{14}$Ac + AMP and (d) C$_{12}$Ac + GMP followed by OM. (a, b) global growth from vesicles and (d) thin films, respectively. (c) Schematic representation of helices' growth from vesicles.

In the following sections, we investigated the changes in molecular environment due to the counter-anion exchange and the change in the molecular organization of C$_n$Ac + nucleotide systems in order to correlate them with the morphological changes of aggregates observed above.

For this purpose, we have coupled different techniques: CD, NMR, IR spectroscopy

and pH measurements.

II.3   Study of kinetics of molecular reorganization during helix formation

II.3.1 Study of chirality transfer using CD spectra

We first followed the chirality transfers derived from chirality inducing from nucleotide counter-anion to C_nAc amphiphile using Circular Dichroism (CD) measurement.

CD spectroscopy is the most versatile tool for the study of assemblies of chiral molecules, it measures the variation of absorption of P and M circularly polarized light. CD spectra are generally recorded in the UV-vis range, but measurements in the short-UV and infrared are also possible. The CD spectra amount to the subtraction of two slightly different spectra, consequently, CD bands are very weak compared to those of the corresponding absorption spectra. However, the intensity and sign of CD bands are extremely sensitive to change in the conformation of the molecules in the close chromophores to which they are allied. Upon aggregation of chiral molecules into fibrous objects, large changes in CD spectra are commonly observed, although the changes are sometimes limited to a simple increase of band intensity.[14,15,16]

The UV-vis and CD spectra of $C_{14}Ac + AMP$ and $C_{12}Ac + GMP$ systems are shown in Figure II.18. The absorptions of both nucleotides were dominated by strong $\pi \rightarrow \pi^*$ transition of nucleobase, and each band was a sum of two or more transitions.[17] The $n \rightarrow \pi^*$ transitions were much weaker than $\pi \rightarrow \pi^*$ transition.

$C_{14}Ac + AMP$

The UV absorption of AMP aqueous solution (15 mM) was observed at 255 nm

(Figure II.18 a, top). When the AMP and C$_{14}$Ac were mixed, this band increased in intensity. After 30 min, the band became broad and slightly blue-shifted.

In the CD measurement, we observed the weak negative band at 255 nm derived from AMP monomers until 15 min. After 30 min, strongly positive CD signal was observed corresponding to the supramolecular aggregate of amphiphiles. This result was well accorded with the apparition of the expression of chirality in the result of OM observation. This CD sign became continuously strong for 2 h (Figure II.18 a, bottom).
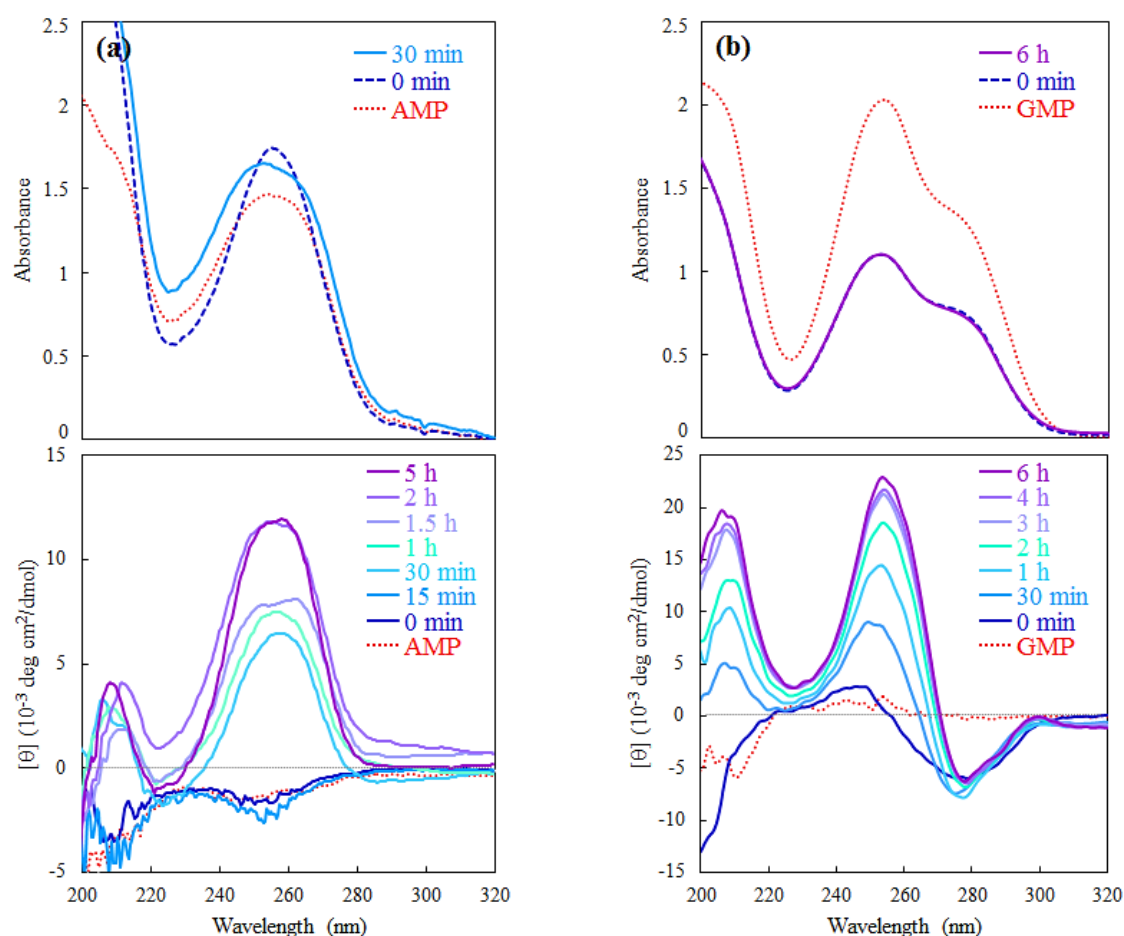
Figure II.18 UV-vis (top) and CD (bottom) spectra of (a) C$_{14}$Ac + AMP, and (b) C$_{12}$Ac + GMP systems.

C$_{12}$Ac + GMP

The absorption of GMP aqueous solution (15 mM) was observed at 279 nm and 253 nm (Figure II.18 a, top). When the GMP and C$_{12}$Ac were mixed, these two bands decreased

(about a half) immediately in intensity and no variation was observed afterwards.

In the CD measurements, owing to chirality transfer occurred very fast, positive-negative Cotton coupling was observed just after mixing. Especially, the CD peak at 253 nm became continuously strong and red-shifted slightly to 257 nm within about 6 h (Figure II.18 b, bottom).

For both cases, the characteristic CD curves of supramolecular aggregates were clearly different from that of monomer. These phenomena were probably assigned to the intermolecular association of nucleobases,[18] corresponding that the amphiphiles were self-assembled supramolecular aggregates and then expressed the supramolecular chirality. The positions of both of nucleoamphiphiles corresponded well to the UV-vis absorption maximums.

II.3.2 ^{1}H-NMR

We followed the kinetics of molecular reorganization using 500 MHz ^{1}H-NMR measurements. We indicated time evolution under the molecular environment by the high-resolution magic angle spinning technique (HR-MAS) to have well-resolved resonances. HR-MAS is performed using a specialized probe which is configured with a Z-gradient aligned along the magic angle. This technique can provide highly resolved structural information on small inhomogeneous samples (5–100 mg).[19] For all measurements, both systems were in H_2O/D_2O (80/20 v/v).

We focused on three chemical shift domains of NMR signals corresponding to two non-exchangeable protons of the adenine base and to the three equivalent protons of the methyl group of acetate ion (black triangle, Figure II.19 and 20), in order to investigate the role of added AMP or GMP and their effects on the acetate complexation.

$C_{14}Ac$ + AMP (15 mM) Data obtained by Carole Aimé[11]

For this system, the evolution of NMR signals of protons of adenosine base are described below; H_8 with white square and H_2 with black circle (Figure II.19).
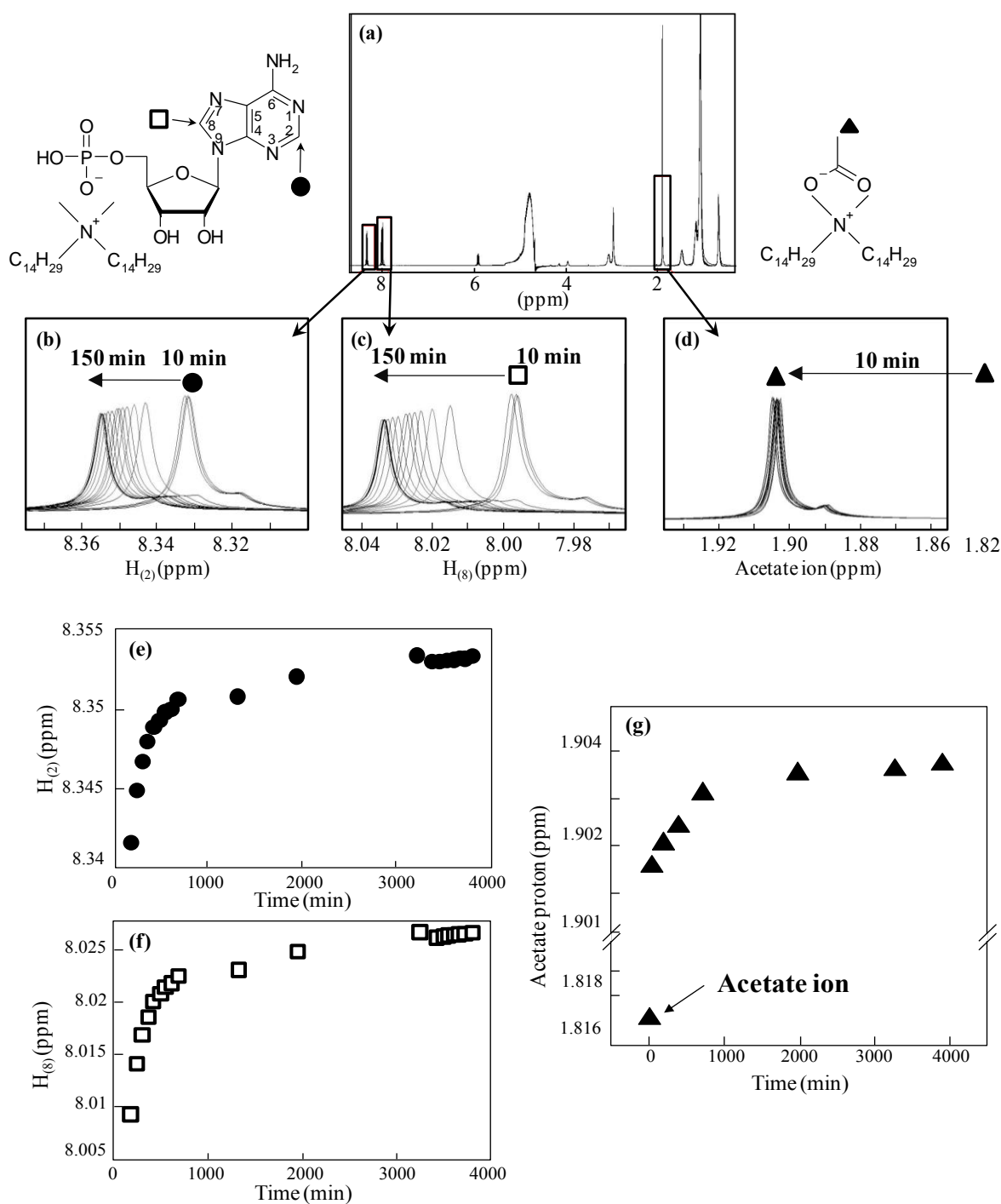
Figure II.19 Kinetics of chemical shifts variation by 500 MHz ^{1}H-NMR in C$_{14}$Ac + AMP system. (a) Spectra of C$_{14}$Ac + AMP. Parts of the NMR spectra of protons (b) H$_2$ and (c) H$_8$ of the adenosine base and (d) the methyl group of acetate ion. Kinetics of chemical shifts variation for (e) H$_2$ and (f) H$_8$ of the adenosine base and (g) methyl group of acetate ion.

Right after mixing, the NMR signal at 1.816 ppm from the acetate ion disappeared. This peak was replaced by the peak characteristic of acetic acid at 1.902 ppm (Figure II.19 d, g). This indicates that ion exchange had occurred rapidly after mixing AMP and $C_{14}Ac$. AMP had replaced the acetate counter-anion at the cationic membrane, leading to the formation of acetic acid. At this stage (about 10 minutes after mixing), OM studies show that no helix is formed.

We have then followed the chemical shifts evolution of the two peaks corresponding to the protons of adenosine nucleobase. Whereas the acetate ion peak quickly reached the final value after about 40 min (half-life is about 3 min) (Figure II.19 d, g) indicating that total ion exchange is very fast, the protons of the nucleobase showed much slower downfield chemical shift evolution (0.02 ppm for H_2 and 0.035 ppm for H_8) during a few thousand minutes with a half-life of 150-200 min (Figure II.19 b, c, e, f). This shows that the reorganization of nucleobases still evolves after a few hours. The chemical shift reached a plateau after 3 days. This corresponds to the kinetics of helix formation as observed by OM.

$C_{12}Ac$ + GMP (7.5 mM)

In the case of $C_{12}Ac$ + GMP, the measurements were done for a final concentration of 7.5 mM for each reagent because the kinetics was too fast at a 15 mM concentration to investigate the chemical shift.

In this system, ion exchange occurred faster than AMP system, the peak of acetate ion reached final value in less than 10 min (half-life ~2 min). This acetate ion's signal at 1.633 ppm was replaced by the peak characteristic of acetic acid at 1.796 ppm (Figure II.20 d, g).

The protons of the guanosine base also showed downfield chemical shift variation from GMP acid solution upon complexation with the surfactant, 0.04 ppm shifted for H_{N2} (black circle) and 0.08 ppm shifted for H_8 (white square) (Figure II.20 b, c). In spite of shorter alkyl chain and the lower concentration, the transition was much faster than $C_{14}Ac$ + AMP and this molecular reorganization was completed within about 20 min after mixing $C_{12}Ac$ and GMP (half-life ~5 min) (Figure II.20 e, f).
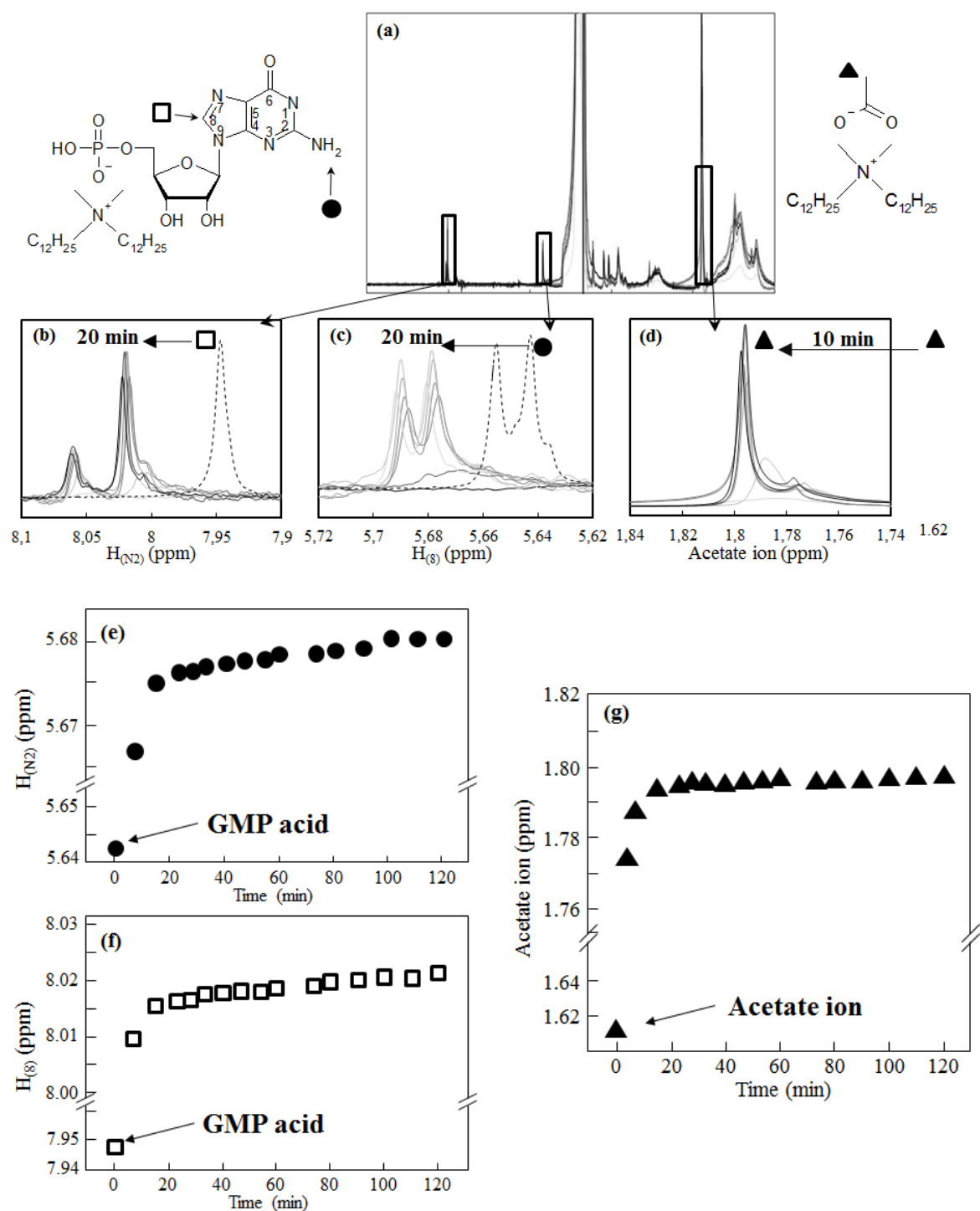
Figure II.20 Kinetics of chemical shifts variation by 500 MHz ^{1}H-NMR in C$_{12}$Ac + GMP system. (a) Spectra of C$_{12}$Ac + GMP. Parts of the NMR spectra of protons (b) H$_{N2}$ and (c) H$_8$ of the adenosine base and (d) the methyl group of acetate ion. Kinetics of chemical shifts variation for (e) H$_{N2}$ and (f) H$_8$ of the adenosine base and (g) methyl group of acetate ion.

II.3.3 pH measurement

Prior to investigating the IR measurements, we studied pH changes of both systems because the molecular structure of protonated/deprotonated nucleotide is strongly dependent on the pH (see Figure II.5).

The pH values of each reagent in aqueous solution (15 mM) are shown in Table II.3. When $C_{14}Ac$ and AMP were mixed, the pH value became 4.15, and it increased to around 5 for 2 h. After several hours, the pH started decreasing to around 3.9 (Figure II.21 a).

In the case of $C_{12}Ac$ + GMP, on the other hand, pH was 3.7 when they were mixed, then it increased to around 3.95 after 2 h stayed at this value (Figure II.21 b).

Table II.3 The pH value of monocationic surfactant and nucleotide in aqueous solution (15 mM).

Reagent (15 mM)	pH
$C_{14}Ac$	7.1
AMP	2.55
$C_{12}Ac$	5.86
GMP	2.5
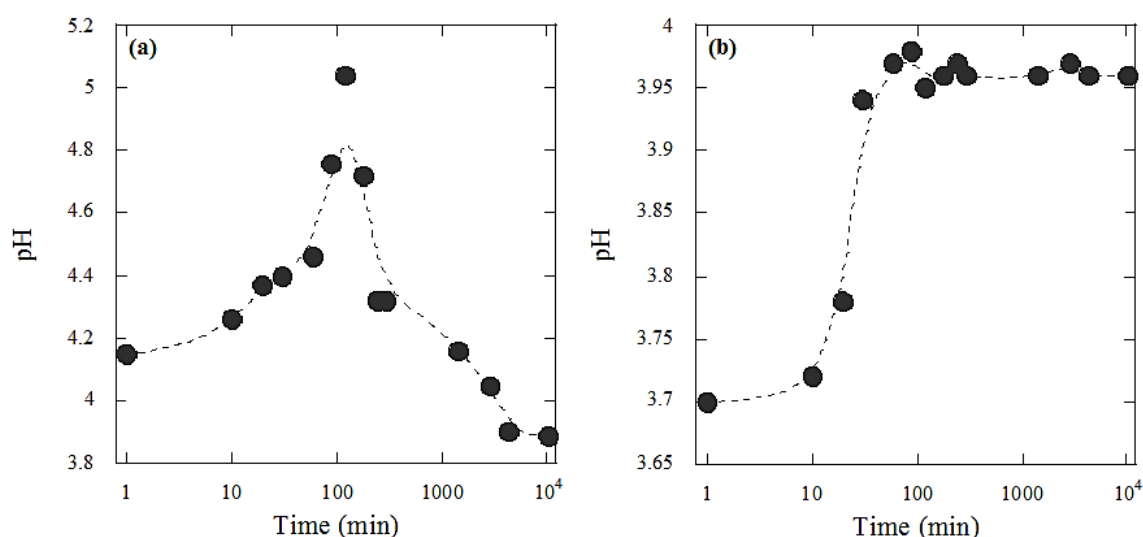
Figure II.21 The pH measurement of (a) $C_{14}Ac$ + AMP and (b) $C_{12}Ac$ + GMP systems in aqueous solution (15mM).

II.3.4 Protonation site of nucleotide followed by IR measurement

We then investigated the molecular formation of protonated/deprotonated nucleotide with different pH by IR study (Figure II.22).
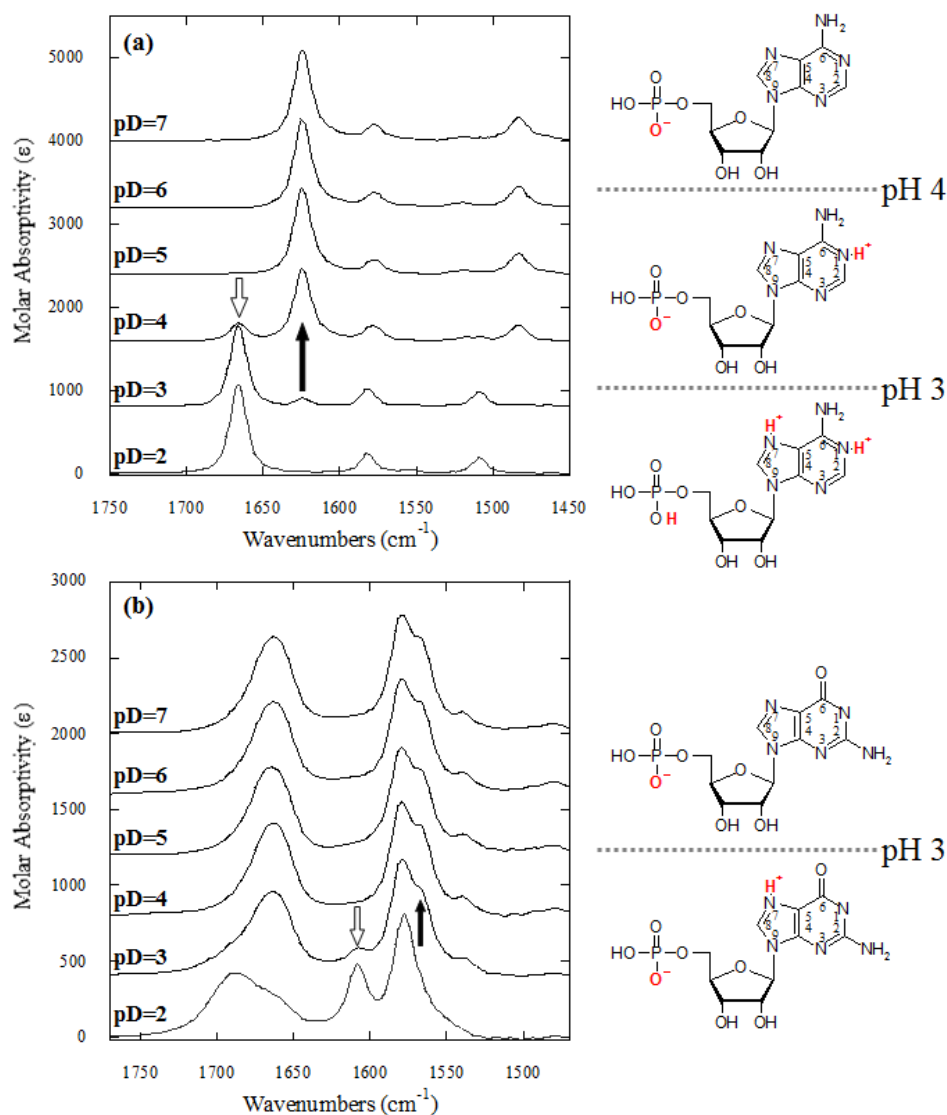
Figure II.22 IR spectra and protonation sites of (a) AMP and (b) GMP with different pH.

The IR bands of AMP and GMP can be measured in the 1750-1450 cm^{-1} region.

For the case of AMP solution, these spectral regions were characteristic of aromatic nucleobase at 1623 and 1666 cm^{-1} (Figure II.22 a). When the pH was 2 ~ 3, we observed a strong band at 1666 cm^{-1}, but this band disappeared by increasing the pH. On the other hand, the

band at 1623 cm^{-1} appeared when pH was 3 and this absorbance became strong from a pH 4 solution. This phenomenon suggested that the band at 1666 cm^{-1} was attributed to the protonated N$_{(1)}$-H and N$_{(7)}$-H bending vibrations, and 1623 cm^{-1} was corresponding to C=N (C$_{(2)}$=N$_{(3)}$, C$_{(6)}$=N$_{(1)}$, and C$_{(8)}$=N$_{(7)}$) stretching vibrations with contributions from N-D bending vibrations.[20]

In the case of GMP, the bands around 1690-1560 were characteristic of the guanosine nucleobase (Figure II.22 b). The band at 1690 cm^{-1} associated with C=O stretching vibration was shifted to 1667 cm^{-1}, whereas the band at 1608 cm^{-1} disappeared and new band at 1568 cm^{-1} appeared when the pH changed from 2 to 3. The band at 1568 cm^{-1} was probably attributed to the protonated N$_{(7)}$-H bending vibrations, and 1580 and 1568 cm^{-1} were associated with C=C and C=N stretching vibrations with contributions from N-D bending vibrations.

The pH of the bulk solution can be directly correlated to the pH at the interface of nucleoamphiphiles. These results indicate that upon addition of nucleotide to C$_n$Ac, AMP was deprotonated at first, but after a day, it was protonated in position *1*. In another system, GMP was deprotonated.

II.3.5 Kinetics of molecular reorganization followed by IR measurement

C$_{14}$Ac + AMP (15 mM)

The frequencies of the antisymmetric (ν_aCH$_2$) and symmetric (ν_sCH$_2$) stretching vibration (at 2924 cm^{-1} and 2854 cm^{-1}, respectively) of the hydrophobic chains indicated that the nucleoamphiphiles were in fluid phase with a high rate of gauche conformations (Figure II.23 a).

No variation in hydrophobic chain organization was observed even 7 days after mixing AMP and C$_{14}$Ac. This indicated that the reorganization of hydrophobic part did not occur during the vesicle-helix morphological transition. This result is particularly interesting that such structural transitions are generally accompanied by an increasing of *trans*

conformations reflecting the alkyl chains organizations.[21,22,23]
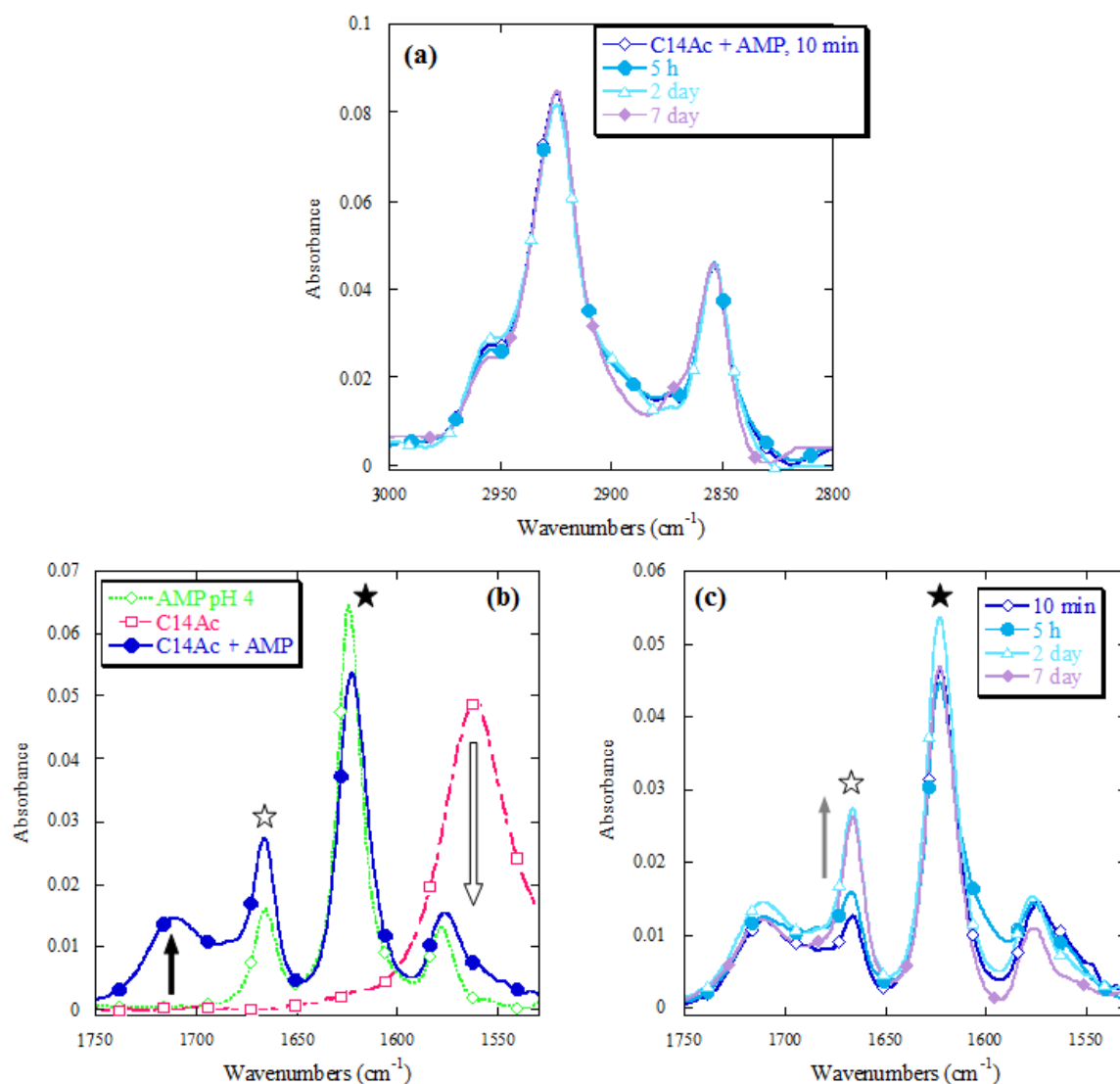
Figure II.23 (a) Kinetics study of alkyl chain reorganization by IR spectroscopy in $C_{14}Ac$ + AMP system (15 mM). (Carole Aimé's data) (b) Comparison of IR spectra obtained with AMP at pH 4 (15 mM), $C_{14}Ac$ (15 mM), and $C_{14}Ac$ + AMP (15 mM) samples. (c) Kinetics study of AMP organization by IR spectroscopy in $C_{14}Ac$ + AMP system (15 mM). (Carole Aimé's data)

Indeed, this was what happened to the hydrophobic chains of gemini-tartrate or gemini-oligo-alanine forming chiral conformation. The fact that the molecules are less organized than the other cases is possibly the origin of much larger-scale assemblies observed with these molecules compared to the two systems mentioned above (a few micrometers compared to tens to hundred nanometers). However, important variations are observed concerning the IR bands characteristic of the complexed counter-anions.

Figure II.23 b shows the FT-IR signals of AMP at pH4, $C_{14}Ac$, and $C_{14}Ac$ + AMP system. The white and black arrows (at 1570 and 1711 cm^{-1}) represent the characteristic bands of acetate ion and acetic acid, respectively.

The band at 1711 cm^{-1} (acetic acid) was not observed with $C_{14}Ac$ without any addition of AMP. This confirmed that its presence in $C_{14}Ac$ + AMP resulted from the exchange of the acetate counter-anion by AMP and consecutive acetic acid formation. In addition, the band at 1570 cm^{-1} corresponding to acetate counter-anion disappeared upon addition of AMP to $C_{14}Ac$.

This rapid kinetics of counter-anion exchange as observed in Figure II.23 c supports the NMR data discussed above: ion exchange occurred less than 10 min after mixing AMP and $C_{14}Ac$. AMP was complexed with the surfactant, and acetic acid was formed.

The black and white stars (at 1623 and 1666 cm^{-1}, Figure II.23 b,c) were characterized by aromatic nucleobase as mentioned above (in Figure II.23 a). The origin of the band at 1623 cm^{-1} can be associated with C=N ($C_{(2)}$=$N_{(3)}$, $C_{(6)}$=$N_{(1)}$, $C_{(8)}$=$N_{(7)}$) stretching vibrations with contributions from N-D bending vibrations. The intensity of this band decreased with time along with the increase of the intensity of the band at 1666 cm^{-1}. This band at 1666 cm^{-1} may be attributed to the formation of hydrogen bonds between neighboring bases.[a] Indeed, this band has previously been reported as a marker of double helix formation of polyAMP through hydrogen bonds.[24] The increase in intensity stabilized after 2 days, exhibiting again, kinetics similar to helix formation observed by OM.

In summary, ion exchange occurred a few minutes after mixing AMP and $C_{14}Ac$, allowing confinement of the nucleotides at the cationic membrane surface. However, the reorganization of the nucleotides, as a result of hydrogen bonding between neighbouring nucleobases at the membrane surface, took much longer as revealed by the behavior of the band at 1666 cm^{-1}, and on the macroscopic scale, helices were formed after only 2 days.

---

[a] This increase could be associated with the protonation of the nucleobase. However, in our case, the sample exhibits a pH of about 4. At this pH, the nucleotide bears a single anionic charge.

C$_{12}$Ac + GMP (10 mM)

Figure II.24 shows the infrared spectra of C12Ac, GMP, and C12Ac+GMP at 10mM. Again, we choose a concentration lower than 15 mM because the reaction at this concentration was too fast in the presence of GMP.
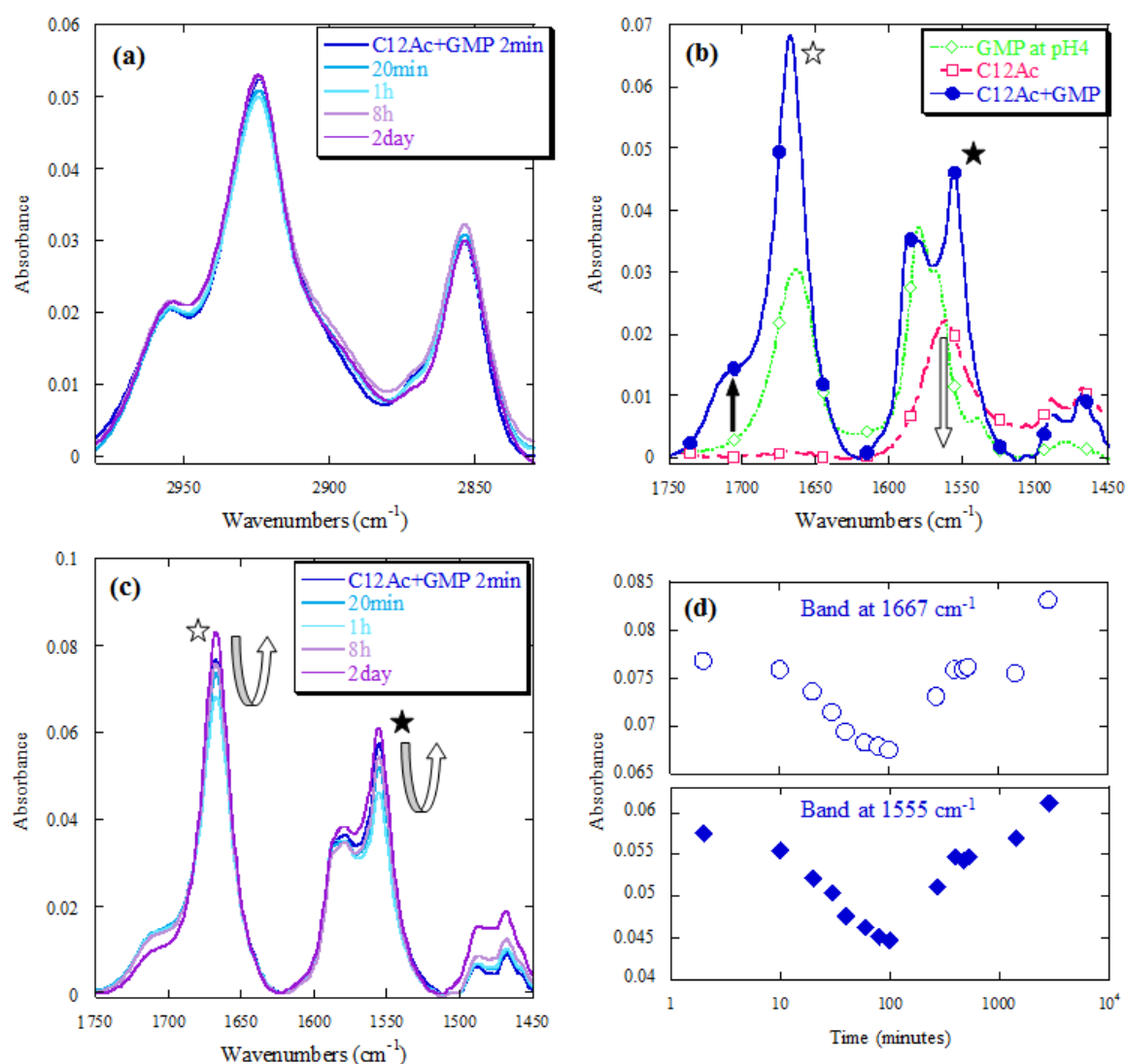
Figure II.24 (a) Kinetics study of alkyl chain reorganization by IR spectroscopy in C$_{12}$Ac + GMP system (10 mM). (b) Comparison of IR spectra obtained with GMP at pH 4 (10 mM), C$_{12}$Ac (10 mM), and C$_{12}$Ac + GMP (10 mM) samples. (c) Kinetics study of AMP organization by IR spectroscopy in C$_{12}$Ac + GMP system (10 mM), and (d) intensity evolution of the band at 1667 cm^{-1} (top) and 1555 cm^{-1} (bottom).

The frequencies for $\nu_a CH_2$ and $\nu_s CH_2$ stretching vibrations of the methylene groups in

the case of $C_{12}Ac$ + GMP also indicated no variation in absorbance accompanied with the organization of hydrophobic alkyl chain even after 2 days (Figure II.24 a).

The white and black arrows (at 1570 and 1711 cm-1), which represent the characteristic bands of the acetate ion and acetic acid, respectively, again confirm the rapid exchange of counterions.

The band at 1667, 1580, and 1568 cm^{-1} were characteristic of guanine nucleobase (Figure II.24 b, black triangle, dashed line). The band at 1670 cm^{-1} is associated with C=C and C=N ($C_{(2)}$=$N_{(3)}$, $C_{(6)}$=$N_{(1)}$, $C_{(8)}$ =$N_{(7)}$) stretching vibrations with contributions from N-D bending vibrations. When $C_{12}Ac$ and GMP were mixed, the bands at 1580 cm^{-1} and 1568 cm^{-1} disappeared rapidly and new bands at 1587 cm^{-1} and 1556 cm^{-1} were observed. These important shifts may be associated to the ordering of G residues in the supramolecular structures as previously reported.[25] Meanwhile in this case, the nature of the interaction (hydrogen bonds or $\pi-\pi$ stacking) between the G residues is not straightforward to understand. In addition, this transition was again too fast for kinetics investigation, confirming the NMR measurements.

After this transition, the intensities of these bands showed very little variation with time. Their intensity all decreased rapidly initially but after 2 hours it started to increase again (Figure II.24 c), reaching a stationary value after 2 days. This initially rapid (10 minutes) transition followed by much slower (2 days) and slight modifications also confirms the NMR observations as well as the helix formation kinetics observed with OM.

II.4 Summary

In the systems investigated above, helix formation is simply induced by the addition of nucleotides AMP or GMP. This process involves different transition steps at the macroscopic level (fluid solution to gel or precipitate), the mesoscopic level (vesicle to helix transition), supramolecular level (chirality transfer), and the molecular level as summarized in Table II.4.

Table II.4 Summary of the kinetics of C*n*Ac + nucleotides at different levels in the bulk (macroscopic), in aggregate (mesoscopic), at the supramolecular level, and at the molecular level.

	Macroscopic aspect		Mesoscopic aspect (OM)	
	right after the nucleotides addition	gel formation/ precipitate	helix: formation beginning	helix: end of the growth
$C_{12}Ac + GMP$	viscosity increase	1 day (gel)	30 min	1 week
$C_{14}Ac + AMP$	no immediate change	1 h (precipitate)	30 min (needles) 1 h (helices)	1 day

	Supramolecular kinetics (CD)		Molecular kinetics (IR, MNR)	
	chirality expression	end of the chirality amplification	acetate to nucleotide ion exchange	nucleotide organization
$C_{12}Ac + GMP$	< 1 min	~ 3 h	~ 2 min (half-life)	~ 10 min
$C_{14}Ac + AMP$	30 min	~ 2 h	~ 4 min (half-life)	~ 2.5 h

The kinetics of molecular organization and chirality transfer at supramolecular aspect are quite different and much faster for the $C_{12}Ac$ + GMP system than for the $C_{14}Ac$ + AMP system. Starting from similar (or even identical) amphiphiles, this underlines the importance and specificity of the counterion nature in ionic assemblies' properties. Particularly, while adenine and guanine have similar stacking propensities, guanine nucleobase exhibits edges having self-complementary hydrogen-bond donors and acceptors, responsible for the higher degree of intermolecular interactions between GMP than between AMP.[26] These factors may account for the very fast kinetics observed with GMP-amphiphiles in spite of their shorter hydrophobic chains. Despite these differences, in both systems helix formation occurs through similar molecular organization mechanism as evidenced by CD, NMR and IR. First, ion exchange occurs in a few minutes, leading to confinement of nucleotides, followed by their reorganization through cooperative inter-nucleotides interactions at the membrane surface. Sequentially, the chirality in supramolecular aggregates is expressed to form the chiral structure.

The helix formation and growth as observed by OM followed much slower kinetics after ion exchange, indicating that it is a cooperative process due to molecular reorganization.

II.5 Study of stoichiometry effect on the morphology of the aggregates

We considered the molecular kinetics with different ratio such as C_nAc : nucleotide for 1 : 1 and 1 : 4 followed by OM observation and IR spectroscopy .

II.5.1 Mesoscopic kinetics followed by OM observation

We have then varied the AMP or GMP to C_nAc ratio from 0.25 to 1.5. The concentration of added AMP or GMP was varied with a constant amphiphile (C_{14} or C_{12}) final concentration of 15 mM. Figure II.25 and 26 show the macroscopic aspect of the samples as well as their OM images.

$C_{14}Ac + AMP$ (15 mM) by Carole Aimé[11]

Depending on the AMP to $C_{14}Ac$ ratio, the macroscopic aspect of samples varied from solution to precipitate (Figure II.25 a). Macroscopically, we obtained more opaque solutions with higher ratios. The morphologies of vesicles, helices, and needles were strongly depended on the AMP/$C_{14}Ac$ ratio, and could roughly be separated into three phases.

For AMP/$C_{14}Ac$ ratios lower than 0.50, $C_{14}Ac$ + AMP solutions remained almost clear and only vesicles were observed (Figure II.25 b). Due to the large presence of acetate counterions, the formation of inter-base interaction between neighbouring nucleotides was prevented. In the 0.75-1.25 range, precipitation and opacity increased with the ratio. Within this range, micrometric helices were observed along with needles (Figure II.25 c) and proportion of needles relative to helices increased with the ratio. Finally, with excess amounts of AMP such as higher ratio than 1.50, only needles were observed by OM (Figure II.25 d).
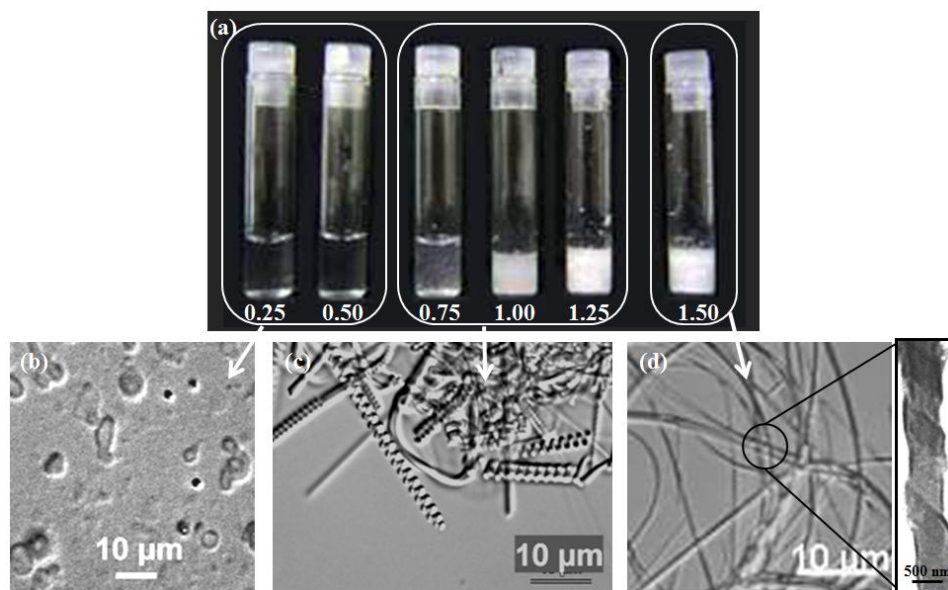
Figure II.25 (a) Photographs of showing the macroscopic aspect of $C_{14}Ac$ (15 mM) + AMP samples with different AMP/$C_{14}Ac$ ratios, from 0.25 to 1.50. OM images of the samples: (b) ratios from 0.25 to 0.50, (c) ratios from 0.75 to 1.25, and (d) ratios above 1.50 with inserting the TEM image of nanometric scale chiral structure.

TEM images showed nanometric chiral cigar-like structure at the nanometric scale. These microneedles could be viewed as nanohelices. Depending on the stoichiometry, the formation of either microhelices or nanohelices was favoured. Precipitation occurred more rapidly in samples with increasing the AMP/$C_{14}Ac$ ratios. The presence of excess AMP resulting in a higher density of needles could account for the faster precipitation.

$C_{12}Ac$ + GMP (15 mM)

For a GMP/$C_{12}Ac$ ratio up to 0.25, $C_{12}Ac$ + GMP remained a clear solution: in contrast to the AMP system, no vesicles were observed at such low ratio and thin films and fibers were observed (Figure II.26 a, b). For a ratio between 0.5 and 0.75, the solutions were still fluid, but micrometric helices appeared along with fibers (Figure II.26 c). For the ratios between 1.00 and 1.50, the solutions became gels and did not flow when the bottles were inverted. Within this range, micrometric helices grew in diameter (Figure II.26 d), and helix density increased with the ratio. Moreover, the formation of helices was much more rapid for a higher ratio of GMP to surfactant (about 3 min for a ratio of 1.5 whereas about 30 min was

required for a ratio of 1).
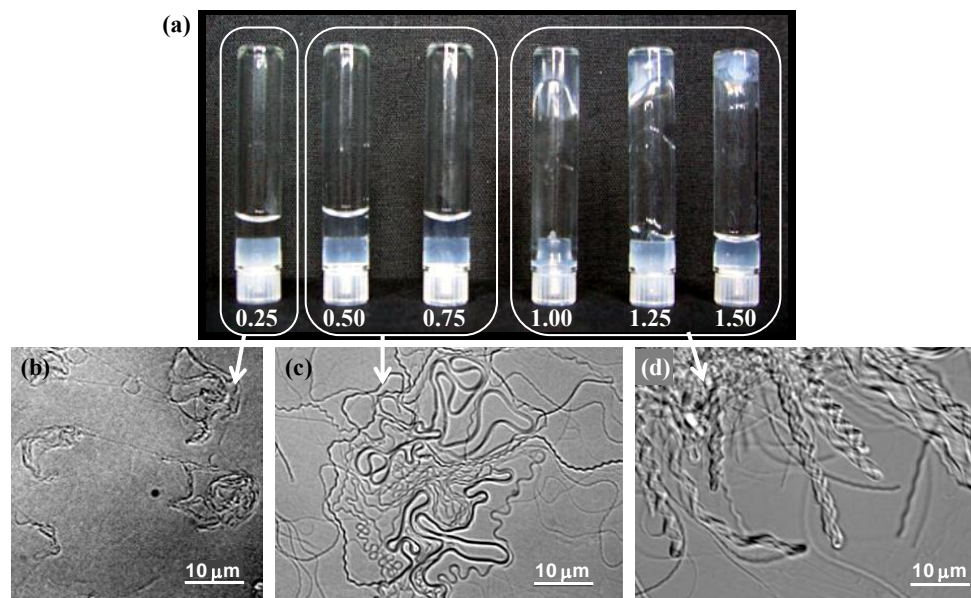
Figure II.26 (a) Photographs of showing the macroscopic aspect of $C_{12}Ac$ (15 mM) + GMP samples with different GMP/$C_{12}Ac$ ratios, from 0.25 to 1.50. OM images of the samples: (b) ratios less 0.25, (c) ratios from 0.50 to 0.75, and (d) ratios above 1.00.

II.5.2 Self-assembly kinetics followed by IR measurement

We then compared the molecular kinetics between vesicles solution (Nuc : C_nAc = 0.25) and helix suspensions (Nuc : C_nAc = 1) We observed complete dispersion of the bands at 1666 cm^{-1} (for $C_{14}Ac$ + AMP, white star in Figure II.27 a), at 1580 and 1568 cm^{-1} (for $C_{12}Ac$ + GMP, black star in Figure II.27 b). This suggested that AMP/GMP molecules were confined approximately to the membranes surface when the concentration ratio C_nAc : nucleotides was 1 : 1 (Figure II.28 a).
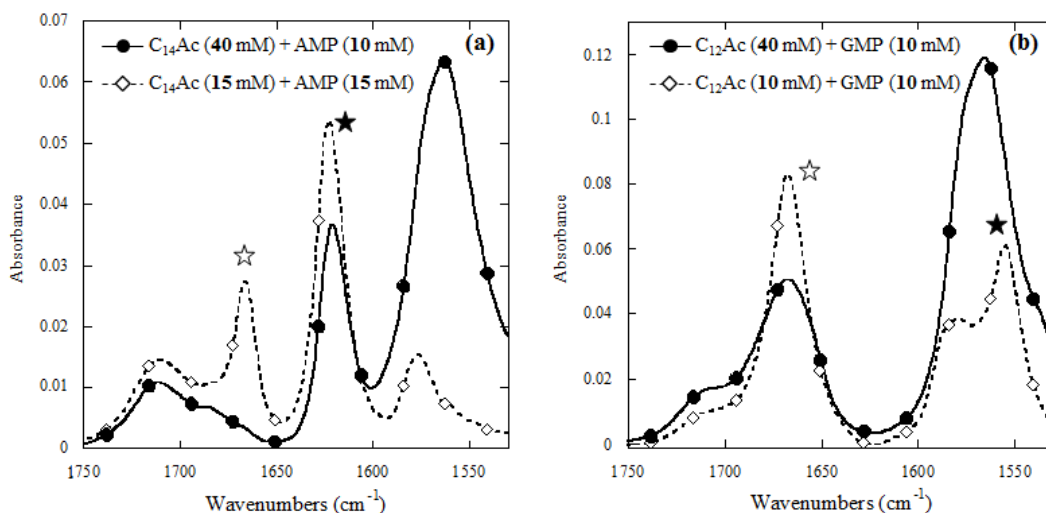
Figure II.27 Comparison of IR spectra obtained by the different concentrations of samples with (a) $C_{14}Ac$ (15 mM) + AMP (15 mM) vs $C_{14}Ac$ (40 mM) + AMP (10 mM) (Carole Aimé's data) , (b) $C_{12}Ac$ (10 mM) + GMP (10 mM) vs $C_{12}Ac$ (40 mM) + GMP (10 mM) in the range of bands characteristic of the counterions.

In contrast, the interactions of inter-bases were absented if the huge excess of acetate amphiphiles existed in mixture solution (Figure II.28 b). Accordingly, this is the evidence that the bands at 1666 cm^{-1} (for $C_{14}Ac$ + AMP) and at 580 and 1568 cm^{-1} (for $C_{12}Ac$ + GMP) can be considered to be a marker for supramolecular helical structure formation through intermolecular interactions such as hydrogen bonds or $\pi-\pi$ stacking derived from the closely packed nucleotide in aggregates. In fact, no helical structures were observed on OM in both cases with the ratio C_nAc : nucleotide for 4 : 1 as hereinafter study.
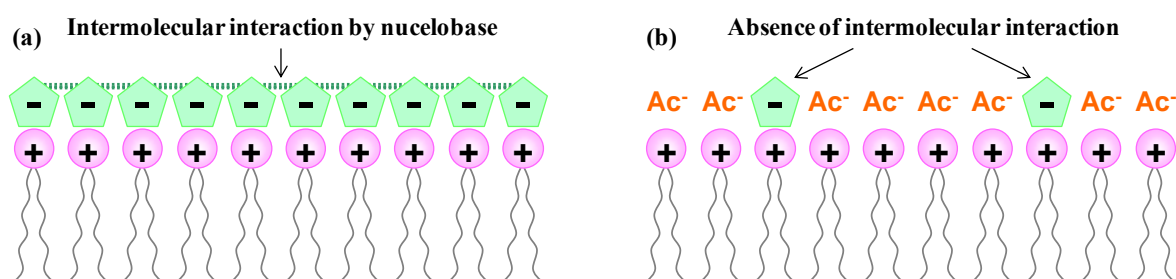
Figure II.28 Schematic illustrations of intermolecular interaction of nuclebases observed by IR spectra. (a) The nucleotides exist in proximate each other (ratio of concentration for each reagent is 1 : 1). (b) Interactions are absented by existe the excess acetate amphiphiles (C_nAc + nucleotide, 4 : 1).

II.6 Conclusion

The weak interactions between nucleic acids AMP or GMP confined at the membranes surface of self-assembled amphiphiles could induce chiral supramolecular structures. This cooperative interaction between nucleotides counter-anions and cationic amphiphiles was much stronger than the ionic interaction between acetate ions and the amphiphiles. This allowed us to directly follow the formation of micrometric chiral structures when nucleotides solution was added to the vesicles solution of cationic non chiral amphiphiles C_nAc. We have observed *in situ* that vesicles were ruptured at first, to form large aggregates (AMP) or continuous films (GMP), and then chiral fibers grew up to form micrometric helices. Detailed microscopy observation showed the growth of these helices with coiling motion from tip of a helix.

Spectroscopic measurements indicated that micrometric helical structures of nucleoamphiphiles resulted from cooperative effects in the molecular organization of nucleobases. Ion exchange is the important step, which can induce the confinement of nucleotides at cationic membrane surfaces. This process occurred within minutes after mixing the two molecules C_nAc and nucleotides. Subsequently the nucleotides confined at membrane surfaces and reorganized themselves through weak interactions such as H bonds and $\pi-\pi$ stacking on nucleobases. The chirality transfer to supramolecular structures also occurred at the same time of nucleotide reorganization. This reorganization and the formation of directional intermolecular interaction is the driving force for helix formation.

C_nAc to nucleotides ratio was also an important factor which determines the helix dimensions, *i.e.* micro to nanometric helices.

The main difference between AMP and GMP systems is allowing the solution properties as precipitate vs gel. Once confined at the cationic membrane surfaces, GMP organizes much more rapidly (~minutes) than AMP (~100 minutes). This could be attributed to

the nature of intermolecular interactions between GMP and between AMP. The formation of supramolecular chiral structures clearly requires fine matching between surfactant structures and their counterions. The control of the nature and kinetics of the interactions between counterions gives access to the morphological tuning of the self-assembly of these new helical bioarchitectures.

II.7 Experimental session

Synthesis of C_nAc

Dialkyldimethylammonium acetate was obtained by ion exchange form complex of amphiphile and boromide counter anion. The cationic surfactant with bromide counter-anion as starting material was obtained by Fuluka and used any further purification.

Dialkyldimethylammonium bromide (n = 12, 14) was mixed with silver acetate (1.5 equivalents) in methanol. The mixture was stirred for 30 min at 50 °C until the formation of black precipitate of silver bromide, whereas the acetate surfactant was soluble in methanol. Silver bromide was filtered on Celite to obtain a colorless solution. After evaporation of methanol, the product was dissolved in a mixture of chloroform/methanol (9/1, v/v), made precipitate with acetone, filtered, and dried under the vacuum.

Preparation of the Samples

Guanosine 5'-monophosphate and adenosine 5'-monophosphate were purchased from Fluka and Acros Organics, respectively, and used without any further purification. A vesicle solution of C_nAc (n = 12, 14) was added to a solution GMP and AMP with the final concentration of each reagent being 15 mM. The samples were not heated but as mixed. Deionized water was used to perform analysis by OM and TEM, and D_2O (Eurisotop CEA Saclay, France) was used for NMR and IR studies. OM was used to ensure that no morphological various occurred by exchanging H_2O for D_2O.

The following notation was used for ^1H NMR splitting patterns: singlet (s), doublet (d), triplet (t), multiplet (m), and double of doublets (dd).

Typical example of C_12GMP ^1H NMR (400 MHz, CD$_3$OD, 25 °C, δ ppm): 8.08 (1H, s), 5.85 (1H, dd, ^3J = 5.14 Hz, ^3J = 6.36 Hz), 4.38 (1H, dd, ^3J = 2.45 Hz, ^3J = 5.14 Hz), 4.18 (1H, m), 4.14 (1H, m), 4.07 (1H, m), 3.28 (4H, m), 3.05 (6H, s), 1.74 (4H, m), 1.38 (4H, m), 1.29 (32H, m), 0.90 (6H, t, ^3J = 6.85 Hz). ^{13}C **NMR (100 MHz, CD$_3$OD, 25 °C, δ ppm)**: 138.45, 89.25, 75.05, 72.36, 65.85, 65.22, 51.20, 49.64, 49.42, 49.21, 48.99, 48.79, 48.57, 48.36, 48.27, 48.11, 48.06, 47.9, 47.82, 47.88, 33.08, 30.75, 30.63, 30.52, 30.48, 30.20, 27.37, 23.74, 23.49, 14.43.

Typical example of C_14AMP ^1H NMR (400 MHz, CD$_3$OD, 25 °C, δ ppm): 8.56 (1H, s), 8.21 (1H, s), 6.09 (1H, dd, ^3J = 6.11), 4.67 (1H, m), 4.234(1H, m), 4.12 (2H, m), 3.28 (4H, m), 3.05 (6H, s), 1.73 (4H, m), 1.38 (4H, m), 1.29 (40H, m), 0.89 (6H, t, ^3J = 13.36 Hz). ^{13}C **NMR (100 MHz, CD$_3$OD, 25 °C, δ ppm)**: 152.76, 141.46, 141.43, 123.10, 123.08, 121.08, 107.86, 88.89, 86.14, 86.10, 76.35, 72.44, 65.96, 65.91, 65.86, 65.20, 51.21, 49.64, 49.42, 49.32, 49.21, 48.99, 48.79, 48.57, 48.36, 48.15, 48.08, 48.00, 47.95, 47.90,

47.84, 47.80, 47.76, 47.70, 47.64, 47.59, 33.09, 30.77, 30.63, 30.49, 30.18, 27.35, 25.62, 23.74, 23.48, 14.44.

Optical microscopy with differential interferential contrast (DIC)

Samples sealed between a slide glass and cover glass were observed with a Nikon Eclipse PhysioStation E600FN with adequate condensers and a prism for DIC observations.

Circular dichroism measurement

The circular dichroism measurement was performed on a JASCO J-815 CD spectrometer with data pitch of 0.1 nm, scanning speed of 100 nm/min, and quartz cuvette with optical path length of 0.1 mm were used. The spectra were measured for 15 mM of each reagent.

Kinetic NMR measurement on aggrefates

^{1}H NMR experiments were performed on a Bruker Avance 500 spectrometer operating at 500.13 MHz and equipped with solid-state NMR facilities. Samples were enclosed in 4 mm diameter Zirconia rotors (50 μl internal volume). Magic-angle sample spinning (MAS) was performed at 8 kHz. A H_2O/D_2O (80/20 v/v) mixture was used for sample preparation. A D_2O lock was used, and the temperature was regulated to 290 K (heating due to air friction when spinning is taken into account). Acquisition was performed using a classical one-pulse sequence with water suppression (presaturation of 50 dB) on a spectral width of 5 kHz. Typically, 32 scans were recorded with a repetition time of 3 s. This leaded to an acquisition time per experiment of 96 s. Spectra were obtained by the application of a Lorentzian filtering of 1 Hz and Fourier transformation of time-dependent signals.

Infrared measurement

IR spectra were performed on a ThermoNicolet Nexus 670 FTIR spectrometer. The samples were prepared in a D_2O, and held in a demountable cell with CaF_2 windows with a 50 mm Teflon spacer. Generally, the spectra were registered during 50 scans at resolution of 4 cm^{-1}. Baseline corrections for absorption spectra were made by subtracting the absorption of D_2O solvent. The pH of nucleotide solution was controlled by addition of DCl and NaOD.

II.8 Annex

II.8.1 Study of morphology transition by inducing the nucleotide to vesicle solution

We have also investigated systems for which that the nucleotides were added to the vesicles formed with dimethylditetradecylammonium chloride $C_{14}Cl$.

15 mM of $C_{14}Cl$ aqueous solution were heated up about 40 ˚C for melting the precipitates, and then kept at room temperature (Figure II.29 a). After cooling, the amphiphiles self-assemble to form vesicle structure and the solution became slightly opaque and fluid. These vesicles showed much higher stability than the system of $C_{14}Ac$ because chloride counter-anion shows much more hydrophobic properties than acetate ion.[27]

When the AMP solution was mixed with vesicle solution of $C_{14}Cl$, some of vesicles transformed to denser structures, but chiral fibrous structures were never observed (Figure II.29 b). On the other hand, the mixing of $C_{14}Cl$ and GMP presented the vesicle to helical fiber transition under the OM observation (Figure II.29 c).
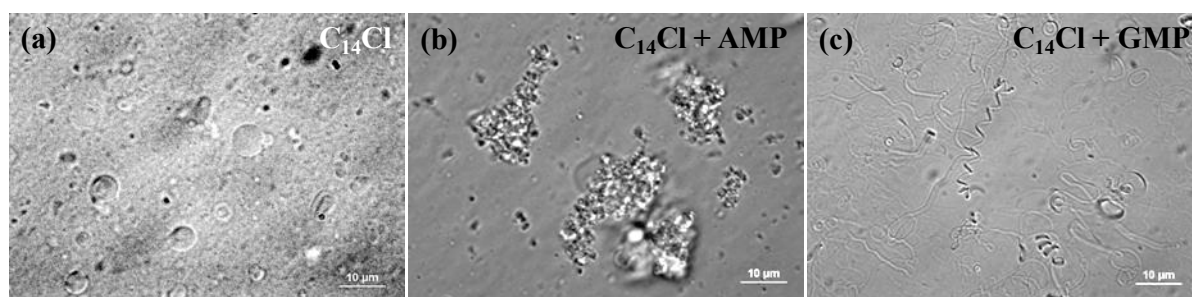
Figure II.29 OM images of (a) vesicles of 15 mM $C_{14}Cl$, (b) denser structures of $C_{14}Cl$ + AMP (15 mM), and (c) helical ribbons of $C_{14}Cl$ + GMP (15 mM). Bars are 10 μm.

Such differences of morphology transition between GMP and AMP systems are probably referable to their solubility and pK_a;, and the pK_{a1} value of AMP is higher than that of GMP whilst AMP is more soluble in water than GMP. Thus, GMP could interact more easily

with cationic vesicle membrane than AMP system.

Now we will look more closely on the kinetics of from the transformation upon addition of GNP to the solution of $C_{14}Cl$. Right after mixing $C_{14}Cl$ and GMP, small amounts of vesicles ruptured to form the denser structures (Figure II.30 a). Form these cores, micrometric chiral fibers started growing after 10 min (Figure II.30 b). After 1 h, we observed helical structures, and these fibers continuously grew for a week (Figure II.30 c-f). For the macroscopic aspect, white precipitates were observed after few hours.
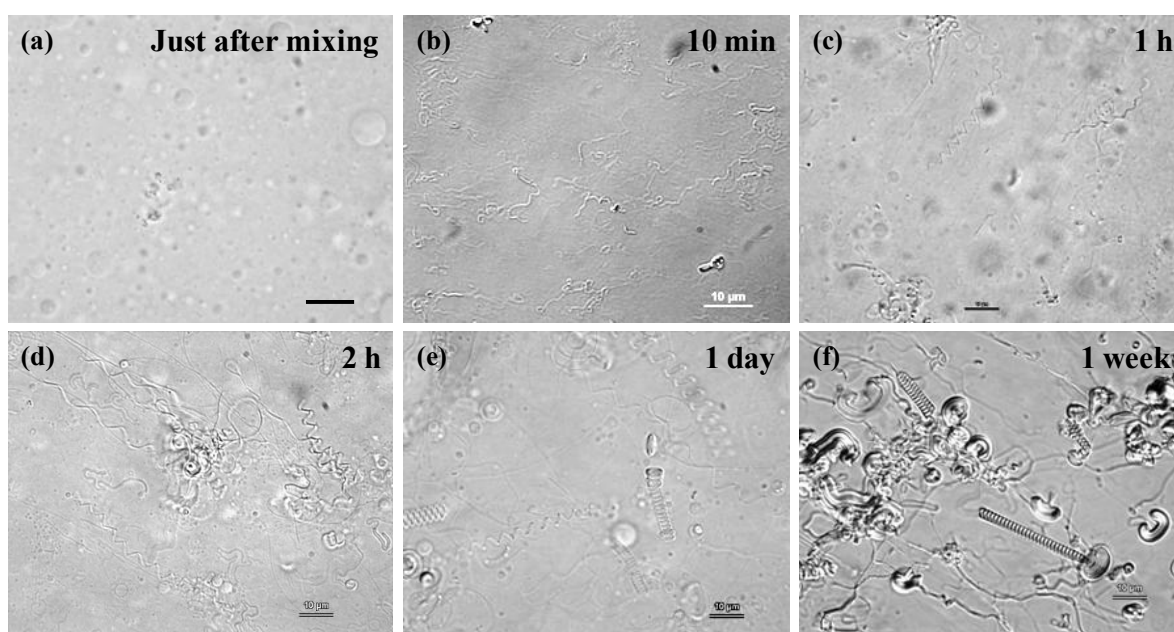
Figure II.30 OM images of helix formation observed with $C_{14}Cl$ + GMP system. The scale bars are 10 μm.

Compared to the $C_{12}Ac$ + GMP system discussed above, the morphology transition of $C_{14}Cl$ + GMP sample occurred much more slowly and furthermore the vesicles of $C_{14}Cl$ remained until a day, indicating that the ion-exchange form chloride to GMP also occurred much more slowly than the system of acetate counter-anion. In fact, the pK_a value of chloride counter-anion (-7) is much lower than acetate ion (4.76) and the interaction between chloride and cationic vesicle membrane is strong, so that ion exchange to nucleotide does not occur as easy as acetate counter-anion. On the other hand, it is interesting that chloride ions are

exchanged by phosphate the pka of which is around 2. In this case, the hydrophilicity of nucleotide is lower than that of chloride and that nucleotides easily form intermolecular interaction either by hydrogen bond or stacking, and cooperatively, the interaction between nucleotides and surfactants become stronger than the interaction with chloride. As a result we could observe the vesicle-helix transition by addition of GMP system. Further investigation about their kinetics with different aspects is necessary to fully understand this phenomenon.

II.8.2   Study of complexation between gemini surfactant and nucleotide trimer

The above mentioned study investigated nucleoamphiphiles composed by cationic surfactant having two hydrophobic chains complexed with monoanionic AMP and GMP, In these cases, the interaction between nucleotide of amphiphiles and nucleoside are driven mainly by non-Watson-Crick type hydrogen bonding and $\pi-\pi$ stacking without any paring. Herein, we studied assembling behavior between gemini amphiphiles complexed with trimeric nucleotide (tridNuc) and nucleoside.

In order to have similar distances between the cationic charges of gemini complexation with the negative charges of phosphate groups of tridNuc, the spacer length of geminiwas chosen to be 4 (Figure II.31).
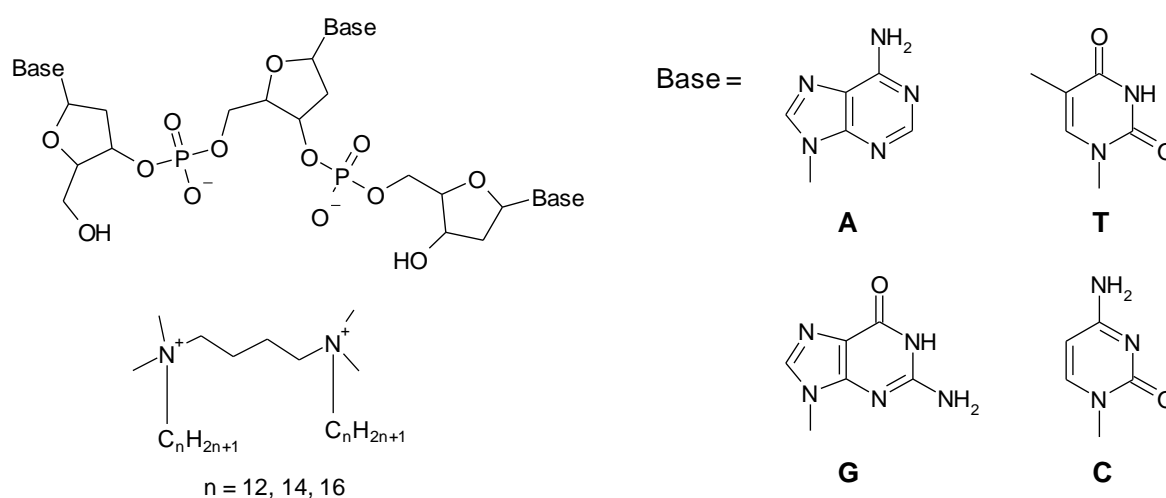
Figure II.31 Molecular structures of gemini surfactant complexed with nucleotide trimer.

The molecular recognition between tridNuc complexed with gemini surfactant and nucleoside was followed by UV-vis measurement. Figure II.32 shows the effect of additive nucleoside on aggregates behaviors of the gemini-tridNuc (tridAMP, tridCMP and tridTMP) aqueous solution using UV-vis spectra. The concentrations of each reagent are 0.5 mM.
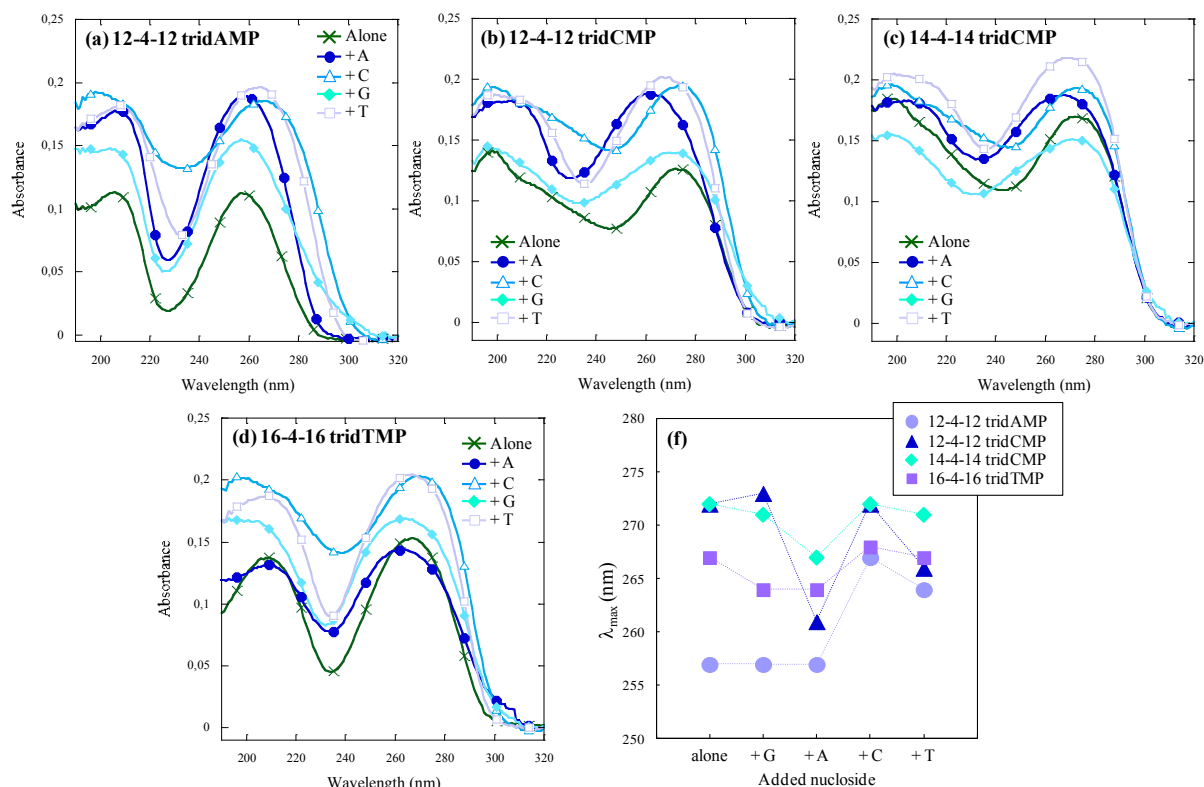
Figure II.32 UV-vis spectra of (a) 12-4-12 tridAMP + nucleoside, (b) 12-4-12 tridCMP + nucleoside, (c) 14-4-14 tridCMP + nucleoseide, and (d) 16-4-16 tirdTMP + nucleoside. Concentrations of each reagent were 0.5 mM. (e) Plot of peak at maximum absorbance (λ_{max}) for the gemini-tridNuc + nucleoseide.

In the case of 12-4-12 trdAMP, strong $\pi \rightarrow \pi^*$ transition of nucleobase was observed at 257 nm. When guanine (G) or adenine (A) was added to this sample, the adsorption showed no shift whereas adsorption bands obtained by mixture of cytosine (C) or thymine (T) exhibited red-shift (267 nm for C and 264 nm for T) (Figure II.32 a).

When nucleosides were added to 12-4-12 tridCMP, the band at 272 nm was strongly blue-shifted upon adding A (to 261 nm) and T (266 nm), for longer alkyl chain (C = 14) only addition of A (peak maximum at 267 nm) showed visible blue shift(Figure II.32 b, c). For

16-4-16 tridTMP, the adsorption bands at 267 nm showed slightly blue-shift upon addition of G and A (at 264 nm), and red-sift upon addition of C (at 268 nm) (Figure II.32 d).

These results indicate that molecular recognition is strongly depending on the alkyl chain length of gemini amphiphile: longer alkyl chain provides lower interaction because gemini surfactant with longer alkyl chain show more hydrophobicity, in contrast high solubility nucleoside (A, C, and T) is responsible for the lack of interaction on the aggregate in water. Within the object of interactions of trimeric nucleotide and nucleoside, assemblage between 12-4-12 tridAMP and C or 12-4-12 tridCMP and A resulted in strong interactions. However we have not yet succeeded in clarifying the driving force of specific interaction provide by base pair.

References

[1] E. T. Kool, *Annu. Rev. Biophys.Biomol. Struct.*, **2001**, *30*, 1-22.

[2] W. Saenger, *Principals of Nucleic Acid Structure*, Springer-Verlag, New-York, **1984**.

[3] (a) T. K. Harris, G. J. Turner, *IUBMB Life,***2002**, *53*, 85-98. (b) V. Verdolino, R. Cammi, B. H. Munk, H. B. Schlegel, *J. Am. Chem. Soc.*, **2008**, *112*, 16860-16873. (c) P. Acharya, P. Cheruku, S. Chatterjee, S. Acharya, J. Chattopadhyaya, *J. Am. Chem. Soc.*, **2004**, *126*, 2862-2869. (d) D. R. Lide, *CRC Handbook of Chemistry and Physics*, 80th ed.; CDC Press: Boca Raton, 1999-2000. (e) R. M. C. Dawson, D. C. Elliott, W. H. Elliott, K. M. Jones, *Data for Biochemical Research*, 3rd ed.; Oxford University Press: Oxford, **1986**. (f) G. D. Fasman, *CRC Handbook of Biochemistry and Molecular Biology, Nucleic Acids*, 3rd ed.; CRC Press: Cleveland, OH, **1975**; Vol. 1. (g) P. O. P. Ts'o, B*asic Principles in Nucleic Acid Chemistry*; Academic Press: New York, **1974**. (h) D. O. Jordan, *The Chemistry of Nucleic Acids*; Butterworth and Co.: WA, **1960**. (i) E. Chargaff, J. N. Davidson, *The Nucleic Acids Chemistry and Biology*; Academic Press: New York, **1955**. (j) S. Bundari, The Merck Index, 12th ed.; Merck and Company: Whitehouse Station, NJ, **1996**. (k) D. Shugar, J. J. Fox, *Biochim. Biophys. Acta*, **1952**, *9*, 199-218.

[4] (a) C. Xu, P. Taylor, P. D. I. Fletcher, V. N. Paunov, *J. Mater. Chem.*, **2005**, *15*, 394–402. (b) P. Barthélémy, S. J. Lee, M. W. Grinstaff, *Pure Appl. Chem.*, **2005**, *77*, 2133–2148. (c) D. Berti, P. Baglioni, S. Bonaccio, G. Barsacchi-Bo, P. L. Luisi, *J. Phys. Chem. B*, **1998**, *102*, 303–308. (d) M. Onda, K. Yoshihara, H. Koyano, K. Ariga, T. Kunitake, *J. Am. Chem. Soc.*, **1996**, *118*, 8524–8530. (e) P. Baglioni, D. Berti, *Curr. Opin. Colloid Interface Sci.*, **2003**, *8*, 55–61. (f) L. Moreau, P. Barthelemy, M. El Maataoui, M. W. Grinstaff, *J. Am. Chem. Soc.*, **2004**, *126*, 7533–7539.

[5] (a) T. Tanaka, K. Nakayama, K. Machida, M. Taniguchi, *Microbiology*, **2000**, *146*, 377-384. (b) G. M. van Wijik, K.Y. Hostetler, H. van den Bosch, *Biochim. Biophys. Acta.*, **1991**, *1084*, 307-310. (c) C. I. Hong, A. J. Kirisits, A. Nechaev, D. J. Buchheit, C. R. West, *J. Med. Chem.*, **1985**, *28*, 171-177. (d) C. Heiz, U. Radler, P. L. Luisi, *J. Phys. Chem. B*, **1998**, *102*, 8686-8691. (e) N .Campins, P. Dieudonné, M. W. Grinstaff, P. Barthélémy, *New J. Chem.*, **2007**, 31, 1928-1934.

[6] (a) P. Chabaud, M. Camplo, D. Payet, G. Serin, L. Moreau, P. Barthélémy, M. W. Grinstaff, *Bioconjugate Chem.*, **2006,** *17*, 466-472. (b) A. Gissot, M. Camplo, M. W. Grinstaff, P. Barthélémy, *Org. Biomol. Chem.*, **2008**, *6*, 1324–1333. (c) C. Ceballos, C. A. H. Prata, S. Giorgio, F. Garzino, D. Payet, P. Barthélémy, M. W. Grinstaff, M. Camplo, *Bioconjugate Chem.*, **2009,** *20,* 193–196.

[7] P. Barthélémy, *C. R. Chimie.*, **2009**, *12*, 171-179

[8] R. Iwata, K. Yoshida, M. Masuda, K. Yase, T. Shimizu, *Chem. Mater.*, **2002**, *14*, 3047-3053. (f) R. Iwata, K. Yoshida, M. Masuda, M. Ohnishi-Kameyama, M. Yoshida, T. Shimizu, *Angew. Chem. Int. Ed.*, **2003**, *42*, 1009-1012.

[9] P. Pescador, N. Brodersen, H. A. Scheidt, M. Loew, G. Holland, N. Bannert, J. Liebscher, A. Herrmann, D. Huster, A. Arbuzova, *Chem. Commun.*, **2010**, *46*, 5358–5360.

[10] (a) P. Baglioni, D. Berti, *Current Opinion in Colloid & Interface Science*, **2003**, *8*, 55-61. (b) F. Baldelli Bombelli, D. Berti, M. Almgren, G. Karlsson, P. Baglioni, *J. Phys. Chem. B*, **2006**, *110*, 17627-.17637.

[11] Carole Aimé, Auto-Assemblages Chiraxu d'Asmphiphiles Cationique., *Thesis of Doctrante, Bordeaux 1 Unversity*, **2007.**

[12] C. Aimé, S. Manet, T. Satoh, H. Ihara, K .Y. Park, F. Godde, R. Oda, *Langmuir*, **2007**, *23*, 12875-128885.

[13] C. Aimé, R. Tamoto, T. Satoh, A. Grelard, E. J. Dufourc, T. Buffeteau, H. Ihara, R. Oda, *Langmuir*, **2009**, *25*, 8489-8496.

[14] B. Xing, C. W. Yu, K. H. Chow, P. L. Ho, D. Fu, B. Xu, *J. Am. Chem. Soc.*, **2002**, *124*, 14846-14847.

[15] S. Mukhopadhyay, U. Maitra, G. Ira Krishnamoorthy, J. Schmidt, Y. Talmon, *J. Am. Chem. Soc.*, **2004**, *126*, 15905-15914.

[16] A. Brizard, R. Oda, I. Huc, *Top. Curr. Chem.*, **2005**, *256*, 167-218.

[17] (a) S. B. Nielsen, T. Chakraborty, S. V. Hoffmann, *ChemPhysChem*, **2005**, *6*, 2619-2624. (b) C. A. Sprecher, W. C. Johonson, Jr., *Biopolymers*, **1997**, *16*, 2243-2264. (c) P. R. Callis, *Photochem. Photobiol.*, **1986**, *44*, 315-321. (d) S. Ullrich, T. Schultz, M. Z. Zgierski, A. Stolow, *Phys. Chem. Chem. Phys.*, **2004**, *6*, 2796-2801.

[18] M .Ikehara, S. Uesugi, K. Yoshida, *Biochemistry*, **1972**, *11*, 836-842.

[19] A. J. Simpson, W. L. Kingery, D. R. Shaw, M. Spraul, E. Humpfer, P. Dvortsak, *Environ. Sci. Technol.*, **2001**, *35*, 3321-3325.

[20] B. Hernandez, R. Navaro, A. Hernanz, G. Vergotten, *Biopolymers*, **2002**, *67*, 440-455.

[21] B. N. Thomas, C.R. Safinya, R. J. Plano, N. A. Clark, *Science*, **1995**, *267*, 1635-1638.

[22] A. Brizard, C. Aimé, T. Labrot, I. Huc, D. Berthier, F. Artzner, B. Desbat, R. Oda, *J. Am. Chem. Soc.,* **2007**, *129*, 3754-3762.

[23] A. Brizard, R. Kiagus Ahmad, R. Oda, *Chem. Commun.,* **2007**, 2275-2277.

[24] A. G. Petrovic, P. L. Polavarapu, *J. Phys. Chem. B*, **2005**, *109*, 23698-23705.

[25] (a) V. Setnicka, M. Urbanova, K. Volka, S. Nampally, J. M. Lehn, *Chem. Eur. J.*, **2006**, *12*, 8737-8743. (b) F. B. Howard, J. Frazier, T. Miles, *Biopolymers*, **1977**, *16*, 791-809.

[26] J. T. Davis, G. P. Spada, *Chem. Soc. Rev.,* **2007**, *36*, 296-313.

[27] S. Manet, Y. Karpichev, D. Bassani, R. Kiagus Ahmad, R. Oda, *Langmuir*, **2010**, *26*, 10645-10656.

Chapter III

In situ helicity inversion of self-assembled nano-helix

III.1 Introduction

In the previous chapter, we introduced *in situ* vesicle to helix morphology transition upon addition of chiral nucleotide counter-anion to achiral vesicles formed by cationic surfactants at constant temperature. In this chapter, we will present the *in situ* handedness inversion of chiral self-assemblies by addition of opposite chiral acid.

As we have seen in the bibliographic chapter, chiral amphiphilic molecules often self-assemble in solution to form aggregates with high aspect ratio such as rods, twisted and helical ribbons, and tubes, suggesting that chirality is intricately associated with the growth and stability of self-assembled fibers of small organic molecules or polymers. Often chirality is expressed in the structure of these fibers at a supramolecular scale of nanometer to micrometer, and their structures may be coiled, twisted, or wound around one another and exist as a right-handed or a left-handed form.

A specific handedness in a helical conformation (right-handed *P*, or left-handed *M*) of these biological or synthetic macromolecules or supramolar assemblies ranges from a molecular level to several hundred nanometers,[1] and in the majority of the cases, the driving force for the helical structures comes from inter/intramolecular π-stacking interaction or hydrogen bonding.[2]

Most naturally occurring biological macromolecules such as proteins and nucleic acids are optically active and adopt a one-handed helix as right-handed α-helix and double-helix, respectively. Their structure play important role in the functions of these biomolecules. For example, the formation of coiled-coil superhelix in collagen is instrumental to provide it tensile strength, important for a structural protein.

Recently, there are many reports about synthetic helical structure obtained by foldamers, oligomers, polymers and self-assembled low molecular weight molecules. The primary advantage of these synthetic structures lies in the controllability of the expressed chirality. The controllable helicity is quite attractive not only to mimic nature, but also for their wide variety of possible applications in materials sciences, chemical and biomaterial sensing, and enantioselective catalysis.[3] The problematics of controlling chirality and thereby

generating specific structures for achieving specific functions continues to be a challenging and rapidly expanding area in the field of foldamers, oligomers, polymers and supramolecular chemistry.

The chirality inversions in helical structures are known both in nature as well as in the synthetic systems. For example, a right-handed helical protein chain can organize into a left-handed helical superstructure,[4] right-handed polymer chains can organize into left-handed superhelical structures.[5]

There are also some examples which demonstrate that macromolecules and supramolecular aggregates can change their helicity between *P* and *M* in a so-called helix-helix transition by applying an external stimulus such as light,[6] solvent (example in Figure III.1 a),[7] temperature (Figure III.1 b),[8] pH value,[9] and chiral additives.[10]
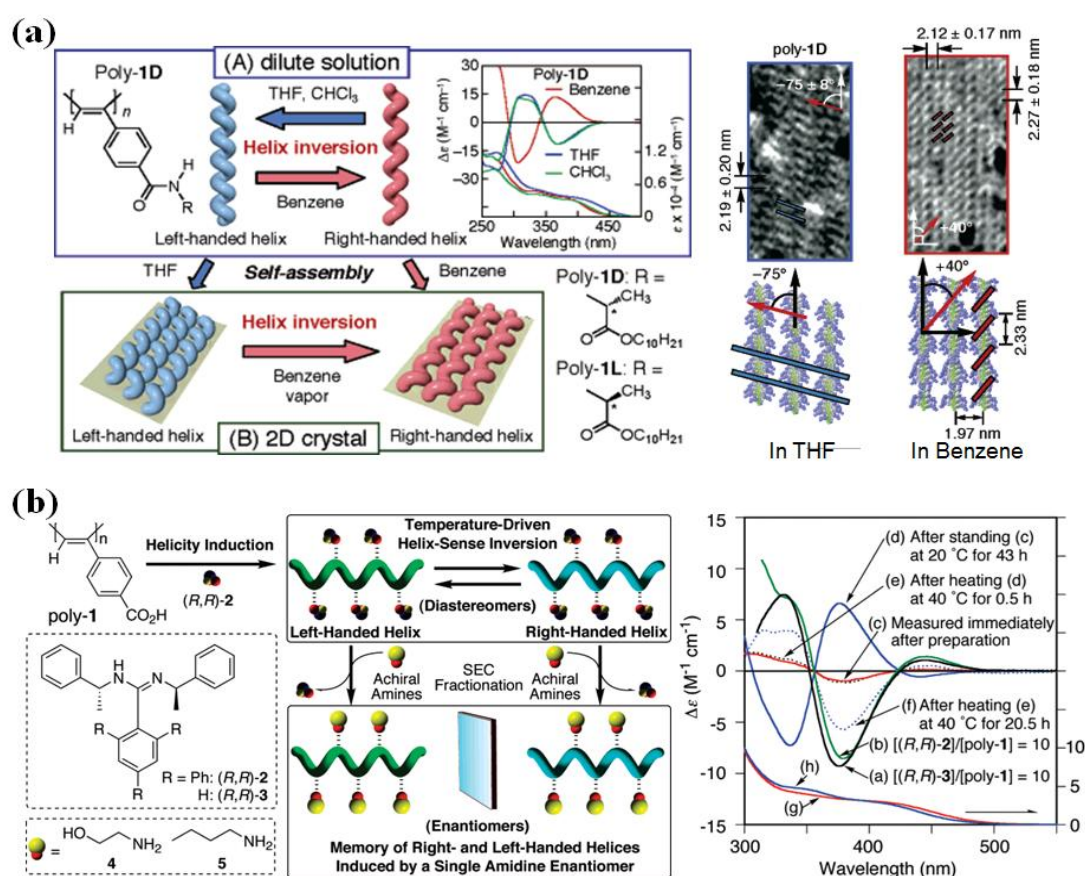
Figure III.1 Examples of reversal helicity inversion driven by (a) solvent exchange,[7(d)] and (b) temperature control. [10(c)]

Most of these examples of chirality inversion concern the molecular or supramolecular level helical organization of macromolecules/foldamers, and the chirality is expressed at nanometer level. These molecules with controllable helicity can exhibit the optical activity and inversion steps are normally demonstrated by spectroscopic method. Because of the present resolution limit of microscopy technique, very little examples exist as to the direct visualization of these helix-helix transitions. Also, only a few examples can be found in the literature about helical inversion on molecular assembly systems,[7(e),9] and the kinetic aspects of these inversion are rarely discussed.[7(e)]

Herein, we will present the system we have developed in order to directly visualize step by step, the *in situ* helicity inversion of chiral supramolecular structures at mesoscopic level (20 nm – microns).

In the last decade, a number of reports from our laboratory have demonstrated that supramolecular nanostructures with controllable chirality can be achieved from non-chiral cationic surfactants by the influence of chiral counter anions.

The complex of non-chiral cationic bis-quaternary ammonium gemini surfactants in the presence of chiral tartrate counter-anion can expand to the gel network of chiral ribbons in water or organic solvent.[11,12] This ambivalent behavior results from the formation of bilayers in both solvents of aqueous and organic.[13] In contrast to the polymers, the gel formation from gemini tartrate is based on non-covalent interaction. Additionally, the self-assembly of gemini tartrate amphiphiles, particularly gemini 16-2-16[a], promote chiral supramolecular structure: the twisted, helical, and tubular formations are observed (Figure III.2). This study has been part of doctoral work of Damien Berthier,[14] Aurélie Brizard,[15] and Carole Aimé.[16]

---

[a] A gemini with two symmetrical 16 carbon chain attached hydrophilic heads connected by an ethylene spacer (2 carbons) that is denoted 16-2-16.
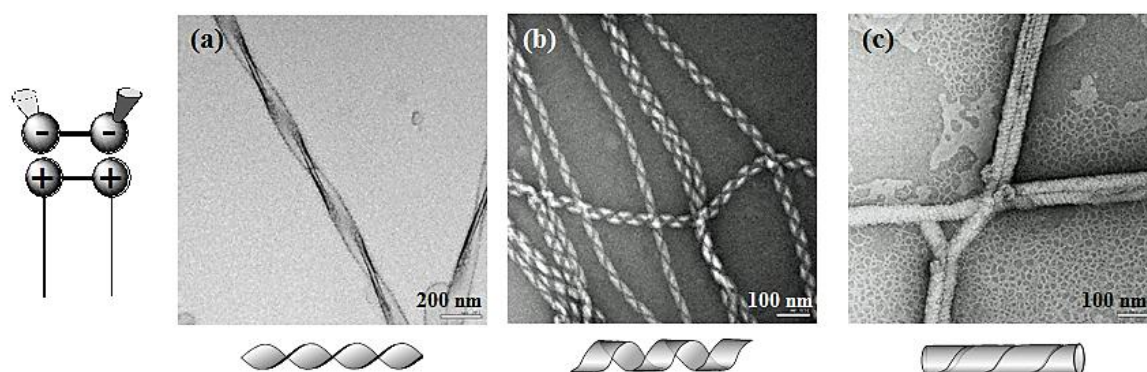
Figure III.2 Transmission electron microscopy (TEM) image of the morphologies obtained From achiral cationic gemini surfactant, with chiral tartrate as the counter ion. The morphologies are (a) twisted, (b) helical and (c) tubular structures.

It has previously been reported from our lab that the supramolecular morphologies of chiral ribbons from 16-2-16 L-tartrate amphiphiles were controlled by several parameters such as modifying the temperature, inducing the small amounts of additives and enantiomeric excess with opposite counter anions which were induced by 16-2-16 D-tartrate.[12,17,18] Particularly, controlling the enamtiomeric excess can produce various morphologies with finely tunable shapes. For example, in the case of racemic mixture of L-tartrate : D-tartrate (1 : 1), flat ribbons were observed. (Figure III.3 a). When the ee was increased, the morphology gradually transforms to twisted (Figure III.3 b, c), helical ribbon (Figure III.3 d), and finally to tubular structure (Figure III.3 e).
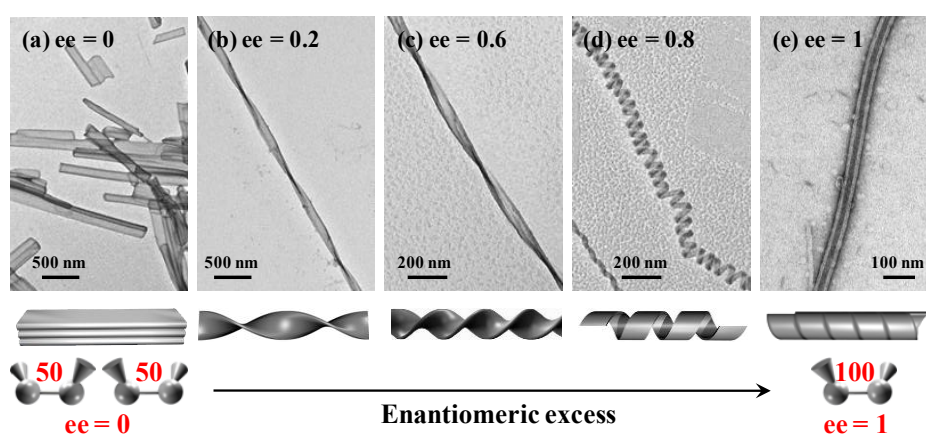
Figure III.3 TEM image of the morphologies variation obtained by different ee function.[17]

As the chiral center in these molecules are not covalently attached to the membrane-forming molecules, i.e. gemini surfactants, but they originate from their counterions, if opposite chiral acid (for example, D-tartaric acid) is added to the gel network formed with nanometric tubules of 16-2-16 L-tartrate, is it possible to induce *in situ* helicity inversion (Figure III.4)? In our approach towards controlling the helicity of chiral fibers, tartaric acid with opposite chirality (*e.g.*, D-) was directly introduced into a pre-formed gel of the amphiphile with L-tartrate. In the process, helicity inversion was induced by the *in situ* counter anion exchange at ambient temperature.
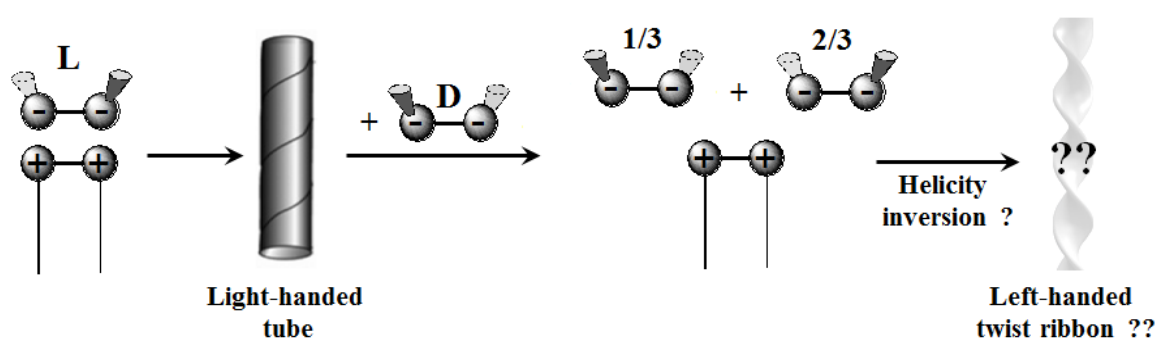
Figure III.4 Schematic illustration of *in situ* helicity inversion from *P* tube to *M* ribbon upon addition of opposite chiral acid.

We attempted to visualize direct helicity inversion using transmission electron microscopy (TEM) observation. The process of chirality transfer was followed by circular dichroism (CD) spectroscopy. In addition, the kinetics of the process was followed by is also followed by polarized attenuated total reflectance (ATR) spectroscopy and small angle X-ray scattering (SAXS) measurement.

III.2 Non equilibrium *in situ* Counter-Anion exchange in Gel Network: effect on the Morphology of Aggregates

III.2.1 Experimental description

The right-handed (*P*) tubular gels networks were formed by 16-2-16 L-tartrate amphiphiles (ee = 1) in water (Figure III.5). 10 mM solution was prepared by heating 16-2-16 L-tartrate powder in water to 50 °C, which was allowed to cool at RT. While cooling, the clear and fluid solution became increasingly opaque and viscous, then became gel with *P* tubular structures after a few hours. When the D-tartaric acid as opposite chirality was filtered through these gel networks, The excess amounts of L- or D-tartaric acid were immediately washed away by a large amount of water after filtration of D-tartaric acid solution. All these procedures were performed under the constant temperature at 21 ˚C.
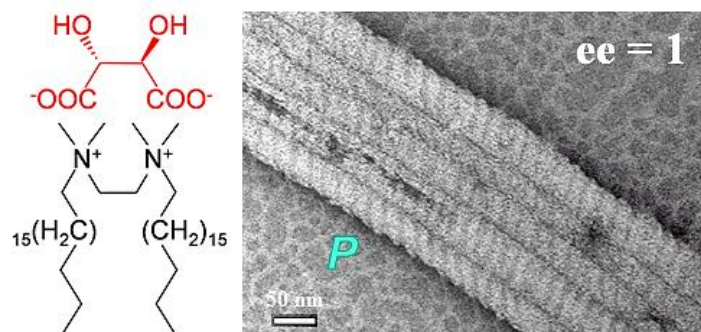
Figure III.5 The structure of 16-2-16 L-tartrate. TEM image of right-handed tubes from 16-2-16 L-tartrate with pure enantiomer (ee = 1). The character *P* is significant right-handed helical structure.

The Figure III.6 schematically shows this procedure. Through the gel network of 10 mM 16-2-16 L-tartrate, the D-tartaric acid solution with a various equivalence of D-tartrate such as 1 eq, 2 eq, 4 eq, and 20 eq is passed through. This gel was immediately washed by large amounts of water to remove the excess of D- and L-tartaric acid, and final concentration was adjusted to 10 mM for each reagent.
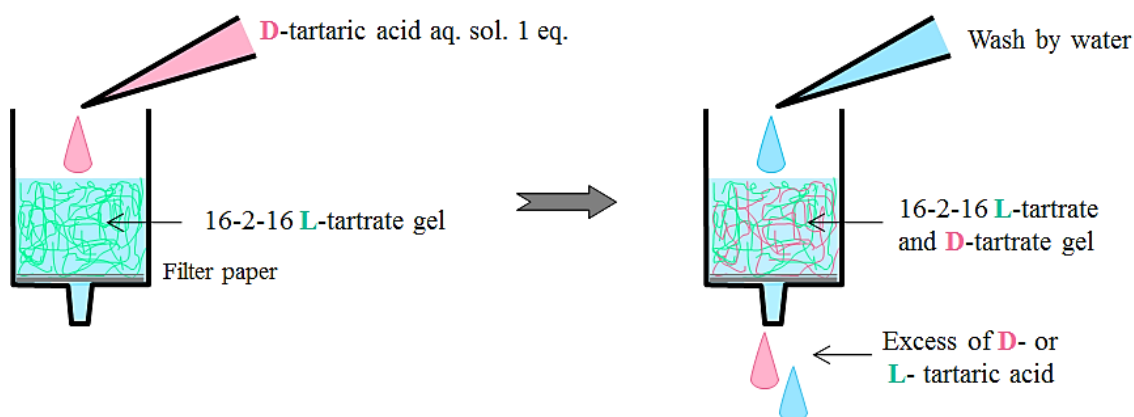
Figure III.6 Schematic illustration of gel preparation method.

III.2.2 Morphologies transitions followed by TEM observation

Variation of the morphology of aggregates with time after the addition of 1 equivalent D tartaric acid. (expected ee = "0").

At first, we prepared a 16-2-16 L-tartrate gel to which an equivalent amount of D-tartaric acid solution (ee = "0") was filtered through.

Initially, the tubular fibers slowly unwound to helical structure (Figure III.7 a). After 30 min, these nanometric P helical structures were further unwound and twist ribbons were observed (Figure III.7 b-c).

With time, their twist pitches increased to micrometric scale. After 4 h, flat ribbons and M twist ribbons were also observed, and the ratio of P and M were 3:2, (Figure III.7 d). After a day, most of the fibers were transformed to flat ribbons (Figure III.7 e), but interestingly we observed a mixture of flat ribbons and P twist ribbons after 1 week (Figure III.7 f) this can be described as follows. Because we washed right after passing through the D tartrate solution, the counter-anion exchange was not completed and in the final mixture, the ratio of L-tartrate counter-anions remained slightly higher.
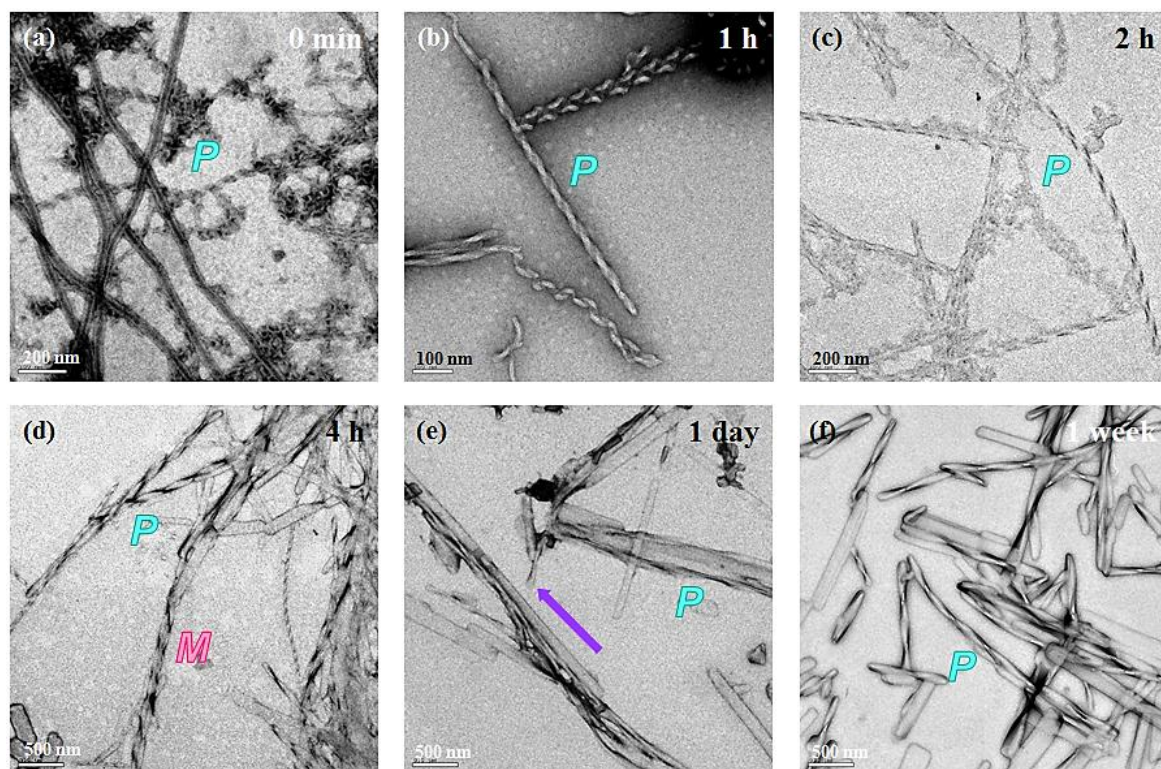
Figure III.7 TEM images of pitch elongation steps of tubular network from 16-2-16 tartrate amphiphiles after the addition of an equivalent of opposite chiral D-tartaric acid. The characters _P_ and _M_ are significant right-handed and left-handed helical structure, respectively.

Variation of the morphology of aggregates with time after the addition of 2 and 4 equivalent D tartaric acid (expected ee = -0.3 and -0.6 respectively).

When two equivalents of D-tartaric acid in solution (ee = "-0.33") were added, initially unfolded _P_ helical ribbons were observed (Figure III.8 a, b). After 1 hour, these _P_ helical ribbons abruptly reversed to _M_ helices (Figure III.8 c), and then they transformed into twisted ribbons with increasing twist pitch until about a week (Figure III.8 d-f).
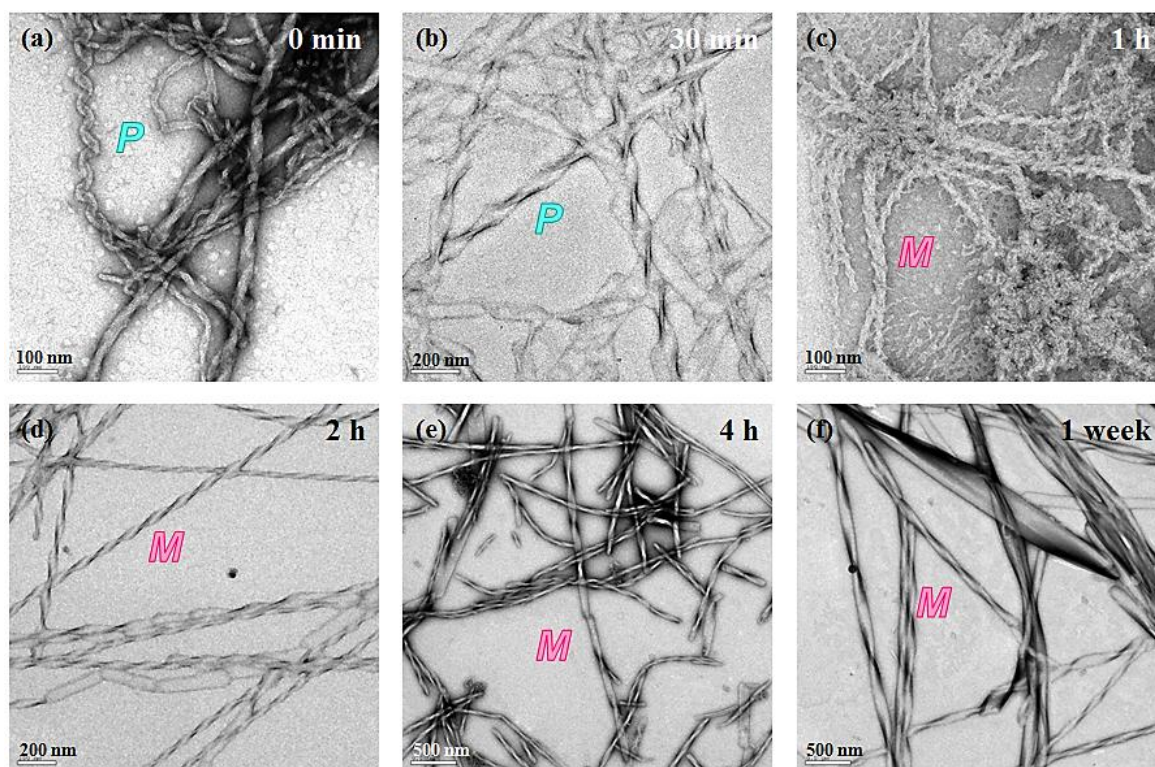
Figure III.8 TEM images of helicity inversion and pitch elongation steps of tubular network from 16-2-16 tartrate amphiphiles by ee changes from 1 to "-0.33" in the case of addition of 2 equivalents opposite chiral D-tartaric acid. The characters *P* and *M* are significant right-handed and left-handed helical structure, respectively.

On the other hand, when 4 equivalents of D-tartaric acid in solution were added, the tubular fibers immediately transformed to *M* helical ribbons (0 min). The chirality inversion occurred very fast replacing the counter anion from L- to D-tartrate on the gemini surfactant (Figure III.9 a). These *M* helical structures transformed into twisted ribbons after 1 day (Figure III.9 d, e). The twist pitches of these helical were a few hundred nanometers (Figure III.9 f). On the macroscopic aspect, initially both samples were translucent solution, and then turned into clouded gel after about 1 hour.
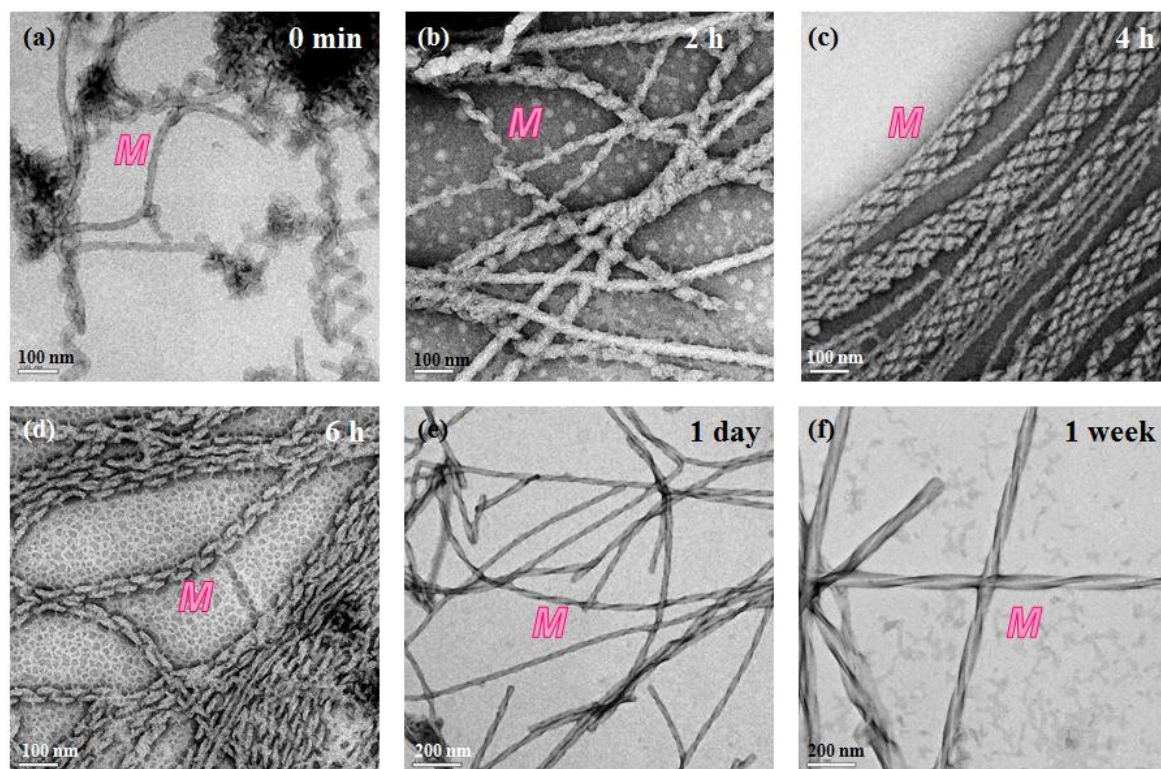
Figure III.9 TEM images of helicity inversion and pitch elongation steps of tubular network from 16-2-16 tartrate amphiphiles by ee changes from 1 to "-0.60" in the case of addition of 4 equivalents opposite chiral D-tartaric acid. The characters *M* are significant right-handed and left-handed helical structure.

Variation of the morphology of aggregates with time after the addition of 20 equivalents D tartaric acid (expected ee = -0.9).

When a large excess of D-tartaric acid such as 20 equivalents were passed through the 16-2-16 L-tartrate gel, immediately the fiber structures collapsed to form vesicle-like structures (Figure III.10 a). And then they reassembled to chiral ribbons after about 30 min (Figure III.10 b). After 1 hour, these ribbons transformed into *M* helical structures (Figure III.10 c), they eventually formed tubular structure after a week (Figure III.10d-f).
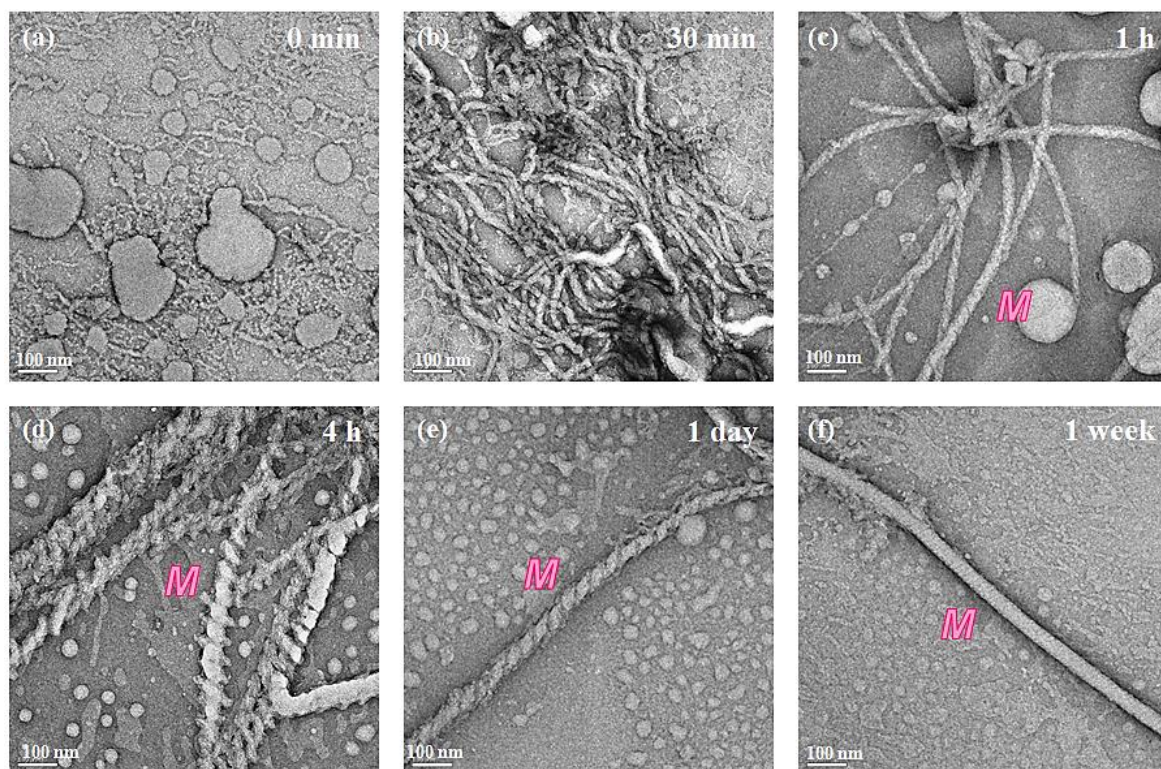
Figure III.10 TEM images of re-assemblies steps of tubular network from 16-2-16 tartrate amphiphiles by ee changes from 1 to "-0.90" in the case of addition of 20 equivalents opposite chiral D-tartaric acid. The characters *M* are significant right-handed and left-handed helical structure.

III.2.3 Pitch variation

We investigate the time-dependent variation of the average twist pitch and their standard deviations as a function of ee.

The helical pitch of the original helices by 16-2-16 L tartrate (ee = 1), was 30 nm ± 5 nm.

- After the filtration of 1eq D-tartaric acid (ee = "0"), the twist pitch was elongated to 60 nm ± 16 nm 30 minutes and after 1 h, it increased to 90 nm ± 40 nm, 200 nm ± 130 nm after 2 h. At 4 h, both *P* and *M* fibers were observed and the twist pitches were 590 nm ± 300 nm for *P* twist ribbons and 790 nm ± 340 nm for *M*. After 6h, 2830 ± 2000 nm for *P* twist ribbons and 1970 nm ± 1100 nm for *M*. After a day, only *P* twist ribbons were observed and their twist pitch

was 3330 nm ± 2000 nm. Finally after a week the pitch shortened a little to 1470 nm ± 600 nm.

- Immediately after the filtration of 2eq D-tartaric acid (ee = "-0.33"), the twist pitch of *P* helical ribbon became 200 nm ± 80 nm, 380 nm ± 200 nm for 30 min, then 1 h later *M* helical ribbons were observed that twist pitch was 62 nm ± 30 nm. After 2h, they were 340 nm ± 140 nm, 520 nm ± 260 nm after 4 h, 770 nm ± 430 nm for 6 h, 1430 nm ± 720 nm for 1day, 1150 nm ± 800 nm for 1 week and finally twist pitch reached 870 nm ± 440 nm from 3 weeks.

- After the filtration of 4 eq D-tartaric acid (ee = "-0.66"), the *M* helical ribbons were observed from the moment D-tartaric acid passed through the gels and their twist pitch was 85 nm ± 40 nm. They evolved to 50 nm ± 15 nm after 30 min, 65 nm ± 20 nm after 2 h, 75 nm ± 20 nm after 6 h, 110 nm ± 60 nm after 1 day, 170 nm ± 100 nm for 2 days, 650 ± 300 nm for 1 week, then twist pitch was stable at 480 nm ± 300 nm.

- After the filtration of 20 eq D-tartaric acid (ee = "-0.9"), all fibers collapsed to undefined structure, then after 1 h *M* helical fibers were re-assembled with their twist pitch being 50 nm ± 10 nm, 70 nm ± 30 nm after 2 h, 60 nm ± 20 nm after 1day, 50 nm ± 10 nm after 1 week, then pitch values reached to 40 nm ± 5 nm.

These results suggest that simple filtration of tartaric acid with opposite chirality can induce the chirality inversion of the self-assembled ribbons, and the final morphologies of the ribbons and the speed of chirality inversion depend strongly on the total amount of D tartaric acid: the chirality inversion occurred much quicker with a larger amount of D tartaric acid.

III.3 Investigation of chirality inversion by CD spectroscopy

In order to obtain more insights into the helix inversion phenomenon, the process was monitored by CD.

Berthier *et al.* have reported the conformation of tartrate ions in the chiral bilayers of gemini amphiphiles (*n*-2-*n* with *n* > 14) with ee = 1 using CD spectrum which were in the absorption region of cotton coupling of carboxylate chromophores at 190-250 nm in aqueous

solution.[19] A strong exciton coupling between carboxylates was observed with a positive peak at 201 nm and negative peak at 219 nm for 16-2-16 L-tartrate. Brizard *et al*. has also shown the effect of enantiomeric excess on chiroptical properties by synthesized gels.[20] Decreasing ee caused a decrease of the intensity of the cotton coupling between the carboxylates.

In this section, we study the variation of chiroptical properties during counter-anion exchange process.

Figure III.11 shows the variation of CD signals after filtration of various amount of D-tartaric acid into the 10 mM 16-2-16 Ltartrate gels.
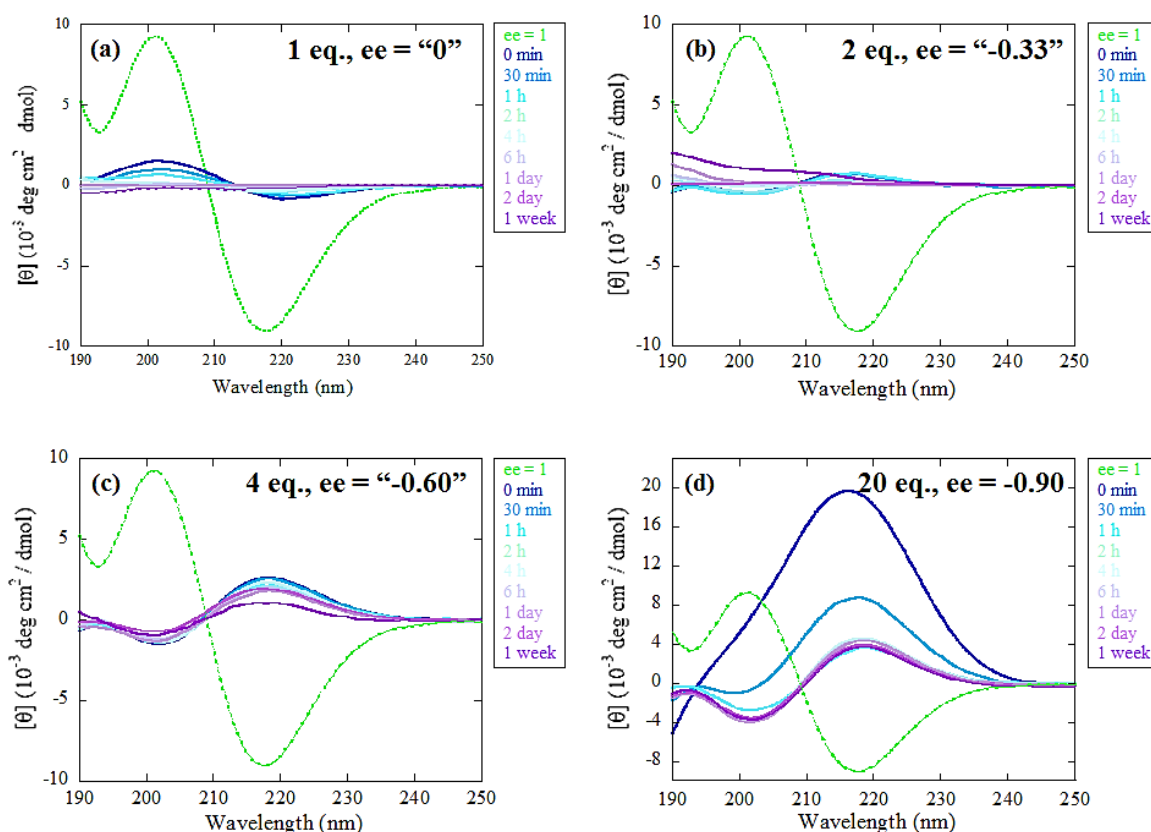
Figure III.11 CD spectra of 16-2-16 tartrate amphiphiles with different ee changes: (a) from 1 to "0", (b) 1 to "-0.33", (c) 1 to "-0.60", and (d) 1 to "-0.90" by addition of opposite chiral D-tartaric acid solution through the 16-2-16 L-tartrate gel.

As it is clearly seen from the Figure III 11, the CD signals change immediately after filtration of D tartrate for all cases.

For the case of ee = "0", both bands at 201 nm and 219 nm were drastically decreased just after filtration of D-tartaric acid solution to 16-2-16 L-tartrate gel. The CD peak continuously decreased with the time, and their cotton coupling finally disappeared after 4 h (Figure III.11 a). It is important to note here that at this point, the TEM images show the presence of some twisted ribbons with long pitch (≥ 1000 nm). This means that the presence of long pitch ribbons is not reflected to the CD signals.

For the case of ee = "-0.3", the signs of CD bands at 201 nm and 219 nm were inversed just after filtration of 2 equivalents of D-tartaric acid through the 16-2-16 L-tartrate gel. The CD peak decreased with time until 6 h, but from 1 day, the shape in the CD spectrum changed and a strong positive signal appeared at low wavelength. This phenomenon was accompanied by the growth of ribbons with a large pitch (> 1000 nm). This is therefore probably caused by the strong scattering of large chiral ribbons (Figure III.11 b).

For ee = "-0.60", the sign of CD spectrum were inversed just after filtration of D-tartaric acid solution. The peak hight remained the same until 6 h, during this time, the ribbons kept helical shapes. After 1day, the CD peaks at 219 nm gradually decreased to about 40 % of the initial hight, whereas peak at 201 nm showed slightly decrese to 61 % of the initial hight. This may correspond to the morphology transition from helical ribbons to twisted ribbons with elongation of pitch value (Figure III.11 c).

Figure III.11 d shows the case of ee = "-0.90". In this case, only the peaks of D-tartaric acid were observed during the first 30 min because too much excess of D-tartaric acid still remained around the gel with micelle or vesicle structure. The inversed peak appeared at around 1 hour and the peak at 219 nm kept the hight after 1week with re-assembling the chiral fibers.
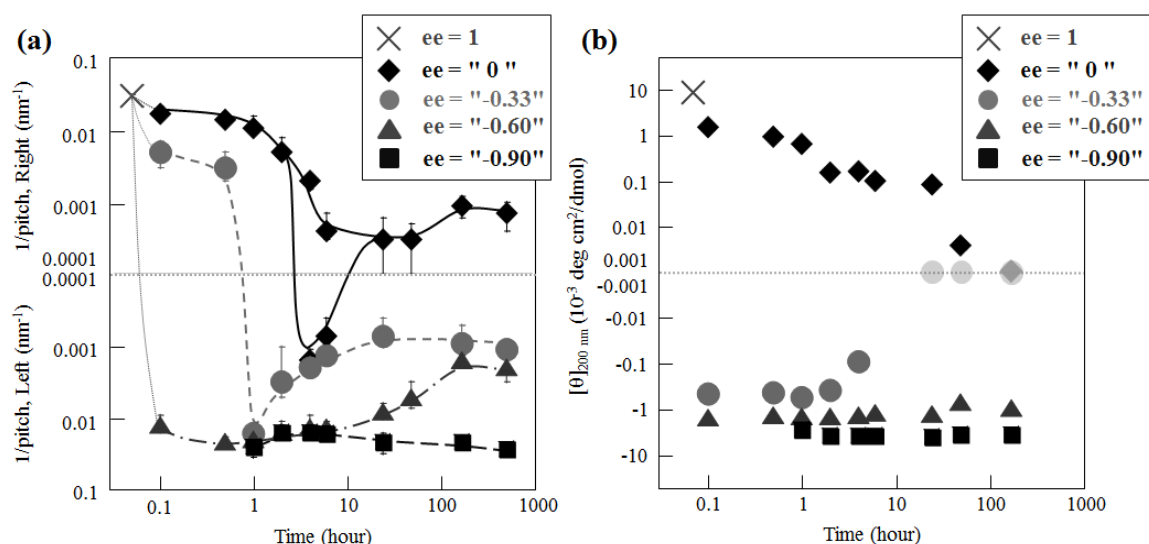
Figure III.12 Aging variation of (a) inversed twist pitches and (b) CD intensities at $[\theta]_{200nm}$ with different ee.

Figure III.12 compares the variation of the twist pitch and CD intensities at 201 nm with time for different ees. This figure clearly shows the strong correlation between the morphologies of chiral fibers as observed by TEM image, with the supramolecular chirality observed with CD signals. This confirms the previous results published by our group (Figure III.13).[20] Meanwhile, a detailed analysis describes that the kinetics of the two data sets shows that the variation of the CD signal is much more rapid than the morphology variation. For example, the case of ee = "0.33", also CD does not see the residual chirality observable with TEM.
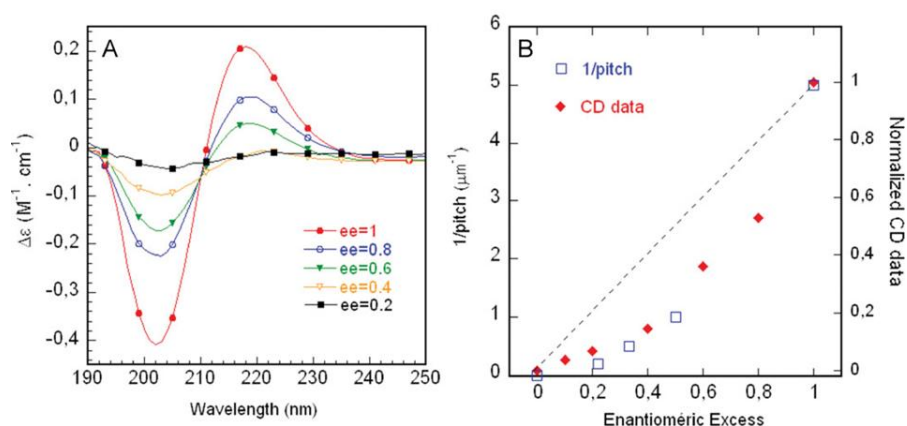
Figure III.13 (a) ECD spectra of various mixtures of the two enantiomers of16-2-16 tartrate. (b) Variation of the inverse of the pitch period (left) and the normalized CD data (right) as a function of enantiomeric excess.[20]

III.4 Molecular and supramolecular kinetics of morphology transition

III.4.1 Study of molecular orientation followed by attenuated total reflectance (ATR) spectroscopy

We then probed the time evolution of the molecular environment during morphology transition using polarized attenuated total reflectance (ATR) spectroscopy. ATR spectroscopy is a very effective technique for using in conjunction with infrared spectroscopy which enables samples to be examined directly in the solid, liquid or gas state without further preparation. One of the features of polarized ATR measurement is that the information of samples can be obtained in relation to the orientation of the molecules with respect to the X, Y and Z axis. The dichroic ratio R_{ATR} for a selected vibrational mode is determined by calculating the ratio of the absorbance measured with the infrared radiation polarized parallel (p) and perpendicular (s) to the plane of incidence ($R_{ATR} = A_p/A_s$). Here, parallel polarized light has vector in the X and Z directions, and the perpendicular polarized light has a vector in the Y direction (see Figure III.14).[21] Therefore, if the molecular orientation of chiral fibers from 16-2-16 tartrate gels is completely isotropic, the R_{ATR} should be 2, conversely the molecular orientation is anisotropic, such as the molecules are oriented planner direction, A_p becomes weak and the value of R_{ATR} approaches 1.
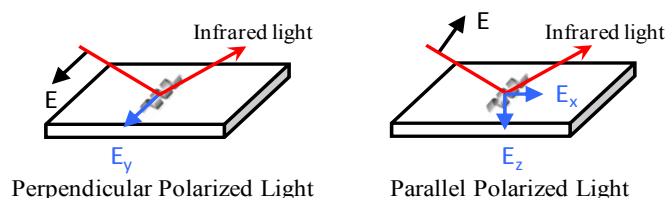
Figure III.14 Schematic illustrations of directions of polarized light and evanescent wave.

We focused on the ATR signals of 16-2-16 tartrate gels in the range of wavenumber

1800-1250 cm^{-1} and 3000-2800 cm^{-1}. These spectral regions are characterized by the strong antisymmetric ($\nu_a CO_2^-$) and symmetric ($\nu_s CO_2^-$) stretching modes of the carboxylate groups of the tartrate at 1606 and 1349 cm^{-1}, respectively; by the bending modes of methyl ($\delta_a CH_3$, $\delta_s' CH_3$ and $\delta_s CH_3$) and methylene (δCH_2) groups of amphiphilic cations in the 1500-1410 cm^{-1} region, and by the antisymmetric ($\nu_a CH_2$) and symmetric ($\nu_s CH_2$) stretching vibration of the methylene groups of gemini amphiphiles at 2918 and 2850 cm^{-1}. The dichroic ratio between two polarizations was evaluated by $\nu_a CH_2$ stretching vibration of hydrocarbon group ay 2918 cm^{-1} and $\nu_s CO_2^-$ stretching vibration of the carboxylate group of tartrate counter-anion at 1349 cm^{-1}.

Figure III.15 shows ATR spectrum of chiral tubules with ee = 1 corresponding to the pure 16-2-16 L-tartrate gel. The value R_{ATR} of at $\nu_a CH_2$ band showed R_{ATR} = 1.5, R_{ATR} at $\nu_a CO_2^-$ and $\nu_s CO_2^-$ band showed 2.2 and 1.9, indicating that the alkyl chains of gemini amphiphiles are oriented perpendicular to the X-Y plane, whereas the carboxylate groups of tartrate were oriented isotropically.
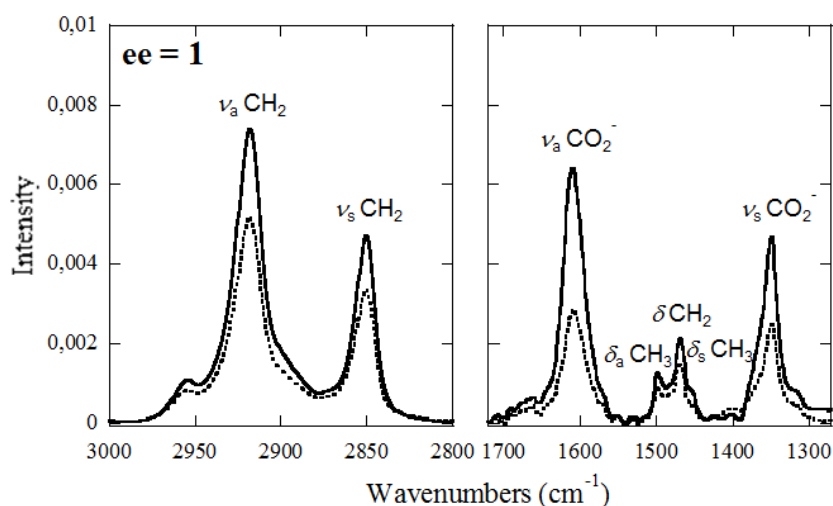
Figure III.15 ATR spectra of 16-2-16 L-tartrate amphiphiles (ee = 0).

Figure III.16 describes ATR spectra of the time evolution in molecular environment correlated to the morphological changes by different ee.
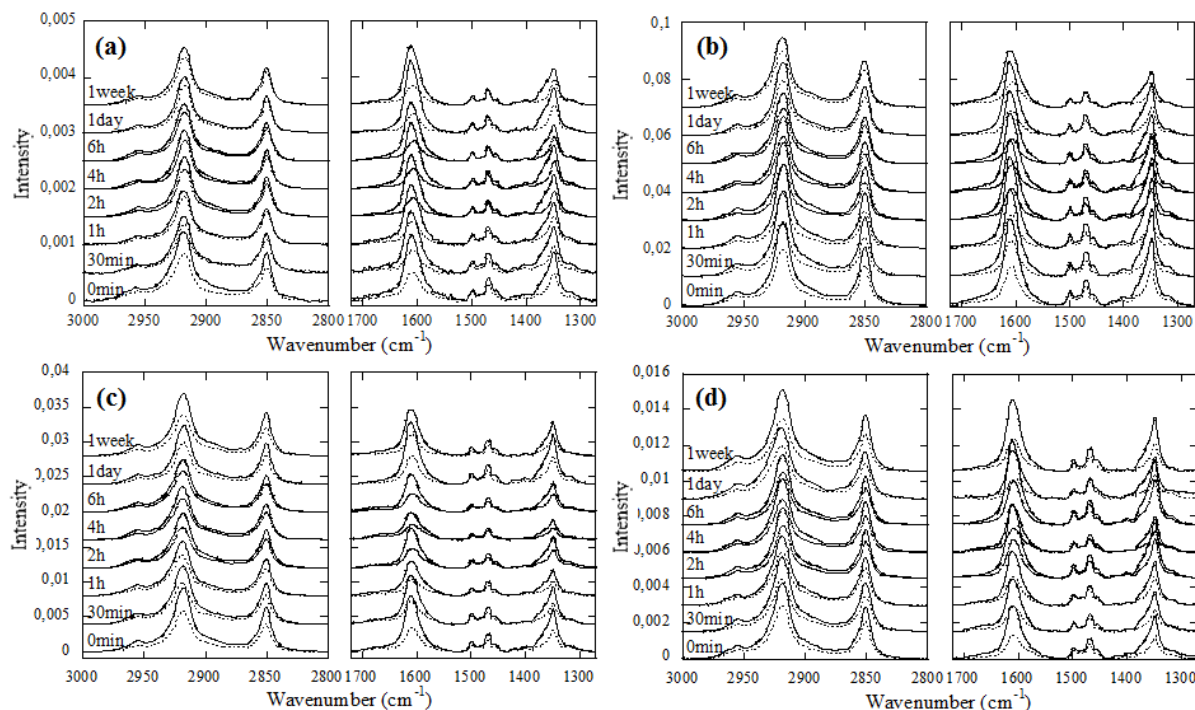
Figure III.16 ATR spectra of molecular kinetics from 16-2-16 tartrate amphiphiles with different ee changes (a) from 1 to "0", (b) 1 to "-0.33", (c) 1 to "-0.60", and (d) 1 to "-0.90" by addition of opposite chiral D-tartaric acid solution through the 16-2-16 L-tartrate gel.

When ee = "0", the $\nu_a CH_2$ band and the $\nu_s CO_2^-$ band from p polarization decreased with the time, whereas $\nu_a CO_2^-$ band increased. Here, we focus on the variation of the R_{ATR} values, at first R_{ATR} of $\nu_a CH_2$ band is 1.46 corresponding to helical morphology, then the R_{ATR} decreased to 1.18 after 4 h. For the R_{ATR} at $\nu_s CO_2^-$ band also decreased from 1.81 to 1.49, however the R_{ATR} at $\nu_a CO_2^-$ band increased from 2.30 to 3.00 (Figure III.16 a). These results indicate that the hydrophobic chains of bilayers and antisymmetric vibration of CO_2^- of tartrate ions become more and more oriented parallel to z direction in the Figure III 13 with time (bilayer is oriented parallel to the ATR window).

For the case of ee = -0.33, the decreasing of R_{ATR} value at $\nu_a CH_2$ band was much slower than ee = 0, and finally R_{ATR} reached 1.26 after 6 h, while corroborate with the increase in the twist pitch. The R_{ATR} value of $\nu_s CO_2^-$ band did not show an important variation (1.81 to 1.75). But R_{ATR} value at $\nu_a CO_2^-$ band increased from 2.30 to 3.10 within 6 h (Figure III.16 b).

For ee = -0.60 or -0.90, once the R_{ATR} value at $\nu_a CH_2$ band decreased to around 1.3 for several hours, then increased again to $R_{ATR} > 1.5$ within 1 week, the R_{ATR} value of $\nu_s CO_2^-$ band showed final value $R_{ATR} = 1.8 \sim 1.9$ after 1 day. The R_{ATR} value of $\nu_a CO_2^-$ band did not show notable change and remained around 2.3 (Figure III.16 c, d). Globally, the orientation of gemini tartrate remained close to isotropic organization before and after the morphological transition.

Figure III.17 shows the plot of R_{ATR} values of $\nu_a CH_2$ and $\nu_s CO_2^-$ and $\nu_a CO_2^-$ as a function of time for the different ee. These data showed that for ee = "0" and "-0.33", the R_{ATR} value of $\nu_a CH_2$ band decrease to approximate 1.1 - 1.3 with time, which indicates that the morphologies of chiral fibers transform from chiral tubules to twisted ribbons or flat ribbons these bilayers gets more and more oriented parallel to the ATR window, and consequently, the alkyl chains gets more oriented perpendicular to the ATR window.
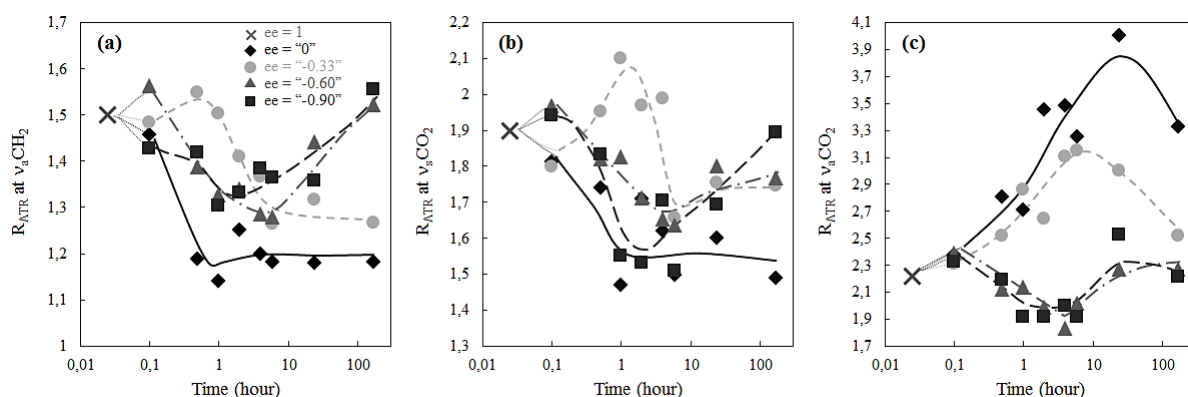
Figure III.17 The aging variation of R_{ATR} with different value of ee changes at (a) $\nu_a CH_2$, (b) $\nu_s CO_2^-$, and (c) $\nu_a CO_2^-$.

For ee = -0.66 and -0.9, R_{ATR} values for both $\nu_a CH_2$ and $\nu_s CO_2^-$ went through a minimum at around 1h, then returned to values close to initial ones (1.5 for $\nu_a CH_2$ and 1.8-1.9 for $\nu_s CO_2^-$).

Figure III.18 describes the relation between kinetics of bilayer orientation (R_{ATR} at νCH_2) and morphology transition at the surface of ATR crystal. For lower ee ("0" and "-0.33"), isotropic oriented alkyl chains of bilayers were gradually oriented perpendicular to the X-Y plane with decreasing the R_{ATR} value to approximate 1. This phenomenon is caused by

morphology transition to flat ribbon or twist ribbon with long twist pitch, suggesting that these bilayers tend to orient parallel to the surface of ATR crystal.
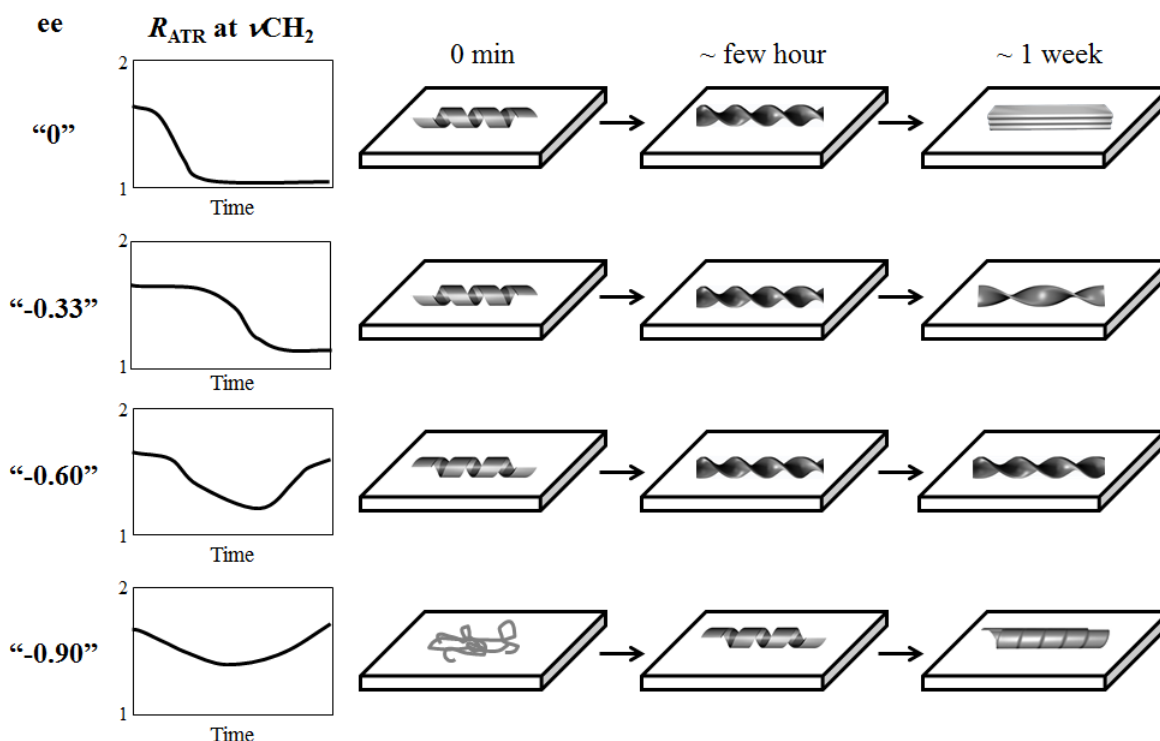
Figure III.18 The Schematic illustration of the summarized relation between kinetics of alkyl chains orientation (R_{ATR}) and morphology transition.

For higher ee ("-0.60" and "-0.90"), once R_{ATR} value decreased during morphology transition/re-organization, but finally return back to initial value, because these bilayers rolled up to twisted and helical ribbons with nanometric twist pitch and alkyl chains were oriented more isotropically than the case of lower ee.

III.4.2 Supramolecular organization studied by Small Angle X-ray Scattering (SAXS)

We then studied the kinetics of suparmolecular organization of the 16-2-16 gemini tartrate amphiphiles during the helicity inversion with ee changes under the hydrated state (100 mM) using Small Angle X-ray Scattering (SAXS) in order to obtain the complementary

information.

SAXS is a useful technique for the determination of microscale or nanoscale structures of several aggregate such as particles, fibers, sheets in terms of such parameters as size, shape, distribution, and surface-to-volume ratio. SAXS can also give the information of molecular packing in the bilayers of self-assembled structures, expanding to provide the information of hierarchical relationship between molecular organization and ($\sim$ Å) and supramolecular structures (nm $\sim$ mm). The average distance (d) between bilayers is roughly calculated by measurement of the scattering intensities as a radial wave vector $q = 4\pi \sin\theta / \lambda$, here 2θ is the angle between the incident X-ray beam and the detector measuring the scattered intensity, and λ is the wavelength of the X-rays which can be expressed by $\lambda = 2d \sin\theta$, therefore $d = 2\pi / q$. The scattered intensity $I(q)$ is the product of the form factor $P(q)$ and the structure factor $S(q)$. The form factor gives the shape of electron density in the aggregates of amphiphiles, and the structure factor takes into account interactions between the aggregates. One can write for the SAXS intensity: $I(q) = P(q)\, S(q)$. When the intensities are from low concentrations of molecular packing of bilayer in aggregate, the structure factor is equal to 1 and no longer disturbs the detection of the form factor $P(q)$.[22]

Previously, our group reported the detailed molecular organization of racemic or enantiomeric 16-2-16 tartrate self-assembled multi-bilayer ribbons in the hydrated state by X-ray powder diffraction and molecular modeling.[23] This study represented the first demonstration of detailed molecular organisation of a hydrated gel at atomic level. Essential features of this study include interdigitation of alkyl-chains within each bilayer and networks of ionic interaction and hydrogen bonds between cations, anions, and water molecules between bilayers, the repeat distance of which is 30.7 Å (Figure III.17 a, b). The dications in the head group of gemini amphiphiles are intrinsically achiral but adopt two mirror-image conformations at their head groups. According to the planar chiral shape of the ethylene spacer from a top view, these conformations will be noted Z and backward-Z, and both conformations are found in the ribbons.[24] In the racemate (ee = 0) structure, the infinite alternation of domains between bilayers having D(backward-Z)D(backward-Z) and LZLZ arrays of head groups and

"Z"   or   "Σ"

tartrate ion is possible without chirality frustration which leads to multi-bilayer ribbons (Figure III.19 b). In contrast, in the case of a pure enantiomer, only two bilayers can stack, separated by a domain with a LZLZ array of head groups and tartrate ions.

Figure III.19 (a) Schematic illustrations of molecular packing, (b) the best fitness of organization from racemic 16-2-16 DL-tartrate and (c) the contact layer between two consecutive gemini bilayers in the racemate structure (left) and pure enantiomeric structure (right). [24]

Figure III.20 shows the SAXS spectra of *in situ* supramolecular kinetics from 16-2-16 tartrate corresponding to helicity inversion with ee changes by counter-anion exchange. For a pure enantiomer (ee = 1), we observed broad peak at $q \sim 0.185$ Å^{-1}. When ee = "0", the peak became much narrower (Bragg peak), i.e., $q = 0.17$-0.20 Å^{-1} for 30 min, , then this peak increased and became sharper with time, suggesting that structure factor appeared strongly as the enantiomeric double-bilayer tubules transformed to multi-bilayer racemic ribbons (Figure III.20 a). Finally, the repeat distance of molecular packing was 33.0 Å.

When ee = "-0.33", the broad band attributed to the form factor was observed until 1 h corresponding to double-bilayer helical structures. After around 1.5 h the peak attributed to the structure factor was observed around $q = 0.17$-0.21 Å^{-1}, and then this peak became stronger and narrower for 1 day corresponding multi-bilayer twisted ribbon (Figure III.20 b). Finally, the repeat distance of molecular packing was 33.4 Å.

For the case of ee = -0.90, no peaks were observed until 1 h. This is probably because

just after mixing, assembled chiral structures collapsed to non-defined structure accompanying that the gels became solution. When the amphiphiles were re-assembled to chiral fibers gel network after 1.5 h, we observed broad peak attributed to the form factor around $q = 0.13$-0.24 Å^{-1}, and this peak kept the shape and intensity with time (Figure III.20 c).
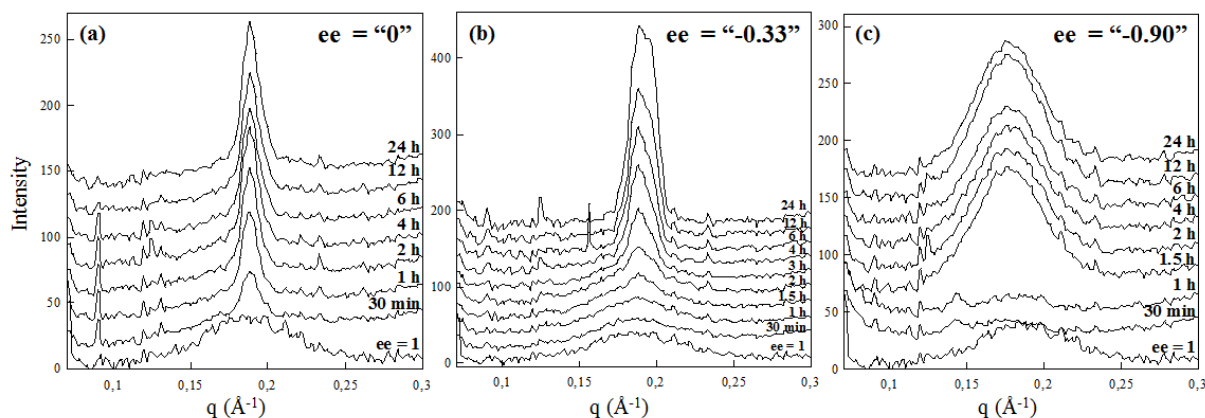
Figure III.20 SAXS scattering of *in situ* supramolecular kinetics from 16-2-16 tartrate amphiphiles with different ee changes (a) from 1 to 0, (b) 1 to -0.33, and (d) 1 to -0.90 by addition of opposite chiral D-tartaric acid solution through the 16-2-16 L-tartrate gel.
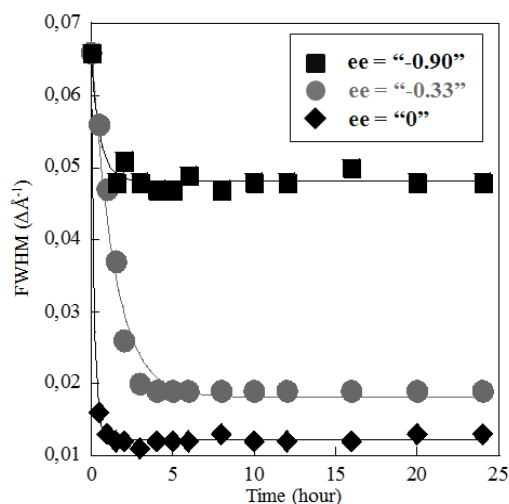
Figure III.21 The quantified plot of peak sharpness from SAXS signals by full width at half maximum.

Figure III.21 shows the plot of peak sharpness, i.e. full width at half maximum (FWHM), of SAXS signals as a function of time. The FWHM value decreased much more with the smaller value of ee, which were strongly depending on the molecular packing of final morphologies. The finaly FWHM values were reached after 2 h for ee = 0, 4 h for ee = -0.33,

and 1.5 h for ee = -0.90.

III.5 Summary

      In situ helicity inversion and morphology transition at constant temperature can be induced simply by the addition of opposite chiral D-tartaric acid solution to tubular gel network of 16-2-16 L-tartrate. These processes with different ee involve different steps, at the mesoscopic level (morphology transformation from *P* to *M* chiral ribbon), and molecular level as summarized in Table III.1.

Table III.1 Summary of the kinetics of morphology transitions with different final ee values at different levels in molecular, supramolecular organization, and at the mesoscopic level.

ee	Molecular kinetics (ATR and SAXS)			Mesoscopic aspect (CD and TEM)		
	Bilayer organization (ATR)	Bilayer stacking kinetics (SAXS)	Repeat distance of molecular pcking (SAXS)	Helicity inversion	Reach final morphology	Final morphology and twist pitch
"0"	30 min	2 h	33.0 Å	-	1 day	*P* twist ribbons 1500 nm
"-0.33"	6 h	4 h	33.4 Å	1 h	1 day	*M* twist ribbons 1150 nm
"-0.60"	-	-	-	0 min	1 week	*M* twist ribbons 420 nm
"-0.90"	-	-	-	1 h (re-assembly)	1 week	*M* tubules 40 nm

      The kinetics of the variation in molecular orientation of alkyl chains depend on the final ee. The lower ee shows faster kinetics of bilayer orientation and stacking in molecular organization. In case of the ee = "0" and "-0.33", ATR signals showed that the bilayers orientation changed gradually from parallel to planner direction upon addition of D-tartaric acid. This phenomenon is cursed by *in situ* morphology transition: when helical ribbons were transformed to flat ribbon or twisted ribbon with long twist pitch (> 1000 nm), their alkyl chains were oriented to perpendicular to the X-Y plane, resulting the bilayers were well attached on the ATR window. On the other hand, ATR signals of higher ee ("-0.60" and "-0.90") showed the

bilayers were oriented more isotropically than lower ee, which corresponded that these bilayers rolled up to twisted and helical ribbons with nanometric twist pitch.

From the SAXS results, the case of lower ee showed clear process of periodic stacking formation, whereas the case of ee = "-0.90", periodic stacking formation were not observed. Indeed, the case of ee = "-0.90", once SAXS signals were disappeared which resulted from the disappearance of chiral bilayers upon addition of a large excess of D-tartaric acid, and then, broad peak attributed to the form factor were observed when the amphiphiles self-assembled chiral structure. On the other hand, for other ees, bilayers existed all the time and they were spontaneously stacked with *in situ* transition from helical ribbons to twisted and/or flat ribbons. The kinetics of bilayer stacking was faster for higher opposite ee (e.g. "-0.9").

The different kinetics existed in this system of *in situ* helix-helix morphology transition, that is the bilayer stacking and helicity inversion.

In the mesoscopic aspect, the helicity inversion occurs much faster with the higher ee, indicating that counter-anion exchange occurs much more rapidly with increasing the additional amounts of opposite chiral acid solution. The faster helicity inversion promoted much slower increase of twist pitch, which also produced the different final morphologies. Actually, during nanometric twisted ribbons (pitch < 1000 nm), weak SAX signals of bilayer stacking were observed.

III.6 *In situ* Counter-Anion exchange in Gel Network at equilibrium: effect on the Morphology of Aggregates

We have then investigated the cases for which the gel network of 16-2-16 tartrate was in contact with residual D and L-tartaric acid solution after counter-anion exchange. The solution of D-tartaric acid was added to the 10 mM 16-2-16 L-tartrate gel such that their final quantities were 1, 2, 4 and 20 equivalent with respect to L tartrate in the gel. In this system, the

excess of D- and L-tartaric acid solution were kept in samples, and then they were washed away only just before the TEM and CD measurement at different times (Figure III.22).
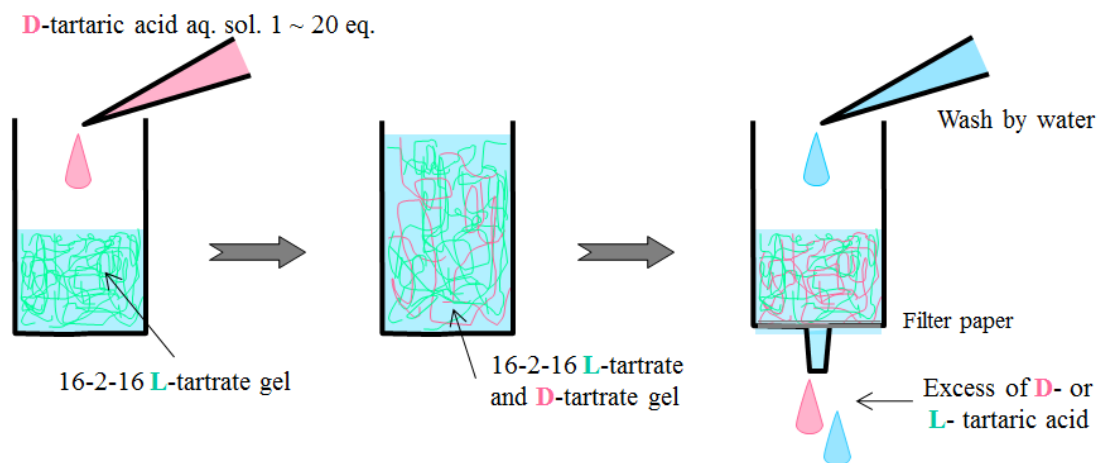
Figure III.22 Schematic illustration of gel preparation method.

III.6.1 Morphologies transitions followed by TEM observation

ee = 0

Figure III.18 shows the morphology transition observed by TEM when excess of tartaric acid solution was added to the gel such that the final ee was 0. The unfolding and pitch elongation of *P*-tubular structures also occurred just after addition of D-tartaric acid solution, after an hour, we also observed inversed *M*-helical ribbons (Figure III.23 a, b). These *P* and *M* helical ribbons were then transformed to twist ribbons with long pitches (Figure III.23 c-e). After 4 hours, only M twist ribbons were observed. The pitches of these ribbons continued to increase and at one week, mostly non-chiral flat ribbons were observed (Figure III.23 f).
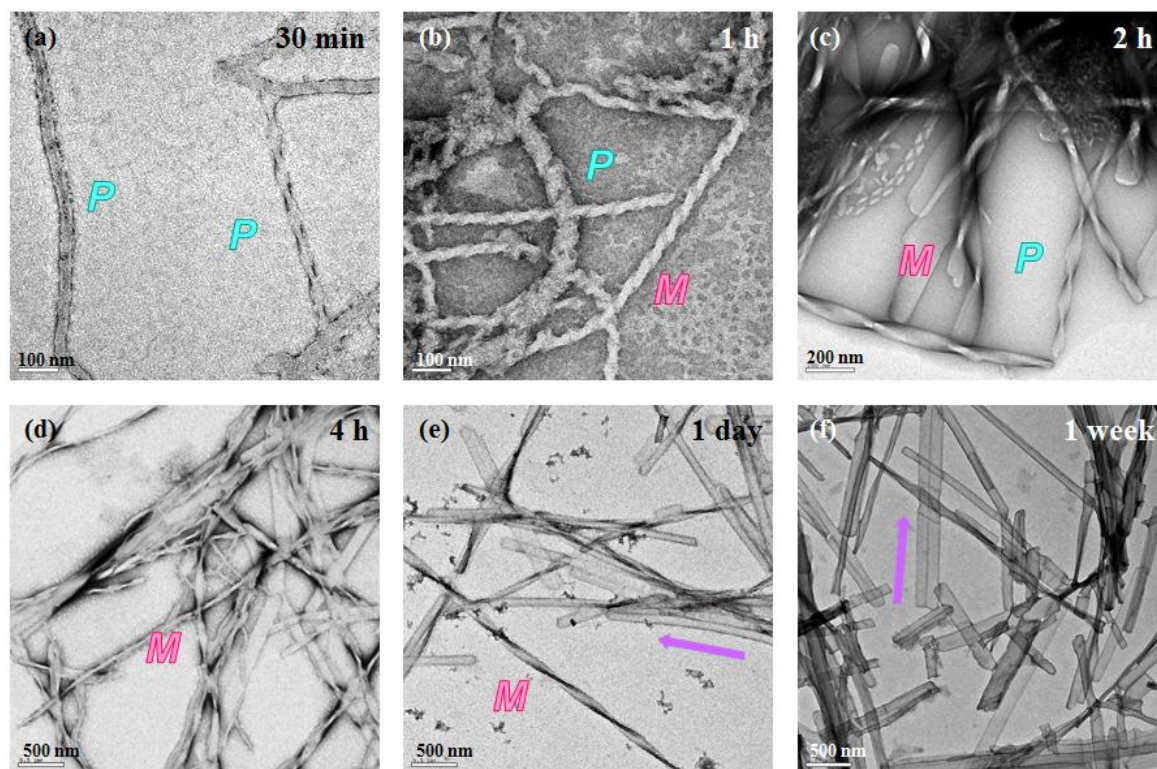
Figure III.23 TEM images of helicity inversion and pitch elongation steps of tubular network from 16-2-16 tartrate amphiphiles by ee changes from 1 to 0 in the case of 1 equivalent opposite chiral D-tartaric acid added and stayed in the gel network.

ee = -0.33

Immediately after the addition of D-tartaric acid, tubules transformed to twist ribbons. After 30 minutes, we observed the mixture of *P*- and *M*-twisted ribbons (Figure III.24 a). After an hour, only M-twisted ribbons were observed, the twist pitches increased continuously from nanometric to micrometric scale around 2 μm with time (Figure III.24 b-d).
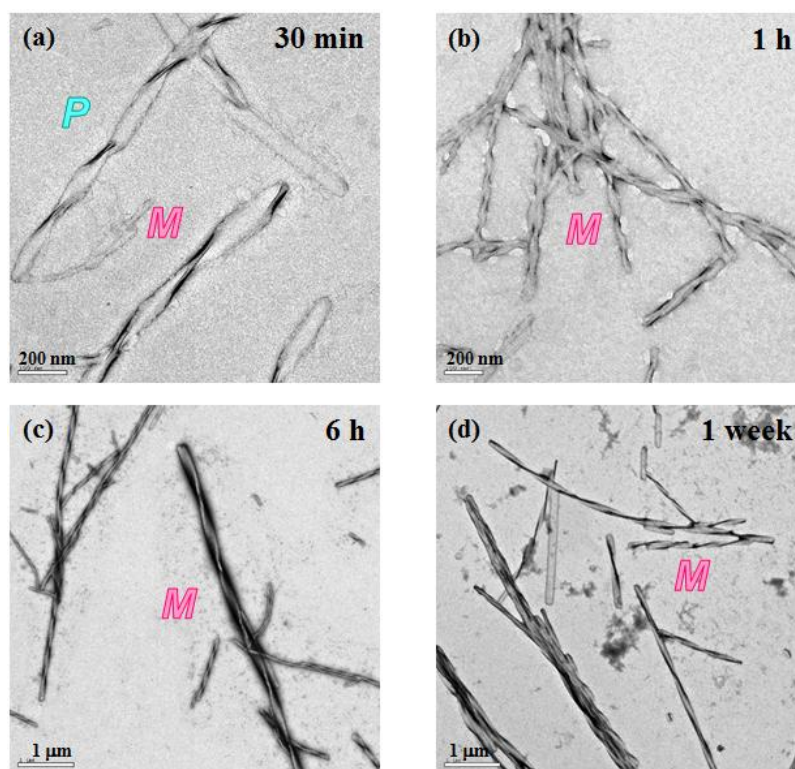
Figure III.24 TEM images of helicity inversion and pitch elongation steps of tubular network from 16-2-16 tartrate amphiphiles by ee changes from 1 to -0.33 in the case of 2 equivalents opposite chiral D-tartaric acid added and stayed in the gel network.

ee = -0.60

In this case, we observed only *M* twisted ribbons just after the addition of D-tartaric acid solution. Again, the twist pitch increased with time, but this increase occurred more slowly than the case of ee = -0.33 (Figure III.25 a-c). After 1 day, *M*-twisted ribbon were observed (Figure III.23 d), but surprisingly, these fibers were aggregated in 2 days, and then only flat sheet-like structures were obtained (Figure III.25 e, f).
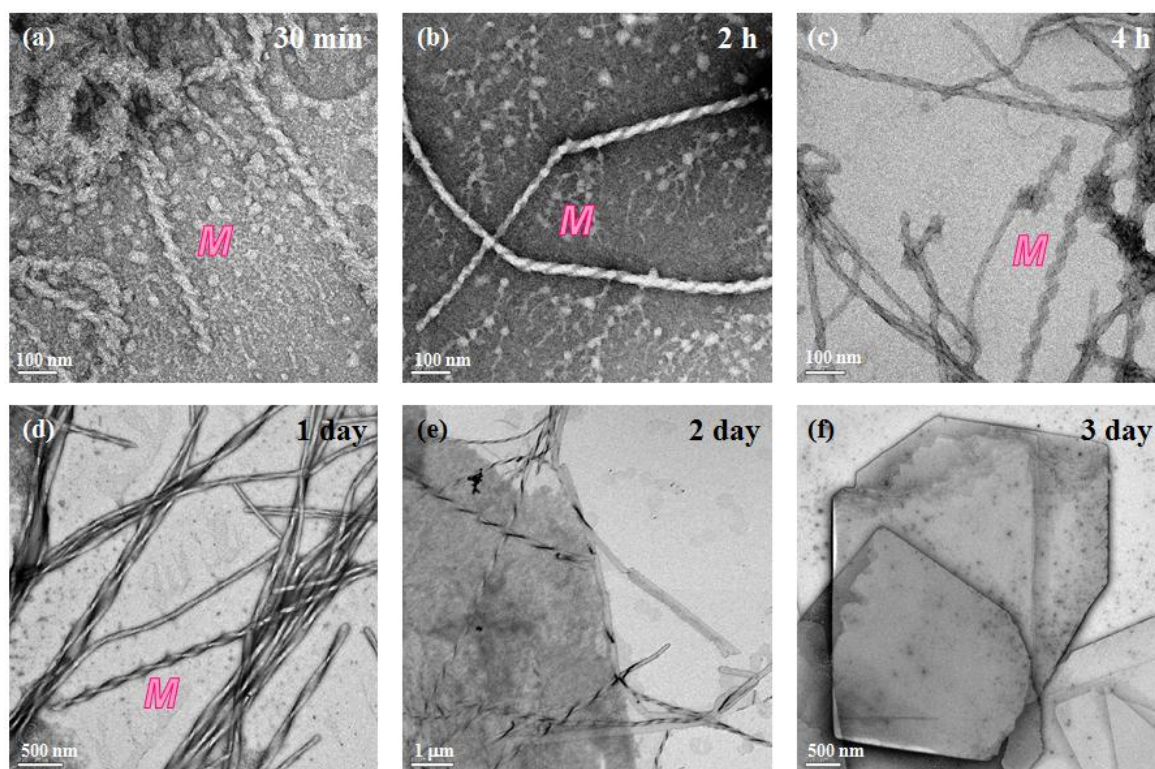
Figure III.25 TEM images of helicity inversion and pitch elongation steps of tubular network from 16-2-16 tartrate amphiphiles by ee changes from 1 to -0.60 in the case of 4 equivalents opposite chiral D-tartaric acid added and stayed in the gel network.

ee = -0.90

For the case of ee = -0.90, chiral fibers re-assembled more quickly than the non-equilibrium (filteration) case, M-twist ribbons were observed for already at 30 min after the addition of D-tartaric acid (Figure III.26 a, b). After 6 hours, the morphology of the chiral ribbons reached final states (Figure III.26 b-d). Their final twist pitches were around 50 nm.
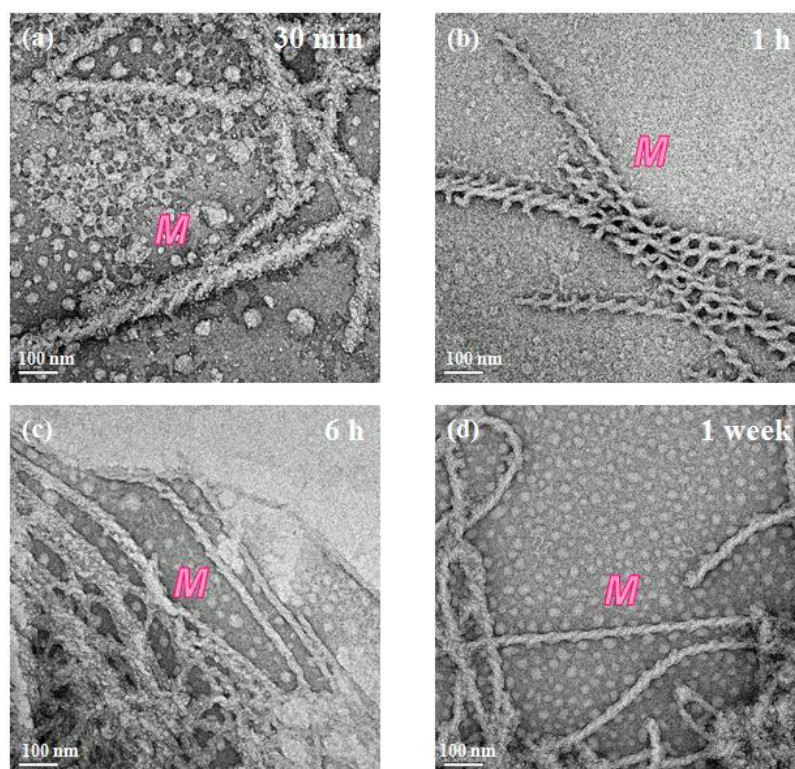
Figure III.26 TEM images of helicity inversion steps of tubular network from 16-2-16 tartrate amphiphiles by ee changes from 1 to -0.90 in the case of 20 equivalents opposite chiral D-tartaric acid added and stayed in the gel network.

III.6.2 Pitch variation

Figure III.27 shows the plot of variations of twist pitch elongation and helicity inversion obtained with this system. Comparing to the previous system, the helicity inversion occurred more quickly but final pitch lengths were simillar. This indicated the counterion exchange occurred very quickly and even with the "filteration method" the ratios of the two enantiomers were very close to those obtained with the "equilibrium" method. The case of ee = -0.60 was a particular case, which showed transformation of ribbons to sheet-like plate structure after several days. Oda's group has recently shown that the expression of chirality at mesoscopic level is intimately related to the crystallinity of the system. A certain amount of flexibility/disorganisation is needed for the chirality expression at tens or hundreds of nanometer level.[25] If the organisation of the molecules is too cristalline, then the expression of chirality is prohibited. As the gel formation is an out of equilibrium phenomenon, It may rearch

the precipitates with platelets directly. Each final pitches of fibers were > 3300 nm ± 2200 nm for ee = 0, 1700 nm ± 900 nm for ee = -0.33, and 58 nm ± 5 nm for ee = -0.90.
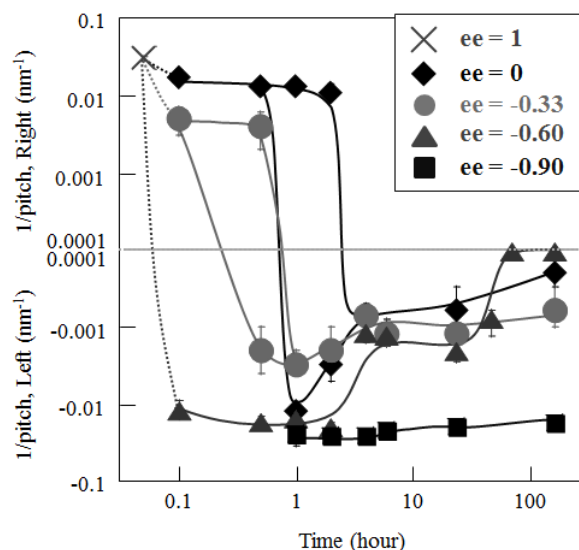
Figure III.27 The aging variation of twist pitches inversion with different value of ee changes.

III.6.3 The chirality transfer followed by CD spectra

The chirality transfer was also followed by CD measurements.

For ee = 0 and -0.33, the CD signals indicated a similar pattern as filtered system (Figure III.28 a, b) at the beginning, the sign of CD bands from cotton coupling at 201 and 219 nm decreased with time. In the case of ee = -0.33 system (both at equilibrium and non-equilibrium), the shape of spectrum changed after sometime, and a positive signal appeared in the range of 190-220 nm due to the scattering by the large ribbons. In the filtered (non-equilibrium) system, the residual chirality for ee = "0" system was expressed as large *P* twist ribbons appeared and a small negative signal was observed at 190-220 nm, whereas in the equilibrium case with ee = 0, a small quantity of M-twist ribbons were observed along with the small positive signal at 190-220 nm.

In the case of ee = -0.60 and -0.90 some differences were observed with the filtered systems. For the case of ee = -0.60, the cotton coupling of CD signs decreased with time as it was observed with filtered case above, but after about two days, a strong positive signal

appeared in 190-220 nm range when the chiral fibers were transformed from nanometric flexible ribbons to micrometric rigid plate (Figure III.28 c). When ee = -0.90, the CD sign continuously decreased until about a week.
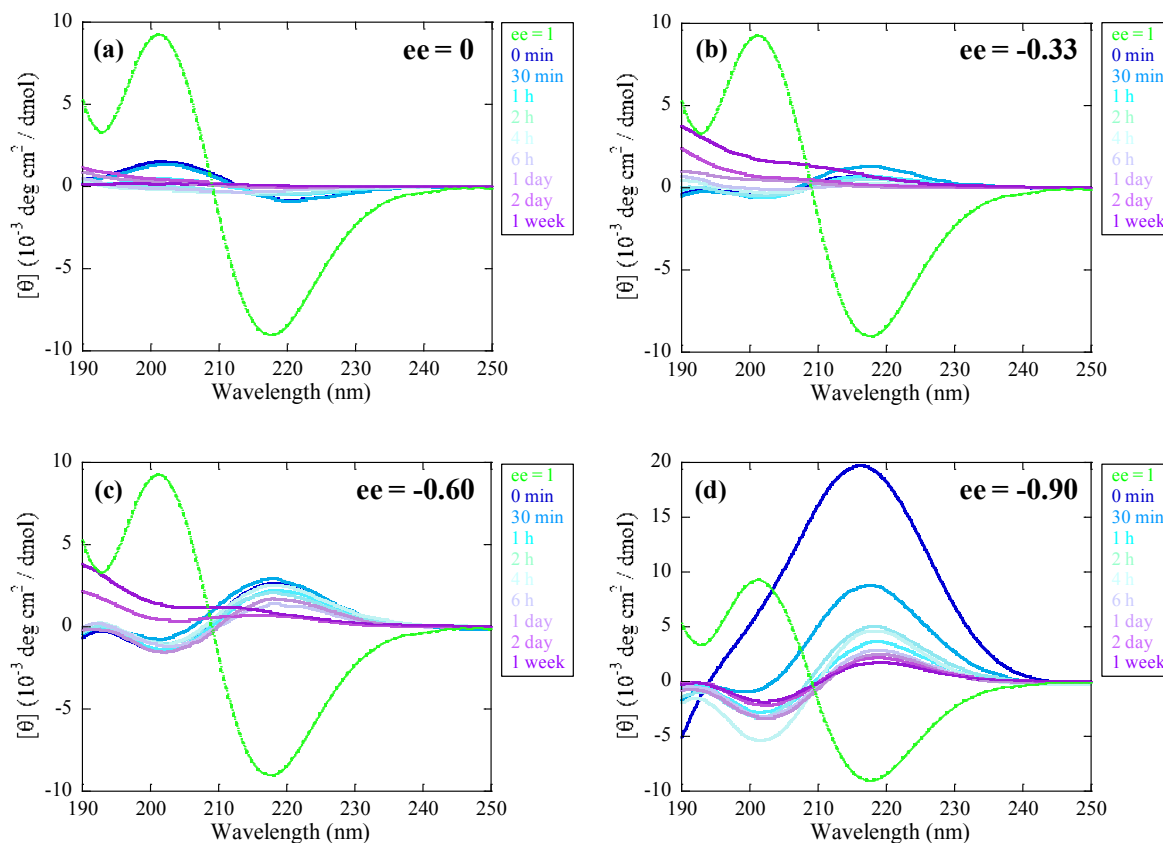
Figure III.28 CD spectra of 16-2-16 tartrate amphiphiles with different ee changes (a) from 1 to 0, (b) 1 to -0.33, (c) 1 to -0.60, and (d) 1 to -0.90 by addition of opposite chiral D-tartaric acid solution in the 16-2-16 L-tartrate gel, and excess of counter-anion stayed in suspension just before CD measurement.

The variations of CD intensities at $\lambda = 200$ nm with time for different ees are shown in Figure III.29.
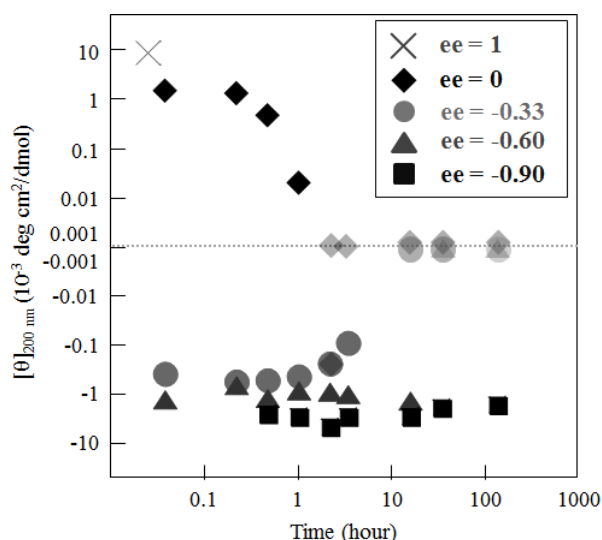
Figure III.29 Aging value of CD intensities of $[\theta]_{200nm}$ with different ee.

The results of CD measurements in this system also show different behavior from the filtered systems. The intensities of cotton coupling derived from flexible helical structures are slightly smaller than the previous systems. On the other hand, the intensities at range of 190-220 nm are stronger. However, it is not yet clear why these different phenomena occur when the gels are rinsed for different time periods after counter-anion exchange.

III.7 Conclusion

In situ right (*P*) to left-handed (*M*) helicity transition in supramolecular aggregates was observed by counter-anion exchange from L-tartrate to D-tartrate upon introducing the opposite chiral acid filtered through the pure enantiomeric fiber network at constant temperature.

The final morphologies were strongly depending on the value of ee changes, nanometric *P* tubules (obtained with ee = 1) transformed to micrometric *P* twisted ribbons containing flat ribbons (from ee = 1 to "0"), micrometric *M* twisted ribbons (to ee = "-0.33"), nanometric *M* twisted ribbons (to ee = "-0.60"), and nanometric *M* tubules (to ee = "-0.90").

There are different processes as to how the helicity inversion occurred: from ee = "0" to "-0.60", the tubular structures were unwound to helical ribbons at first, which transformed to twisted ribbons, and then formed flat ribbons (for ee = "0") then continuously ribbons with opposite helicity were formed. On the other hand, in the case of ee = "-0.90", once the fiber network disappeared first, then re-assembled to form tubules with opposite helicity. In addition, the speeds of helicity and morphology transitions showed difference of depending on the final ee.

The ATR and SAXS measurement showed detailed molecular orientation and packing condition. The ATR signals showed that the bilayers oriented quickly parallel to planner direction upon addition of D tartaric acid, for ee = "0" and "-0.33", they formed flat ribbons or ribbons with long twist pitch, therefore, they remained mainly oriented parallel to the surface whereas for ee = "0.60" and "-0.90", these bilayers rolled up to re-form twisted and helical ribbons. The SAXS signals showed that during the chirality decrease and inversion observed with ee = "0", "-0.33", "-0.60", bilayer structures remained, (as concluded by the form factor) whereas for the system with ee = "-0.90", these bilayers disappeared right after the addition of D tartaric acid, then re-formed after about an hour. The kinetics of bilayer stacking is quicker for ee = "0" systems.

Whilst the twist pitches after chirality inversion were similar for the non equilibrium (filtered) and equilibrium cases, the final morphologies show differences for ee = -0.66 and -0.9. These *in situ* morphology transformation is clearly a kinetically controlled phenomenon.

This system **shows** the first direct visualization of *in situ* chirality inversion of chiral supramolecular structures at mesoscopic level (20 nm - microns) basesd on the direct counterion exchange in solution of the supramolecular (and not macromolecular) chiral fibrous structures.

III.8 Experimental session

Synthesis

The weighing is measured with a balance of precision Metler-Toledo of an accuracy of 0.01 mg under the air-conditioned part at 22 ˚C. Ultrapure water (18.2 MΩ cm) was obtained from Purelab ultra ELGA system.

Synthesis of 16-2-16 Br$_2$

The synthesis of 16-2-16 amphiphile with bromide counterion, which is developed by R. Zana *et al.*, had been proposed via the alkylation of alkanedil-α,ω-bis (dimethylamine) by alkyl bromides.[26] This synthesis was done by nucleophilic substitution of tetramethylethylenediamine (TMEDA) with a 1-bromo hexadecane (scheme 2-1).[27]

The reaction was carried out in the acetonitrile at 80 ˚C under stirring for 48 hours, with refluxing under inert atmosphere in an assembly with cooling condenser. In order to obtain the surface-active dialkylated compound without monoalkyl impurity, excess of 1-bromo hexadecan was introduced: the stoichiometry of the 1-bromo hexadecan starting material must be three times of TMEDA (M = 116.21 g.mol^{-1}, d = 0.77). In the end of the reaction, the product was filtered to eliminate the excess of 1-bromo hexadecane, then recrystallized several times by dissolution with a minimum volume of chloroform/methanol (9/1, v/v) mixture solvent and precipitation with acetone. The successive recrystallization was carried out until obtaining a white product which will be washed with acetone, then dried with the high vacuum. The NMR analysis confirmed that the peaks of the gemini (16-2-16) product, without remaining any more 1-bromo hexadecane intermediate.

Typical example of 16-2-16 Br$_2$ *^{1}H NMR (400 MHz, CDCl$_3$, 25 ˚C, δ ppm)*: 4.81 (4H, s), 3.72 (4H, s), 3.51 (12H, s), 1.81 (4H, m), 1.25 (m), 0.88 (6H, t, ^{3}J=6.59 Hz) *^{13}C NMR (100 MHz, CDCl$_3$, 25 ˚C, δ ppm)*: 65.98, 56.79, 51.14, 31.98, 29.79, 29.75, 29.66, 29.62, 28.44, 29.42, 26.36, 23.13, 22.75, 14.19
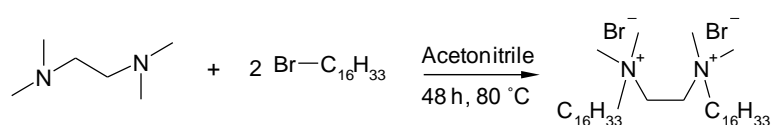
Scheme 2.1 Synthesis of gemini 16-2-16 bromide.[28]

Synthesis of 16-2-16 L-tartrate

16-2-16 L-tartrate amphiphiles was obtained by ion exchange from complex of bromide counter anion after *in situ* formation of silver salt with tartrate in methanol solution (scheme 2-2).[11,12,16] The cationic surfactant with bromide counter-anion as starting compound was synthesized from bromoalkane with tetramethylethylenediamine.

The L-tartaric acid was mixed with silver carbonate (1 equiv.) to prepare silver L-tartrate in methanol and the mixture was stirred for 1 h at 25 °C. 16-2-16 bromide was added to the solution of silver L-tartrate and stirred for 30 min at 40 °C and filtered on Celite to obtain a colorless solution. After evaporation of methanol, the product was dissolved in a mixture of chloroform/methanol (9/1, v/v), made precipitate with acetone, filtered, and dried.

Typical example of 16-2-16 L-tartrate *^{1}H NMR (400 MHz, CDCl$_3$, 25 °C, δ ppm)*: 4.23 (2H, s), 3.92 (4H, dm), 3.30 (4H, m), 3.10 (12H, d) 1.64 (4H, m), 1.22 (50H, m), 0.81 (6H, t) *^{13}C NMR (100 MHz, CDCl$_3$, 25 °C, δ ppm)*: 178.01, 66.10, 51.30, 32.47, 30.70, 30.53, 30.26, 30.20, 30.02, 29.90, 26.75, 23.23, 14.60
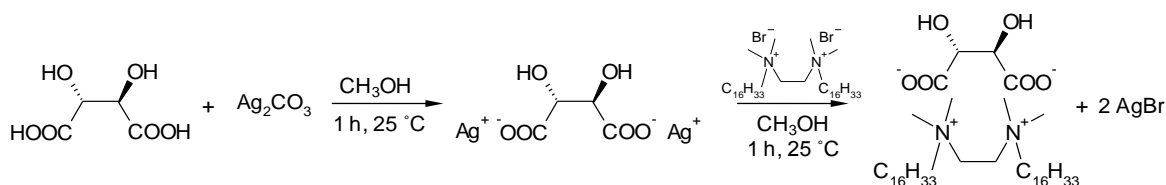
Scheme 2.1 Synthesis of gemini 16-2-16 tartrate.

Transmission electron microscope

A small drop of 16-2-16 tartrate samples in water was deposited on 400-mesh carbon-coated copper grid. After a few minutes, the excess liquid was blotted with filter paper. These air-dried specimens were stained by applying a small drop of a 0.2 wt% uranylacetate aqueous solution and removed the excess solution with a filter paper. The samples were then metallized by platinum (at an angle 10 °) using vacuum chamber (Balzers). The replication was done for 20 sec. TEM observation were performed using a Philips EM 120 electron microscope operating at 120 kV and the images were collected by 2k × 2k Gatan ssCCD camera.

Circular dichroism measurement

The circular dichroism measurement was performed on a JASCO J-815 CD spectrometer with data pitch of 0.1 nm, scanning speed of 100 nm/min, and quartz cuvette with optical path length of 0.1 mm for nucleoamphiphiles and 1 mm for 16-2-16 tartrate amphipihles were used. The spectra were measured for 10 mM gels.

Attenuated Total Reflection Spectroscopy measurement

The ATR spectra were performed on a NICOLET 6700 FT-IR. The samples were prepared in Millipore water, at a final concentration of 10 mM. After washing the excess of D and L-tartrate, the liquid of gels were immediately blotted with filter paper on the ATR plate. The spectra were recorded with parallel (p) and perpendicular (s) polarization of the incident light with respect to the ATR plate. Generally, the spectra were registered during 800 scans at resolution of 8 cm^{-1} and a two-level zero filling. All the orientation information is then contained in the dichroic ratio $R_{ATR} = A_p/A_s$, where A represents the absorbance of the considered band for the p or s polarization of the incident light, respectively.

Small-Angle X-ray Scattering

The experiments were performed on a Rigaku Nanoviewer (Micro-souce generator, MicroMax 007, 800 W rotating anode coupled with a Confocal Maxflux Mirror). The X-ray diffraction patterns were collected on an intensified CCD (Chip Charge-coupled Device) with a sample to detector distance of 422 mm, at exposure times of 30-45 min. The samples were prepared in Millipore water, at a concentration of 100 mM for 16-2-16 L-tartrate and D-tartaric acid solution were filtered through the gel network such a way that final ee's are 0, -0.33, -0.60, and -0.90. These samples were washed by water and removed the water immediately. Gels were put between two Mylar windows with spacer of 1 mm. The temperature of the samples was regulated at 20 ˚C unless indicated differently.

References

[1] (a) D.A. Frankel, D. F. O'Brien, *J. Am. Chem. Soc.*, **1994**, *116*, 10057-10069. (b) E. Yashima, T. Matsushima, Y. Okamoto, *J. Am. Chem. Soc.*, **1997**, *119*, 6345-6359. (c) A. E. Rowan, R. J. M. Nolte, *Angew. Chem.*, **1998**, *110*, 65-71; *Angew. Chem.*, **1998**, *78*, 63-68. (d) J. J. L. M. Cornelissen, M. Fischer, N. A. J. M. Sommerdijk, R. J. M. Nolte, *Science*, **1998**, *280*, 1427-1430. (e) J. H. K. K. Hirschberg, L. Brunsveld, A. Ramzi, J. A. J. M. Vekemans, R. P. Sijbesma, E. W. Meijer, *Nature*, **2000**, *407*, 167-170. (f) M. Fujiki, *Macromol. Rapid Commun.*, **2001**, *22*, 539-563.

[2] (a) J. P. Hill, W. Jin, A. Kosaka, K. Fukushima, H. Ichihara, T. Shimomura, K. Ito, K. Hashizume, N. IshIII, T. Aida, *Science*, **2004**, *304*, 1481-1483. (b) F. J. M. Hoeben, P. Jonkheijm, E. W. Meijer, A. P. H. J. Schenning, *Chem.Rev.*, **2005**, *105*, 1491-1546. (c) W. Jin, T. Fukushima, M. Niki, A. Kosaka, N. IshIII, T. Aida, *Proc. Natl. Acad. Sci. USA*, **2005**, *102*, 10801-10806. (d) A. Ajayaghosh, R. Varghese, S. J. George, C. Vijayakumar, *Angew. Chem.*, **2006**, *118*, 1159-1162.; *Angew. Chem. Int. Ed.*, **2006**, *45*, 1141-1144. (e) Y. Yan, K. Deng, Z. Yu, Z. Wei, *Angew. Chem.*, **2009**, *121*, 2037-2040.

[3] E. Yashima, *Analytical Sciences*, **2002**, *18*, 3-6.

[4] V. N. Malashkevidh, R.A. Kammerer, V. P. Efimov, T. Schulthess, J. Engel, *Science*, **1996**, *274*, 761-765.

[5] J. J. L. M. Cornelissen, M. Fischer, N. A. J. M. Sommerdijk, R. J. M. Nolte, *Science*, **1998**, *280*, 1427-1430.

[6] (a) G. Maxein, R. Zentel, *Macromolecules*, **1995**, *28*, 8438-8440. (b) Q. Li, L. Green, N. Venkataraman, I. Shiyanovskaya, A. Khan, A. Urbas, J. W. Doane, *J. Am. Chem. Soc.*, **2007**, *129*, 12908-12909.

[7] (a) B. M. W. Langeveld-Voss, M. P. T. Christiaans, R. A. J. Janssen, E. W. Meijer, *Macromolecules*, **1998**, *31*, 6702-6704. (b) H. Goto, Y. Okamoato, E. Yashima, *Macromolecules*, **2002**, *35*, 4590-4601. (c) W. Peng, M. Motonaga, J. R. Koe, *J. Am. Chem. Soc.,* **2004**, *126*¸ 13822-13826. (d) S. Sakurai, K. Okoshi, J. Kumaki, E. Yashima, *J. Am. Chem. Soc.,* **2006**, *128*¸ 5650-5651. (e) R. S. Johnson, T. Yamazaki, A. Kovalenko, H. Fenniri, *J. Am. Chem. Soc.,* **2007**, *129*¸ 5735-5743.

[8] (a) J. R. Koe, M. Fujiki, M. Motonaga, H. Nakashima, *Chem. Comm.*, **2000**, 389-390. (b) M. Fujiki, *J. Am. Chem. Soc.,* **2000**, *122*¸ 3336-3343. (c) T. Hasegawa, K. Morino, Y. Tanaka, H. Katagiri, Y. Furusho, E. Yashima, *Macromolecules*, **2006,** *39,* 482-488. (d) K. Nagai, K. Maeda, Y. Takeyama, T. Sato, E. Yashima, *Chem Aian J.*, **2007**, *129*, 12908-12909. (e) N. Delsuc, T. Kawanami, J. Lefeuvre, A. Shundo, H. Ihara, M. Takafuji, I. Huc, *ChemPhysChem*, **2008**, *9*, 1882-1890.

[9] Y. Li, H. Wang, L. Wang, F. Zhou, Y. Chen, B. Li, Y. Yang, *Nanotechnology*, **2011**, *22*, 135605.

[10] (a) E. Yashima, Y. Maeda, Y. Okamoto, *J. Am. Chem. Soc.,* **1998**, *120*¸ 8895-8896. (b) K. Morino, K. Maeda, E. Yashima, *Macromolecules*, **2003**, *36*, 1480-1486. (c) E. Yashima, K. Maeda, Y. Furusho, *Acc. Chem. Res.*, **2008**, *41*, 1166-1180.

[11] R. Oda, I. Huc, S. J. Candau, *Angew. Chem. Int. Ed.*, **1998**, *37*, 2689-2691.

[12] R. Oda, I. Huc, M. Schmuts, S. J. Candau, F. C. Mackintosh, *Nature*, **1999**, *399*, 566-569.

[13] R. Oda, *Molecular Gels* Kluwer Academic Publishers, Dordrecht, The Netherlands **2005**.

[14] Damien Berthier, Chiralité, Amphiphiles et Polymères., *Thesis of Doctrante, Bordeaux 1 Unversity*, **2002.**

[15] Aurélie Brizard, Confinement de Contre Ions Tartrate et Oligo-Peptidiques sur des Membranes Cationiques., *Thesis of Doctrante, Bordeaux 1 Unversity*, **2005**.

[16] Carole Aimé, Auto-Assemblages Chiraxu d'Asmphiphiles Cationique., *Thesis of Doctrante, Bordeaux 1 Unversity*, **2007.**

[17] A. Brizard, C. Aimé, T. Labrot, I. Huc, D. Berthier, F. Artzner, B. Desbat, R. Oda, *J. Am. Chem. Soc.,* **2007**, *129*¸ 3754-3762.

[18] Carole Aimé, Auto-Assemblages Chiraxu d'Asmphiphiles Cationique., *Thesis of Doctrante, Bordeaux 1 Unversity*, **2007.**

[19] D. Berthier, T. Buffeteau, J. M. Léger, R. Oda, I. Huc, *J. Am. Chem. Soc.*, **2002**, *124*, 13486-13494.

[20] A. Brizard, D. Berthier, C. Aimé, T. Buffeteau, D. Cavagnat, L. Ducasse, I. Huc, R. Oda, *Chiraliy*, **2009**, *21*, 153-162.

[21] (a) N. J. Everall, A. Bibby, *Appl. Spectrosc*, **1997**, *51*, 1083-1091. (b) I. Cornut, B. Desbat, J. M. Turlet, J. Dufourcq, *Biophysical Journal*, **1996**, *70*, 305-312. (c) F. Picard, T. Buffeteau, B. Desbat, M. Auger, M. Pézolet, *Biophysical Journal*, **1999**, *76*, 539-551. (d) T. Buffeteau, E. Le Calvez, B. Desbat, I. Pelletier, M. Pézolet, *J. Phys. Chem. B*, **2001**, *105*, 1464-1471. (e) E. Hutter, K. A. Assiongbon, J. H. Fendler, D. Roy, *J. Phys. Chem. B*, **2003**, *107*, 7812-7819.

[22] (a) A. Guinier, G. Fournet, *Small Angle Scattering of X-rays*, Wiley, New York, **1995**. (b) C. Petit, A. Taleb, M. P. Pileni, *J. Phys. Chem. B*, **1999**, *103*, 1805-1810.

[23] R. Oda, F. Artzner, M. Laguere, I. Huc, *J. Am. Chem. Soc.*, **2008**, *130*, 14705-14712.

[24] A. Brizaed, C. Aimé, T. Labrot, I. Huc, D. Berthier, F. Artzner, B. Desbat, R. Oda, *J. Am. Chem. Soc.*, **2002**, *129*, 3754-3762.

[25] R. Kiagus-Armad, A. Brizard, C. Tang, R. Blatchly, B. Desbat, R. Oda, *Chem. Eur. J.*, **2011**, *17*, 9999-10009.

[26] R. Zana, M. Benrraou, R. Rueff, *Langmuir*, **1991**, *7*, 1072-1075.

[27] R.Oda, I. Huc, S. J. Candau, *Chem. Commun.*, **1997**, 2105-2016.

[28] J. Israelachvili, *Intermolecular & Surface Forces*, 2nd.; Academic Press : London, **1992**.

Chapter IV

Mineralization through bio-inspired materials:

Bibliographic study

IV.1 Introduction

In nature, there are numerous examples of exceptionally strong building materials formed by organic-inorganic assemblies. This organization widely exists in the skeletons of animals or plants, and plays a key role in expressing the biological functions. These materials often show the complex hierarchical organization from the nanometric to macroscopic scales.[1,2] For example, the deepwater sponge *Pheronema raphanus* gives on the macro-, micro- and nanoscle of the hierarchical organization composited with organic matrix and silicon oxide (Figure IV.1).
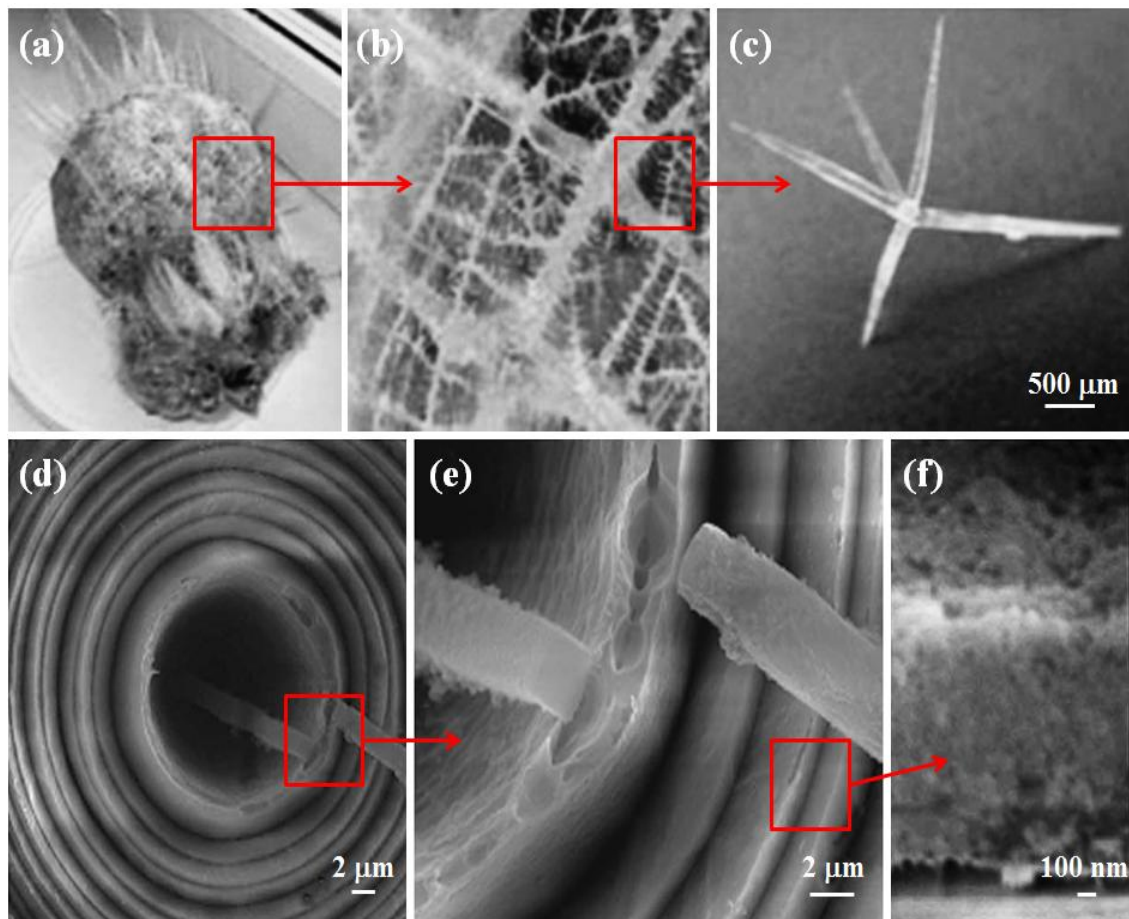
Figure IV.1 Example of hierarchy of organization. Deepwater sponge *Pheronema raphanus* gives different aspect. Macroscale: (a) common view of sponge, (b) fragment of surface sponge body, and (c) pentactinal spicule. Microscale: (d) ringlike structure of the transversal cut of spicule after treatment to remove the organic matrices and (e) local area. Nanoscale: (f) Silicon oxide nanoparticles.[3]

These types of structures are well known examples of biomineralization formed by organic template. However, the influence of the template morphologies on the mechanism of structure formation is not well understood.

In recent years, much effort has been directed towards developing organic/inorganic hybrid materials to mimic and understand the complex structure-property relationship of their natural counterparts. The biomimetic mineralization from synthesized organic template has a possibility to engineer complex architectures starting from nanometric regime ("bottom-up" fabrication). One such method is inspired from the self-assembled organic systems, which can form various structures, which can be used as templates for inorganic nanomaterials formation. Particularly, there have been many reports of silica based materials with controllable shapes and porosity, generated from organic templates.

In this chapter, we will first discuss about mineralization observed in nature followed by representative examples of biomimetic mineralizations to show the present advances in the design of functional nanomaterials. In the context of our work on silica based mineralization studies, we shall put special emphasis on the literature on sol-gel silicification onto self-assembled organic templates, which can produce tunable shapes.

IV.2 Study of biomineralization

Biominerals are composites of hard materials (inorganic minerals) and soft materials (organic macromolecules) that perform a variety of roles in organisms of protection, skeletal support, and sensory detection.[4] These specialized structures are the products of cooperative interactions between biomolecules and mineral-forming ions secreting into a membrane-delineated or extracellular space.[5]

Figure IV.2 shows selected examples of the diversity of inorganic materials present in the living world.
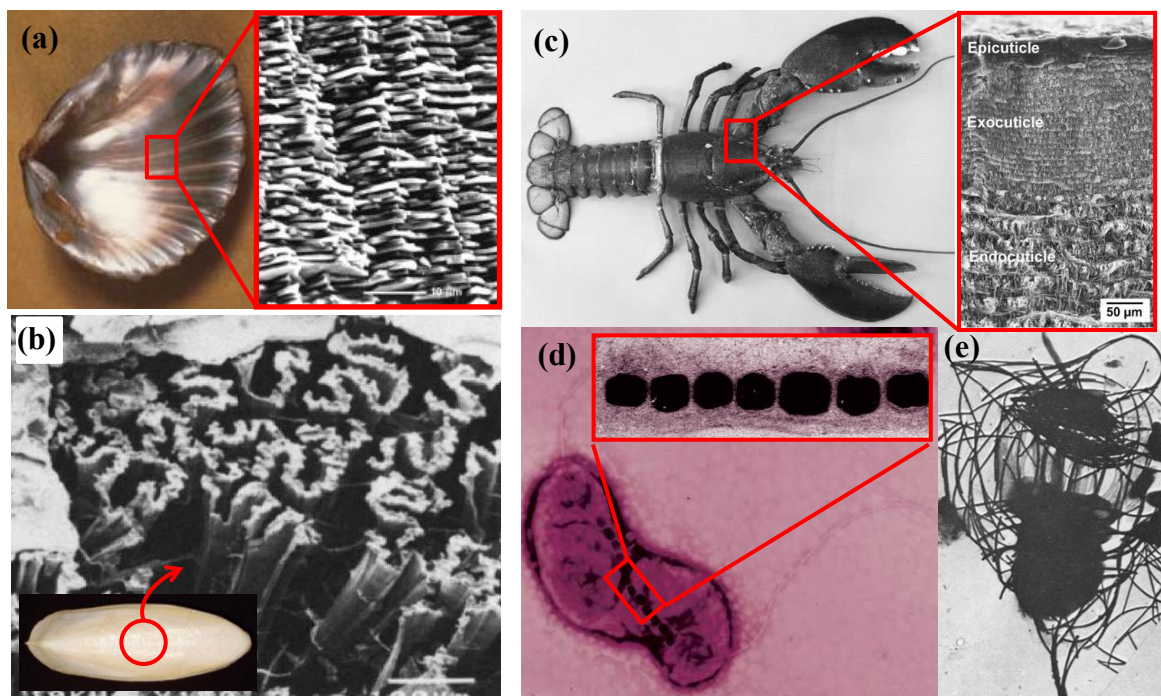
Figure IV.2 Examples of biological mineralization. (a) Seashell and SEM image of flat polygonal crystals of aragonite that make up gastropod nacre,[6] (b) TEM image of fractured section of cuttlefish bone showing lamellar and columnar-structure containing aragonite crystals,[8] (c) lobster homarus americanus and SEM image of exoskeleton composed by chitin layer and $CaCO_3$,[10] (d) TEM image of cell of a typical magnetotactic bacterium containing the chain of magnetic crystals,[12] and (e) TEM image of extracellular lorica formed by the unicellular choanoflagellate with the basket consists of curved silica rods.[16]

Calcium carbonate is one of the most common minerals as a component of many inorganic/organic hybrid materials in nature. For example, the inner shell layer of mollusks shows iridescent luster (Figure IV.2 a). This luster results from specific inorganic-organic crystalline structures, which is called nacre as well-known as mother of pearl. Nacre is composited by arranged layers of polygonal aragonitic platelets ($CaCO_3$) with around 5-15 μm in wide and 0.5 μm in thickness, which are separated by sheets of interlamellar organic matrices such as chitin, lustrin, and proteins.[6,7] Cuttlefish bones are also composed primarily of aragonite, that micrometric structure consists of narrow layers connected by numerous upright pillars (Figure IV.2 b).[8] The exoskeleton of crustacean is also a multiphase biological

composite material which consists of an organic matrix (crystalline a-chitin fibers and non-crystalline proteins) and $CaCO_3$ minerals (typically crystalline calcite and amorphous $CaCO_3$) (Figure IV.2 c).[9,10]

Another example, magnetotactic bacteria have unique intracellular structures called magnetosomes[11], which comprise magnetic mineral crystals surrounded by a lipid bilayer membrane about 3-4 nm thickness (Figure IV.2 d).[12] These bacteria usually mineralize either iron oxide magnetosomes, which contains crystals of magnetite (Fe_3O_4)[13] or iron sulphide magnetosomes, which contain crystals of greigite (Fe_3S_4)[14]. Overall, magnetosome crystals show high chemical purity, narrow size ranges, specific crystal morphologies and exhibits specific arrangements within the cell.[15] These magnetic crystals have often been playing the natural sensors within the cell.

Silicon dioxide (SiO_2) is also an important mineral for building the functional hybrid structures. For example, the baschoanoflagellate has extracellular basket-like cage, called a lorica, comprised of a two-layered arrangement of siliceous costae made up of rod-shaped units of approximately equal length (Figure IV.2 e).[16] This structure is sufficiently bulky to resist the locomotory effects of flagellar activity.[17]

As illustrated through the examples shown above, biomineralization produces organic/inorganic composite materials, which are used by biological organisms to carry out different functions. The inorganic/organic composite materials from various minerals have important functions in biological organism. Table IV.1 shows the main inorganic minerals that participate in the biomineralization and can express the biological functions in organism.[18]

Calcium carbonate $(CaCO_3)$ is commonly known minerals which has three different crystal formations, calcite, aragonite, and vaterite, and also has amorphous formation. Especially, two crystals (calcite and aragonite) are the main components for biomineralization in the organism (such as some animal bones, seashell, trilobite, etc…), that can be applied to the function such as extraneous protection, skeleton support, and eye lens.

Calcium phosphate and calcium oxalate are also distributed widely in biological organism with expressing the numerous functions such as exoskeletons and calcium store. The skeleton support is also deposited by silicon oxide that forms amorphous glass.

Other examples, minerals are also put to special uses as gravity balance device ($CaCO_3$, $CaSO_4$, and BaSO4), cellular support ($SrSO_4$), magnetic sensor in magnetotactic bacteria (Fe_3O_4) and iron storage and mobilization ($Fe_2O_3 \cdot n$H2O).

Table IV.1 The organism and function of the main inorganic materials found in biological systems. According to the review by Mann (1988).[18]

Mineral		Formula	Organism	Function
Calsium carbonate	Calcite	$CaCO_3$	Algae	Exoskeletons
			Trilobites	Eye lens
	Aragonite	$CaCO_3$	Fish	Gravity device
			Molluscs	Exoskeletons
	Vaterite	$CaCO_3$	Ascidians	Spicules
	Amrphous	$CaCO_3 \cdot n$H$_2$O	Plants	Ca store
Ca phosphate	Hydroxyapatite	$Ca_{10}(PO_4)_6(OH)_2$	Vertebrates	Endoskeletons
			Teeth	Ca store
	Octa-calcium	$Ca_8H_2(PO_4)_6$	Vertebrates	Precursor
Calcium Oxalate	Whewellite	$CaC_2O_4 \cdot H_2O$	Plants	Ca store
	Weddellite	$CaC_2O_4 \cdot 2H_2O$	Plants	Ca store
Group IIA metal sulphates	Gypsum	$CaSO_4$	Jellyfish larvae	Gravity device
	Barite	$BaSO_4$	Algae	Gravity device
	Celestite	$SrSO_4$	Acantharia	Cellular support
Silicon dioxide	Silica	$SiO_2 \cdot n$H$_2$O	Algae	Exoskeletons
Iron oxides	Magnetite	Fe_3O_4	Bacteria	Magnetotaxis
			Chitons	Teeth
	Goethite	α-FeOOH	Limpets	Teeth
	Lepidocrocite	γ-FeOOH	Chitons (Mollusca)	Teeth
	Ferrihydrite	$5Fe_2O_3 \cdot 9H_2O$	Animals and plants	Fe storage proteins

The organic macromolecules play an important role in the control of mineral growth, such as crystal morphology and aggregation. However, the most of molecular interactions in hierarchy levels of growth of mineralization are not well understood.

IV.3 Study of biomimetic mineralization[19]

For the design of inorganic/organic biomimetic materials, the main aim is not only to simply emulate a particular biological architectures and systems, but also to elucidate the mechanistic intricacy involved in these processes, ideas, and use such knowledge for the preparation of new synthetic materials and devices.[20,21] The exploration and application of bio-inspired synthetic strategies have resulted in the generation of complex materials with specific size, shape, orientation, composition, aggregation and hierarchical organization.

The control of crystallization in biomimetic mineralization relies on nucleation and tuning of crystal shapes by morphological control of soft materials as template.

IV.3.1 Nucleation and process of crystallization

The control of nucleation plays an important role as the first step for building up the inorganic/organic complex structures in biomineralization.

The typical theory of nucleation process is the spontaneous formation of spherical molecular clusters that continue to grow only when the size-depending free energies is larger than the threshold value of critical radius.[22] This model shows the possibility to predict the size of critical nucleus, associated activation energy, nucleation rate, and dependence on supersaturation. The structure and composition of nucleation are considered to bulk crystalline phase, the formation of subcritical supramolecular complexes and multi-step assembly of large unit cell structures.[23]

Recently, Jiang et al. reported the nucleation mechanism of hydroxyapatite (HAP, $Ca_{10}(PO_4)_6(OH)_2$) nanocrystals in the presence of chondroitin sulphate (ChS) from the view

point of kinetics, interfacial structure, and properties of strong interaction between ChS and calcium.[24] By adsorption of ChS on the surface of substrate, highly oriented HAP crystals can be obtained. This work contributes to an understanding of the fundamental mechanism of biomineralization on self-assembled structures.

Figure IV.3 shows the classical and non-classical crystallization process. In the classical process, nucleation clusters grow to form primary nanoparticles which are amplified to a single crystal (Figure IV.3 a). This particle can also assemble with mesoscale to form an iso-oriented crystal, where the nanocrystalline building units can fuse to form a single crystal (Figure IV.3 b). If primary nanoparticles are modified by polymer or other additives before amplification or assembly, they can form the mesocrystal which can even form from pure nanoparticles (Figure IV.3 c). There is also a possibility that amorphous particles are formed, which can transform before or after their assembly to complex morphologies (Figure IV.3 d).
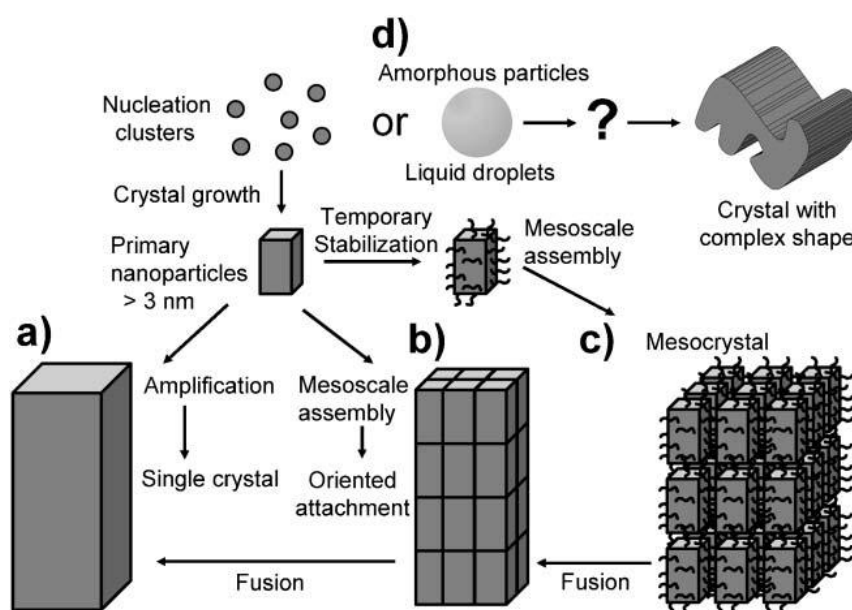

Figure IV.3 Schematic illustration of crystallization pathway with (a, b) classical and (c, d) non-classical method.[19,25]

IV.3.2 Study of organic template towards morphological control of minerals

In this section, we shall stress upon the role of the organic template in the control of the crystallization of the inorganic mineral. The performance of soft materials (organic part) as a template is important factor in order to design the mineral formation to mimic the biomineralization process. There are many reports in the literature on this study, for example, metal nanostructures (*e.g.* Ag, Ni, Co, Au nanowires) on peptide nanotubes[26,27,28,29] or amyloid fibers,[30] and Pr particle chains on DNA.[31] Even whole self-assembled bacterial superstructures can be applied to template superstructures of organic/inorganic hybrids such as silica, magnetite, and cadmium sulfate which are incorporated into the bacterial structures.[32] Similarly, pollen grains can be used as the biotemplates for complex with inorganic replications such as calcium carbonate and phosphate, ailica, and titanina *via* sol-gel condensation.[33,34]

Self-assembled Langmuir monolayers obtained by amphiphilic molecules are also important template because the molecular density of a monolayer is easily controlled at air-water interface with a Langmuir film balance.

Volkmer et al. have reported that controlled precipitation of $CaCO_3$ obtained by the monolayers of calixarenes and resorcarenes.[35] This method describes that higher charge density of Langmuir monolayer produce the polymorph and crystal orientation under the monolayer, rather than the geometrical arrangement of the ionic group of monolayers.

In 1986, Mann et al. have demonstrated the use of phospholipid unilamellar vesicles as the organic template for the membrane-mediated growth of iron oxide crystals.[36] They found that the lipid vesicles not only acted as passive hosts to enclose mineralization reactions, but also strongly influenced the growing mineral phase through the molecular recognition of chemical, electrostatic, and chiral complementarity. However, the mineral formation inside of vesicles was still quite difficult.

More recently, Yang et al. performed the crystallization process of $CaCO_3$ on a negatively charged stearic acid monolayer[37] or phospholipid monolayer[38] at air-water interface

where final calcite crystals were obtained by the direct transformation from amorphous $CaCO_3$ particle precursor. By adjusting the surface pressure of lipid monolayers, the shape and size of crystals can be controlled (example in Figure IV.4).
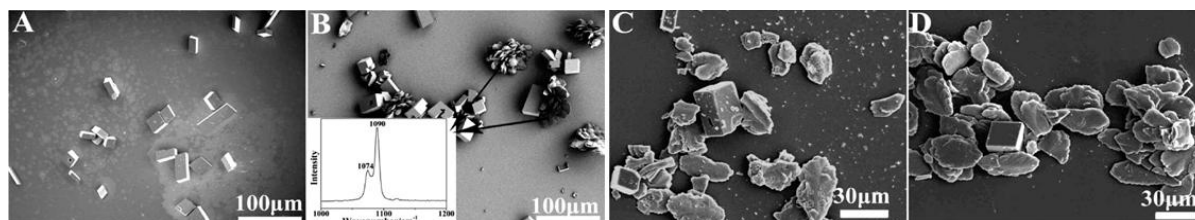

Figure IV.4 SEM images of CaCO₃ particles collected under the phospholipid monolayer at different surface pressures (a) 0 mN/m, (b) 2 mN/m, (c) 25 mN/m, and (d) 40 mN/m.[38]

In 2009, Pouget et al. have directly visualized development of crystal formation that nanoscopic prenucleation clusters of amorphous calcium carbonate (ACC) could organize spontaneously to polycrystalline structure.[39] They have developed template-directed ACC formation by using cryotransmission electron microscopy (cryo-TEM). The mineralization was performed on organic template of stearic acid monolayer.[40]

In the beginning of few minutes, prenucleation clusters with 0.6 ~ 1.0 nm diameters were observed (Figure IV.5 a, step **0**). These clusters were immediately organized to nucleation of amorphous nanoparticles (around 30 nm) (Figure IV.5 b, step **1**). Those particles were adsorbed on the surface of organic template, continuously the ACC particles grew and clustered at the surface of organic media (Figure IV.5 c, step **2**). Next, randomly oriented nanocrystalline domains were formed inside of amorphous particles (step **3, 4**), then crystalline domains were oriented at the interface of monolayer (step **5**) and develop into a single crystal with critical size with 300-500 nm (Figure IV.5 d, step **6**).

Diffraction patterns of particles also showed the development of crystallinity during mineralization. As increasing the crystalline domains, the amorphous parts gradually disappeared.
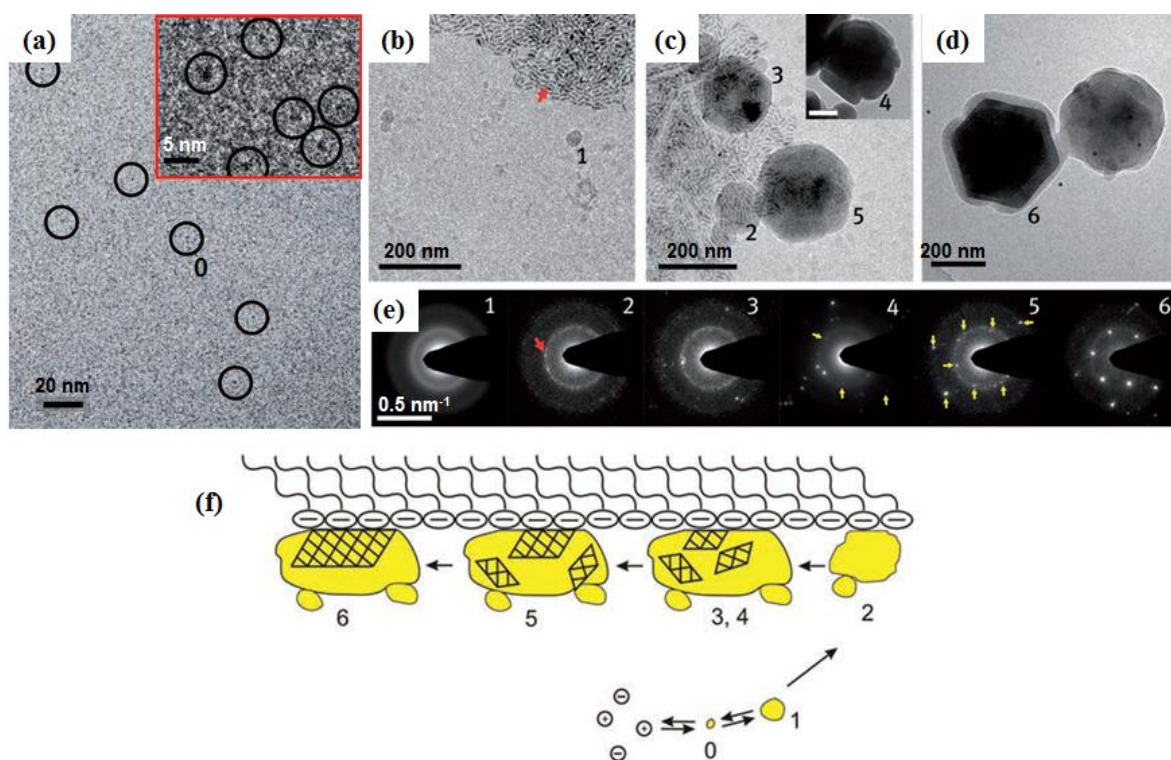
Figure IV.5 (a-d) Cryo-TEM images of the early, intermediate, and mature stages, and (e) diffraction patterns marked in (b) to (d). (f) Schematic illustration of the mineralization steps on the interface of organic matrix.[39]

By stabilization of nucleation of amorphous particles at the interface of organic templates, template-directed mineral formation provides possibility to control the size and shapes of inorganic materials in biological as well as in synthetic systems.

In the next section, we will mention the demonstration that self-assembly protocol of small organic molecules is an extremely powerful tool to generate mineralized structures with controllable shapes, and, possibly, with engineered functions.

IV.4 Chiral silica *via* sol-gel polycondensation from self-assembled organic template

The self-assembled structures of amphiphilic molecules are attractive candidates for utilization as organic templates due to their various shapes and controllable kinetics in their supramolecular aggregates (studied above in chapter I). Especially, the formation of amorphous silicon oxide has been reported through the sol-gel polycondensation from chiral supramolecular structures of amphiphiles as template. In this section, we will present the silicification method and some examples.

In 1998, Shinkai reported that sol-gel polycondensation of TEOS in the presence of cholesterol could transcribe to replica of silica fibrous structure.[41] Since this work, Shinkai has made a particularly important contribution to this field using the gels as a medium to the design of various silica morphologies, such as fiber-linear,[42] the lamella,[43] helical fibers[44] and spherical structures.[45]

In this section, we focus on the chiral silica architectures obtained by organic template from self-assembled chiral supramolecular structures *via* sol-gel polycondensation and developing the control of inorganic shapes.

IV.4.1 Polymerized silica by sol-gel polycondensation method

Silicon alkoxides ($Si(OR)_4$) are ideal chemical precursor for sol-gel synthesis because they react readily with water. The polymerization has several steps, the first reaction is called hydrolysis, because a hydroxyl ion becomes attached to the silicon atom as follows:

$$Si(OR)_4 + H_2O \rightarrow HO\text{-}Si(OR)_3 + R\text{-}OH$$

Continuously, $(OH)\text{--}Si\text{-}(OR)_3$ would be polymerized to link together in a condensation reaction to form a siloxane ($Si\text{--}O\text{--}Si$) bond:

$$(RO)_3\text{-Si-OH} + \text{HO-Si-}(OR)_3 \rightarrow (RO)_3\text{-Si-O-Si-}(OR)_3 + H_2O$$

or

$$(RO)_3\text{-Si-OR} + \text{HO-Si-}(OR)_3 \rightarrow (RO)_3\text{-Si-O-Si-}(OR)_3 + R\text{-OH}$$
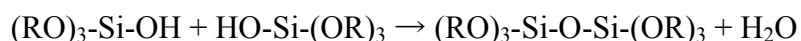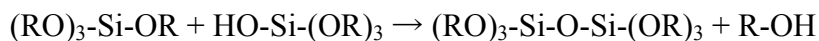
Thus, polymerization is associated with the formation of a 1, 2, or 3- dimensional network of siloxane (Si–O–Si) bonds accompanied by the production of H-O-H and R-O-H species.

Tetraethoxysilane (TEOS) is the most common chemical precursor for sol-gel polycondensation, which is negatively charged after prehydrolysis step. Sol-gel process requires the presence of an acceptor site links hydrogen, or positive charges. Thus, the cationic surfactants based on quaternary ammonium have been frequently used as organic template.[46] The driving force of organization is the presence of cationic charges on the amphiphiles, resulting in the containment of anionic silica precursors on contact with the surface of bilayer. By addition of aminosilane or quaternized aminosilane as a co-structure-directing agent, anionic surfactant can be also used for the organic templates.[47]

IV.4.2 Morphology control of chiral silica nanofibers

Chiral silica morphologies based on the organic template of self-assembled chiral amphiphiles can be tuned by various factors such as mechanical strength, and control of kinetics of sol-gel transcription process by physical or chemical properties.

In 2004, Che has presented the mesoporous silica structure with twisted hexagonal rod-like morphology by using amino acid-based surfactant as template, TEOS and aminosilane as inorganic sources (Figure IV.6).[47]
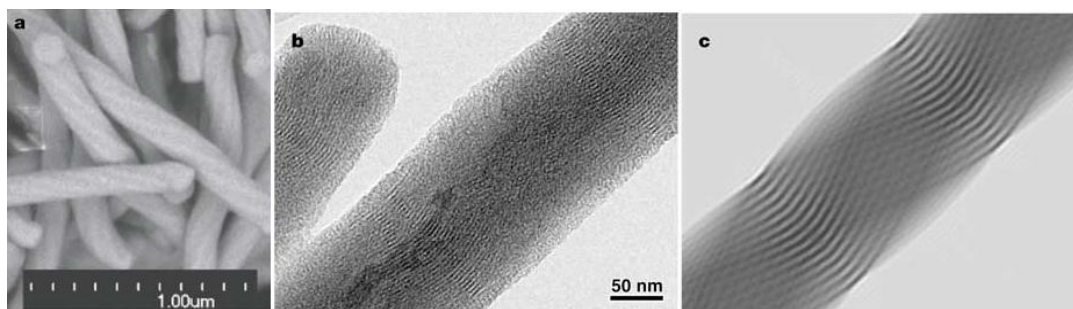
Figure IV.6 (a) SEM and (b, c) TEM images of chiral mesoporous silica.[47]

More recently, Che and his co-workers have demonstrated how to control the morphology of this inorganic architecture. The shape and size control were produced by various stirring rates during sol-gel polycondensation under the various stirring rates (Figure IV.7).[48]
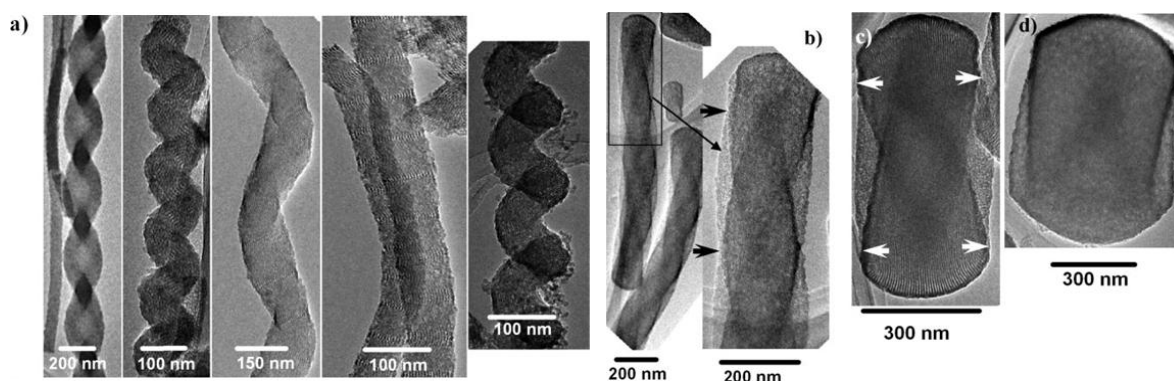
Figure IV.7 TEM images of chiral mesoporous silica synthesized at various stirring rates (a) 200 rpm, (b) 400 rpm. (c) 600 rpm, and (d) 800 rpm.[48]

When the starring rate was lower than 300 rpm, the sample showed various twisted ribbon-like structures that the length of hexagonal rods ranged from several micrometers to 20 μm and outer diameters varied from 50 to few hundred nanometers. By increasing the stirring rates, the morphologies became uniformly twisted rod-like with a hexagonal cross-section and the length of the rods decreased whilst their diameter increased, respectively. This method suggests that stirring can be used as a convenient tool for controlling not only the size and shape of chiral particles but also the chiral structure and helical pitch length for preparation of inorganic architectures.

The shapes and size are also controlled by the different reaction condition of solvent. For example, Yang et al. constructed different shapes of mesoporous silica nanofibers based on cationic surfactant as template and TEOS as silica precursor in the presence of ammonia as catalyst. The shapes of these nanofibers could be tuned by tunable by changing the solvent ratio (2-propanol/water) as well as the concentration of NH$_3$ (Figure IV.8).[49]
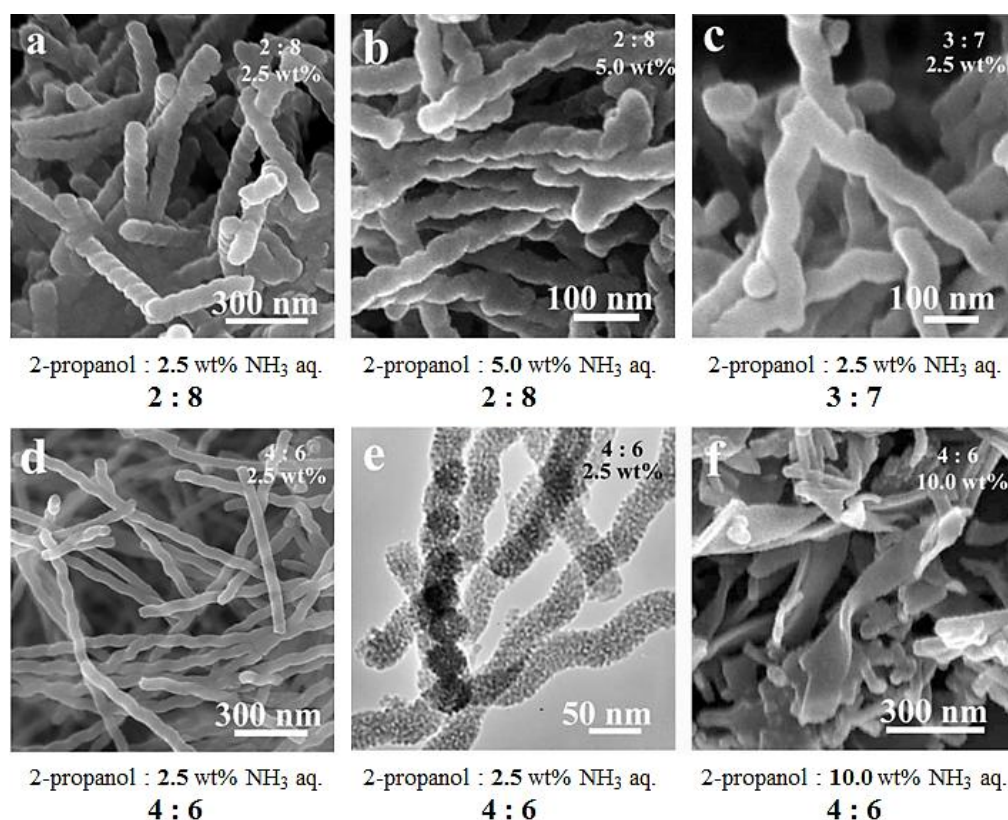
Figure IV.8 (a, b, c, d, f) FESEM and (e) TEM images of calcined nanostructured silica prepared in a mixture of NH$_3$aq. and 2-propanol.[49]

On increasing the volume ratio of 2-propanol to water, helical silica morphologies transformed from worm-like to straight fibers with decrease of helicity (Figure IV.8 a, c, d). This phenomenon was probably due to the high solubility of surfactant in alcohol which probably promoted the less chirality in supramolecular assembly during transcription. On increasing the NH$_3$ concentration, the morphological shapes of silica changed from single-stranded helical nanofibers (Figure IV.8 d, e) to twisted ribbons (Figure IV.8 f).

More recently, Yang et al. have also reported the preparation of tunable morphology of chiral biphenylene-silica by different ratio of ethanol/water solvent.[50] The chiral silica obtained by using amino acid-based surfactant as template and 4,4'-bis-(triethoxysilyl)-1,1'-biphenyl as silica precursor. In this case, the lower ethanol/water volume ratio (1 : 4) provided twisted ribbons, whereas higher ratio (1 : 1.5) provided helical ribbons (Figure IV.9).

Ethanol : Water = **1 : 4**   Ethanol : Water = **1 : 1.5**
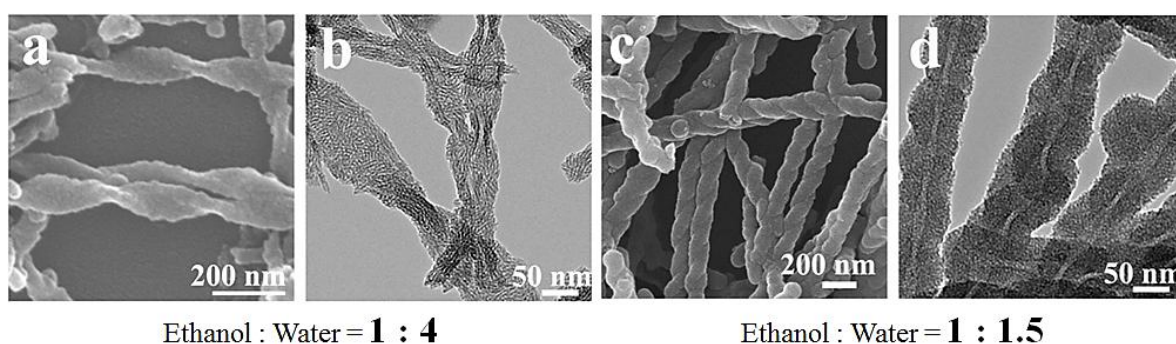
Figure IV.9 (a, c) FESEM and (b, d) TEM images of chiral biphenylene-silica prepared in a mixture of ethanol/water solution: (a, b) 1 : 4 and (c, d) 1 : 1.5.[50]

Hung et al. have successfully fabricated single and double helical silica nanofibers by using single-chain amphiphile composed by butyl, azobenzene group, and sugar moiety (C$_4$AG) as organic template and TEOS silica precursor.[51] Generally C$_4$AG can form double helices, therefore, double helical silica nanofibers were obtained *via* sol-gel polycondensation (Figure IV.10 a, b). Interestingly, upon decoupling the double helices of C$_4$AG system with cationic surfactant such as cetyltrimethylammonium bromide (CTAB), single helical silica nanoribbons could be obtained (Figure IV.10 c, d). In the later case, the silica source might be adsorbed to the single helical organic template by electrostatic force between the positively charged CTAB (Figure IV.10 e).
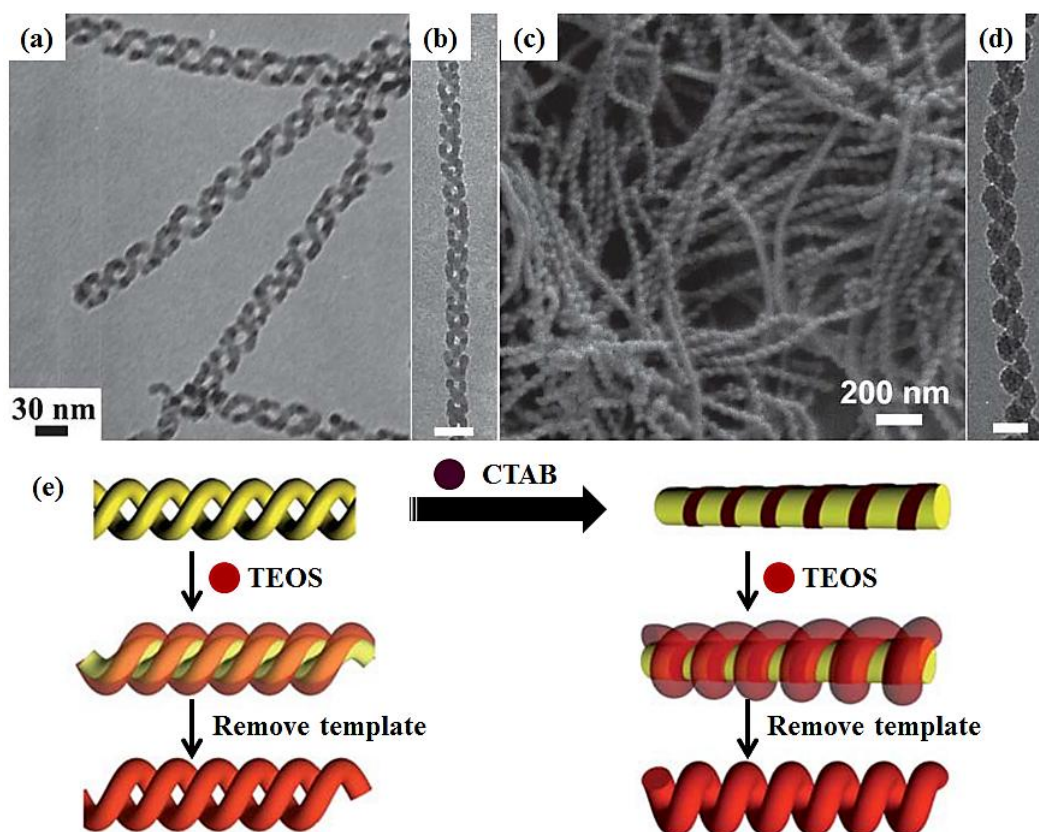
Figure IV.10 TEM images of (a, b) double helical and (c, d) single-stranded silica nanofiber. (e) Possible scheme of helical silica formation in the system of C$_4$AG/CTAB.[51(a)]

The work on sol-gel transcription of silica morphologies obtained by gel network of cationic bis-quaternary ammonium gemini surfactants with tartrate counter-anion began early 2000, the project was a collaboration between Oda's group and the group of Shinkai. They have successfully transcribed the chiral ribbons based on self-assemblies for which the chirality was controlled by enantiomeric excess (ee) of organic molecules (ee = 1 means pure enantiomer with gemini L-tartrate). The replication protocol used in this work consisted in mixing the gemini and the silica precursor (TEOS, 4.6%) in the presence of benzylamine (2.3%) as catalyst in mixture of water/pyridine (1 : 1). When the ee was decreased from 1 to 0.2, the twist pitches of inorganic fibers increased (Figure IV.8).[52] However, these twist pitches were smaller than those organic twisted ribbons because shrinkage of silica fibers may have occurred during the calcination process.

Figure IV.8 SEM images of chiral silica fibers with different helical pitch obtained by varying ee of gemini tartrate gel as organic templates.[52]

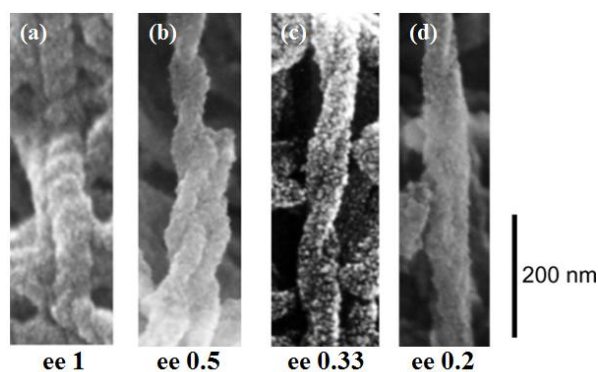Few years later, Delclos, Aimé et al. have reported the detailed study on the morphological control of the hybrid gemini-tartrate system. They have shown that not only the twist pitch of these hybrid nanosystems can be controlled by ee, their shapes are tunable between twisted, helical ribbons or tubes. Various parameters such as temperature, solvent or reactant concentrations can have distinct and opposite effects on their structures.

They have also shown that the relative kinetics of the organic assembly formation on one hand and the inorganic polycondensation on the other hand have remarkable effects on the final morphologies of the inorganic nanostructures.[53] As an example, Figure IV.9 shows the transmission electron microscopy (TEM) image of the organic tubes and their silica nanoreplicates illustrating how the morphologies of silica replicates strongly depend on the aging time of the organic template. Even if only 3 days are needed for the organic gels to form organic nanotubules, it should be noted that 5 day aged organic gel transcribed into twisted ribbons whereas 21 day aged ones underwent a morphological change to helical silica ribbons. It was only when the gels were aged for longer than 45 days that the resulting inorganic fibers kept their tubular structures. The average diameter of an inorganic helix is 25 nm, and the length is of the order of micrometer.
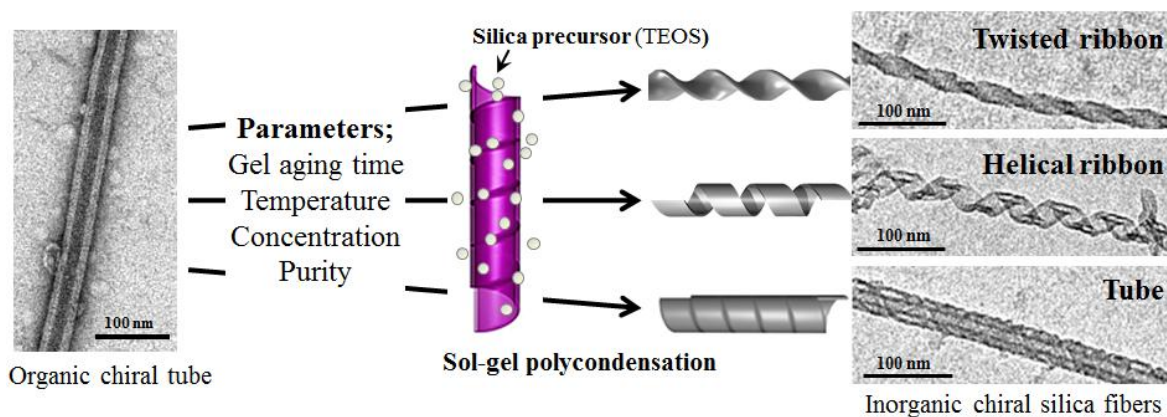
Figure IV.9 TEM images of the morphology of inorganic ribbons obtained by transcription of organic 16-2-16 L-tartrate gels obtained after various parameters, particularly aging times of organic gels can promote the tunable shape such as twisted (5 days), helical ribbons (21 days), and tubes (45 days).[53]

IV.5 Conclusion

In nature, there exist numerous examples of biominerals, which are usually composites of hard inorganic and soft organic materials in highly organized formation with attractive shapes, structures, and functions. These biomineralized structures perform important functions in the organisms. Scientists have long been inspired to mimic these processes, in order to design new hybrid materials with easy synthetic access, and possibly to achieve new functions, alongside the ones already displayed in the natural world. The natural organic/inorganic hybrid structures provide numerous inspirations for designing of noble synthesized hybrid materials.

Numerous organic templates have been studied, among them, self-assembled supramolecular structures from amphiphilic molecules are particularly fascinating organic templates due to their easily tunable shape, size and kinetics.

In recent years, many researchers have demonstrated chiral inorganic structures based on the chiral surfactants as organic template and tetraethoxysilane as silica precursor *via* sol-gel

polycondensation. The shape and size of chiral silica are controlled in the process of transcription from organic template by several parameters such as mechanical stress, solvent, temperature, purity, enantiomeric excess *etc*.

Our group has demonstrated that chiral silica structures with selective formations can be successfully transcribed from organic gel network of gemini tartrate amphiphiles. The shapes, such as twisted, helical ribbon to tubular structure, are controlled by simply changing the temperature of replication, the presence of additives, ee control, gel concentration, and kinetics of mineralization depending on the gel aging time. These inorganic architectures can find potential applications as enantioselective catalyst, as well as attractive immobilization supports for biomolecules, chemicals, and inorganic nanoparticles.

In the next chapter, we will discuss the organization of noble metal nanoparticles using chiral silica structure as inorganic template, and their optical properties.

References

[1] J. Aizenberg, J. C. Weaver, M. S. Thanawala, V. C. Sundar, D. E. Morse, P. Frattzl, *Science*, **2005**,*309*, 275-278.

[2] S. S. Voznesenskiy, Y. N. Kul'chin, A. N. Galkina, *Nanotechnologies in Russia*, **2011**, *6*, 43-78.

[3] S. S. Voznesenskii, A. N. Galkina, Yu. N. Kul'chin, A. A. Sergeev, *Nanotechnologies in Russia,* **2010***, 5*, 142–152.

[4] H. A. Lowenstam, *Science*, **1981**, *211*, 1126-1131.

[5] S. Mann, *Biomineralization: Principles and concepts in bioinorganic materials chemistry*, Oxford University Press, **2001**.

[6] L. Addadi, S. Weiner, *Nature*, **1997**, *389*, 912-915.

[7] (a) F. Nudelman, B. A. Gotliv, L. Addadi, S. Weiner, *J. Struct. Bio.*, **2006**, *153*, 176-187. (b) B. J. F. Bruet, H. J. Qi, M. C. Boyce, R. Panas, K. Tai, L. Frick, C. Ortiz, *J. Mater. Res.*, **2005**, *20*, 2400-2419.

[8] S. Mann, *Nature*, **1993**, *365*, 499-505.

[9] (a) H.A. Lowenstam, *Science*, **1981**, *211*, 1126–1131. (b) S. Weiner, L. Addadi, *J. Mater. Chem.*, **1997**, *7*, 689–702. (c) S. Mann, *J. Mater. Chem.*, **1995**, *5*, 935-946. (d) G. Falini, S. Albech, S. Weiner, L. Addadi, *Science*, **1996**, *271*, 67-69.

[10] D. Raabe, P. Romano, C. Sachs, H. Fabritus, A. Al-Sawalmih, S. B. Yi, G. Servos, H. G. Hartwig, *Mater. Sci. Eng. A*, **2006**, *421*, 143-153.

[11] D. L. Balkwill, D. Maratea, R. P. Blakemore, *J. Bacteriol.*, **1980**, *141*, 1399–1408.

[12] D. A. Bazylinski, R. B. Frankel, *Nature Reviews Microbiology*, **2004**, *2*, 217-230.

[13] R. B. Frankel, R. P. Blakemore, R. S. Wolfe, *Science*, **1979**, *203*, 1355–1356.

[14] (a) M. Farina, D. M. Esquivel, H. G. P. Lins de Barros, *Nature*, **1990**, *343*, 256–258. (b) S. Mann, N. H. C. Sparks, R. B. Frankel, D. A. Bazylinski, H. W. Jannasch, *Nature*, **1990**, *343*, 258–260. (c) B. R. Heywood, D. A. Bazylinski, A. J. Garratt-Reed, S. Mann, R. B. Frankel, *Naturwiss.*, **1990**, *77*, 536–538.

[15] D. A. Bazylinski, *ASM News*, **1995**, *61*, 337–343.

[16] B. S. C. Leadbeater, *Protoplasma*, **1979**, *98*, 311-328.

[17] (a) P. Andersen, *Mar. Microbial. Food Webs*, **1989**, *3*, 35–50. (b) B. S. C. Leadbeater1,Y. QiBin Yu, J. Kent, D. J. Stekel, *Proc. R. Soc. B*, **2009**, *276*, 3-11.

[18] S. Mann, *Nature*, **1988**, *332*, 119-124.

[19] A. W. Xu, Y. Ma, H. Colfen, *J. Mater. Chem.*, **2007**, *17*, 415-449.

[20] E. Dujardin, S. Mann, *Adv. Mater.*, **2002**, *39*, 3392-3406.

[21] C. Sanchez, H. Arribat, M. M. Giraud-Guille, *Nature Mater.*, **2005**, *4*, 277-288.

[22] (a) D. H. Everett, *Basic Principles of Colloid Science*, Royal Society of Chemistry, London, **1988**. (b) O. Sohnel, J. Garside, *Precipitation*, Butterworth-Heinemann, Oxford, **1992**.

[23] H. Colfen, H. Schnablegger, A. Fischer, F. C. Jentoft, G. Weinberg, R. Schlogl, *Langmuir*, **2002**, *18*,

3500-3509.

[24] H. D. Jiang, X. Y. Liu, G. Zhang, Y. Li, *J. Biol. Chem.*, **2005**, *280*, 42061-42066.

[25] H. Colfen, S. Mann, *Angew. Chem., Int. Ed.*, **2003**, *42*, 2350-2365.

[26] T. Klaus, R. Joerger, E. Olsson, C. G. Granqvist, *Proc. Natl. Acad. Sci. U. S. A.*, **1999**, *96*, 13611-13614.

[27] M. Knez, A. M. Bittner, F. Boes, C. Wege, H. Jeske, E. Maiss, K. Kern, *Nano Lett.*, **2003**, *3*, 1079–1082.

[28] R. Djali, Y. Chen, H. Matsui, *J. Am. Chem. Soc.*, **2002**, *124*, 13660-13661.

[29] M. Reches, E. Gazit, *Science*, **2003**, *300*, 625-627.

[30] T. Scheibel, R. Pharthasarathy, G. Sawicki, X. M. Lin, H. Jager, S. L. Lindquist, *Proc. Natl. Acad. Sci. U. S. A.*, **2003**, *100*, 4527-4532.

[31] M. Mertig, L. Colombi Ciacchi, R. Seidel, W. Pompe, A. DeVita, *Nano Lett.*, **2002**, *2*, 841-844.

[32] S. A. Davis, S. L. Burkett, N. H. Mendelson, *Nature*, **1997**, *385*, 420-423.

[33] S. R. Hall, H. Bolger, S. Mann, *Chem. Commun.*, **2003**, 2784-2785.

[34] S. R. Hall, V. M. Swinerd, F. N. Newby, A. M. Collins, S. Mann, *Chem. Mater.*, **2006**, *18*, 598-600.

[35] D. Volkmer, M. Fricke, C. Agena and J. Mattay, *J. Mater. Chem.*, **2004**, *14*, 2249-2259.

[36] S. Mann, J. P. Hannington, R. J. P. Williams, *Nature*, **1986**, *324*, 565–567.

[37] Y. J. Chen, J. W. Xiao, Z. N. Wang, S. Yang, *Langmuir*, **2009**, *25*, 1054–1059.

[38] J. Xiao, Z. Wang, Y. Tang, S. Yang, *Langmuir*, **2010**, *26*, 4977–4983.

[39] E. M. Pouget, P. H. H. Bomans, J. A. C. M. Goos, P. M. Frederik, G. de With, N. A. J. M. Sommerdijk, *Science*, **2009**, *323*, 1455-1458.

[40] S. Mann, B. R. Heywood, S. Rajam, J. D. Birchall, *Nature*, **1988**, *334*, 692-695.

[41] Y. Ono, K. Nakashima, M. Sano, K. Kanekiyo, K. Inoue, J. Hojo, S. Shinkai, *Chem. Comm.*, **1998**, 1477-1478.

[42] Y. Ono, Y. Kanekiyo, K. Inoue, J. Hojo, S. Shinkai, *Chem. Lett.*, **1999**, *28*, 23-24.

[43] (a) J. H. Jung, Y. Ono, S. Shinkai, *Langmuir*, **2000**, *16*, 1643-1649. (b) J. H. Jung, Y. Ono, S. Shinkai, *Angew. Chem., Int. Ed.*, **2000**, *39*, 1862-1865.

[44] J. H. Jung, H. Kobayashi, M. Masuda, T. Shimizu, S. Shinkai, *J. Am. Chem. Soc.*, **2001**, *123*, 8785-8789.

[45] J. H. Jung, Y. Ono, K. Sakurai, M. Sano, S. Shinkai, *J. Am. Chem. Soc.*, **2000**, *122*, 8648-8653.

[46] J. S. Beck, J. C. Vartuli, W. J. Roth, M. E. Leonowicz, C. T. Kresge, K. D. Schmitt, C. T-W. Chu, D. H. Olson, E. W. Sheppard, S. B. McCullen, J. B. Higgins, J. L. Schlenker, *J. Am. Chem. Soc.,* **1992**, *114*, 10834-10843.

[47] S. Che, Z. Liu, T. Ohsuna, K. Sakamoto, O. Tersarki, T. Tatsumi, *Nature*, **2004**, *429*, 281-284.

[48] H. Jin, Z. Liu, T. Ohsuna, O. Terasaki, Y. Inoue, K. Sakamoto, T. Nakanishi, K. Ariga, S. Che, *Adv. Mater.*, **2006**, *18*, 593–596.

[49] Y. Yang, M. Suzuki, S. Owa, H. Shirai, K. Hanabusa, *J. Mater. Chem.*, **2006**, *16*, 1644–1650.

[50] B. Li, Z. Xu, W. Zhuang, Y. Chen, S. Wang, Y. Li, M. Wang, Y. Yang, *Chem. Commun.,* **2011**, *47*, 11495–11497

[51] (a) Y. Y. Lin, Y. Qiao, C. Gao, P. F. Tang, Y. Liu, Z. B. Li, Y. Yan, J. B. Huang, *Chem. Mater.*, **2010**, *22*, 6711–6717. (b) Y. Y. Lin, Y. Qiao, J. B. Huang, *Soft Mater.*, **2011**, *7*, 6358–6398.

[52] K. Sugiyasu, S. Tamaru, M. Takeuchi, D. Berthier, I. Huc, R. Oda, S. Shinkai, *Chem. Commun.*, **2002**, 1212–1213.

[53] T. Delclos, C. Aimé, E, Pouget, A. Brizard, I. Huc, M. H. Delville, R. Oda, *Nano Letters*, **2008**, *8*, 1929-1935.

Chapter V

Gold nanoparticles deposition on silica nanohelices:

A novel 3D substrate for optical sensing

V.1 Introduction

Recently, the organization of metal nanoparticles on 1D and 2D surfaces has attracted a great deal of attention, due to its potential applications in nanoscale integrated photonics.[1,2,3] In general, arranged nanoparticles are obtained by constructing the hybrid nanostructures in which nanoparticles are self-assembled on the surface of organic/inorganic substrate such as nanotubes, wires, and fibers. Such composite materials may combine the unique mechanical and electronic properties of the substrates with the rich size- and shape-dependent optical properties from metal nanoparticles. Nanoparticles that have been used to produce nanoparticles/substrate hybrid nanostructures include metal nanoparticles, such as Au[4] Pt,[5] or semiconductor nanocrystals such as CdSe.[6]

Especially, noble metal nanoparticles such as Au (noted here as GNPs) and Ag have great advantages due to the unique optical properties such as surface plasmon resonance, electron properties, and molecular recognition properties. For example, GNPs have found widespread use as contrast agents for immunogold labeling of biomolecules (Figure V.1).[7]
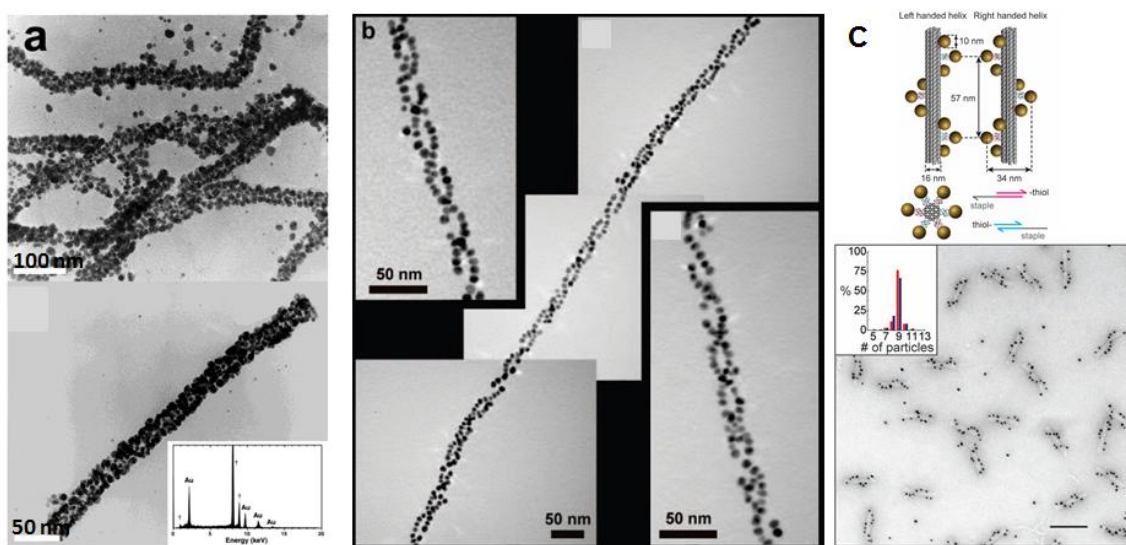

Figure V.1 TEM images of GNPs assembled on (a) tobacco mosaic virus nonawires,[7] (b) peptide twisted nanoribbons,[8] and (c) DNA origami.[9]

One of the most important aspects of the noble metal NPs (Au, Ag, Cu) that will be discussed here in some detail is that they exhibit rich surface-plasmon-related light absorption and scattering properties which cover the visible and IR spectral regions. When the GNPs are assembled closely with each other, their surface plasmon resonances are coupled together, resulting in the enhancement of the electric field in the gap between neighboring nanoparticles.[10] Such systems, therefore, are attractive candidates for the amplification of optical signals, including fluorescence,[11] Raman scattering,[12] and second-harmonic generation.[13]

Especially the amplification of Raman scattering, called surface enhanced Raman Spectroscopy (SERS), is useful for the detection of biological compounds at very low concentrations. SERS provides rich spectral and structural information of molecules on gaseous, liquid, and solid samples adsorbed on the noble metal substrate, such as fluids, blood, tissues and dye molecules and is considered to have a large potential application for biomedical sensing, immunoassays,[14] optically triggered drug delivery[15] and simultaneous cancer imaging.[16] The optical property induced by the localized surface plasmon resonance (LSPR) strongly depends on the local environment (particle size, shape, composition and surface coating).

SERS substrates have typically been assembled novel metal nanoparticles on planar surface (Figure V.2).[10,17,18,19]
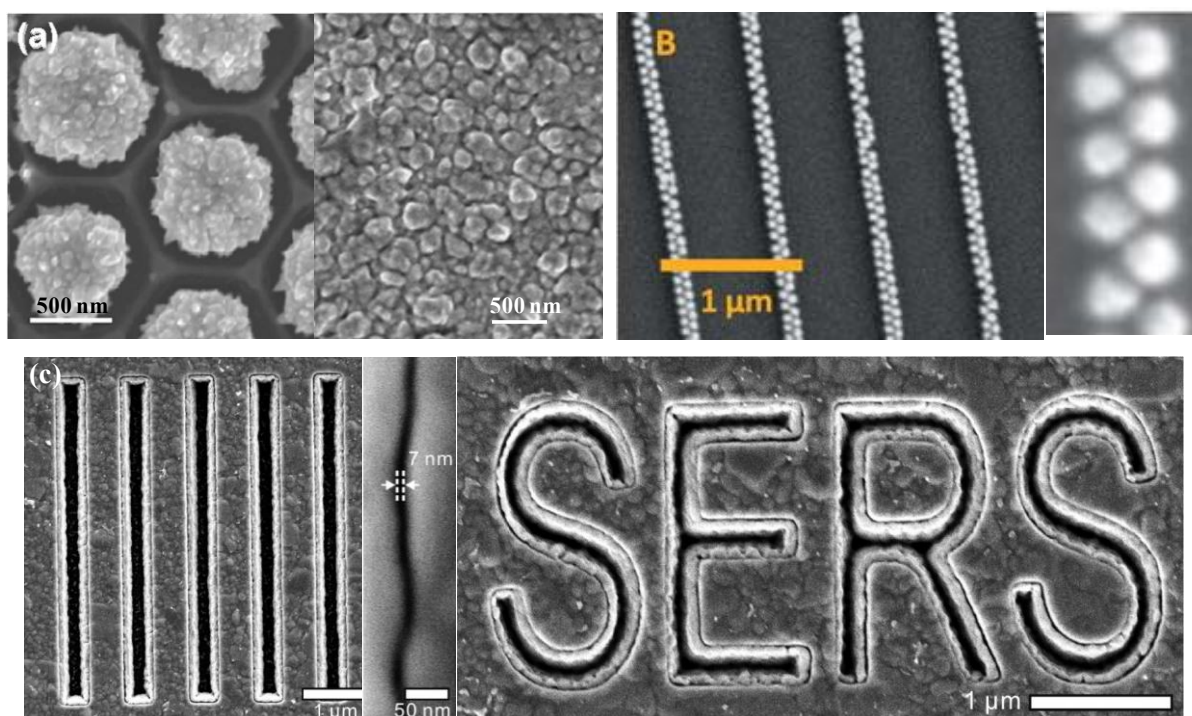
Figure V.2 Examples of SERS substrate. (a) GNPs film self-assembled on the indium tin oxide upon deposition of GNPs in the alumina template (right) and after removal of template (left).[17] (b) Double-line arrays of GNPs on the glass slide upon confinement of a monodisperse gold colloid with wrinkled stamps.[18] (c) Silver-air-silver nanogap structures obtained from Ag film over nanosphere substrate.[19]

More recently, substrates having morphologies other than two dimensional surfaces have been developed. Among various structures, hybrid structures based on silica nanofibers have attracted interest[20,21] as they can be used as bases for alignment of nanoparticles. Meanwhile, much fewer approaches are reported using 3D helical structures. Indeed, compared to traditional 1D nanostructures (flat ribbons or wires), the great advantage for 3D morphologies (helices and twisted ribbons, tubules) is the extremely high surface to volume ratio for the development of inorganic nanomaterials. In particular, nanohelices exhibit unconventional physical properties due to their periodic helical structure and flexibility, which is ideal for inducing polarization effects under mechanical stress.[22] Therefore, these nanoobjects are useful building blocks for functional nanodevices.[23,24]

A few years ago, our group reported the synthesis of chiral nanometric silica ribbons and tubes with tunable shapes based on self-assembled amphiphilic molecules.[25] The

amphiphiles were cationic bis-quaternary ammonium gemini surfactants in the presence of tartrate counter-anions, which formed extended networks of nanometric twisted or helical ribbons with tunable shapes and sizes, leading to gelation of water.[26] These organic nanoassemblies were successfully transcribed to inorganic 3D helical nanostructures (detail of procedure has mentioned above in Chapter IV).

In order to achieve organization of GNPs on the surface of silica-nanohelices, it is important to exploit the bonding between silane coupling agent and GNPs' stabilizing agent. GNPs are adsorbed on the surface of silica through the organic linkers. Table V.1 shows the typically organosilanes (X) and coupling agent of GNPs (Y).

Table V.1 Enumeration of typically silane coupling agent and GNPs' stabilizing agent.

	Silane coupling agent (X)		Stabilizing agent (Y)
AEAPS	N-[3-(Trimethoxysilyl)propyl]ethylenediamine	MUA	11-mercaptoundecanoic acid
MPTMS	(3-mercaptopropyl)trimethoxysilane	CIT	Trisodium citrate
MPTES	(3-mercaptopropyl)triethoxysilane	THPC	Tetrakis(hydroxymethyl)phosphonium chloride
APTES	(3-aminopropyl)triethoxysilane	CTAB	Cetyltrimethylammonium bromide

Groups with various linkages can be readily introduced to the surface of silica substrate by means of organosilane and to the GNPs stabilized by thiol or amino groups. Appropriate modifications and reactions of functionalized silica-nanohelices and GNPs have allowed the utilization of a variety of interactions between silica surface and GNPs such as electrostatic or covalent bonding (Figure V.3 and Table V.2).
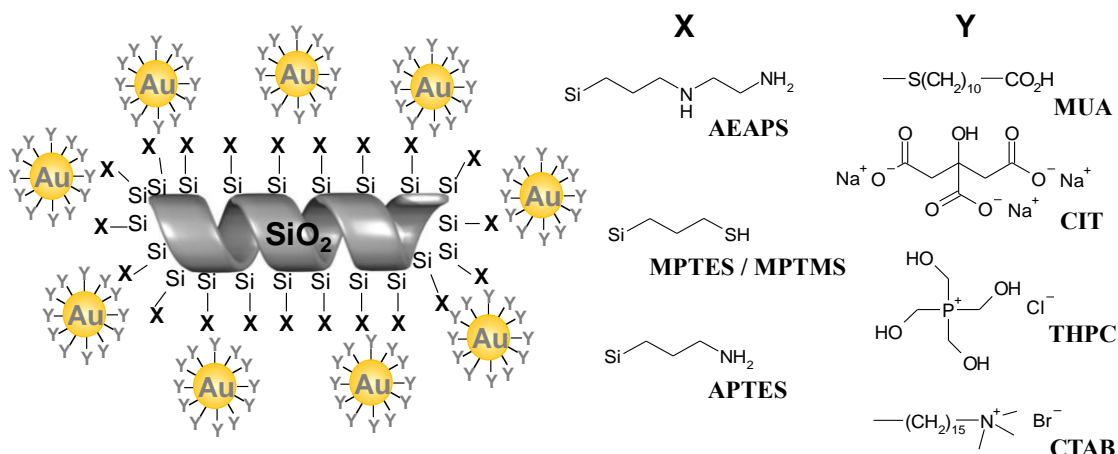
Figure V.3 Schematic composition of electrostatically and cobalently bonded GNPs/silcananohelices composites.

Table V.2 Ligand and bonding types employed between GNPs and surface of silica composite.

X	Y	Bonding	Reference
APTES	MUA	Electrostatic	27, 28
APTES	THPC	Covalent	29
MPTES	THPC	Covalent	28
APTES	CIT	Electrostatic	30
AEAPS	CIT	Electrostatic	31
MPTES	CIT	Covalent	32
MPTES	CTAB	Covalent	33, 34
APTES	CTAB	Covalent	33, 34

Comparing the anchoring groups of amine (-NH$_2$) and thiol (-SH), these functional groups bind to the GNPs *via* different strength. Commonly -SH has been known to form strong S-Au covalent bonds, whereas the binding of amino to gold surface is described by a weak covalent binding.[34,35] But if APTES functionalized SiO$_2$ are in solution within range of pH 6-9.5, the amino groups are protonated and generally the bonding is described to form electrostatic interaction between –NH$_3^+$ and GNPs when capped by anionic agent such as citric acid.[36]

In this study, we describe new methods to prepare GNPs/silica-nanohelices hybrid nanostructures which form 3D gel network in liquid phase. Gold nanoparticles (GNPs) with various sizes (1 ~ 20 nm) are assembled on the surface of functionalized nanometric silica

helices with controllable shape and pitch. The functionalization of the silica helices has been performed using (3-aminopropyl)triethoxysilane (APTES) or (3-mercaptopropyl)triethoxysilane (MPTES). GNPs have been prepared by different methods using different "shape-inducing" agents such as sodium citrate (CIT), tetrakis(hydroxymethyl)phosphonium chloride (THPC), and cetyltrimethylammonium bromide (CTAB). The morphology of GNPs/silica-nanohelices hybrid nanostructure has been investigated by transmission electron microscope (TEM), and optical properties have been studied by UV-vis spectroscopy and Raman scattering experiments.

V.2 Surface modification of silica nanohelices

V.2.1 Preparation of silica-nanohelices

Silica-nanohelices were prepared by sol-gel transcription from 3D gel network which were obtained from cationic bis-quaternary ammonium gemini surfactants having the formula C_2H_4-1,2-((CH_3)$_2$N$^+$C$_{16}$H$_{33}$)$_2$) (noted as 16-2-16) in the presence of tartrate counter-anions as organic template in aqueous solution.[25] Figure V.4 shows the TEM image of the organic tube and silica nanofibers with tunable shapes between twisted, helical ribbons or tubes. When the gels are aged for more than 45 days, the resulting inorganic fibers show tubular structures whereas when aged for 21 days, the nanotubules undergo a morphological change back to the helical ribbons upon transcription. When the even younger gels (5 days) are transcribed, the tubules transform to twisted ribbons. The average diameter of inorganic helix is 25 nm, and the length is of the order of micrometer.
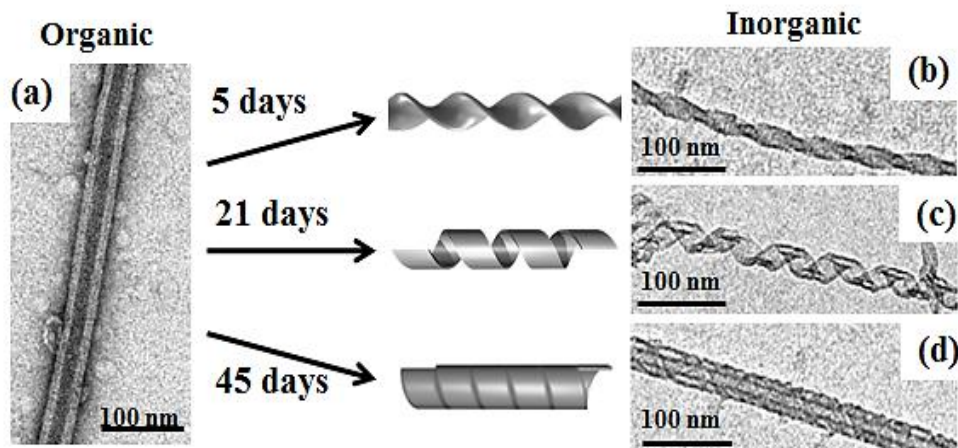
Figure V.4 TEM images of the morphology of inorganic nanostructures obtained by transcribing organic 16-2-16 L-tartrate gels after various aging times. (a) Organic gel forms nanotubules after two days. Interestingly, the subsequent formations of chiral inorganic ribbons are controlled by different aging times of organic gel before the transcription: (b) twisted ribbons are observed with gels aged for 5 days, (c) helices with gels aged for 21 days, and (d) nanotubes after 45 days.

We have also observed silica-nanohelices in 3D nature by using Scanning Electron Microscopy (SEM) and Atomic Force Microscopy (AFM) (Figure V.5). The SEM and AFM images clearly showed the unwounded 3D helicoidal structures. The periodicity of helical pitch is around 50 nm (Figure V.5 c).
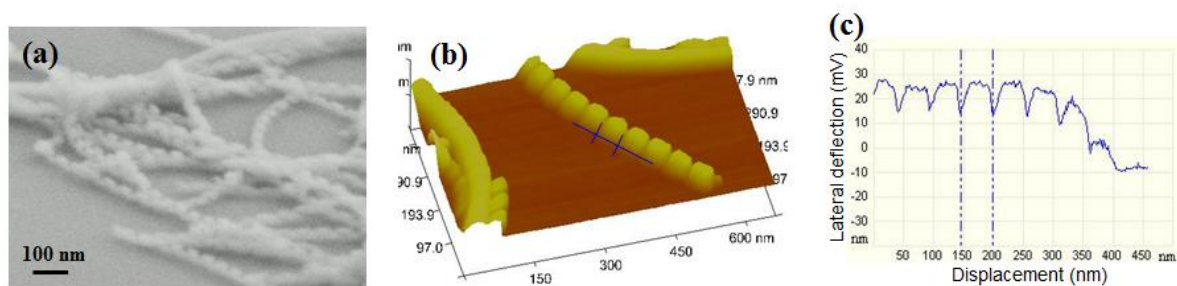

Figure V.5 (a) HRSEM and (b) AFM image of nanometric helical ribbons showing the 3D nature of the objects and its pitch. (c) The helical pitch obtained by AFM measurement.

The limited concentration of initial organic gels was 1-10 mM in order to transcription of nanometric silica-helices. In majority of the cases, we have chosen to use dilute organic gel concentration ($<$ 2 mM), since at this concentration, fewer intersection knocks were observed.

163

Silica-nanohelices were functionalized *via* a surface chemical modification with silane coupling agent. As beginning, silica-nanohelices were modified by amino group using APTES or thiol group using MPTES *via* secondary sol-gel polycondensation. Actually, APTES and (3-mercaptopropyl)trimethoxysilane (MPTMS) are the most common silane coupling agents which can induce the functional group (-NH$_2$ and -SH) to silica materials promoting the specific bonding with Au. But MPTMS is too high reactive to stimulate the polymerization in water, so that we select MPTES as coupling agent of –SH group.

V.2.2 Silica-nanohelices modified by APTES

At first, the reaction was performed under stirring, but silica-helices were cut down to shorter fibers and aggregated (Figure V.6 a). Therefore, APTES was dispersed homogeneously in silica-helices suspension under the ultra sonication for an hour, and then the suspension was kept in hot bath (85 ˚C) for 12 h; accordingly we could obtain less-aggregated longer silica-nanohelices with amino-functionalization (Figure V.5 b). Finally, we obtained functionalized 0.12 wt % of silica-nanohelices from 1 mM of organic gel, and 0.35 wt % silica-helices from 5 mM organic gel.
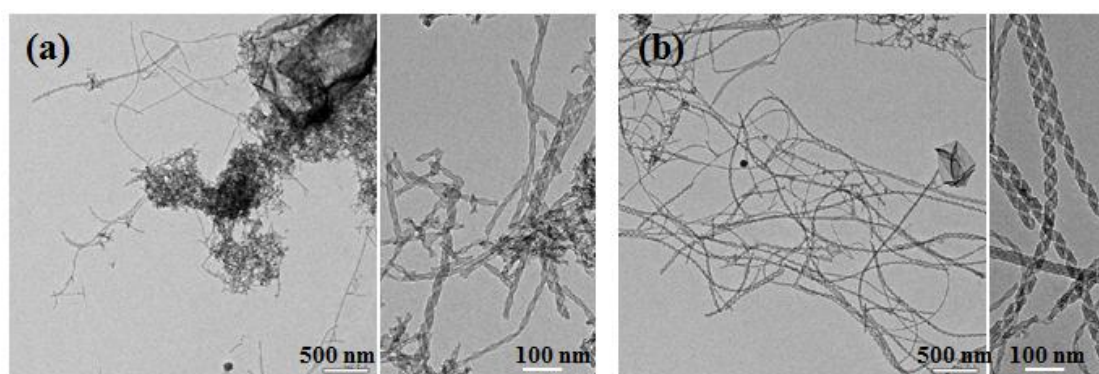

Figure V.6 TEM images of the amino-functionalized silica-nanohelices. The modification performed under (a) stirring (60 rpm.) vs (b) ultra sonication.

V.3 GNPs adsorbed on silica-nanohelices

Two approaches were adopted to synthesise GNPs with various sizes (1 ~15 nm) depending on the targeted size. The first one consisted in preparing gold nanoparticles of the desired size in the bulk solution using citrate (CIT) or cetyltrimethylammonium bromide (CTAB) as stabilizers and performing their further deposition on the modified helices. The second one aimed at generating very small GNPs (1.1 nm) *via* a stabilisation with tetrakis(hydroxymethyl)phosphonium chloride (THPC) whose sizes could be increased after deposition on the silica helices.

V.3.1 CIT-stabilized GNPs

In this section, we describe the adsorption of CIT-stabilized Au NPs on modified silica surface.

Au NPs of different sizes were synthesized following the method of Frens et al.[37] GNPs having different sizes within the range of 8-70 nm can be prepared by varying reactant concentrations of [Au^{3+}]/[CIT] ratio (e. g. 0.17 for 10 nm, 0.28 for 12 nm, and 0.37 for 14 nm).[38,39] When GNPs of 10 nm in diameter were synthesized, the concentration of Au salts were 0.5 mM in aqueous solution. The colloid solution color was dark red (Figure V.7).
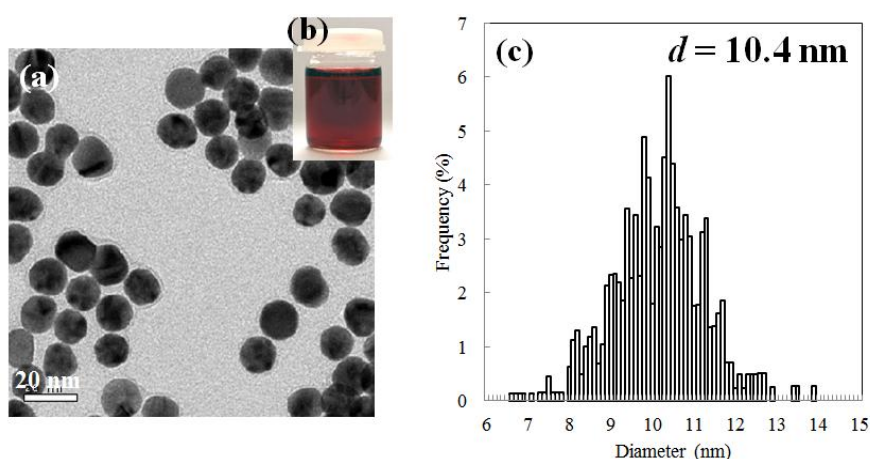

Figure V.7 (a) TEM images of CIT-stabilized GNPs, (b) GNPs colloidal solution, and (c) particle size distribution.

GNPs adsorbed on silica nanohelices

In order to obtain the homogeneous adsorption of GNPs on silica-naohelices, three different factors are important. In the following study 10 nm diameter GNPs were used along with the amino functionalized silica-nanohelices.

The first factor is the order of mixing; in the fist case, GNPs suspension are put into the silica-nanohelices suspension whereas in the second case, silica-nanohelices suspension are put into GNPs suspension (Figure V.8). When 1 ml of GNPs (0.5 mM, 0.098 mg/ml) of Au salt) were added to 50 µl (0.175 mg) of silica-nanohelices (0.35 wt %, 3.5 mg/ml,) suspension under ultrasonication, GNPs were adsorbed inhomogeneously and locally-aggregated on the silica-nanohelices (Figure V.8 a). On the other hand, when 50 µl of silica-nanohelices suspension were added to the 1 ml of GNPs, more homogeneous and less aggregated GNPs adsorption was observed (Figure V.8 b). Note that the concentration of GNPs and silica nanohelices are fixed as the values shown above hereafter.
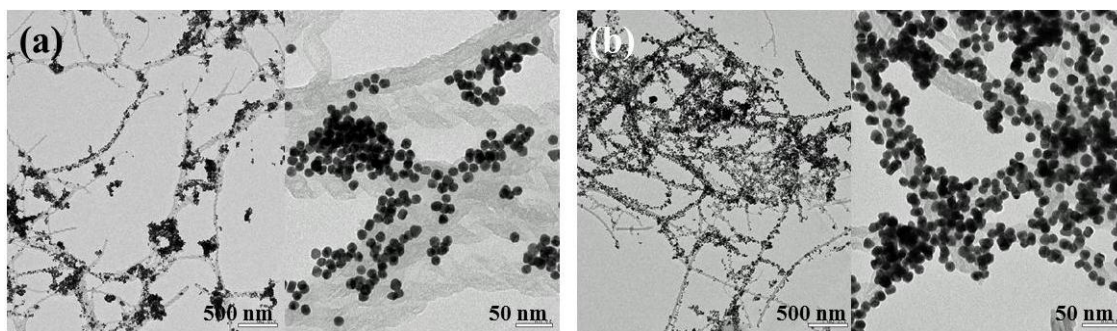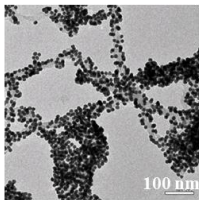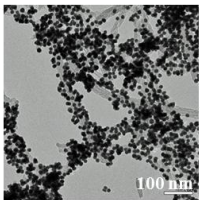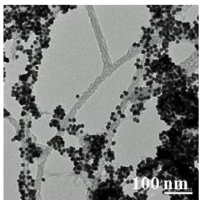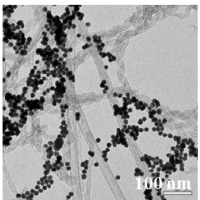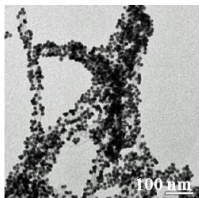

Figure V.8 TEM images of (a) CIT-stabilized GNPs added to silica-nanohelices, and (b) silica-nanohelices added to GNPs.

The other factors are summarized in Table V.3.

Table V.3 Summary of various conditions that CIT-GNPs (1 ml) adsorbed on the surface of silica-nanohelices modified by APTES.

APTES functionalization	Volume of 0.35 wt % silica-nanohelices (µl) per 1 ml GNPs (0. 5 mM of Au salt)				
	10	**50**	**100**	**200**	**300**
Single	Inhomogeneous	Inhomogeneous	Inhomogeneous	Inhomogeneous	No image
Double	Too much GNPs	Homogeneous	Homogeneous	Homogeneous	Poor adsorption

The ratio between the quantity of GNPs and silica-nanohelices suspension is a also important factor. From TEM observation, when the amount of silica-helices is decrease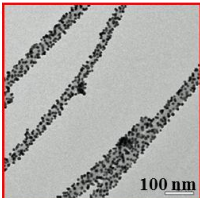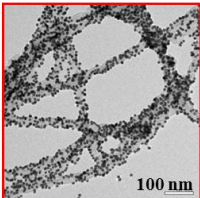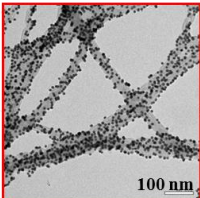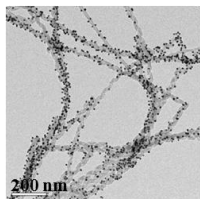d (~ 50 µl silica added to 1 ml GNPs), GNPs coated more homogeneously on the surface of silica. However, when the quantity of silica suspension was decreased to 10 µl, too much GNPs were adsorbed on the silica surfaces.

The most important factor is the number of functionalization by APTES. Comparison of single and double amino modification (the upper and the lower parts in Table V.3, respectively), GNPs could be adsorbed much more homogeneously on silica surface with double modification. With the silica surface modified once, GNPs showed aggregation along with inhomogeneous adsorption. This may be because the surface density of amine group is not high enough and the interaction between the GNPs is stronger than the GNPs/silica nanohelices interaction, therefore GNPs may prefer to aggregate with each other than to adsorp to the silica surface.

From these results, the best condition can be summarized by 50 ~ 200 µl of double amino-functionalized silica suspension (0.35 wt %, 3.5 mg/ml) added to the 1 ml of GNPs colloid solution (0.5 mM, 0.098 mg/ml).

In terms of macroscopic aspect, dark red colloid solution tuned to dark blue precipitate upon addition of single amino-modified silica-nanohelices, whereas in the case of double modification, the suspension tuned to red precipitate (Figure V.9).
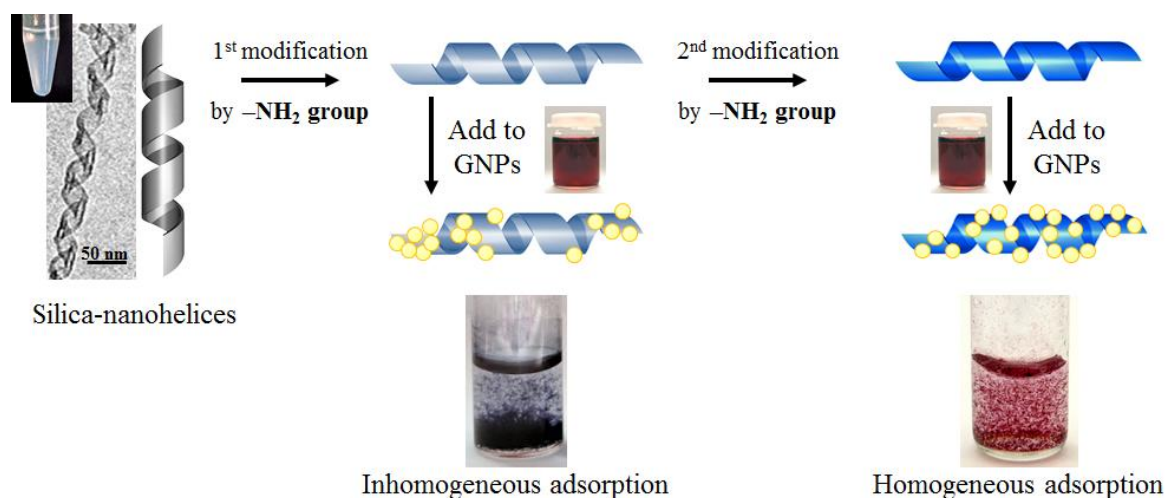
Figure V.9 Comparison of macroscopic aspect: dark blue precipitate obtained by single amino-modified silica-nanohelices and red precipitate obtained by double amino-modified silica-nanohelices.

Effect of organic gel concentration

Finally, we also compared the concentration of organic gel before transcription. We compared between 5 mM and 1 mM gels. After transcription, they yielded 0.35 and 0.12 wt % of silica-nanohelices suspension in water respectively. Better adsorption was shown with lower concentration of silica-nanohelices which is probably because lower the concentrations of gels are, less intersections are present (to which GNPs tend to accumulate) (Figure V.10).
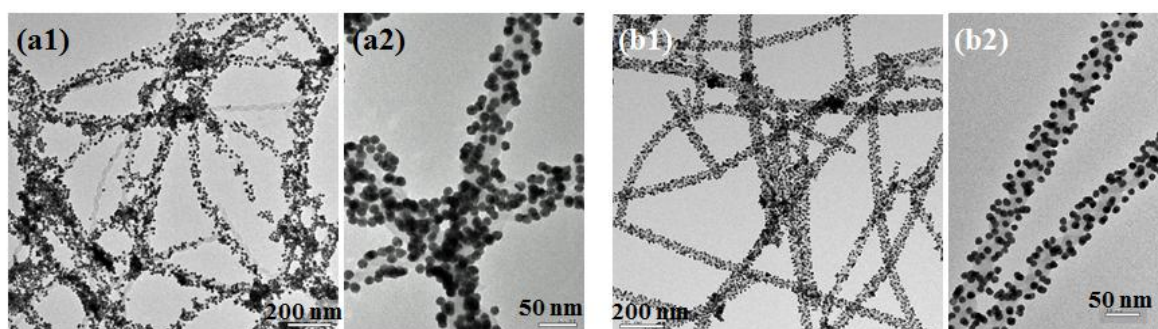
Figure V.10 TEM images of GNPs adsorbed on different concentration of silica-nanohelices with (a) 0.35 wt % and (b) 0.12 wt %.

Effect of citric acid concentration on the GNPs adsorption

We also attempted the GNPs adsorption on surface of −SH functionalized silica-nanohelices. However, in this case GNPs were adsorbed on silica with strongly inhomogeneous aggregation (Figure V.11 a). In order to investigate the effect of the concentration of citric acid (CIT), excess CIT was rinsed out from the GNP suspension with water using strong centrifugation (10000 rpm, 30 min). The suspension of GNPs with lower concentration of CIT is then obtained. When the suspention of −SH functionalized silica (50 µl) was then added to the 1 ml of washed GNPs suspension as obtained above, much better adsorption was observed, but GNPs showed still localized aggregation (Figure V.11 b).

Figure V.11 TEM images of GNPs adsorption on the surface of −SH group modified silica-nanohelices; (a) without rinse and (b) rinse of excess CIT coupling agent.

V.3.2 THPC-stabilized GNPs

The smaller Au nanoparticles with the diameter of around 1 ~ 2 nm were prepared by reduction of $KAuCl_4$ with tetrakis(hydroxymethyl)phosphonium chloride (THPC) using modification reported by Duff et al.[40] The obtained particle diameter was 1.4 nm and the concentration of Au salts were 0.97 mM in aqueous solution. The colloid solution color was brown (Figure V.12 a-c).
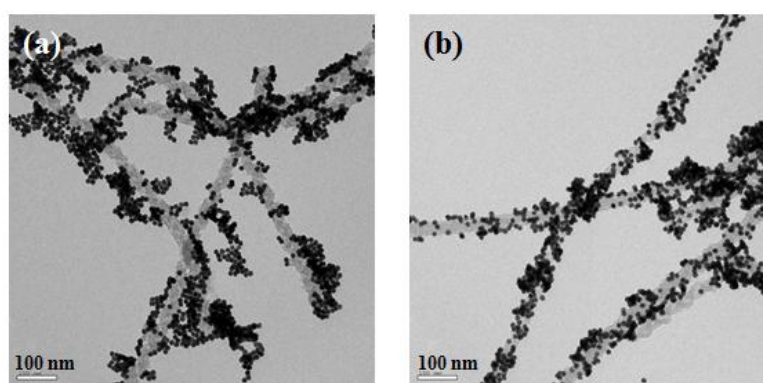

Figure V.12 (a) TEM images of THPC-stabilized GNPs, (b) GNPs colloidal solution, and (c) particle size distribution. (d) Precipitate of GNPs/silica-nanohelices suspension and (e) that TEM image of after adsorption.

It was much easier to obtain homogeneous adsorption of THPC-stabilized GNPs on the silica surface. These GNPs could be adsorbed on silica surface functionalized by both APTES and MPTES. For the volume ratio, the much higher quantity of silica helices can be used; up to ~200 µl of 0.12 wt% silica for 200 µl GNP solution. After adsorption of GNPs, brownish yellow precipitates were observed (Figure V.12 d). All of silica-helices were coated by small GNPs (Figure V.12 e).

V.3.3 CTAB-stabilized GNPs

The positively charged nanoparticles were synthesized by using a seed-mediated growth method in the presence of cetyltrimethylammonium bromide (CTAB) as cationic capping agent.[38,41] The preparation process consisted of several steps: at first, the small seeds

within 3.5 nm diameter were synthesized by chemical reduction of gold salt with a strong reducing agent (sodium borohydride) in the presence of a capping agent (CIT), then these seeds were added to the seed growth solution containing more metal salt, a weak reducing agent (e. g., ascorbic acid) and surfactant-directing agent (CTAB). The obtained particle diameter was 8.8 nm and the concentration of Au salts were 0.25 mM in aqueous solution. The color of the colloid solution was reddish violet (Figure V.13).
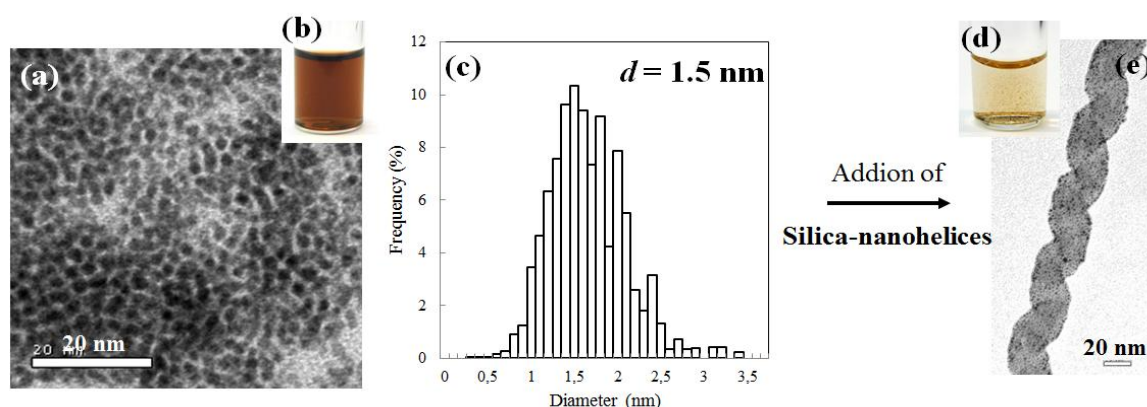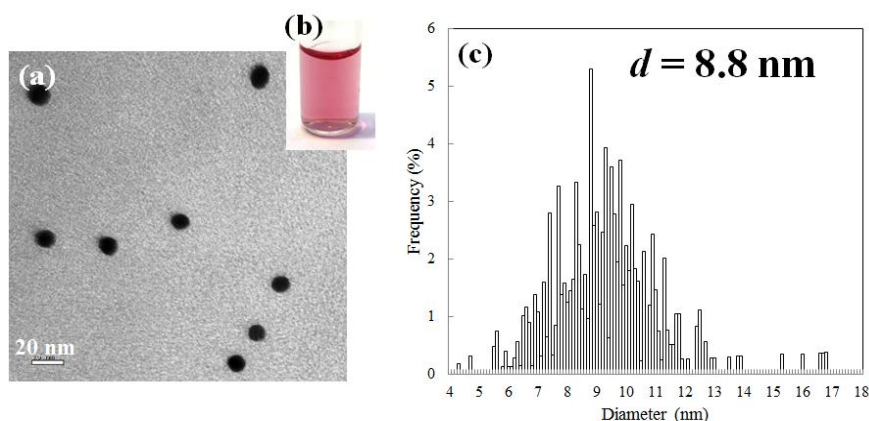

Figure V.13 (a) TEM images of CTAB-stabilized GNPs, (b) GNPs colloidal solution, and (c) particle size distribution.

CTAB-stabilized GNPs were well immobilized on MPTES functionalized silica-helices. On the contrary the GNPs stabilized by CTAB showed poor adsorption on the APTES functionalized one. This is probably because CTAB bilayer as coupling agent acts as cationic surfactants and there is consequent charge repulsion with amino functionalized silica surface.

In fact, the immobilisation of CTAB-stabilized GNPs on the MPTES-functionalized silica-nanohelices was not straight forward. As a beginning, suspension of silica-nanohelices functionalized twice by MPTES were put into CTAB-GNPs solution, but GNPs could not be immobilized on the surface because CTAB formed thick bilayer around the particles and this bilayers prevented the covalent bonding between –SH group and Au. Therefore, it was necessary to break closely packed bilayers adsorbed on the GNP during immobilization on the silica surface. This was done by the addition of ethanol in order to break the CTAB bilayer

adsorbed on the GNPs and to allow them to bind to the surface of silica through the thiol group, therefore allowing GNPs to be adsorbed on the surface of silica-nanohelices through the thiol group.

Effect of the quantity of silica vs GNPs in suspension

The 5 to 100 µl of MPTES-functionalized silica-nanohelices suspension (0.12 wt%) were dispersed into 500 µl of GNPs suspension (0.25 mM of Au salt) under the ultrasonication. 500 µl of ethanol was then added to the suspension in order to break the CTAB bilayer adsorbed on the GNPs and to allow them to bind to the surface of silica through the thiol group. The sonication was continued for 10 min, and solution color tuned to pink. The GNPs/silica-nanohelices samples were collected by centrifugation. Due to the concentration of these CTAB stabilized GNPs following the above described method is lower than the CIT-stabilized GNPs. Furthermore, the suspension was diluted twice by ethanol, therefore the final concentration of particles is 0.25 mM with respect to 0.5 mM of KAuCl4 in the case of GNPs stabilized by citrate. Therefore, we have investigated the range of the quantity of silica-helices between 5 µl -100 µl instead of 10 µl - 1 ml with CIT-stabilized GNPs (Figure V.14).

When 100 µl of MPTES-functionalized silica-nanohelices suspension (0.12 wt%) were dispersed into 500 µl of GNPs suspension (0.25 mM) under the ultrasonication. 500 µl of ethanol was then added to the suspension. The sonication was continued for 10 min, and solution color tuned to pink. As the quantity of silica was deceased, the solution color tuned violet (10-50 µl of silica suspension) (Figure V.14 a) and particles became non-spherical shapes and/or formed aggregates (5 µl of silica suspension) (Figure V.14 e). Therefore, the better condition was addition of silica-nanohelices with the range of 10-25 µl for 500 µl of GNPs suspension. Interestingly, the aspect of these silica/GNPs suspensions were quite different from those obtained with silica/GNPs(citrate). CIT-GNPs easily tuned to precipitate upon addition of silica-nanohelices in water as well as alcohol, whereas the CTAB-GNPs/silica-nanohelics showed much better dispersion in ethanol. This may be because CTAB acts as dispersion stabilizer for GNPs as well as silica helices caused by adsorption of alkyl chains of amphiphiles

on the both surface of GNPs and silica fibers.
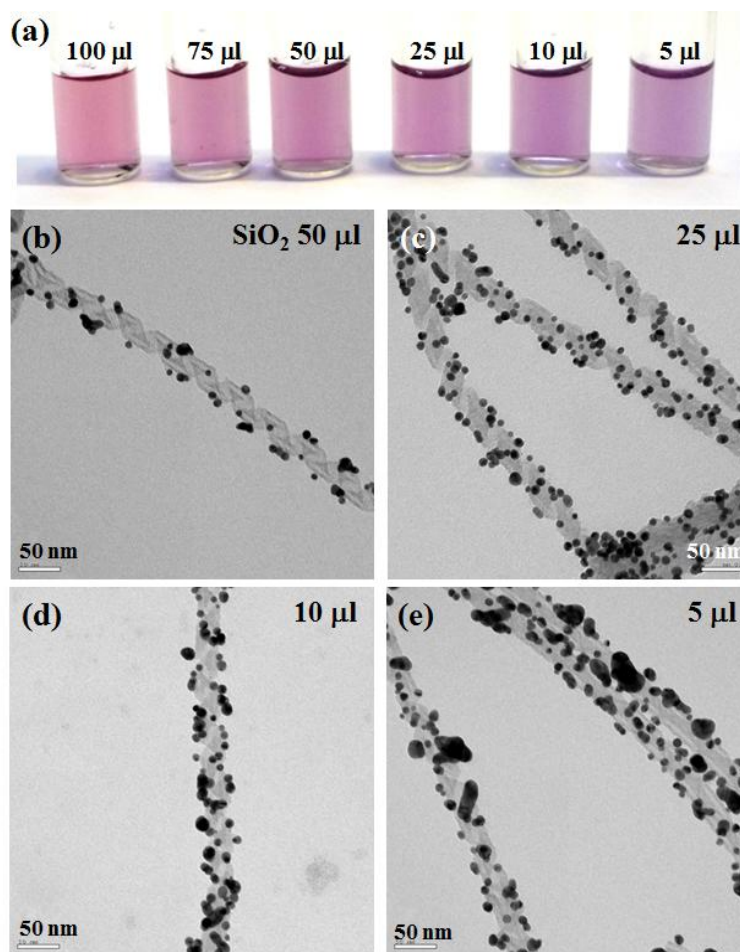
Figure V.14 (a) Macroscopic aspect of GNPs/silica-nanohelices suspension prepared by different volume of silica. (b-e) TEM images of CTAB-stabilized GNPs immobilized on the various amounts of silica- nanohelices. The volumes of silica-nanohelices suspension were (b) 50 µl, (c) 25 µl, (d) 10 µl, and (e) 5 µl.

In order to remove the excess CTAB, the GNPs/silica-nanohelices samples were washed by centrifugation (6500 rpm) and dispersion in ethanol before the preparation of TEM grids.

Step by Step GNPs adsorption

When the adsorption process was repeated, it promoted more GNPs immobilizing onto the silica surface while keeping the spherical shapes (Figure V.15). When 100 µl of

silica-helices (0.12 wt %) suspension was mixed with 500 µl of GNPs, few GNPs could be immobilized on the silica surface (Figure V.15 a). After the suspension was submitted to centrifugation and the upper phase became transparent. This was removed and replaced by, another 500 µl of GNPs solution. As this process was repeated several times, more and more GNPs were adsorbed on silica surface (Figure V.15 b-d). and the solution color became darker.
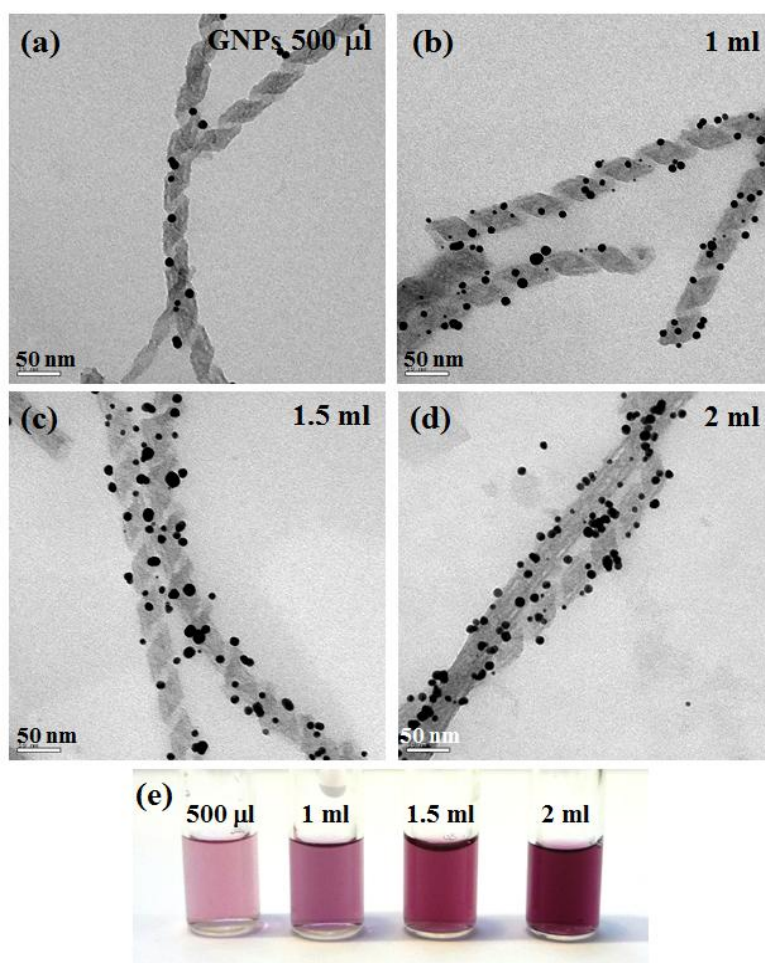
Figure V.15 (a-d) TEM images of CTAB-stabilized various amounts of GNPs immobilized on the 100 µl silica-nanohelices. The various amounts of GNPs were (a) 500 µl, (b) 1ml, (c) 1.5 ml, and (d) 2 ml. (e) Macroscopic aspect of GNPs/silica-nanohelices suspension prepared by varying amounts of GNPs for 100 µl of silica-nanohelices.

Comparing the single step and several steps of adsorption GNPs, the latter case could provide more consistent shape and less aggregation, but less coating of GNPs than the case of single step.

We also investigated the hybrid nanostructures obtained from the CTAB-stabilized GNPs adsorbed on the surface silica-nanohelices by optical properties of LSPR using UV-vis spectra (Figure V.16).

Free GNPs exhibited strong LSPR peak at 519 nm. When 500 µl of GNPs were adsorbed on the various quantity of silica surface, the LSPR peak showed red-shift. While the peak was shifted to 522 nm when 100 µl of silica was added, more important peak shift was observed (to 533 nm) with smaller quantity of silica (5 µl) accompanied by the broadening of the peak (Figure V.16 a). This suggests that the GNPs formed larger and nonspherical particles on the nanofiber surface as also confirmed from TEM analysis of these samples.[10]
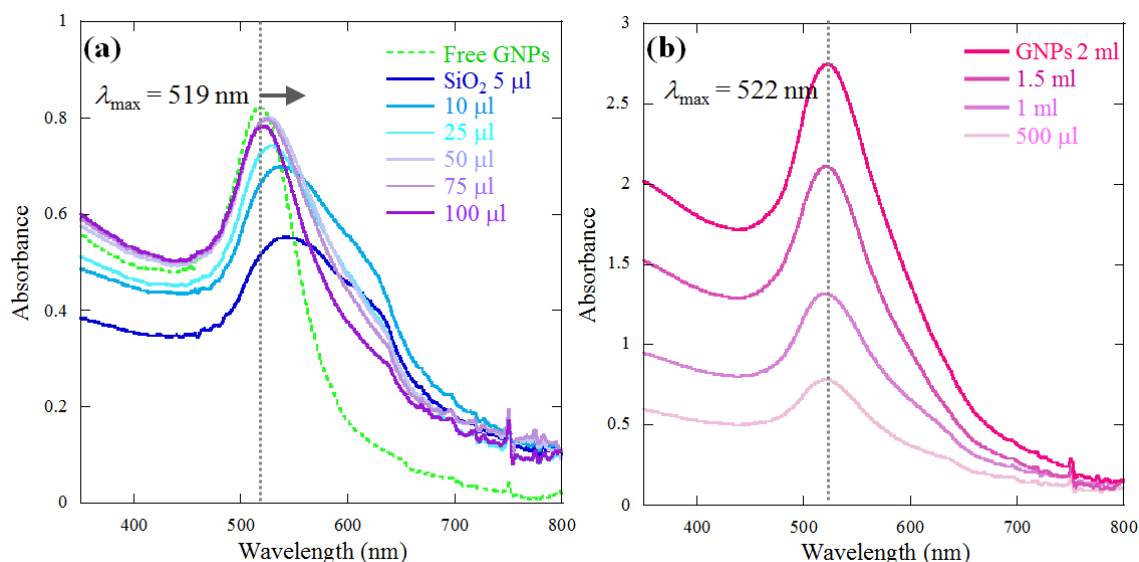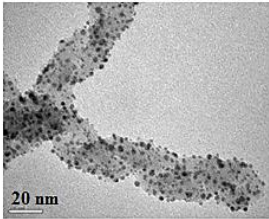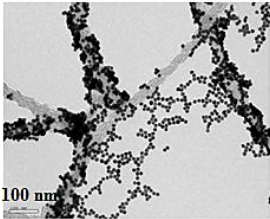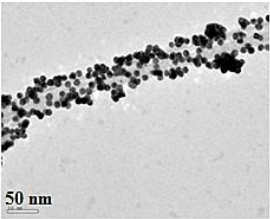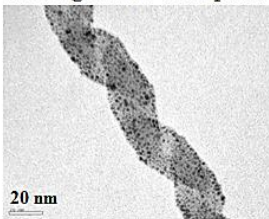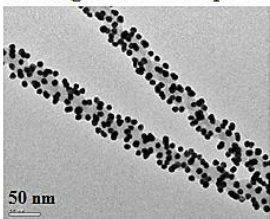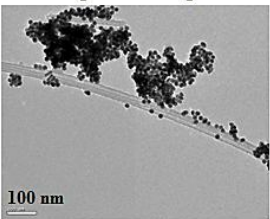
Figure V.16 UV-vis spectra of LSPR bands obtained that (a) various amounts of silica-nanohelices coated by GNPs, or (b) various amounts of GNPs adsorbed on the silica surface.

For the case of hybrid nanostructures obtained by further addition of GNPs with repeat process, on the other hand, the intensity increased with increasing the amounts of GNPs, and the red-shift was not observed (Figure V.16 b). This behavior suggests that the method of varying amounts of GNPs could promote more uniformly GNPs/silica-nanohelices nanostructures.

V.3.4 Summary of GNPs adsorption on silica-nanohelices

In this section, we demonstrated the adsorption of various GNPs stabilized by different capping agents on the silica-nanohelices. The results of various conditions as described above are summarized in Table V.4.

Table V.4 Summary of condition of various GNPs adsorbed on the surface of silica-nanohelices. (a, b) GNPs/silica-nanohelices suspension kept in water, and (c) in ethanol.

	(a) THPC-stabilized GNPs	(b) CIT-stabilized GNPs	(c) CTAB-stabilized GNPs
-SH functionalized silica-nanohelices by MPTES	Homogeneous adsorption	GNPs aggregated and Inhomogeneous adsorption	good adsorption
-NH$_2$ functionalized silica-nanohelices by APTES	Homogeneous adsorption	Homogeneous adsorption	GNPs aggregated and poor adsorption

Results from Table V.3 show that the homogeneity of the adsorption of GNPs was size dependent: for 1-2 nm size THPC-stabilized nanoparticles, there was no difference in-between the nature of the silica functional groups (-SH or NH$_2$). Both silica were well covered by THPC-stablized small nanoparticles.

For bigger size nanoparticles, there seem to be a competition between the different potential ligands and the process leading to the maximum decrease in the surface energy prevails. With respect to the energy difference due to stabilization, the processes can be ordered depending on the chemical bond strength: S-Au interaction > N-Au interaction > Carboxylate-Au interaction.

The competition between electrostatic (CIT) and donor ± acceptor (APTES) stabilization in these conditions gave rise to a nice distribution of the GNPs along the silica helices with a good compromise between the two stabilizations probably due to stabilizers of opposite charges (ammonium and citrate). On the other hand, in the presence of MPTES functionalized silica, these GNPs showed strong local aggregation and did not show homogeneous distribution over the silica surfaces. As a result, there were domains where GNPs showed thick aggregations and others where no GNPs adsorption was observed.

The GNPs stabilized by CTAB showed poor adsorption in water both for APTES functionalized and MPTES functionalized silica (data not shown). This is probably because the bilayers formed by CTAB at the surface of GNPs prohibit their adsorption on silica surfaces. In the case of APTES functionalized silica, there may also be charge repulsion between ammonium from amine groups (APTES) and quaternary ammonium (CTAB). Upon addition of ethanol, the solubility of CTAB increases, breaking their aggregates on GNPs. This can promote stronger interaction between GNPs with silica surfaces. In the case of MPTES functionalized silica, CTAB-GNPs showed relatively good adsorption with silica. In the presence of APTES functionalized silica, however, these GNPs still did not show good adsorption, instead, GNPs aggregated among themselves. In this case, the addition of ethanol destabilized the GNPs and provoked their aggregation. Globally, however, the CTAB-stabilized GNPs showed less homogenous adsorption than CIT- and THPC-stabilized GNPs.

Several other factors are also crucial for the quality of GNP covered silica helices. The first one is the addition order of the reactants in the reaction medium; we have indeed observed that in all cases, the coverage was much more homogeneous when the silica nanohelices were added into the GNPs solution rather than when the GNPs solution was added to the suspension of silica nanohelices. The concentration of organic gel is also a key point. Using dilute suspensions of helices (< 2 mM) allowed to obtain silica helices with very little

quantities of intersection knots in which the GNPs tend to be trapped and form inhomogeneous distribution.

V.4 The growth of small THPC-stabilized GNPs at the surface of silica-nanohelices and study of optical properties

V.4.1 The particle growth promoted by replacement of solvents

The hybrid nanostructure obtained by THPC-stabilized GNPs and silica-nanohelices exhibit interesting property.

Such hybrid nanohelices were generally stable even after a week in water. They grew to 2 nm after a month. Interestingly, when these nanocomposite structures were put into polar organic solvent such as alcohol (ethanol, methanol, hexafluoroisopropanol (HFIP)) or acetonitrile, the size of the particles on the surface of the helices increased to a few nanometers after a day (Figure V.17).
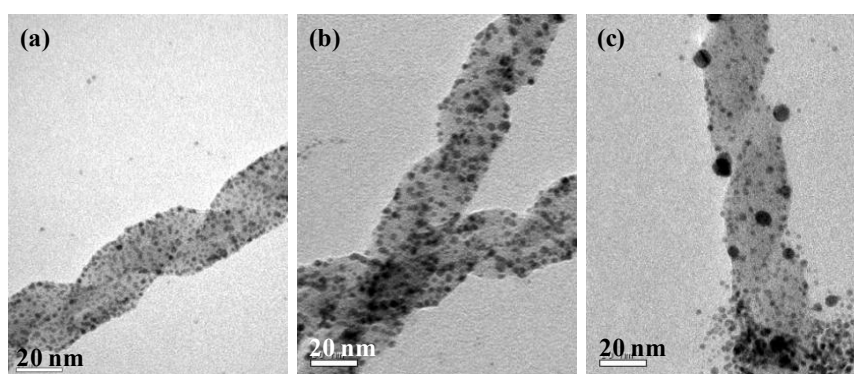
Figure V.17 TEM images of THPC stabilized GNPs immobilized on the surface of silica-nanhelices. GNPs/silica-nanohelices hybrid structures were kept in water (a), in ethanol (b), and acetonitrile (c) after 1 day.

Figure V.18 illustrates this growing process in HFIP. While kept in HFIP, the color of precipitate was slowly tuned from brownish yellow to reddish brown for red-brown for a week

(Figure V.18 a1-a3). The GNPs immobilized on the surface of silica-nanohelices grew quickly to ~ 2 nm after 2 h (Figure V.18 c1), ~3 nm after 1 day (Figure V.18 d1), then to about 5 nm after 1 week (Figure V.18 e) in suspension of HFIP, alongside with a decrease of their number observed per silica helix, indicating that the particles coalesce and show an Ostwald ripening process.[42,43] Such a growth could be stopped as soon as the solvent was exchanged by water (Figure V.18 b2, c2, d2). The size of these GNPs then remained identical even after a week (Figure V.18 e).
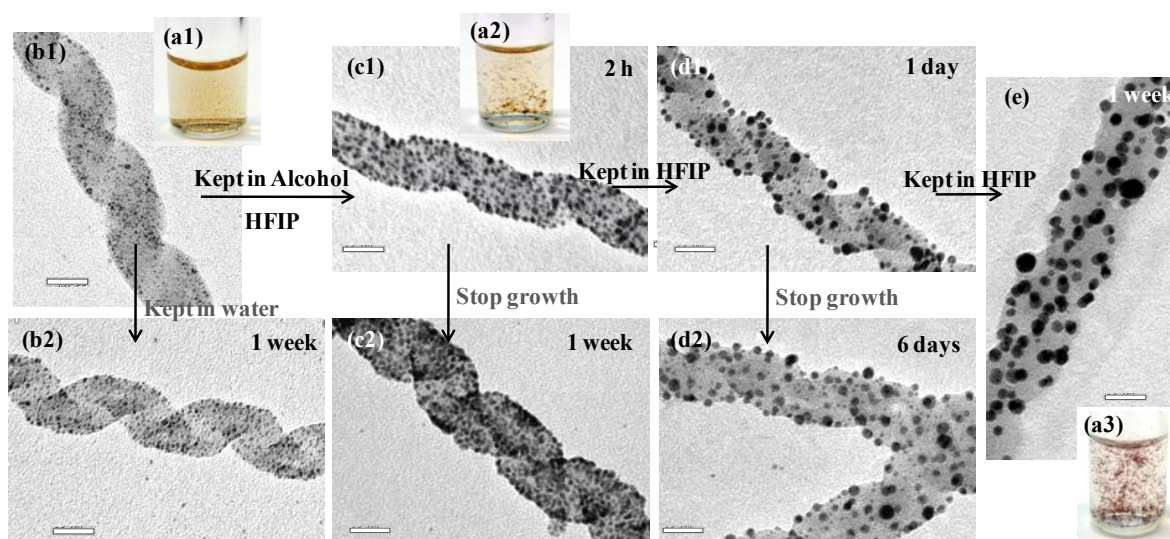
Figure V.18 (a) Macroscopic aspect of precipitate of GNPs/silica-nanohelices hybrid structures. (b-e) TEM images of growth process of GNPs at the surface of silica-nanohelices. (b1) GNPs with 1.5 nm diameter were immobilized on the surface of silica-helices. (c1, d1, e) GNPs grew up to around 5 nm in suspension of HFIP. (b2) GNPs kept their diameter in water for a week. (c2, d2) The samples were replaced in water, the growth of GNPs were stopped. Bars are 20 nm.

Figure V.19 shows the variation of the particle diameter with time. The free GNPs alone as well as the GNPs/nanosilica nanocomposite suspension in water did not show the growth process (Figure V19, black square and open circle respectively).
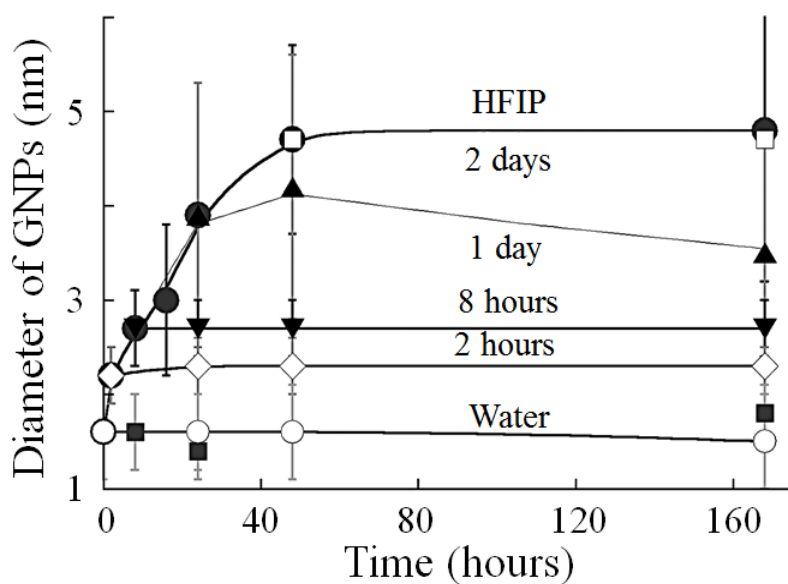
Figure V.19 The time evaluation vs diameter change by GNPs growth. Diameter measurements were performed on an average of 500 particles.

In general, small GNPs (< 2 nm) do not show localized surface plasmon resonance (LSPR) band (Figure V.20) owing to the onset of quantum size effects observed for NP < 3 nm.[44] The color of the suspension of such GNPs as well as those adsorbed at the surface of nanohelices is brown. When the GNPs/nanosilica samples are kept in water, no LSPR peak appeared even after one week, it took 3 weeks to see a weak band appear (Figure V.20 a). However, when the samples were kept in HFIP, a broad LSPR band appeared at 526 nm after only 2h (Figure V.20 b). As the GNPs grew larger (~ 5 nm), this LSPR band increased in intensity, became sharper, and the color of the suspension turned to red.[45,46] In the literature, some examples have shown that small GNPs could grow on fiber or particle surface.[47,48,49] However, in these cases, the authors used polar organic solvent as a reducing agent capable of reducing the free metallic cations which were still present in solution.[50,51] In the present case, at the condition in which the nanohelices are stored, no free gold ions are present because excess of GNPs and Au salt were completely washed away by water before solvent replacement. Clearly the growth of GNPs is due to the coalescence of smaller GNPs.

The resonant frequency of the plasmon absorption band of the metal nanoparticle due collective oscillation of the free electrons confined to the surface is sensitive to changes in the size of the particle and as the diameter gets higher the energy required to collectively excite the

motion of the surface plasmon electrons decreases. For free GNPs with diameters from 3.5 to 37 nm, the energy required to excite the surface plasmon corresponds to a maximum absorbance around 524 nm.[45] This process also depends on the shape of GNPs, chemical nature, as well as the surrounding medium.[52,53,54] Upon adsorption on the helix surface and by consequence placed in close proximity to one another on the helix surface, the LSPR of the GNPs did not show notable shift and remains located at 525 nm.[55]
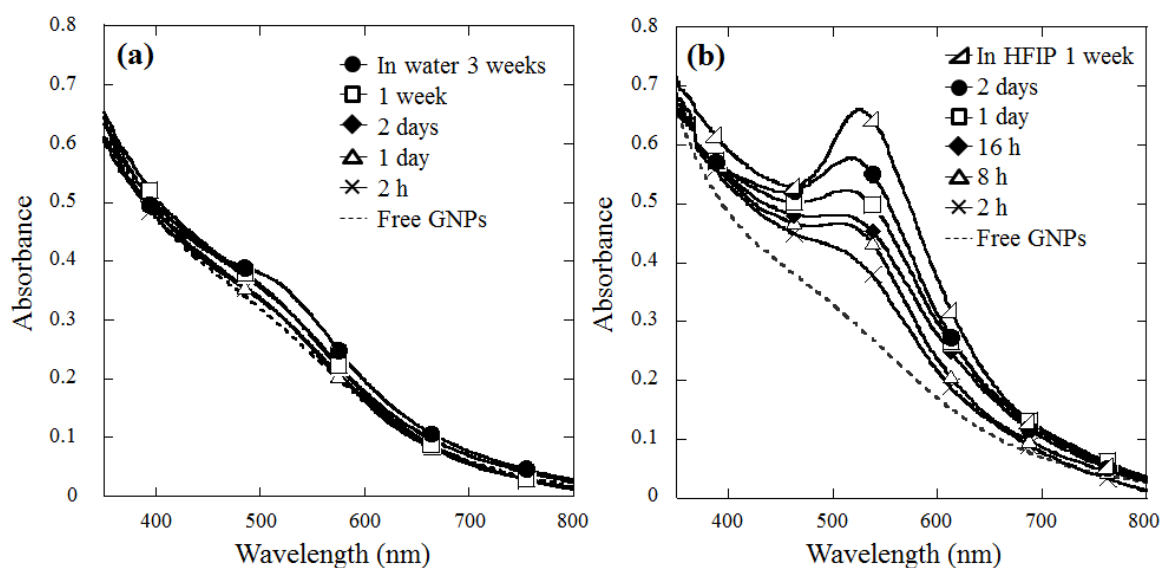
Figure V.20 UV-vis spectra of the GNPs/silica-nanohelices suspension kept in (a) water and (b) kept in HFIP.

V.4.2 The particle growth on the surface of silica-helices by addition of gold salt and reducing agent

The particle growth on the surface of silica-helices was also promoted by addition of a growth solution containing both a gold salt and a reducing agent. Various volumes (10-100 μl) of 1 mM KAuCl$_4$ solution and 4.8 mM L-ascorbic acid (LAA) solution were added at once to 500 μl silica-nanohelices suspension coated with THPC-GNPs. After sonication of the suspension composed of the mixture of silica nanohelices and KAuCl$_4$, a 1:1 equivalent of LAA solution (10-100 μl) was added. The color of the solution immediately turned to reddish brown.

As increasing the addition of mixture volume, the suspension color became more erubescent (Figure V.21).
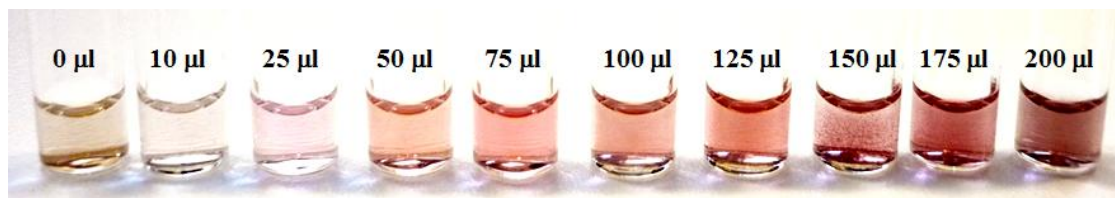
Figure V.21 Macroscopic aspect of GNPs growth on the surface of silica-nanohelices obtained by addition of fresh gold salt and reducing agent (10 ~ 200 µl for each solution).

TEM images of these silica-nanohelices are shown in Figure V.22 a. The size of the GNPs increased homogeneously and continuously, keeping spherical shape with the increasing quantity of added 1:1 volume mixture of gold salt and LAA solution up to around 5 nm. At this point, the volume of the added solution is 100 µl. Upon further addition of the solutions, the size of the particles became extremely heterogeneous leading to highly non spherical particles.
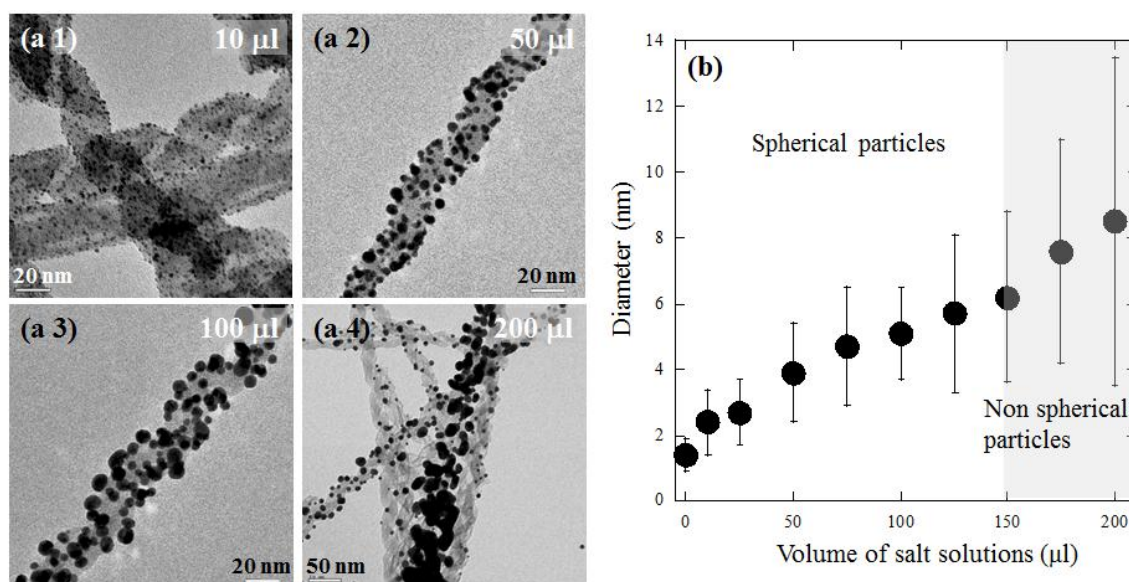
Figure V.22 (a1) to (a4) TEM images of growth process of GNPs at the surface of silica-nanohelices; the volumes of growth solution used for GNPs growth were (a1) 10 µl, (a2) 50 µl, (a3) 100 µl, and (a4) 200 µl. (b) Variation of the GNPs diameter with the added volume of growth solution (diameter measurements were performed on an average of 500 particles).

UV-vis. spectra of GNPs on the silica substrate for different Au^{3+} salt concentrations are shown in Figure V.23. No LSPR peaks are observed for the silica suspension without added salt solution (GNPs diameter ~1 nm). This corresponds indeed to the brown color of the suspension. Upon addition of 10 to 25 µl salt solutions, a broad LSPR peak appeared at 530 nm. This peak became more pronounced and blue-shifted to 523 nm with further increase of the added salt solution (50 and 100 µl).
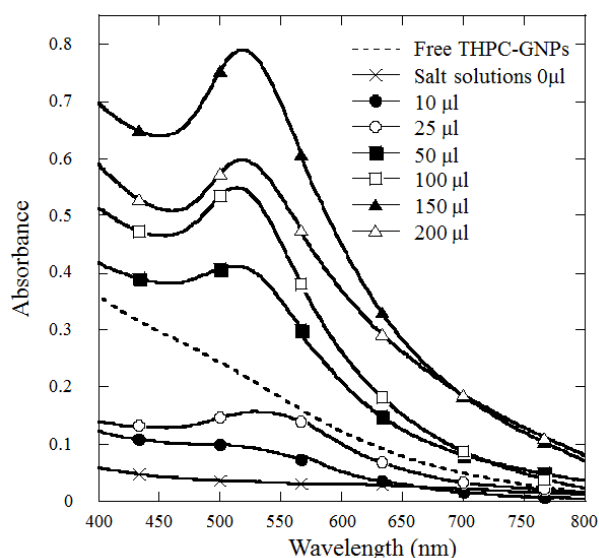
Figure V.23 UV-vis spectra of LSPR bands derived from GNPs growth at the surface of silica-nanohelices upon addition of salt solutions.

This method therefore provides an easy control of the size of ultra-small GNPs (USGNPS) on silica substrates.

It was also clearly observed that this growth is a kinetically controlled phenomenon. Figure V.24 shows comparison of the method of addition of gold salt and reducing agent in several steps (a-c) and in single step (d). Upon addition of 10 µl of growth solution into 100 µl GNPs/silica suspension, GNPs grew up to 2.4 ± 0.7 nm (Figure V.24 a). When another 20 µl of growth solution was added to this suspension, GNPs grew up to 3.5 ± 1.0 nm (Figure V.24 b). Further addition of 20 µl of growth solution resulted in the growth of GNPs to 4.3 ± 1.2 nm (Figure V.24 c). Addition of growth solution in several steps led to poor and inhomogeneous adsorption. On the other hand, when 50 µl of growth solution was added to suspension at once,

we could observe the homogeneous adsorption of larger sized GNPs with diameter 4.4 ± 1.2 nm (Figure V.24 d). The latter showed relatively homogeneous adsorption of larger size GNPs whereas the former showed separation between helices covered heavily by large GNPs and those which were poorly covered.
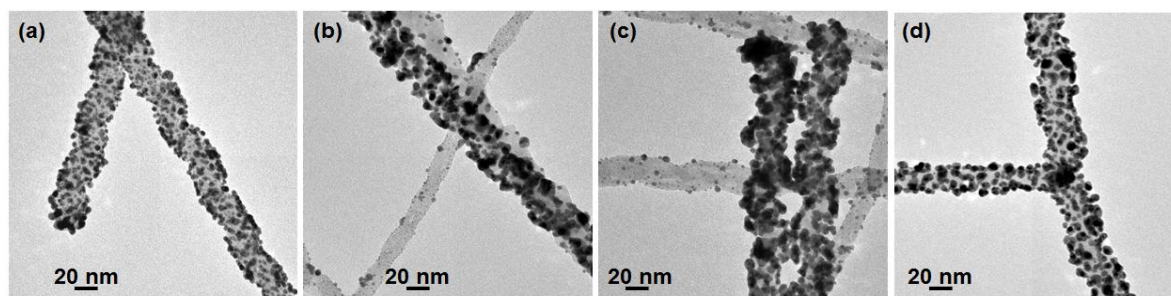
Figure V.24 Comparison of the particle growth upon addition of gold salt and reducing agent in (a-c) several steps or (d) single step. The volumes of growth solution added; (a) 10 µl, (b) 20 µl of second addition, (c) 20 µl of third addition, and (d) 50 µl in single step.

V.5 Larger GNPs deposited on the silica nanohelices

As we observed above, small GNPs show too moderate LSPR peaks. We then investigated how the confinement of larger GNPs on silica nanohelices could affect the LSPR signals.

For this study, we used CIT-stabilized GNPs (size range ~ 10-20 nm) in the presence of silica nanohelices functionalized with APTES. Figure V.25 shows silica nanohelices with GNPs of various sizes (10, 12, 14 nm) and their corresponding SPR peaks.

As we observed above, small GNPs show moderate LSPR peaks. We then investigated how the confinement of larger GNPs at silica nanohelices can affect the LSPR signals. CIT-stabilized GNPs adsorbed on silica exhibit much more pronounced LSPR bands than those obtained with GNPs stabilized with THPC.
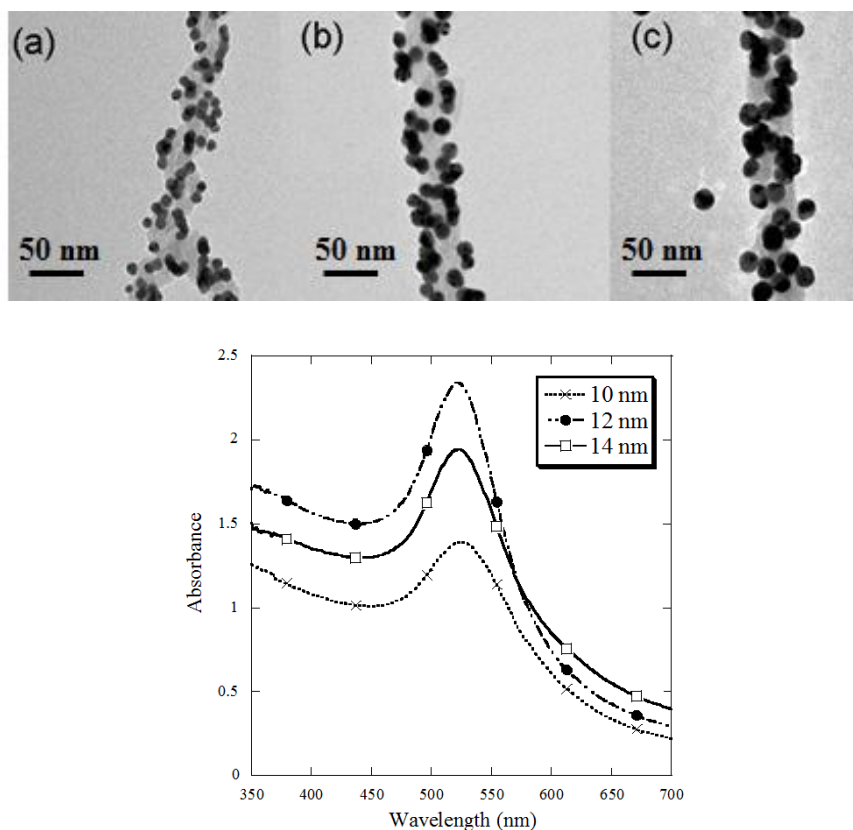
Figure V.25 silica nanohelices with GNPs, (a) 10 nm, (b) 12 nm, (c) 14 nm. (d) UV-vis spectra of GNPs adsorbed on the surface of silica nanohelices.

V.6 GNP/silica nanohelices used as SERS substrate

V.6.1 SERS study of chemical compound

As it has frequently been demonstrated, the localized SPR exhibited by noble metal nanoparticles beyond a certain size can be exploited in the context of surface enhanced Raman scattering (SERS). It has also been demonstrated that the gold surface morphology has an important effect on the enhancement of the Raman signal.[56] Figure V.26 shows the SERS spectra of benzenethiol (BT) used as molecular probe adsorbed on hybrid nanostructures containing various diameters of spherical GNPs. The SERS spectrum is characteristic of BT adsorbed on

Au substrate.[57,58,59] The main bands are observed at 1075 cm^{-1}, 1025 cm^{-1}, 1000 cm^{-1}, assigned to ν_1, ν_{18a} and ν_{12} ring modes, respectively. The intensity of ν_1 mode at 1000 cm^{-1} was used to calculate the enhancement factors (EF) according to EF = $(I_{SERS} \times C_{BT})/(I_{BT} \times C_{SERS})$, where I_{SERS} is the surface-enhanced Raman intensity of BT whereas I_{BT} is obtained by a free BT solution, C_{SERS} and C_{BT} are the molecular concentrations of BT in aqueous solution in the presence and in the absence of GNPs/silica-nanohelices respectively.
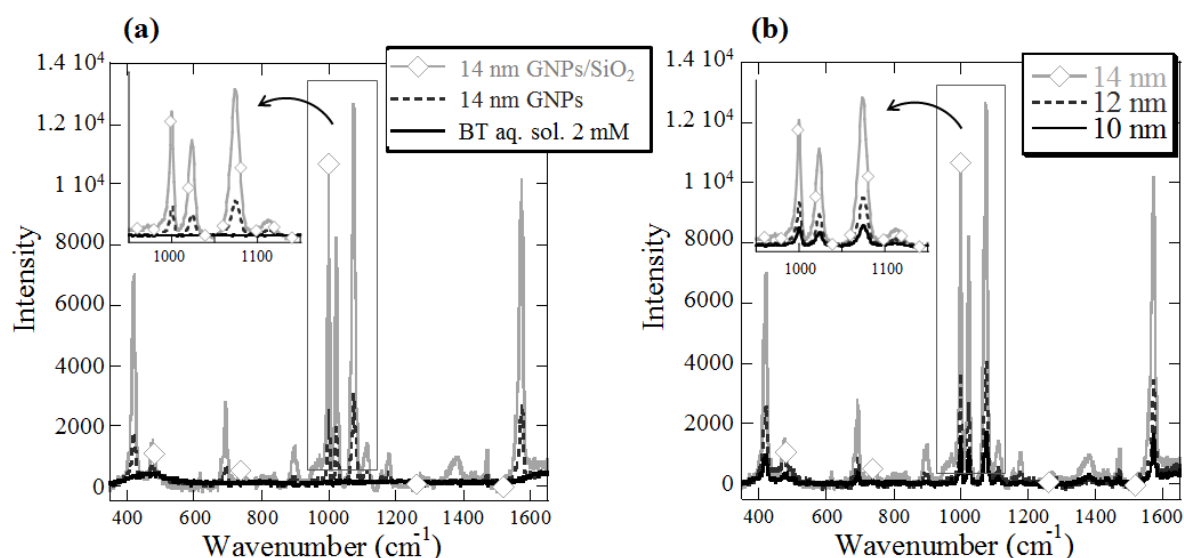
Figure V.26 Raman and SERS spectra of Benzenethiol. (a) Comparing the Raman signals of 10^{-2} M BT aqueous solution, SERS spectrum of 10^{-6} M BT molecules adsorbed on GNPs colloid solution, and SERS spectrum of 10^{-6} M BT molecules adsorbed on GNPs/silica-nanohelices hybrid structures. (b) SERS spectrum of 10^{-6} M BT molecules adsorbed on GNPs/silica-nanohelices hybrid structures with different diameters (10, 12, 14 nm).

The Raman spectrum obtained for a 10^{-2} M BT solution in water and the SERS spectra of 10^{-6} M BT with GNPs colloid solution and with GNPs/silica-nanohelices hybrid structures are shown in Figure V.26 a. In the absence of GNPs, no signal was detected with BT solution even at concentrations as high as 10^{-2} M. Indeed, the lowest detection limit for the concentration of BT by Raman scattering is 10^{-1} M. Meanwhile, highly enhanced Raman signals were observed when BT was adsorbed on the GNPs surface. Furthermore, when these GNPs were adsorbed and organized on the surface of silica-nanohelices a dramatic enhancement of Raman signal was observed. This enhancement factor strongly depended on

the particle size (Figure V.26 b); the EF of the nanohybrid with 10, 12 and 14 nm GNPs is 8.6×10^4, 2.0×10^5, 5.7×10^5 respectively. The EF in the presence of free GNPs is 8.5×10^4 (12 nm) and 1.2×10^5 (14 nm). This indicates that GNPs organized at the surface of silica-nanohelices lead to an enhancement of the signal by a factor of 5 as compared to those free in solution.

We then investigated the effect of the BT concentration for different GNPs sizes. Figure V.27 (a) shows the variation of the enhancement factor deduced from the intensity of the band at 1000 cm^{-1} vs. the BT concentration. We observe a general trend indicating that the EF increases with decreasing concentration. This phenomenon seems to be even more efficient for the biggest nanoparticles.

The SERS intensity is lower for high concentration; this could be explained by a Langmuir like process leading to saturation of the adsorption sites. The decrease of the SERS signal would reflect the staking of the adsorbed molecules and a reabsorption of the scattered light. Alternatively, an increase of the aggregation state of the GNPs nanoparticle for large BT concentration could also decrease the Raman signals.

In order to understand such phenomena on the variation of SERS intensity as a function of BT concentration, we compared them with TEM images of the systems (Figure V.27 b-e). As it is clearly visible, smaller GNPs (10 nm) show much more homogeneous adsorption on the surface of silica nanohelices at all studied concentration (10^{-7} - 10^{-4} M) compared to 14 nm GNPs. Indeed, the larger GNPs seem to show desorption from the silica and to aggregates separately at high concentration (10^{-4}M), which will probably explain the decrease in SERS intensity in the presence of high concentration of BT (Figure V.27 c). This is probably because the preparation of smaller particle uses higher concentration of sodium citrate as reducing agent, which gives more anionic feature to the smaller particles than to the larger particle. Furthermore, it is much easier to fit on the curve of a silica helix with the smaller particles (10 nm) because of their less bulky space. Consequently, the smaller particles adsorb better on the surface of amine functionalized silica-nanohelices even at high concentration of BT.
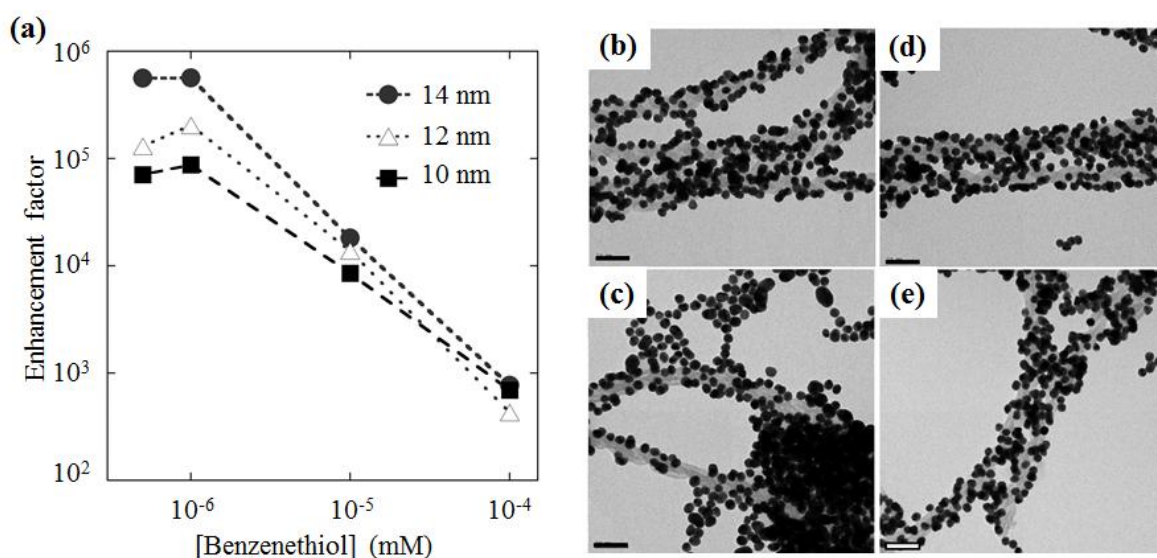
Figure V.27 (a) Variation of the enhancement factor at 1000 cm^{-1} vs. concentration of BT. TEM images of different concentrations of BT 10^{-5} M and 10^{-6} M with two different GNPs sizes 10 nm and 14 nm. (b) 14 nm, 10^{-6} M; (c) 14 nm, 10^{-5} M; (d) 10 nm, 10^{-6} M and f) 10 nm, 10^{-5} M GNPs/silica-nanohelices. Desorption and aggregation of GNPs (14 nm) is clearly seen for high concentration of BT (c). Scale bar 50 nm.

V.5.2 SERS study of medical agents as bioactive molecules

We then investigated several bioactive molecules. Thiamine is well known as Vitamin B1, which exists in nature.

Figure V.28 shows the SERS signals of thiamine aqueous solution. The observed SERS signals were characterized by the intense peak at 1650 cm^{-1} due to the N4'H$_2$ bending vibration, pyridine ring stretching mode at 1633 cm^{-1},1601 cm^{-1}, 1564 cm^{-1} and 1373 cm^{-1}, C-H (CH$_2$-CH$_2$ + C$_b$H$_2$) deformation mode and thiazole ring stretching mode at 1272 cm^{-1} and 1301 cm^{-1}, and strong pyridine ring deformation mode at 754 cm^{-1}.[60,61] The limited concentration of thiamine for detection of Raman signal is 10^{-1} M. When thiamine was adsorbed on the GNPs/silica-nanohelices hybrids structure, and the Raman signals could be detected below 10^{-6} M, which means the EF can be up to around 10^{5}. Comparison between 12 nm and 14 nm of GNPs, indeed bigger GNPs showed stronger intensity, however these differences were slight.
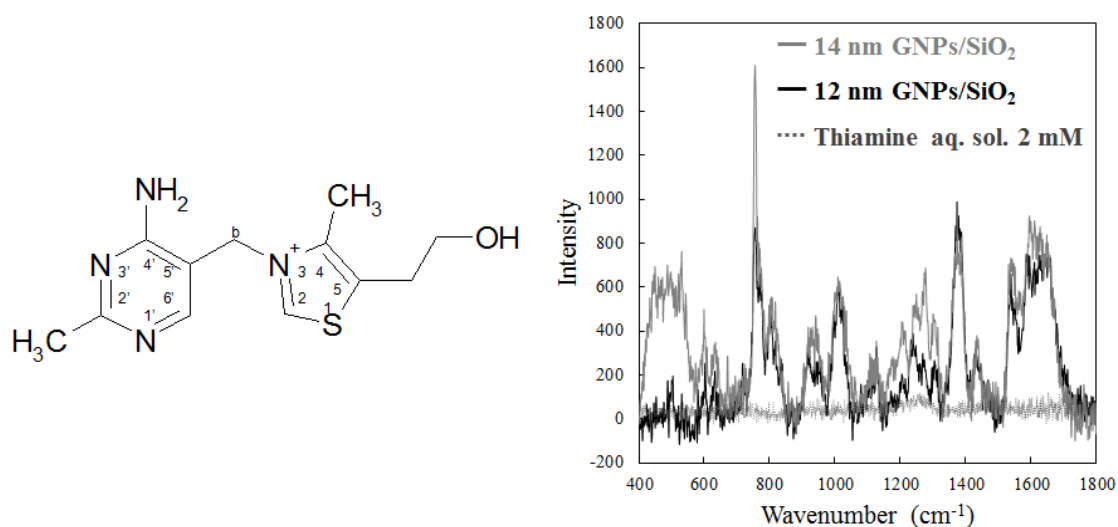
Figure V.28 Molecular structure of thiamine (upside) and SERS spectra of 10^{-6} M thiamine adsorbed on the 12 nm and 14 nm GNP/silica-helices suspension.

However, we also compared the SERS spectra from 14 nm free GNPs and 14 nm GNPs/silica-nanohelices in the presence of thiamine (Figure V.29). The concentration of thiamine molecule was 10^{-6} M. Enhanced Raman signals were obtained in both cases, no differences of enhancement were obtained. In this case, the presences of silica helices do not enhance the Raman signals because positive charged amine in thiazole group of thiamine showed charge repulsion to amine functionalized silica surface.
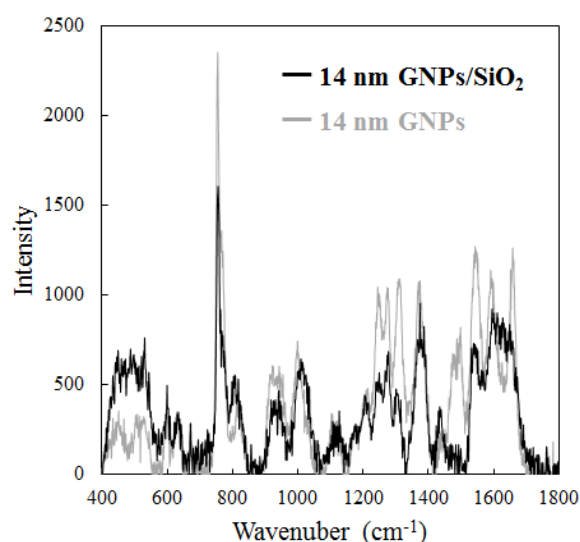
Figure V.29 SERS spectra of 10^{-6} M thiamine adsorbed on the 14 nm colloid solution and 14 nm GNP/silica-helices suspension.

We have also studied SERS systems of various medical agents such as aspirin, acetaminophen, ibuprophen and salicylic acid. Upon addition of these molecules, the GNPs remained adsorped on the silica nanohelices, but none of them showed SERS effects. This is probably because the interaction between –NH or –COOH of target molecules and the GNPs is not strong enough to be adsorbed around the GNPs.

We have also studied mono, oligo and polynucleotide. First we investigated the solution of polyadenosine (pA). A solution of 10^{-5} M pA was prepared in the presence of 0.5 mM $MgCl_2$. When pA was added to the solution of free GNPs colloid, the color of the solution remained red indicating a homogeneous suspension of GNPs even in the presence of pA. At this point, a weak signal of pA appeared (Figure V.30). When pA was added to the suspension of GNPs/silica suspension, the color turned immediately from red to blue, and the signal of pA decreased. TEM image of this solution showed that GNPs were still adsorbed on silica fibers but these silica fibers were strongly aggregated.
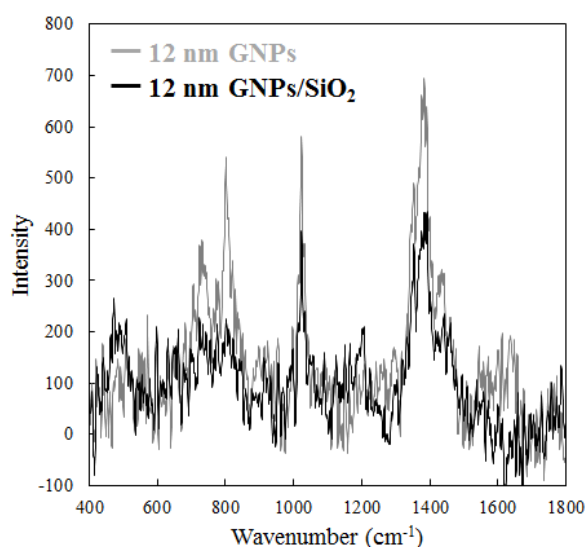
Figure V.30 SERS spectra of 10^{-5} M pA adsorbed on the 12 nm GNPs colloid solution, and on the 12 nm GNP/silica-helices suspension.

We also investigated adenosine 5'-monophosphate (AMP). When AMP solution was added to the free GNPs solution, the enhanced Raman signal of AMP appeared. On the other hand, when it was added to the suspension of GNPs/silica-nanohelices, the signal of AMP

became almost non detectable (Figure V.31). It is likely that AMP was on functionalized silica surface due to the interaction between phosphate (AMP) and amine group of silica surface.
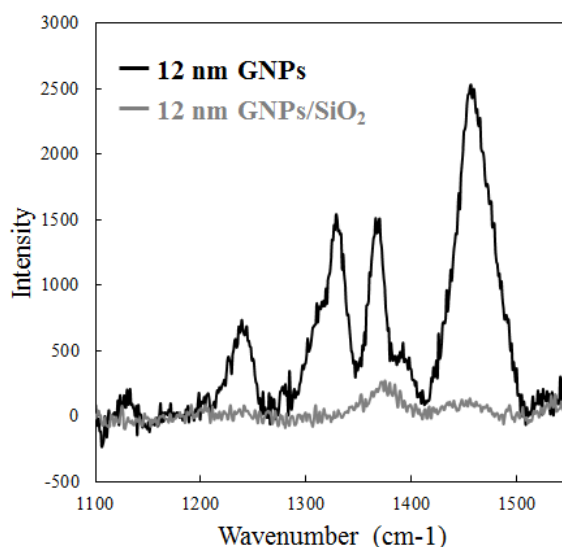
Figure V.31 SERS spectra of 10^{-5} M AMP adsorbed on the 12 nm GNPs colloid solution, and on the 12 nm GNP/silica-helices suspension.

The results obtained with pA indicate that the interaction between GNPs and the interaction between anionic polynucleotide and APTES functionalized silica nanohelices maybe stronger than the interaction with GNPs resulting the extinction of Raman signals of polynucleotide. Hence, we performed SERS experiment using CTAB-stabilized GNPs adsorbed on mercapto functionalized silica-nanohelices. In this case, the GNPs are covalently attached to the silica helices. However, CTAB stabilized GNPs exhibits strong LSPR band of CTAB themselves, which hinders the detection of the targeting molecules. Therefore we could not use this system for SERS substrate.

Therefore, we tried another strategy. We designed binder molecules which can be substituted from ester to amide upon addition of molecules with amine group (Figure V.32). Here, we used trimeric AMP (tridAMP). First, binder molecules were reacted with the GNPs adsorbed on silica helices, then tridAMP was added to the solution. From the ATR results, the band at 1720 cm^{-1} (white arrow) characteristic of ester group disappeared and the band at 1650 cm^{-1} (black arrow) characteristic of amide group appeared upon addition of tridAMP, suggesting that tridAMP could be immobilized on the GNPs/silica-nanohelices structures.
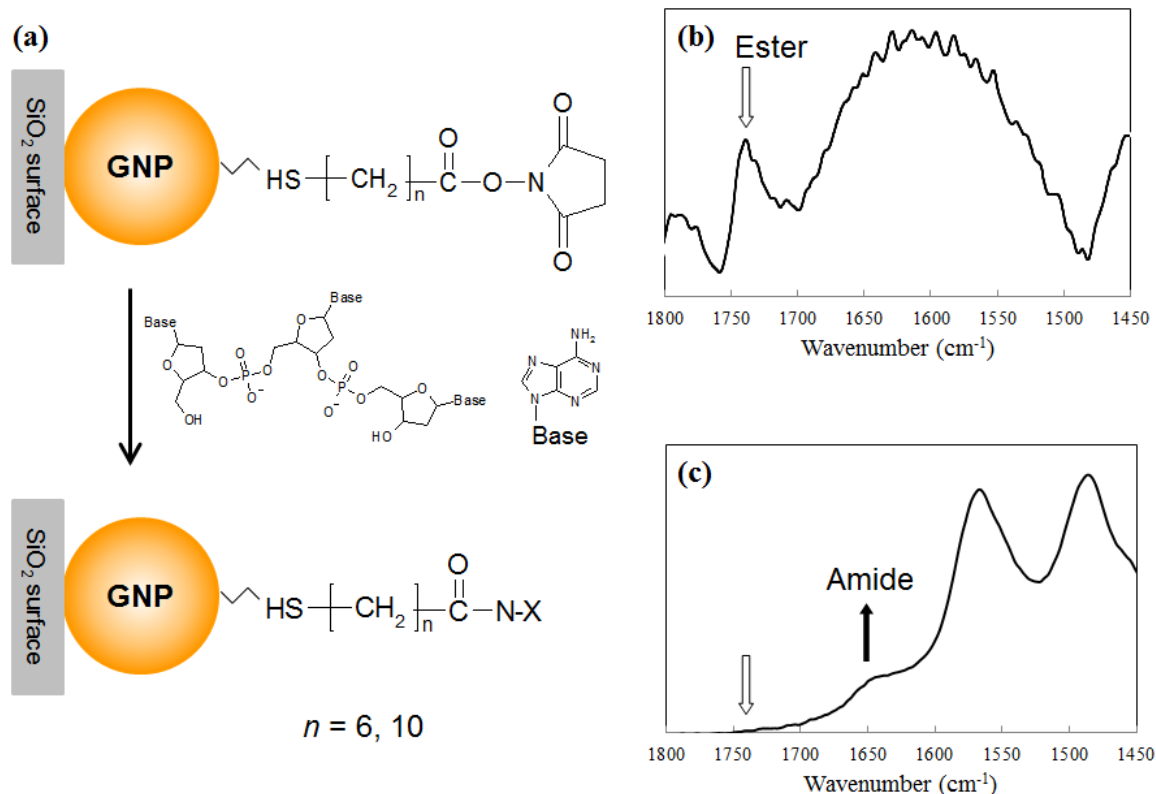
Figure V.32 (a) Binder molecule and ATR spectra of (a) before and (c) after addition of tridAMP.

However, these systems did not demonstrate SERS effect. It is probably because the distance between GNP and target molecule is too long to induce the signal enhancement due to the long alkyl chain of binder molecules. Meanwhile, using the same principle with shorter binder molecule, this approach may give a promising alternative which provides the possibility to detect the various molecules by injecting the small binder molecules.

V.6 Conclusion

We developed the procedure for synthesizing new systems which consist of the various kinds of Au nanoparticles adsorbed on the surface of helical silica nanofibers. Promoting the size and surface charge of an Au nanoparticle is strongly depended on the stabilizing agent.

Helical silica nanofibers synthesized from the organic self-assemblies of 16-2-16 L-tartrate amphiphiles by sol-gel transcription were functionalized with APTES or MPTES and GNPs/silica-nanohelices hybrid structures were obtained with GNPs having various sizes. The quantity of adsorped GNPs as well as their homogeneity depended on various factors such as the GNPs size, silica surface function (APTES or MPTES), as well as the stabilization agents of GNPs.

When the nanohybrid structures based on THPC stabilized GNPs with 1 ~ 2 nm diameter were kept in some of the organic solvents such as alcohol, GNPs at the surface of silica-nanohelices grew to 5 ~ 6 nm with time whereas such a growth was not observed with hybrid helices suspension in water. Such a growth was also observed by addition of gold solution to the suspension of silica adsorbed with THPC-GNPs: the diameter of GNPs increased with the concentration of gold salt also up to around 5 nm. Beyond this concentration, the size of the particles became extremely heterogeneous leading to highly non spherical particles.

The surface plasmon resonance of the nanohybrid systems increased with particle sizes. For the GNPs with 10 to 14 nm diameter, these hybrid systems clearly showed surface enhanced effect on Raman spectroscopy. The enhancement factor obtained on the surface of hybrid nanostructure was 5.7×10^5 for benzenethiol.

Using the functionalized 3D silica nanohelices, we designed novel SERS substrate based on 3D gel network of GNPs/silica-nanohelices hybrid nanostructures. The 3D network of these GNPs/silica-nanohelices hybrid structures can potentially be used as ultra-sensitive chemical and biological sensors for liquid phase. Indeed, typical SERS substrates reported in the literature are made from novel metal nanopaticles assembled on planar surfaces or patterned surface.[17,18,19,56,62] Thus, novel GNPs/silica-nanohelices is a promising system for the powerful SERS substrate to detect dilute solution of molecules. Meanwhile only the model molecule benzenthiol showed the SERS effect with the present GNPs/silica-nanohelices hybrid

nanostructures, For other molecules that we have investigated, Au did not show strong enough binding (typically amino or carboxyl groups). In order to overcome this problem, we can modify of the surface of GNPs by active functionalized groups such as amino or carboxyl groups. Other molecules which show specific binding such as sugar, nucleobase, or urea groups can be considered. This opens up the possibility that various molecules can be adsorbed on GNPs and hence detected by SERS. The problem can also be addressed by the reverse approach. Direct immobilization of target molecules (*e.g.*, peptide, DNA) on silica-nanohelix can also be attempted. These silica can then be further coated by GNPs and used as SERS substrates.

Compared to the commonly used 2D SERS substrates, the use of such 3D network systems can open a totally new perspective towards high detection of molecules of interest through accumulation under flow.

V.7 Experimental session

Preparation and Functionalization of Silica-Nanohelices

Once adequate ageing time of the gels is reached, these organic self-assemblies were used as templates to prepare silica nanostructures through a sol-gel transcription procedure.[24] In a typical preparation, 500 μl of 5 wt% tetraethylorthosilicate (TEOS) was prehydrolyzed in water (pH 6) for 12 hours at room temperature before each run, and then added to 500 μl of 1 or 5 mM organic gels with various aging times (typically, 20 days or >45 days). The reaction mixture was vortexed (2000 rpm) for a few seconds, and then kept at 20°C for more than 36 hours. The samples were then thoroughly washed with ethanol to remove all organic components and excess TEOS. Finally the yields were 1.2 mg for 1 mM and 3.5 mg for 5 mM of initial organic gels in 1 ml suspension.

Functionalization of Silica-Nanohelices

The silica-nanohelices were then functionalized via a surface chemical modification with (3-aminopropyl)triethoxysilane (APTES) or (3-mercaptopropyl)triethoxysilane (MPTES). The washed silica-nanohelices were re-dispersed in water (pH 6), and 15 μmol/m^2 of APTES (0.48 μl for 1 mM or 2.4 μl for 5 mM initial organic gel) or MPTES (0.5 μl for 1 mM or 2.5 μl for 5 mM initial organic gel) was added. The amounts of APTES/MPTES were calculated as below.

In order to calculate the surface area of silica-nanohelices (S), density was assumed 1 in 5 mM of organic gels. S was calculated by

$$l = V/\pi(R^2-r^2), \text{ with } R = 15\times10^{-7} \text{ cm}, r = 10\times10^{-7} \text{ cm}, V = 1.8\times10^{-3} \text{ cm}^3$$

$$l = 4.60\times10^{6} \text{ m}$$

$$S = 2\pi(R+r)l$$

$$S = 0.72 \text{ m}^2$$

Generally, silane coupling agent was induced at least 15 μmol/m^2.

$$V_{APTES/MPTES} = 15S \times M_{APTES/MPTES}, (d_{APTES/MPTES} \cong 1)$$

$$V_{APTES} = 2.4 \text{ μl and } V_{MPTES} = 2.5 \text{ μl}$$

The reaction mixture was submitted to ultrasonication for 2 hours, and then kept in water overnight at 85 ˚C. After washing with ethanol, the step of functionalization by APTES or MPTES could be repeated. This procedure led us to in the average 0.12 wt% of silica-helices from 1 mM of organic gel, and 3.5 wt% silica-helices from 5 mM initial organic gel.

Synthesis of GNPs

In order to get various sizes of GNPs between 2 to 14 nm, three types of stabilizers were used: trisodium citrate (CIT), Cetyltrimethylammonium bromide (CTAB) and tetrakis(hydroxymethyl)phosphonium chloride (THPC).

CIT-stabilized GNPs

The Au particles of about 10 nanometers were synthesized according to the method reported by Frens *et al.*[37-39]

All the glassware which was used in these experiments was cleaned by 1 : 2 mixture of concentrated nitric acid and hydrochloric acid, and then immediately rinsed with ultra pure water. In a typical preparation, 40 ml of ultra pure water was boiled in advance and 10 ml of 0.1 wt % potassium tetrachloroaurate ($KAuCl_4$) aqueous solution was added to the boiling water. As the gold solution reached 100 ˚C, 5 ml of 0.9 wt % of trisodium citrate solution was added under vigorous stirring. After the addition of citrate in the gold solution, the color turned to blue, dark purple, and finally tuned to dark red in 20 min indicating the formation of GNPs. If bigger GNPs are needed, the size can be controlled by varying the $[Au^{3+}]$/[citrate] ratio (0.17 for 10 nm, 0.28 for 12 nm and 0.37 for 14 nm).

THPC-stabilized GNPs

The smaller Au nanoparticles with the diameter of around 1 ~ 2 nm were prepared by reduction of $KAuCl_4$ with tetrakis(hydroxymethyl)phosphonium chloride (THPC) using a modification of the work reported by Duff *et al.*[40]

An aqueous solution of sodium hydroxide (36 ml, 6.6 mM) and 0.8 ml of a THPC solution (67.0 mM) were mixed in a flask and vigorously stirred for 25 min. The aqueous solution of $KAuCl_4$ (1.35 ml, 1 wt %) was quickly added to the mixture under stirring for 30 min. The color of the solution rapidly changed from colorless to brown.

CTAB-stabilized GNPs

The positively charged nanoparticles have been synthesized by using a seed-mediated growth method in the presence of cetyltrimethylammonium bromide (CTAB) as cationic capping agent.[38,41] The preparation process has several steps: at first, the small seeds within 3.5 nm diameter are synthesized by chemical reduction of gold salt with a strong reducing agent (sodium borohydride) in the presence of a capping agent (citrate), then these seeds are added to the seed growth solution containing more metal salt, a weak reducing agent (e. g., ascorbic acid) and surfactant-directing agent (CTAB).

For the gold seeds synthesis, 0.25 mM $HAuCl_4$ and 0.25 mM trisodium citrate were dissolved in 20 ml ultra pure water. Ice cold $NaBH_4$ aqueous solution (0.6 ml, 0.1 M) was added to the mixture under stirring. The solution immediately tuned to red-orange indicating the formation of GNPs with the diameter of 3.5 ± 0.7 nm.[63] The seeds were stored at 25 °C for 3 h before use to allow excess borohydride to be decomposed by water.

For the preparation of spherical GNPs, the growth solution were prepared by 18 ml mixture containing 0.25 mM $HAuCl_4$ and 0.08 M CTAB, and the solution was heated up with stirring, then it was cooled to room temperature. 100 μl of 0.1 M ascorbic acid solution and growth solution were mixed, and 2 ml of 3.5 nm seed solution was added to the mixture under vigorous stirring for 10 min. The final color was dark red, and the particle size was 9 ± 1.5 nm. These GNPs could be used soon after the synthesis and were stable for a month due to the presence of bilayer of CTAB acting as stabilizer.

UV-vis spectroscopy

The study of localized surface plasmon resonance was recorded by Cary 300 UV-vis spectroscopy. The data were recorded with 1.0 nm data interval and 600 nm/min scan rate. The quartz cuvette with optical path length of 10 mm was used for the measurement.

TEM observation

TEM was performed at room temperature on a Philips EM 120 electron microscope operating at 120 kV and the images were collected by 2k × 2k Gatan ssCCD camera. Drops of diluted dispersions of the hybrids were deposited on carbon films coated 400-mesh copper grids. The excess liquid was blotted with filter paper.

Raman scattering and SERS spectroscopy

Benzenethiol (BT, from Sigma-Aldrich) was used as probe to quantify the enhancement of Raman scattering by the new 3D helical structures coated by gold nanoparticles. BT diluted solutions were prepared in water from a stock solution at 10^{-3}M. The ratio of SERS substrate and BT was 9/1 (vol/vol). Raman and SERS spectra of BT were recorded with a Labram HR800 (Horiba JobinYvon) using a 633 nm excitation of a Helium/Neon ion laser. The laser beam was focused on the sample using an objective 10x. The laser power was fixed at 5 mW. The accumulation time were 5 s and 120 s for pure BT and diluted BT, respectively.

References

[1] M. Quinten, A. Leitner, J. R. Krenn, F. R. Aussenegg, *Opt. Lett.*, **1998**, *23*, 1331-1333.

[2] (a) S. A. Maier, M. L. Brongersma, P. G. Kik, S. Meltzer, A. A. G. Requicha, H. A. Atwater, *Adv. Mater.*, **2001**, *13,* 1501-1505. (b) S. A. Maier, P. G. kik, H. A. A. Atwater, S. Meltzer, *Nat. Mater.*, **2003**, *2,* 229-232. (c) E. Ozbay, *Science*, **2006**, *311,* 189-193.

[3] S. I. Bozhevolnyi, V. S. Volkov, E. Devaux, J. Y. Laluet, T. W. Ebbesen, *Nature*, **2006**, *440,* 508-511.

[4] (a) S. Fullam, D. Cottell, H. Rensmo, D. Fitzmaurice, *Adv. Mater.*, **2000**, *12,* 1430-1432. (b) K. Y. Jiang, A. Eitan, L. S. Schadler, P. M. Ajayan, R. W. Siegel, *Nano Lett.*, **2003**, *3*, 275-277. (c) A. V. Ellis, K. Vijayamohanan, R. Goswami, N. Chakrapani, L. S. Ramanathan, P. M. Ajayan, G. Ramanath, *Nano Lett.*, **2003**, *3*, 279-282.

[5] H. C. Choi, M. Shim, S. Bangsaruntip, H. J. Dai, *J. Am. Chem. Soc.*, **2002**, *124*, 9058-9059.

[6] (a) S. Banerjee, S. S. Wong, *Nano Lett.*, **2002**, *2*, 195-200. (b) J. M. Haremza, M. A. Hahn, T. D. Krauss, S. Chen, J. Calcines, *Nano Lett.*, **2002**, *2*, 1253-1258.

[7] (a) E. Dujardin, C. Peet, G. Stubbs, J. N. Culver, S. Mann, *Nano Lett.*, **2003**, *3*, 413-417. (b) K. M. Bromley, A. J. Patil, A. W. Perriman, G. Stubbs, S. Mann, *J. Mater. Chem.*, **2008**, *18*, 4896-4801.

[8] C. L. Chen, P. Zhang, N. L. Rosi, *J. Am. Chem. Soc.*, **2008**, *130*, 13555–13557.

[9] A. Kuzyk, R. Schreiber, Z. Fan, G Pardatscher, E. M. Roller, A. Hogele, F. C. Simmel, A. O. Govorov, T. Liedl. *DNA-Based self-Assembly of Chiral Plasmonic Nanostructures with Tailored Optical Response*, Mesosclae and Nanoscale Phyics **2011**, arXiv:1108.3752.

[10] S. Zhang, W. Ni, X. Kou, M. H. Yeung, K. Sun, J. Wang, C. Yan, *Adv. Funct. Mater.*, **2007**, *17*, 3258-3266.

[11] (a) K. Aslan, Z. Leonenko, J. R. Lakowicz, C. D. Geddes, *J. Phys. Chem. B* **2005**, *109*, 3157-3162. (b) K. Aslan, J. R. Lakowicz, C. D. Geddes, *J. Phys. Chem. B* **2005**, *109*, 6247-6251.

[12] (a) R. G. Freeman, K. C. Grabar, K. J. Allison, R. M. Bright, J. A. Davis, A. P. Guthrie, M. B. Hommer, M. A. Jackson, P. C. Smith, D. G. Walter, M. J. Natan, *Science*, **1995**, *267*, 1629-1632. (b) B. Nikoobakht, M. A. El-Sayed, *J. Phys. Chem. A*, **2003**, *107*, 3372-3378. (c) A. Tao, F. Kim, C. Hess, J. Goldberger, R. R. He, Y. G. Sun, Y. N. Xia, P. D. Yang, *Nano Lett.*, **2003**, *3*, 1229-1233. (d) C. J. Orendorff, A. Gole, T. K. Sau, C. J. Murphy, *Anal. Chem.*, **2005**, *77*, 3261-3266.

[13] T. Hayakawa, Y. Usui, S. Bharathi, M. Nogami, *Adv. Mater.* **2004**, *16*, 1408-1412.

[14] L. R. Hirsch, J. B. Jackson, A. Lee, N. J. Halas, J. L. West, *Anal. Chem.*, **2003**, *75*, 2377-2381.

[15] S. R. Sershen, S. L. Westcoott, N. J. Halas, J. L. West, *J. Biomed. Mater. Res.*, **2000**, *51*, 293-298.

[16] C. Loo, A. Lowery, N. Halas, J. West, R. Drezek, *Nano Lett.*, **2005**, *5*, 709-711.

[17] G. Duan, W. Cai, Y. Luo, Y. Li, Y. Lei, *Applied Physics Letters*, **2006**, *89*, 181918 (3 pages).

[18] N. Pazos-Pérez, W. Ni, A. Schweikart, R. A. Alvarez-Peubla, A. Fery, L. M. Liz-Marzán, *Chem. Sci.* **2010**, *1*, 174-178.

[19] H. Im, K. C. Bantz, N. C. Lindquist, C. L. Haynes, S. H. Oh, *Nano Letters*, **2010**, *10*, 2231-2236.

[20] M. S. Hu, H. L. Chen, C. H. Shen, L. S. Hong, B. R. Huang, K. H. Chen, L. C. Chen, *Nat. Mater.*, **2006**, *5*,

102-106.

21 S. Zhang, W. Ni, X. Kou, M. H. Yeung, K. Sun, J. Wang, C. Yang, *Adv. Funct. Mater.*, **2007**, *17*, 3258-3266.

22 J. P. Singh, D. L. Liu, D. X. Ye, R. C. Picu, T. M. Lu, G. C. Wang, *Appl. Phys.Lett.*, **2004**, *84*, 3657-3659.

23 B. A. Korgel, *Science*, **2005**, *309*, 1683-1689.

24 P. X. Gao, W. Mai, Z. L. Wang , *Nano Lett.* **2006**, *6* (11), 2536-2543.

25 T. Delclos, C. Aimé, E. Pouget, A. Brizard, I. Huc, M. H. Delville, R. Oda, *Nano letters*, **2008**, 8, 1929-1935.

26 (a) A. Brizard, C. Aimé, T. Labrot, I. Huc, D. Berthier, F. Artzner, B. Desbat, R. Oda, *J. Am. Chem. Soc.*, **2007**, *129*, 3754-3762. (b) R. Oda, I. Huc, M. Schmutz, S. J. Candau, F. C. Mackintosh, *Nature*, **1999**, *399*, 566-569. c) R. Oda, M. Laguerre, I. Huc, F. Artzner, *J. Am. Chem. Soc.*, **2008**, *130*, 14705-14712.

27 H. Hiramatsu, F. E. Osterloh, *Langmuir*, **2003**, *19*, 7003-7011.

28 T. H. Galow, A. K. Boal, V. M. Rotello, *Adv. Mater.*, **2000**, *12,* 576-579.

29 S. L. Westcott, S. J. Oldenburg, T. R. Lee, N. J. Halas, *Langmuir*, **1998**, *14*, 5396-5401.

30 B. Sadtler, A. Wei, *Chem. Commun.*, **2002**, 1604-1605.

31 F. Osterloh, H. Hiramatsu, R. Porter, T. Guo, *Langmuir*, **2004**, *20*, 5553-5558.

32 M. S. Fleming, D. R. Walt, *Langmuir*, **2001**, *17*, 4836-4843.

33 I. Pastoriza-Santos, J. Pérez-Juste, L. M. Liz-Marzan, *Chem. Mater.*, **2006**, *18*, 2645-2647.

34 F. Chen, X. Li, J. Hihath, Z. Huang, N. Tao, *J. Am. Chem. Soc.*, **2006**, *128*, 15874-15881.

35 (a) D. V. Leff, L. Brandt, J. R. Heath. *Langmuir*, **1996**, *12*, 4723-4730. (b) E. Podstawka, Y. Ozaki, L. M. Proniewicz, *Appl. Spectrosc*, **2005**, *59*, 1516-1526.

36 R. R. Bhat, J. Genzer, *Nanotechnology*, **2007**, *18*, 025301.

37 G. Frens, *Nature Physical Science*, **1973**, *241*, 20-22.

38 S. Basu, S. K. Ghosh, S. Kundu, S. Panigrahi, S. Praharaj, S. Pande, S. Jana, T. Pal, *J. Colloid Interface Sci.* **2007**, *313*, 724-734.

39 S. Pramanik, P. Banerjee, A. Sarkar, S. C. Bhattacharya, *J. Luminescence* **2008**, *128*, 1969-1974.

40 (a) D. G. Duff, A. Baiker, *Langmuir* **1993**, *9*, 2301-2309. (b) D. G. Duff, A. Baiker, *Langmuir* **1993**, *9*, 2310-2317.

41 (a) B. Nikoobakht, M. A. El-Sayed, *Chem. Mater.*, **2003**, *15*, 1957-1962. (b) A. Gole, C. J. Murphy, *Chem. Mater.*, **2004**, *16*, 3633-3640.

42 L. Ratke, P. W. Voorhees, *Growth and Coarsening: Ostwald Ripening in Material Processing*. Springer, New York, **2002**, pp. 117–118.

43 R. Heinz, A. Stabel, F. C. De Schryver, J. P. Rabe*J. Phys. Chem.*, **1995**, *99*, 505–507.

44 Daniel, M.-C.; Astruc, D. *Chem. ReV.* **2004**, *104*, 293.

45 McLean, J. A.; Stumpo, K. A.; Russell, D. H. *J. Am. Chem. Soc.*, **2005**, *127*, 5304.

46 M. N. Martin, J. I. Basham, P. Chando, S. K. Eah, *Langmuir* **2010**, *26*, 7410.

47 Patzke, G. R.; Krumeich F.; Nesper, R. *Angew. Chem. Int. Ed.*, 2002, *41*, 2446-2461.

[48] J.P. Singh, D. L. Liu, D. X. Ye, R. C. Picu, T. M. Lu, G. C. Wang, *Appl. Phys.Lett.* **2004**, *84*, 3657.

[49] K. T. Yong, M. T. Swihart, H. Ding, P. N. Prasad, *Plasmonics* **2009**, *4*, 79.

[50] J. H. Kim, W. W. Bryan, T. R. Lee, *Langmuir* **2009**, *24* (19), 11147.

[51] C. Radloff, R. A. Vaia, *Nano Letters* **2005**, *5* (6), 1187.

[52] Barbic, M.; Mock, J. J.; Smith, D. R.; Schultz, S. J. *J. Appl. Phys.***2002**, *91*, 9341.

[53] Kottman, J. D.; Martin, O. J. F.; Smith, D. R.; Schultz, S. *Chem.Phys. Lett.* **2001**, *341*, 1.

[54] Mock, J. J.; Smith, D. R.; Schultz, S. *Nano. Lett.* **2003**, *3*, 485.

[55] I. Hussain, S. Graham, Z. Wang, B. Tan, D. C. Sherrington, S. P. Rannard, A. I. Cooper, M. Brust, *J. Am. Chme. Soc.*, **2005**, *127*, 16398.

[56] Y. Shen, J. Wang, U. Kuhlmann, P. Hildebrandt, K. Ariga, H. Moehwald, D. G. Kurth, T. Nakanishi, *Chem. Eur. J.* **2009**, 15, 2763-2767

[57] K. T. Carron, L. G. Hurley, *J. Phys. Chem.* **1991**, *95*, 9979.

[58] C. A. Szafranski, W. Tanner, P. E. Laibinis, R. L. Garrell, *Langmuir* **1998**, *14*, 3570.

[59] B. Ren, G. Picardi, B. Pettinger, R. Schuster, G. Ertl, *Angew. Chem. Int. Ed.* **2005**, *44*, 139.

[60] G. Socrate, *Infrared and Raman Characteristic Group Frequencies: Tables and Charts, third ed. Wiley Chichester, England*, **2001**, 173.

[61] N. Leopold, S. Cînta-pînzaru, M. baia, E. Antonescu, O. Cozar, W. Kiefer, J. Popp, *Vibrational Spectroscopy*, **2005**, *39*, 169-176.

[62] E. Hutter, J. H. Fendler, *Adv. Mater.*, **2004**, *16*, 1685-1706.

[63] N. R. Jana, L. Gearheart, C. J. Murphy, *J. Phys. Chem. B*, **2001**, *105*, 4065-4067.

General Conclusion

General conclusion

In this work, we have presented the dynamic self-assembly systems obtained by amphiphilic molecules. Particularly, we have developed *in situ* morphology transformation caused by "out-of- equilibrium" process.

Chapter I described bibliographical study on various chiral supramolecular structures expanding to morphological control, and *in situ* transformation to different morphologies. A number of literature report morphology transition from chiral to achiral structure, however achiral to chiral transformation, especially at constant temperature, have not yet reported.

In chapter II, we demonstrated the vesicle to helix *in situ* transformation. The cationic amphiphile based on quaternary ammonium headgroups with acetate counter-anion (C_nAc) we have used stronger affinity with anionic nucleotides due to their cooperative interaction than with acetate anions. As a result, upon addition of nucleotide solution into the vesicle solution formed by non-chiral C_nAc surfactant, acetate is exchanged *in situ* to nucleotide and the nucleo-lipids are formed. This allowed us to directly follow the morphology transition from spherical vesicles to micrometric helices *in situ via* counter-anion exchange. On the molecular aspect, ion exchange occurred very quickly in few minutes. These nucleotides which were confined at the membrane surface reorganized themselves through the H bond and $\pi-\pi$ stacking. Subsequently, the chirality transfer to supramolecular aggregation occurred, along with the nucleotide reorganization. The kinetics of such a chirality expression at supramolecular level occurred more slowly than the ion exchange (few hours). This suggests that the control of kinetics of counter-anion interactions gives possibility to design tunable morphology of self-assembled new helical architectures.

In chapter III, we reported the *in situ* right (*P*) to left-handed (*M*) helicity transition in supramolecular aggregates by counter-anion exchange from L-tartrate to D-tartrate. Gemini-tartrate amphiphile form chiral nanometrical fibers with various shapes such as flat, twisted, helical ribbons and tubules as a function of various parameters such as enantiomeric

excess, temperature and composition. In this study we particularly focused on the *in situ* enantiomeric excess control, which was produced by filtration/addition of opposite chiral acid solution with the various equivalents. The final morphologies were strongly dependent on the final ee value: lower ee (ee = "0" and "-0.33") provided twist ribbons with long twist pitches. The helicity inversion occurred much rapidly with higher ee value (ee = "-0.60" and "-0.90"). This system **shows** the first direct visualization of *in situ* chirality inversion of chiral supramolecular structures at mesoscopic level (20 nm – microns).

We then used these chiral organic assemblies as templates to form chiral inorganic hybrid nanostructures. Chiral nanoribbons of gemini-tartrate can be transcribed to 3D silica nanohelices *via* sol-gel polycondensation. By functionalizing them with amino or mercapto group, gold nanoparticle with various size (1 ~ 15 nm) can be organized on silica-nanohelices. Depending on the coupling agent, GNPs showed unique behavior in suspension: small particle (1 ~ 2 nm) showed growth at the surface of silica, and larger particle (> 10 nm) showed strong SPR peaks. Especially, the 3D network of novel GNPs/silica-nanohelices composites based on CIT-stabilized GNPs can potentially be used for SERS-based sensing applications such as ultra-sensitive chemical and biological sensors in liquid phase. Compared to the traditional 2D SERS substrate, our 3D network system can open a totally new perspective towards high detection of molecules of interest through accumulation under flow.

Nano/Micro Auto-Assemblages Chiraux de Tensioactifs Cationiques:
du comportement dynamique des architectures supramoléculaires jusqu'aux nanomatériaux hybrides

Nous avons étudié les comportements dynamiques d'auto-assemblage des tensioactifs cationiques non-chiral en présence du contre-anion chiral.

Lorsque le nucléotide anionique chiral est ajouté à des vésicules cationiques, la transition morphologique se produit et transforme in situ des vésicules sphériques en hélices micrométriques.

D'autres types de Gemini tensioactifs cationiques forment des rubans nanométriques hélicoïdaux, en présence de tartrate contre-anions. La forme et l'hélicité de ces rubans peuvent être contrôlés in situ par la variation de l'excès énantiomérique.
En outre, les nanohélices organiques peuvent être transcrite en nanohélices 3D de silice via une polycondensation sol-gel.

Ces nanohelices de silice fonctionnalisées avec des groupes aminés peuvent interagir fortement avec des nanoparticules d'or (GNPs; 1 ~ 20 nm). Le réseau 3D de -nanohélices GNPs/silice sont potentiellement utilisables pour des applications de capteurs basée sur les SERS comme ceux chimiques et biologiques ultra-sensibles en phase liquide.

Chiral Nano/Micro Self-Assemblies of Cationic Surfactants:
from dynamic behavior of supramolecular architectures towards hybrid nanomaterials

We have studied the dynamic self-assembly behaviors of non-chiral cationic surfactants in the presence of chiral counter-anion.

When the chiral anionic nucleotides are added to cationic vesicles, morphology transition occurs and spherical vesicles transform in situ to micrometric helices.

Other types of cationic surfactant, gemini surfactants form nanometric helical ribbons in the presence of tartrate counter-anion. The shape and helicity of these self-assembled structures can be controlled in situ by the variation of enantiomeric excess.

In both cases, they form gels in water by creating extended networks of nanometric to micrometric chiral fibers.

Additionally, the organic nanohelices can be transcribed to 3D silica nanostructures via sol-gel polycondensation. These silica nanohelices functionalized with amino group can interact strongly with gold nanoparticles (1 ~ 20 nm). The 3D network of GNPs/silica-nanohelices can potentially be used for SERS-based sensing applications such as ultra-sensitive chemical and biological sensors in liquid phase.